EFFICIENT HIGH-PRECISION MODELING OF IRREGULARITIES IN LAMINATED SYSTEMS

By

Jae Seok Ahn

Dissertation

Submitted to the Faculty of the

Graduate School of Vanderbilt University

In partial fulfillment of the requirements

for the degree of

DOCTOR OF PHILOSOPHY

in

Civil Engineering

August, 2010

Nashville, Tennessee

Approved

Professor Prodyot K. Basu

Professor Sankaran Mahadevan

Professor Caglar Oskay

Professor Carol A. Rubin

To my parents, Young-Su An

and

Duk-Hyang Hur

ACKNOWLEDGEMENTS

At first, I would like to say a special word of thanks for my advisor, Dr. Prodyot K. Basu. This work would not have been possible without his guidance and encouragement. Especially, he gave me opportunity of studying abroad and has always encouraged me in not only my studies but also my life in America. His love for students and his passion for academic work made an indelible impression on me. I am especially indebted to Dr. K.S. Woo, professor in Yeungnam University, who has been supportive of my research work and given me much sincere advice in living abroad. Also, I would like to thank my committee members, Dr. Sankaran Mahadevan, Dr. Caglar Oskay, and Dr. Carol Rubin, for their advice and suggestions on my dissertation.

In addition, I would like to express my gratitude to National Research Foundation of Korea for giving me scholarship in the program for the students to take overseas degree. I am also thankful for valuable advice from Dr. J.H. Jo in Korea Electric Power Corporation especially when I was coding my research software. I am grateful for friendship and encouragement to many graduate students in Yeungnam University as well as in Vanderbilt University. Furthermore, encouraging words of my great friends, Y.H. Yun and Y.J. Lee, revived my dropping spirits in living away from home.

Finally, I want to express my heartfelt gratitude to my parents, my elder brother-in-law, C.H. Kim, and my sister, J.Y. Ahn. Especially I would like to thank my parents, Y.S. An and D.H. Hur, whose love and guidance are with me in whatever I pursue.

TABLE OF CONTENTS

Page

LIST OF TABLES

LIST OF FIGURES

CHAPTER I

INTRODUCTION

1.1. Overview and Motivation

In order to design objects using modern materials like composites, engineers represent the physical behavior in terms of mathematical models. Apart from embodying the physical laws governing the behavior, such representations often incorporate certain simplifying assumptions to enable quick solutions with readily available technology, without adversely affecting the performance. However, as modeling and computational technologies advance, more realistic modeling approaches are being developed by dropping some of the simplifying assumptions so that the real behavior could be represented accounting for various kinds of irregularities which are unavoidable in practice. Moreover, in spite of the appearance of homogeneity in the macro scale, real materials cannot be treated as being homogeneous at smaller scales, say, at meso or micro scales. Currently, researchers are trying to devise efficient modeling methods for inhomogeneous systems accounting for the presence of various irregularities.

In engineering design, irregularities can be defined as discontinuities or abrupt changes in geometry and/or material properties. Generally, such irregularities create a disruption in the stress pattern, resulting in the spiky formation in the stress/strain field. These locations of steep stress gradients may lead to damage initiation and propagation, culminating in failure. For instance, irregularities like crack or delamination would appear in the normal aging process or abnormal service conditions even if the initial

conditions of the components did not apparently have any irregularity at the time of manufacture. After an irregularity is initiated, the rate of its propagation affects the fatigue life of the system or a component under cyclic loading conditions. In practice, even under most ideal conditions, irregularities cannot be avoided to satisfy the functional requirements, strength requirements and various constraints on the object being designed. For instance, synergistic systems like composites are heterogeneous for being a combination of different materials. Another example is that of irregularities in aircraft structure and skin. Spar and ribs in the wing are provided with cutouts for weight reduction and other functional reasons. Moreover, the presence of the holes in the wing ribs redistributes the membrane stresses in the skin material which, in turn, may affect the stability of the component significantly.

Specially, materials like engineered composites consist of a synergistic combination of two categories of materials, reinforcement and matrix, with significantly different physical or chemical properties. From the point of view of mechanical behavior, fiber-reinforced composites are similar to reinforced concrete, one of the popular materials of civil engineering construction. The reinforcements, being much stronger, impart the mechanical strength; whereas the matrix keeps the reinforcements in place and also protects them against brittle failure. The composite materials are commonly classified into fibrous composites, particulate composites, and laminated composites. Among them, the laminated composites are made in layers with fiber reinforcement in each layer embedded in a resinous matrix. The laminated composite material may have a flat (as a plate) or curved (as a shell) configuration of unidirectional fibers or woven fibers in a matrix. The orientation of fibers in each layer is changed for optimal performance. In

commercial laminated composites, reinforcement material may consist of fibers (woven or otherwise) of glass, aramid, carbon, kevlar, or suitable combinations thereof. Polymers like epoxy resin, polyimide, polyester, vinyl ester, etc., are used as the matrix material. Due to the property of high strength combined with lightweight, composites have found widespread applications in aerospace components, marine vehicles, sports equipments, automobile bodies, bicycle frames, medical prosthetics, and more.

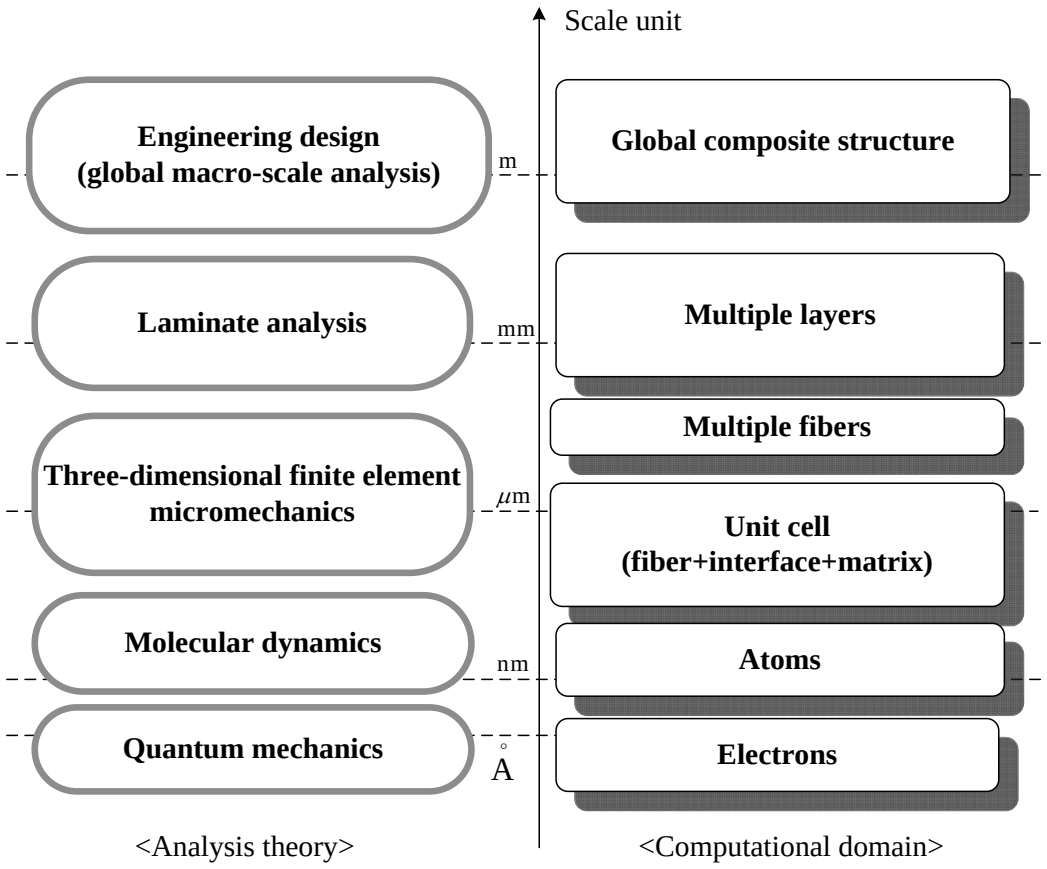

Fig. 1.1 Basic scope of analysis for laminated composite materials

As shown in Fig. 1.1, from the point of view of scales involved, the analysis of structural elements made of laminated composite materials comprises of several steps.

For instance, from the macro mechanical point of view, a lamina is considered as a continuum. It signifies the absence of irregularities in a lamina. This assumption of homogeneity in a lamina is enforced by using weight-averaged apparent macroscopic properties. Also, the anisotropic nature of the properties of a lamina is based on orientation of the fibers and can be characterized, say, as orthotropic or transversely isotropic. In the presence of damage in a lamina, a micromechanical approach may need to be considered. As laminated composites have complex structure, several failure modes are possible for representing the damage states. Apart from the presence of flaws or manufacturing defects, a composite structure or component may undergo damage due to impact of objects, shock loading, or exposure to large number of loading cycles. The type of damage in a particular case can be determined by the type of the fiber and matrix materials, the proportion of each material component, the disposition of fibers, and, of course, the nature of stresses created by external loads. The damage may appear as

- Fiber breaking: tension in fiber direction
- Fiber buckling: compression in fiber direction
- Matrix fracture: tension in transverse direction
- Matrix compression failure/matrix crazing: compression in transverse direction
- Fiber debonding: fiber-matrix bond fails
- Delamination: separation between layers

One of the important applications of composite laminates is its use in bonded patch repair of damaged metallic, and non-metallic structures and components. Generally, for patchwork, using materials different from those in the original component has been a popular method of strengthening a damaged structure. In the past, aluminum or steel plates for patch repair works were employed in order to cover the damaged area with

cracks or other flaws. The connection between damaged component and such patch material used rivets. However, due to the holes created in the parent material and the rigidity of rivets, the repair work introduced additional irregularities in the skin surrounding the patch. In order to avoid this problem, more recent repair techniques have use bonded composite materials which offer both strength and weight advantages. Such fiber-reinforced composites can be laminated with different fiber orientations. Epoxy resin is often used as a bonding adhesive between the fiber-reinforced composite and the surface of the parent material. Heat and pressure are sometimes needed in order to ensure proper adhesion to the metal surface. Physically the patch repair work is an additional source of irregularity over and above the already existing irregularity within the original system. In other words, when the original component has cracks or holes, it has geometrical irregularities. The addition of patch repair work introduces additional geometric and material irregularities. The use of composite patch material, introduces another source of material irregularity in the system. Furthermore, if debonding occurs between the patch and parent material, further geometric irregularity appears in the system. Accounting for all these irregularities in the repaired component is no doubt of considerable complexity to the analyst. In bonded patch repair work, there are two distinct situations of stress transfer which have the potential to cause interfacial failure or local failure in the parent material. Premature failure of this kind before the limit capacity of the component is reached can be of special concern. Also, for optimal performance of complex structures, components may need to be customized. For greater efficiency, it may be sometimes be desirable to induce a pretension in the patch during the repair

process to further attenuate the stress intensity factor (SIF) in the cracks being patch repaired and thus extend the fatigue life of the structure or component.

Over the past few decades, research on the systems with various irregularities has been undertaken utilizing analytical solutions, physical experiments, and numerical simulations. As analytical solution of complex problems of practical interest is not possible, one has to apply numerical discrete modeling techniques, sometimes, coupled with experimental verification. Also, as practical problems of interest numerical simulation may often be highly compute intensive demanding significant resources, it is imperative that reliable discrete numerical methods which are computationally efficient will be welcome.

The increasing power of personal computers and advances in numerical simulation techniques has enabled accurate prediction of the behavior of complex problems. Of the many numerical methods like finite difference methods, finite element methods, boundary element methods, meshless methods, wavelet methods, etc., it is true that finite element methods has been most widely adopted as the standard modeling and simulation tool for problems of the continua. Although the conventional finite element methods based on lowest order elements and mesh refinement are widely used to analyze systems with irregularities, it is found to be inferior to some advanced implementations of the method by way of solution accuracy, computational efficiency, and ease of use. In laminated systems which have built-in irregularities, when augmented with others like cutouts, patches, delamination, debonding, etc. and environmental factors, the development of a more advanced finite element modeling scheme may be in order.

1.2 Literature Review

1.2.1 Basic Laminate Analysis

In laminated composites, a lamina, often called as layer, is inherently heterogeneous from microscopic point of view. The simplest representation of laminated composite material considers macro-mechanical behavior of a lamina signifying homogeneous linear elastic continuum without any discontinuity. In this macroscopic representation, displacement formulations of composite plates or shells have been based on two-dimensional (2D) elasticity theory, three-dimensional (3D) elasticity theory or combinations thereof.

2D modeling of laminated plates or shells by way of dimensional reduction from 3D to 2D represents a way of the extension of the assumptions made in single-layer plate or shell theories, like Kirchhoff-Love theory or classical plate theory (Ugural, 1998), Reissner-Mindlin theory or shear deformation plate theory (Reissner, 1945; Mindlin, 1951), and higher order theories by Hildebrand et al. (1938). These theories are often called C_z^1 function theories (Rohwer et al., 2005). Among some C_z^1 function theories, the classical lamination theory, CLT (Reissner and Stavsky, 1961; Stavsky, 1961; Dong et al., 1962; Yang et al., 1966; Whitney and Leissa, 1969) is the extension of the classical plate theory, as shown in Eq. 1.1.

$$\begin{Bmatrix} u(x,y,z,t) \\ v(x,y,z,t) \\ w(x,y,z,t) \end{Bmatrix} = \begin{Bmatrix} u_0(x,y,t) \\ v_0(x,y,t) \\ w_0(x,y,t) \end{Bmatrix} + z \begin{Bmatrix} -\dfrac{\partial w_0(x,y,t)}{\partial x} \\ -\dfrac{\partial w_0(x,y,t)}{\partial y} \\ 0 \end{Bmatrix} \tag{1.1}$$

In this equation, (*x*, *y*, *z*) represent the Cartesian coordinate system with *z*-axis normal to the reference surface of the plate with (*u*, *v*, *w*) representing displacements of a point in these directions, *t* refers to the time variable, and (u_0, v_0, w_0) are mid-surface displacement components. In CLT, transverse shear strains are neglected, and the number of degrees of freedom (NDF) is three. Unlike CLT, in the first-order shear deformation lamination theory (FSLT) (Whitney and Pagano, 1970; Reissner, 1972, 1979), transverse normal displacements do not remain perpendicular to the mid-surface after deformation and thus the transverse shear strains are included, as in Eq. 1.2.

$$\begin{Bmatrix} u(x,y,z,t) \\ v(x,y,z,t) \\ w(x,y,z,t) \end{Bmatrix} = \begin{Bmatrix} u_0(x,y,t) \\ v_0(x,y,t) \\ w_0(x,y,t) \end{Bmatrix} + z \begin{Bmatrix} u_1(x,y,t) \\ v_1(x,y,t) \\ 0 \end{Bmatrix} \tag{1.2}$$

Here (u_1, v_1) are rotations of a transverse normal with respect to *y*-axis and *x*-axis leading to NDF equal to 5. As transverse normal displacement is not a function of coordinate *z* in the thickness direction, FSLT requires shear correction factors (Srinivas et al., 1970; Chow 1971; Bert, 1973; Whitney, 1973; Wittrick, 1987). The shear correction factors depend not only on the laminas and geometric parameters, but also on the natural boundary conditions at top and bottom surfaces. So it is difficult to determine the shear correction factors for arbitrarily laminated composite plate structures resulting from the assumption that the transverse shear strain is constant through the whole thickness. Additionally, Hinton and Owen (1984) proposed expressions as the extension of the degenerated shell concept (Ahmed et al., 1970) with first-order shear deformation plate theory for applying laminated plates and shell. As an extension of FSLT, the quadratic variations (Sun and Whitney, 1973; Whitney and Sun, 1973) and cubic variations (Lo et al., 1977, 1978) of in-plane displacements through the plate thickness were introduced by

adding some terms to FSLT, which are often called higher order C_z^1 functions theories. The basic form of the higher order C_z^1 function theories for *n*-layered plate or shell is as follows.

$$\begin{Bmatrix} u(x,y,z,t) \\ v(x,y,z,t) \\ w(x,y,z,t) \end{Bmatrix} = \begin{Bmatrix} u_0(x,y,t) \\ v_0(x,y,t) \\ w_0(x,y,t) \end{Bmatrix} + \sum_{i=1}^{n} z^i \begin{Bmatrix} u_i(x,y,t) \\ v_i(x,y,t) \\ 0 \end{Bmatrix} \tag{1.3}$$

Here NDF is 3+2*n*. In such theories, the additional degrees of freedom except the terms related to FSLT are often difficult to explain in physical terms. Reddy (1984) used the third-order laminated plate theory by imposing the condition of vanishing transverse shear strains on the top and bottom surface of the plate based on the previously published third-order theory (Lo et al., 1977, 1978) in order to reduce NDF, as shown in Eq. 1.4, noting that *h* represents the plate thickness.

$$\begin{Bmatrix} u(x,y,z,t) \\ v(x,y,z,t) \\ w(x,y,z,t) \end{Bmatrix} = \begin{Bmatrix} u_0(x,y,t) \\ v_0(x,y,t) \\ w_0(x,y,t) \end{Bmatrix} + z \begin{Bmatrix} u_1(x,y,t) \\ v_1(x,y,t) \\ 0 \end{Bmatrix} - \frac{4z^3}{3h^2} \begin{Bmatrix} u_1(x,y,t) + \dfrac{\partial w_0(x,y,t)}{\partial x} \\ v_1(x,y,t) + \dfrac{\partial w_0(x,y,t)}{\partial y} \\ 0 \end{Bmatrix} \tag{1.4}$$

When using higher-order polynomials for in-plane displacements, there is no need to use shear correction factors. These theories provide a slight increase in accuracy relative to the FSLT approaches at the expense of increased computational effort. Based on above third-order laminate plate theory by Reddy (1984), Senthilnathan et al. (1987) separated the transverse displacement w_0 into a bending contribution w_b and a shear contribution w_s. The resulting displacement fields are as shown in Eq. 1.5.

$$\begin{Bmatrix} u(x,y,z,t) \\ v(x,y,z,t) \\ w(x,y,z,t) \end{Bmatrix} = \begin{Bmatrix} u_0(x,y,t) \\ v_0(x,y,t) \\ w_b(x,y,t) + w_s(x,y,t) \end{Bmatrix} - z \begin{Bmatrix} \dfrac{\partial w_b(x,y,t)}{\partial x} \\ \dfrac{\partial w_b(x,y,t)}{\partial y} \\ 0 \end{Bmatrix} - \frac{4z^3}{3h^2} \begin{Bmatrix} \dfrac{\partial w_s(x,y,t)}{\partial x} \\ \dfrac{\partial w_s(x,y,t)}{\partial y} \\ 0 \end{Bmatrix} \quad (1.5)$$

This theory can reduce NDF to four. However, it was pointed out (Rohwer, 1992) that results of the theory would sometimes be worse than those by FSLT. As an example of using different polynomial degrees for in-plane and transverse displacements, Whitney and Sun (1974) proposed a quadratic polynomial for transverse displacement, *w*, keeping the in-plane displacements, *u* and *v*, linear. On the other hand, Kwon and Akin (1987) modified the theory by eliminating the term linear in *w* by placing the reference surface in the mid-surface and enforcing zero shear strains at upper and lower surfaces. This form is given by Eq. 1.6.

$$\begin{Bmatrix} u(x,y,z,t) \\ v(x,y,z,t) \\ w(x,y,z,t) \end{Bmatrix} = \begin{Bmatrix} u_0(x,y,t) \\ v_0(x,y,t) \\ w_0(x,y,t) \end{Bmatrix} + z \begin{Bmatrix} u_1(x,y,t) \\ v_1(x,y,t) \\ 0 \end{Bmatrix} - z^2 \begin{Bmatrix} 0 \\ 0 \\ w_2(x,y,t) \end{Bmatrix} \quad (1.6)$$

with

$$\begin{Bmatrix} \dfrac{\partial w_2(x,y,t)}{\partial x} \\ \dfrac{\partial w_2(x,y,t)}{\partial y} \end{Bmatrix} = -\frac{4}{3h^2} \begin{Bmatrix} u_1 + \dfrac{\partial w_0(x,y,t)}{\partial x} \\ v_1 + \dfrac{\partial w_0(x,y,t)}{\partial y} \end{Bmatrix} \quad (1.7)$$

This allowed NDF to be reduced to five. As pointed out by (Rohwer, 2005), no shear correction factor is needed here, but the accuracy is found to be inferior to FSLT utilizing a proper shear correction factor. Reissner (1975) used cubic in-plane displacement variation and quadratic out-of-plane variation for application to laminated plates, as in Eq. 1.8.

$$\begin{Bmatrix} u(x,y,z,t) \\ v(x,y,z,t) \\ w(x,y,z,t) \end{Bmatrix} = \begin{Bmatrix} u_0(x,y,t) \\ v_0(x,y,t) \\ w_0(x,y,t) \end{Bmatrix} + z\begin{Bmatrix} u_1(x,y,t) \\ v_1(x,y,t) \\ 0 \end{Bmatrix} + z^2\begin{Bmatrix} 0 \\ 0 \\ w_2(x,y,t) \end{Bmatrix} + z^3\begin{Bmatrix} u_3(x,y,t) \\ v_3(x,y,t) \\ 0 \end{Bmatrix} \quad (1.8)$$

Attention of some important behaviors in multilayered structures is to describe a piecewise continuous displacement field through the plate thickness direction, which is known as zigzag behaviors, and fulfill inter-laminar continuity of transverse stresses at each layer interface. However, most laminate theories based on CLT or FSLT are incapable of accurately representing these effects or, often give highly erroneous results even if the global behavior such as gross deflection, critical buckling loads, and fundamental vibration frequencies can often be accurately determined, if thinner laminates are involved. Especially, in thick laminated systems, CLT or FSLT cannot give reliable results even in global laminate response. Thus the analysis of some composite structural components may require the use of 3D elasticity theory. The analytical solutions based on 3D elasticity theory for various laminated systems were obtained by some researchers (Pagano, 1969, 1970; Pagano and Hatfield, 1972; Srinivas et al., 1970; Srinivas and Rao, 1970; Noor, 1973a, 1973b; Savoia and Reddy, 1992; Varadan and Bhaskar, 1991; Ren, 1987). In finite element analysis, conventional solid elements based on 3D elasticity theories have been usually used to provide a more realistic description of the kinematics of composite laminates for representing discrete layer transverse shear effect in the assumed displacement fields. Reddy (1987) adopted layerwise approach based on 3D elasticity theory with piecewise expansions of three displacement components. In the layerwise theory, displacement field within any layer can be written as

$$\begin{Bmatrix} u(x,y,z,t) \\ v(x,y,z,t) \\ w(x,y,z,t) \end{Bmatrix} = \sum_{i=1}^{n} \begin{Bmatrix} u_i(x,y,t)\alpha_i(z) \\ v_i(x,y,t)\alpha_i(z) \\ w_i(x,y,t)\beta_i(z) \end{Bmatrix} \tag{1.9}$$

Here, for N layers, the number of free degrees of freedom will be $3N(n+1)$, which can be reduced to $3(Nn+1)$ by applying displacement compatibility at the layer interfaces. Based on this concept, Ahmed and Basu (1994) proposed higher-order layerwise theory to effectively account for aforementioned deficiencies of continuous functional representations across the thickness of a plate or shell due to abrupt changes in material properties, in which displacements are defined over layer thickness in terms of in-plane coordinates only. Although conventional solid elements or the layerwise approach can provide accuracy to satisfy the conditions like the interlaminar continuity of the transverse stresses and zigzag behavior of displacement fields, the critical problem of such techniques is increased computational effort. For computational efficiency, Owen and Li (1987a, 1987b) assumed piecewise linear variations of the in-plane displacements and a constant value of the lateral displacement across the thickness. Also, Lee et al. (1990, 1994) presented the model for laminated plates with a layer-wise cubic variation of the in-plane displacement. These modifications can partially satisfy the conditions of zigzag behavior in displacements and interlaminar continuity of transverse stresses. As other ways to improve efficiency of analysis, some mixed variational principles in terms of displacements and transverse stresses have been suggested for laminated plates and shells (Murakami, 1986; Murakami and Toledano, 1987; Carrera, 1996, 1998, 1999; Cho and Kim, 2001). However, these theories also have some disadvantages like using C_{xy}^{1} basis functions requiring too complicated formulations as compared to displacement-based formulations, or only obtaining good results for limited number of problems. So,

displacement-based formulations have still been in the mainstay for analyzing laminated composite plates and shells.

For more efficient analysis in terms of solution accuracy and computational efficiency, techniques using sequential methods, multistep methods, or methods based on a combination of different mathematical models have been proposed. Sequential or multistep methods can be divided into two categories such as non-iterating sequential methods and iterating sequential methods. For non-iterating sequential methods, Thompson and Griffin (1990) modeled the global region using FSLT finite elements, while the local region by 3D finite elements. One of the main criticisms of non-iterative sequential methods is that influence of the local region on the global region is not well understood. In other words, the equilibrium of forces along the boundaries between different models is not maintained while the displacement continuity is ensured. In order to avoid this shortcoming, iterative sequential methods were suggested by Mao and Sun (1991) and Whitcomb and Woo (1993a, 1993b). Park and Kim (2002) described two re-analysis procedures, which utilize the post-processing results for improvement. These methods attempt to iteratively establish force equilibrium along the boundaries as well as impose displacement continuity, mainly using the same mathematical model. One of the main disadvantages of these methods is the problem of incorporation of nonlinearity into the analysis. Unlike sequential or multistep methods, simultaneous mixed methods combine different mathematical models to analyze the entire computational domain, including the use of distinctly different levels of *h*- or *p*-refinements in specified local regions. Here different sub-regions with different mathematical models are explicitly accounted for and is, thus, easily amenable to nonlinear analysis. One simple scheme of

simultaneous application of mixed methods to composite laminate analysis is the concept of selectively grouping the plies in the vicinity of the location where accurate stress values are desired (Wang and Crossman, 1978; Pagano and Soni, 1983; Jones et al., 1984; Chang et al., 1990; Sun and Liao, 1990). Another scheme to apply simultaneous mixed methods is to use multipoint constraint equations or Lagrange multipliers. Here the variational statement is supplemented with additional terms to enforce compatibility between adjacent sub-regions. For 2D problems, Aminpour et al. (1992) used an assumed one-dimensional (1D) interface function in conjunction with a hybrid variational formulation to couple sub-regions with incompatible mesh discretizations, using a 2D mathematical model like FSLT within the entire computational domain. Although the Lagrange multiplier approach can be used to couple sub-regions which use different mathematical models, the method to connect different mathematical models have rarely been used, because the implementation would be very cumbersome. The most popular approach for connecting different mathematical models (like, simultaneous 2D to 3D modeling of plates and shells) is to implement special transition elements (Surana, 1980; Liao et al., 1988; Davila, 1994; Garusi and Tralli, 2002).

1.2.2 Free-Edge Stresses and Delamination

For laminated systems, finding free-edge stresses and representing delamination can be regarded as a challenging problem due to geometrical irregularities and associated stress singularity. It is well known that high interlaminar stresses at the free edges arise from discontinuity of elastic properties between layers. The stress distribution in the vicinity of the free edges is in the 3D state even if the laminated components are only

subjected to in-plane loading. These high stresses can lead to delamination of laminates at a load lower than the failure strength. Therefore, the accurate determination of the interlaminar stresses is crucial to correctly describe the laminate behavior and to prevent its early failure, characterized by the onset of delamination. Over the years, the interlaminar stress distribution at free edge in composite laminates has been investigated by many researchers. However, no exact solution is known to exist because of the inherent complexities involved in the problem. Amongst analytical methods, the first approximate solution for interlaminar shear stresses was by Puppo and Evensen (1970). Other approximate theories were used by Pagano (1978a, 1978b), based on assumed in-plane stress. Wang and Choi (1982a, 1982b) studied the free edge singularities with quasi-3D analytical solution. Kassapoglou (1990) used the principle of minimum complementary energy and the force balance method for general unsymmetrical laminates under combined in-plane and out-of-plane loads. The first numerical method of edge effect was given by Pipes and Pagano (1970). Altus et al. (1980) developed a 3D finite difference solution to study the edge-effect problem in angle-ply laminates, and Spiker and Chou (1980) used hybrid-stress finite element. Whitcomb et al. (1982) showed the reliability of quasi-3D finite element approach. Until that time, in analytical and numerical techniques, the stresses and strains had been assumed to be independent of the axial coordinate. Thus analysts only had to be independent of the axial coordinate. Robbins and Reddy (1996) presented displacement based variable kinematic formulations with the assumption that the stresses and strains are dependent on all three coordinates. Tahani and Nosier (2003a, 2003b) developed an elasticity formulation for finite general cross-ply laminated systems subjected to extension and thermal loading.

The delamination process in laminated plates is usually divided into delamination initiation and delamination propagation. At first, for delamination initiation, the point or average stress criteria proposed by Whitney and Nuismer (1974) have often been used in the macro level. Kim and Soni (1984) applied the criteria to carbon fiber reinforced plastics under in-plane tensile and compressive loading giving experimental and analytical solutions. Davila and Johnson (1993), and Matthews and Camanho (1999) developed a technique by combining the previous stress analysis with a characteristic distance, which are applied to composite bolted joints and post buckled dropped-ply laminates, respectively. Next, to characterize the growth of delamination, the use of linear elastic fracture mechanics has become common practice and has proven to be effective if other material nonlinearities can be neglected. So, in the context of a fracture mechanics approach, the propagation of an existing delamination is analyzed by comparing the amount of energy release rate (ERR) with interface toughness. Moreover, the behavior of delamination in laminated systems is sometimes dominated by interlaminar tension and shear stresses at discontinuities that create a mixed-mode (I, II and III) stress field. For determining the ERR in delamination analysis, *J*-integral methods (Rice, 1968), virtual crack extension methods (Hellen, 1975; Hwang et al., 1998) or modified crack closure integral (Rybicki and Kannimen, 1977) or the, so-called, virtual crack closure technique (VCCT), etc. have often been used. Especially, VCCT (Rybicki et al., 1977; Raju, 1987; Krueger, 2002; Quaresimin and Ricotta, 2006) is preferable for computing ERRs of laminated plates because of its simplicity. Also, Glaessgen et al. (2002) observed that shell VCCT models of debonding specimens in which the adherents are of different thickness can predict the correct total ERR, but that the mixed modes do not converge

with mesh refinement. This phenomenon is similar to the well known oscillatory behavior of in-plane linear elastic stress field near the tip of a bi-material interfacial crack (Raju and Crews, 1988). Consequently, in recent times, formulations have been suggested to overcome the above mentioned difficulties (Camanho et al., 2003; Jin and Sun, 2005; Turon et al., 2006; Davila et al., 2007).

1.2.3 Patch Repair Work

Patch repair work have been proved to be quick but inexpensive method of repairing structures with defects or local damage, for service life enhancement. The objectives of the repair work are to restore the static strength and durability of the structure and to decrease high stresses caused by damage in the form of cutouts of different shapes, indentations, inclusions, and cracks. The repair work can be done to one face or both the faces of the damaged component. The patch material can be metallic or non-metallic. It can be either adhesively bonded or bolted to the damaged components. It is well known that the traditional approach of fastening steel or aluminum patches to the damaged region has drawbacks as compared to the more recent technique of patch repair using composites, because mechanical fastening or riveting would result in additional stress concentrations in the structure and could be problematic particularly in regions of high stresses or strains. In order to overcome the disadvantages of traditional techniques, bonding of composite patches has been more preferred (Baker, 1984, 1987). The important components of analysis for the patch repairs are the prediction of the strength and representation of the effectiveness of the technique used. Sometimes the determination of fracture parameters such as SIF or ERR at the tip of pre-existing crack

like damage can give a precise idea on the performance of bonded composite repair. The SIFs and the ERRs in some patch repair works have been calculated by some researchers (Jones and Chiu, 1999; Ting et al., 1999; Umanaheswar and Singh, 1999; Bouiadjra et al., 2002; Ayatollahi and Hashemi, 2007). All these publications showed that SIF and ERR exhibit asymptotic behavior as the crack size increases after patch repair. This behavior is due to the fact that there is stress transfer from the cracked plate to patching component throughout the adhesive layer. The properties of adhesive play an important role on the performance of a bonded composite repair. Bouiadjra et al. (2002) showed that an adhesive with high shear modulus (an undesirable property) leads to weaking of SIF at the tip of a repaired crack.

The geometrical configuration of bonded patch repairs is classified as symmetric (double-sided) and asymmetric (single-sided) types. The symmetric arrangement with reinforcements bonded on two surfaces of a plate ensures that there is no out-of-plane bending over the repaired region, provided the plate is subjected to extensional loads only. Generally, for a cracked plate with the symmetrically bonded patch repairs, with increasing crack length, the crack extension force shows asymptotic behavior. In practical applications, however, single-sided repair work is often unavoidable if only one face of the component being repaired is accessible. If the component has adequate support against out-of-plane deflection, the effect of asymmetric patch can be similar to that of symmetric patch. Otherwise, an unsupported one-sided repair may considerably lower the repair efficiency because of out-of-plane bending caused by shift of the neutral plane away from that of the component being repaired. Such performance degradation of single-sided patch repair was recognized in some literature (Ratwani, 1979; Jones, 1983;

Wang et al., 1998; Belhouari et al., 2004). Their results suggested that SIFs for a single-sided repair would increase indefinitely with increasing crack length due to influence of secondary bending in the repaired component.

Achour et al. (2003) and Ouinas et al. (2007b) have implemented numerical analysis of repaired cracks at regular and semicircular notched edges. Barut et al. (2002) analyzed the behavior of bonded patch repair with cutout using experimental measurements and 3D finite elements. Also, to increase the durability and damage tolerance, many researchers have undertaken experimental tests and numerical analysis on patched thin plates (Denney and Mall, 1997) and patched thick plates (Jones et al., 1988). Patch debonding is also of importance since its presence increases the possibility of crack growth in the repaired structure by reducing the effective area of the patch. Some researchers have studied behavior of composite patch debonding in adhesively bonded repairs (Naboulsi and Mall, 1996, 1997; Denney and Mall, 1997) by using 2D finite element model consisting of three layers coupled with experimental studies, in order to investigate the effects of pre-existing debonding of various sizes in different locations, on the fatigue crack growth and life of repaired components with cracks. The results showed variations in fatigue life and SIF with changing location and size of debonding. Megueni et al. (2004) and Ouinas et al. (2007a) used conventional finite element analysis to compute the SIF in cracks repaired by composite bonded patches taking into account pre-existing debonding. They also found that the presence of debonding increases the SIF considerably. Papanikos et al. (2007) examined initiation and progression of composite patch debonding on variation of patch thickness, patch width, adhesive thickness, and applied load. As a whole, it was noticed from the results that the debonding affected the

effectiveness of the repairs significantly.

1.3 Objectives and Scope

The proposed study comprises of five major objectives.

The first objective of this study is to develop 2D and 3D representations of laminate behavior in the context of advanced laminate theories using higher order basis functions. The resulting formulations are to be implemented as m-file codes of MATLAB. The developed software is to be verified for anisotropic multilayer plates and isotropic problems. In addition to simple problems, those with increasing complexities are considered.

The second objective is to implement an efficient scheme for high-precision analysis of laminated systems, based on *p*-convergent finite element method. For modeling simplicity, computational efficiency and higher accuracy, models with a combination of elements with 2D and 3D representation of laminate behavior are considered by introducing suitable transition elements between the first two element types. The implemented scheme is verified or validated with basic problems as well as challenging ones with irregularities.

The third objective is to develop and implement the ordinary Kriging interpolation for obtaining improved solution during post-processing of the solution followed by verification or validation with example problems.

The fourth objective is to apply the developed modeling schemes and tools to more challenging practical problems such as patch repair in the presence of cracks, cutouts, delamination, etc. Studies on optimal performance of patch repairs through parametric

studies are also be undertaken.

The fifth objective is to determine the effect of geometric nonlinearity on the response of single patch repaired systems.

Some highlights of the tasks associated with these objectives are as follows.

(1) To achieve the first objective, it is necessary to develop the following *p*-version finite element models for laminated systems

   (a) *Full discrete-layer model* (FDLM): it is implemented independently of each other in the assumed in-plane displacement fields and the out-of-plane displacement field within a lamina.

   (b) *Partial discrete-layer model* (PDLM): it adopts FDLM for in-plane behavior within a lamina and 2D models of laminate analysis for out-of-plane behavior.

   (c) *Equivalent single-layer model* (ESLM): it has assumptions of first-order shear deformation theory and plane stress theory and is formulated by 2D higher-order approximating functions.

   (d) The aforementioned three formulations are to be implemented as MATLAB scripts.

   (e) These implementations are verified or validated with a number of test problems.

(2) For achieving the second objective involving the use of models with mixed element types, the following steps are to be followed.

   (a) *Discrete-layer transition model* (DLTM): it is formulated to allow smooth transition among the different element types used in the same model.

   (b) The MATLAB script based on this formulation is to be appended to the one developed under the first objective.

(c) The resulting software is applied to test problems for verification as well as to some practical problems to evaluate the efficiency of the scheme.

(3) The third objective is part of post-processing of computed results and is realized through the following steps

(a) Ordinary Kriging interpolation is implemented in the context of *p*-version of finite element method.

(b) The resulting algorithm is to be implemented.

(c) The proposed scheme is to be verified with the help a few example problems.

(4) To realize the fourth objective, the steps to be undertaken are

(a) In order to meaningfully solve problems with irregularities, the following special computational schemes are to be implemented.

i. Linear mapping and blending mapping for curved boundaries

ii. Extension of VCCT to 2D models with *p*-convergent elements.

iii. Extension of VCCT to 3D models with *p*-convergent discrete-layer elements.

iv. Implementation of Gauss-Lobatto quadrature technique with arbitrarily unlimited number of quadrature points.

v. Implementation of frontal solver for problems with very large number of degrees of freedom.

(b) Formulate and implement the following capabilities related to external loads,

i. Membrane loading

ii. Uniformly distributed transverse loading

iii. Distributed sinusoidal loading.

(c) Develop capabilities to handle the following problem types

i. Stepped plates

ii. Skew plates

iii. Free-edge stress problems in layered plates.

iv. Plates with cut-outs

v. Plates with crack.

vi. Delamination analysis

(5) To achiever the fifth objective, the following steps are followed.

(a) In implementing the capability to handle geometric nonlinearity the total Lagrangian approach is to be used.

(b) Transverse deflections are assumed as large but the strains continue to be small.

(c) Newton-Raphson scheme will be used during load increment.

(d) The resulting formulation will be implemented and verified.

(e) Comparison of results with those by linear analysis will be undertaken.

CHAPTER II

FORMULATION OF LAYER MODELS BASED ON *P*-FEM

2.1 Overview

The *p*-version of finite element method (*p*-FEM) using basis functions based on *Legendre polynomials* or *integrals of Legendre polynomials* differs from the conventional finite element methods (*h*-FEM) using basis functions usually based on *Lagrange polynomials*, in the sense that a structure can be modeled with higher-order finite elements hierarchically, and convergence can be achieved by simply increasing the order of the elements over a fixed mesh without the buildup of round off errors, as opposed to mesh refinement using a large number of first- or second-order elements in the case of conventional finite element based models.

Over the past decades, the *p*-FEM has matured into a powerful numerical modeling tool. The first experimental software COMET-X based on *p*-FEM was developed by Basu et al. (1977) at Washington University, St. Louis, USA, which was released in 1977. Later on, the advantages of *p*-FEM became quite obvious through numerical analysis, experimental verification, and and sound mathematical proof (Woo and Basu, 1988; Akhtar and Basu, 1989; Ahmed and Basu, 1989; Crull and Basu, 1989; Ghosh and Basu, 1996). Past research on *p*-FEM has demonstrated that apart from significantly less computational effort as compared to *h*-FEM to achieve the same degree of accuracy, *p*-FEM is robust, that is, unaffected by problem parameters. Also, *p*-FEM can handle discontinuities like cracks, notches, and cutouts of arbitrary shape without the need for

any special treatment. Another advantage is that due to modeling simplicity resulting from the need for only a few very large elements satisfying primarily the geometric, loading and constraint requirements, and ease of achieving solution convergence, the analyst's time is saved significantly. Also, the same *p*-FEM code can be used in *p*-mode, *h*-mode, or *hp*-mode. The *hp*-mode attracted special attention as the best strategy in the presence of irregularities. In this situation, it may, sometimes, be helpful to strongly grade the mesh near irregularities like, say, a reentrant corner.

In this chapter, the formulation of layered models for laminate analysis is presented, using displacement-based approximating functions in the context of *p*-FEM. At first, 1D and 2D shape functions for vertex modes and nodeless side and internal modes are introduced; in conventional finite element formulations nodeless modes are not considered. These shape functions will be used only for assuming the displacement fields of different p-levels, and not for geometric mapping. In the present study only *p*-FEM based, non-isotropic (or, nonparametric) elements are considered. Using these 1D and 2D shape functions, finite elements for layered models such as FDLM, PDLM, ESLM, and DLTM for simulating 2D and 3D behavior of plates, or suitable combinations thereof are developed in the following.

2.2 Hierarchic Shape Functions of *P*-FEM

1D hierarchical shape functions are classified as nodal modes and side modes, as shown in Fig. 2.1. For any *p*-level, (*p*-1) side modes are created. Here, *p* represents the degree of polynomial of the approximating function. In terms of standard coordinate ξ, the shape functions corresponding to the two nodal modes are

$$N_i(\xi) = \frac{1 + x_i x}{2} \qquad \text{in} \quad i = 1,2 \tag{2.1}$$

where x_i denotes the standard coordinates corresponding to the *i*-th mode.

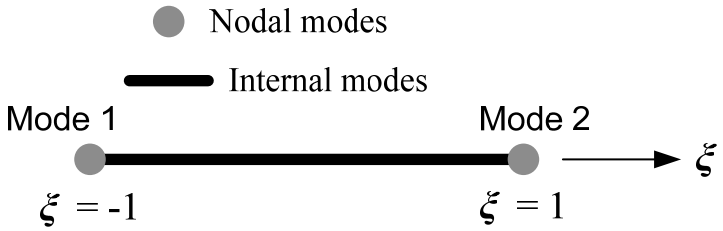

Fig. 2.1 Configuration of 1D element in *p*-FEM

To ensure orthogonality in the energy norm, at any *p*-level ($p \geq 2$), the internal modes are based on *integrals of Legendre polynomials*, as defined in Eq. 2.2.

$$S_i(\xi) = \sqrt{\frac{2i-3}{2}} \int_{-1}^{\xi} \Psi_{i-1}(r)\, dr \qquad \text{in } i=3,4,\ldots,p+1 \tag{2.2}$$

Here, Ψ refers to *Legendre polynomials*, which is defined in Eq. 2.3 as

$$\Psi_k(r) = \frac{1}{2^k k!} \frac{d^k}{dr^k} (r^2 - 1)^k \qquad \text{in } k=0,1,,2\ldots \tag{2.3}$$

2D hierarchic shape functions for a quadrilateral element can be built by using the 1D shape functions. The 2D shape functions can be classified by vertex (or nodal) modes, edge (or side) modes, and internal (or bubble) modes. The assignment of variables for a quadrilateral element with respect to 2D standard coordinates ξ and η is shown in Fig. 2.2. The shape functions for four 2D vertex modes can be obtained by a combination of the shape functions of two 1D nodal modes, as in Eq. 2.4.

$$V_k(\xi,\eta) = N_k(\xi)\, N_k(\eta) \qquad \text{in } k=1,2,3,4 \tag{2.4}$$

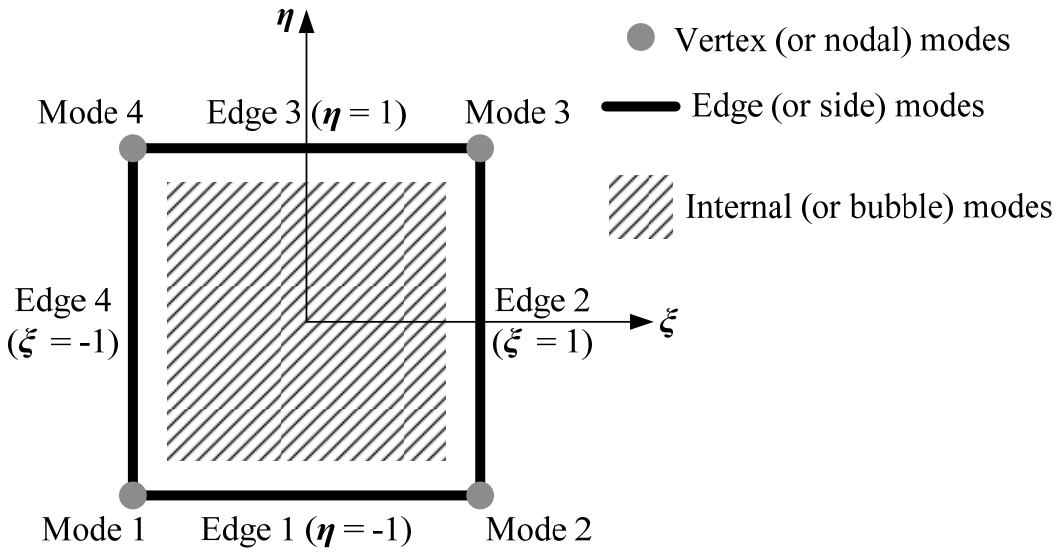

Fig. 2.2 Configuration of 2D element in *p*-FEM

Fig. 2.3 shows the surface plots of these shape functions for four vertex modes. In the case of higher *p*-levels, edge modes are needed for each side and are defined as

$$E_{4(k-1)+e+n}(\xi,\eta) = N_e(\eta)\, S_{k+1}(\xi) \qquad \text{in } e=1, 3; \quad k=2,4,\ldots,p; \quad n=\sum_{j=1}^{p-4>0} j \tag{2.5}$$

$$E_{4(k-1)+e+n}(\xi,\eta) = N_e(\xi)\, S_{k+1}(\eta) \qquad \text{in } e=2, 4; \quad k=2,4,\ldots,p; \quad n=\sum_{j=1}^{p-4>0} j \tag{2.6}$$

Here the subscript *e* represents an edge number in the standard element shown in Fig. 2.2. Surface plots of the shape functions of edge modes for Edge 1 are shown in Fig. 2.4. The surface plots of the shape functions of edge modes for Edges 2, 3, and 4 will be similar to those in Fig. 2.4, except that non-zero edge functions will appear in the edge under consideration. In addition, if the *p*-level is greater than 3, internal modes will have to be defined. Thus for any *p*-level>3, say, 4,5,6,…etc., the internal-modal shape functions can be obtained from a combination of higher order 1D shape functions, as in Eq. 2.7.

$$I_k(\xi,\eta) = S_{i+2}(\xi)\, S_{s+2-i}(\eta) \quad \text{in } i=1,2,\ldots,s\text{-}3;\ \ k = 4s + i + \sum_{j=0}^{p-4>0} j\ ;\ \text{s=4,5,}\ldots\text{,}p \tag{2.7}$$

Figs. 2.5 and 2.6 display the surface plots of the shape functions of internal modes from p-level=4 to p-level=10. Meanwhile, the number of total nodal (or vertex), edge, and internal modes in the 2D approximation, $M(p)$, is given by

$$M(p) = \begin{cases} 4 & \text{in } p = 1 \\ 4p + \dfrac{(p-2)(p-3)}{2} & \text{in } p \geq 2 \end{cases} \tag{2.8}$$

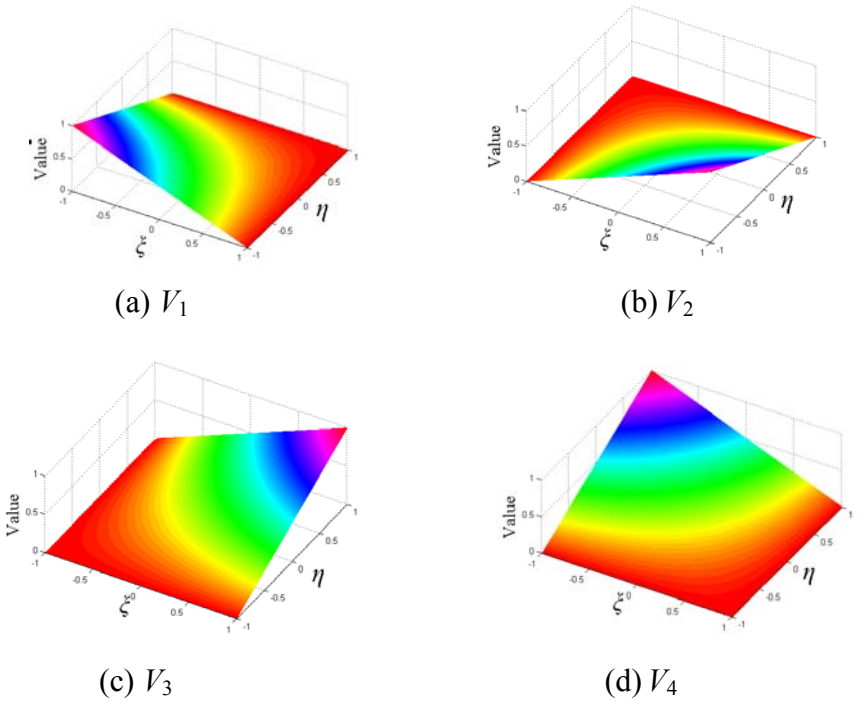

(a) V_1 (b) V_2

(c) V_3 (d) V_4

Fig. 2.3 Four nodal or vertex shape functions

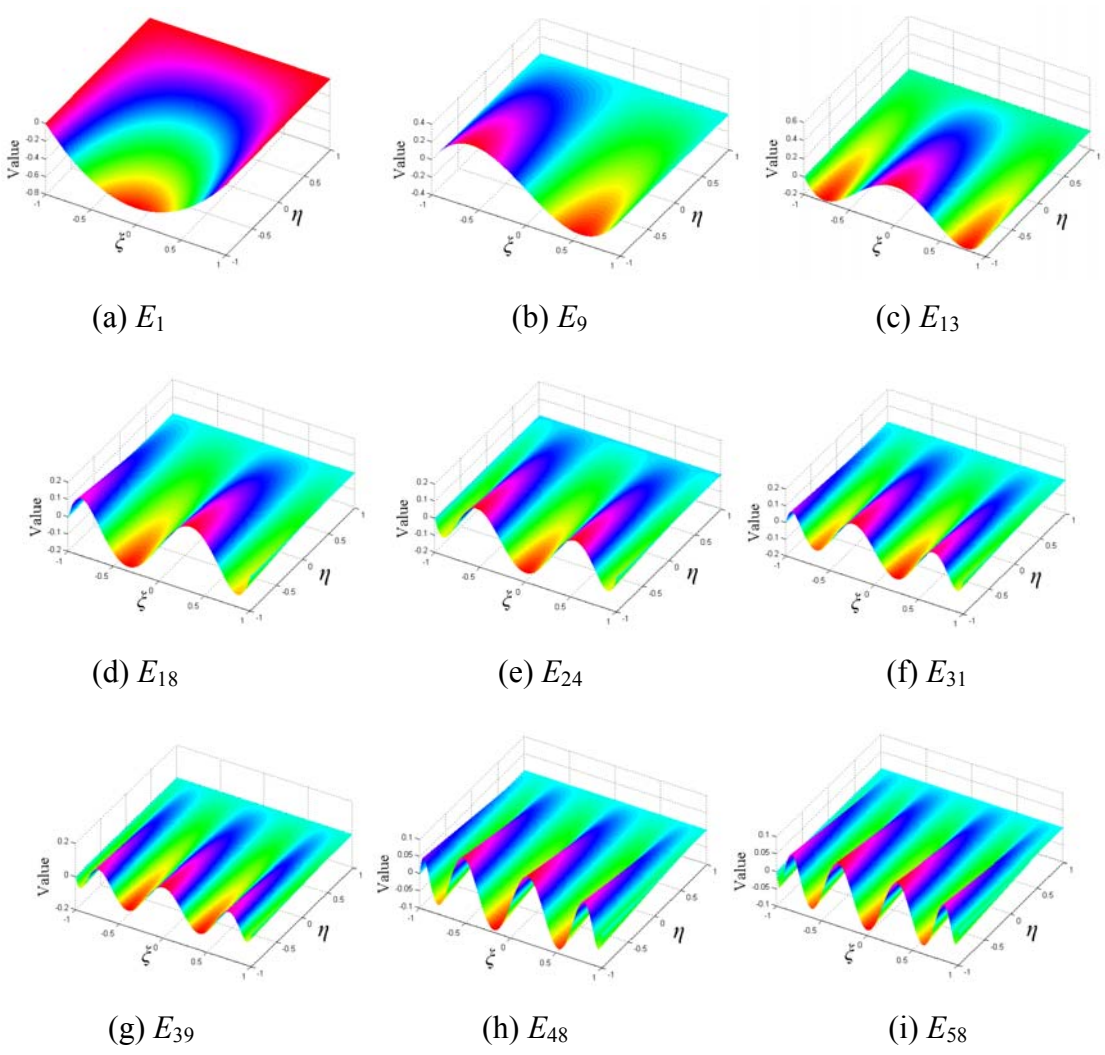

(a) E_1 (b) E_9 (c) E_{13}

(d) E_{18} (e) E_{24} (f) E_{31}

(g) E_{39} (h) E_{48} (i) E_{58}

Fig. 2.4 Shape functions of edge modes on Edge 1 in p=2~10

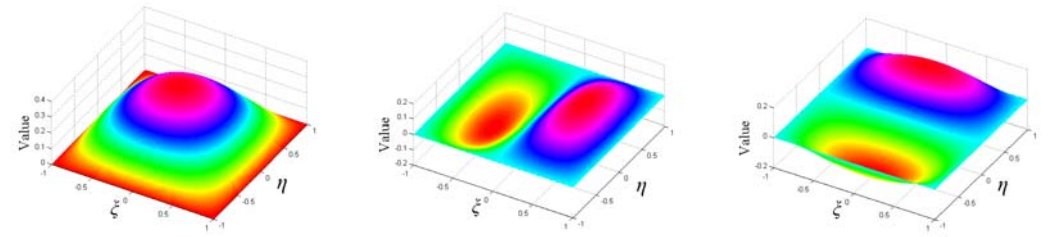

(a) I_{17} (b) I_{22} (c) I_{23}

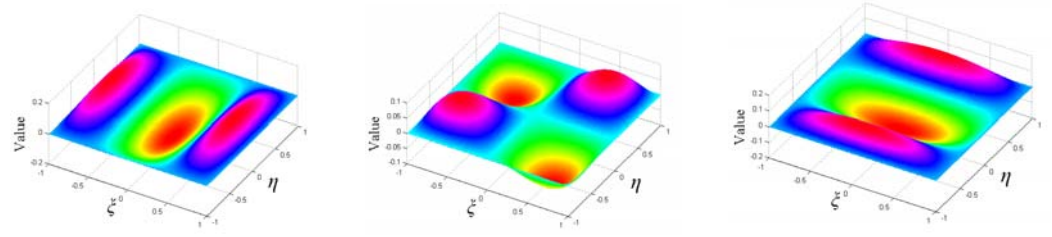

(d) I_{28} (e) I_{29} (f) I_{30}

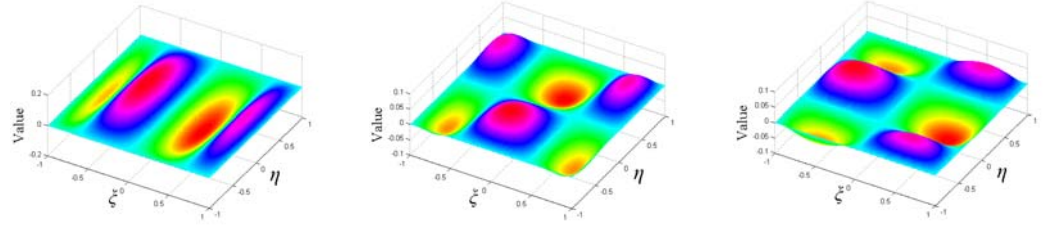

(g) I_{35} (h) I_{36} (i) I_{37}

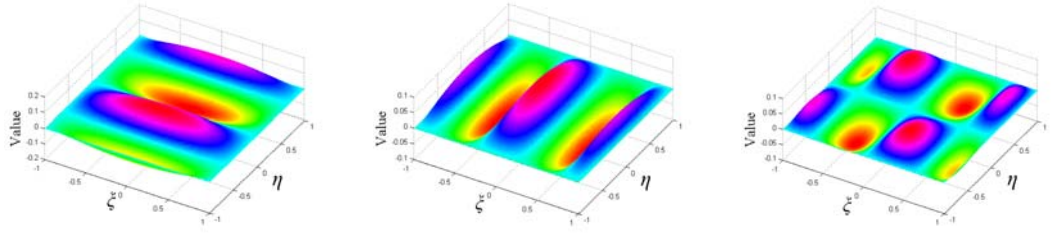

(j) I_{38} (k) I_{43} (l) I_{44}

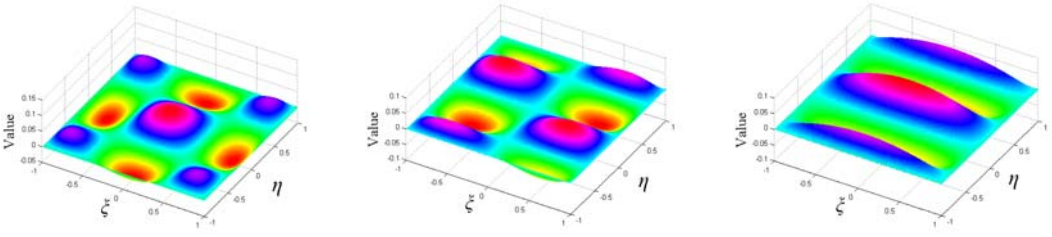

(m) I_{45} (n) I_{46} (o) I_{47}

Fig. 2.5 Internal modal shape functions from *p*-level=4 to *p*-level=8

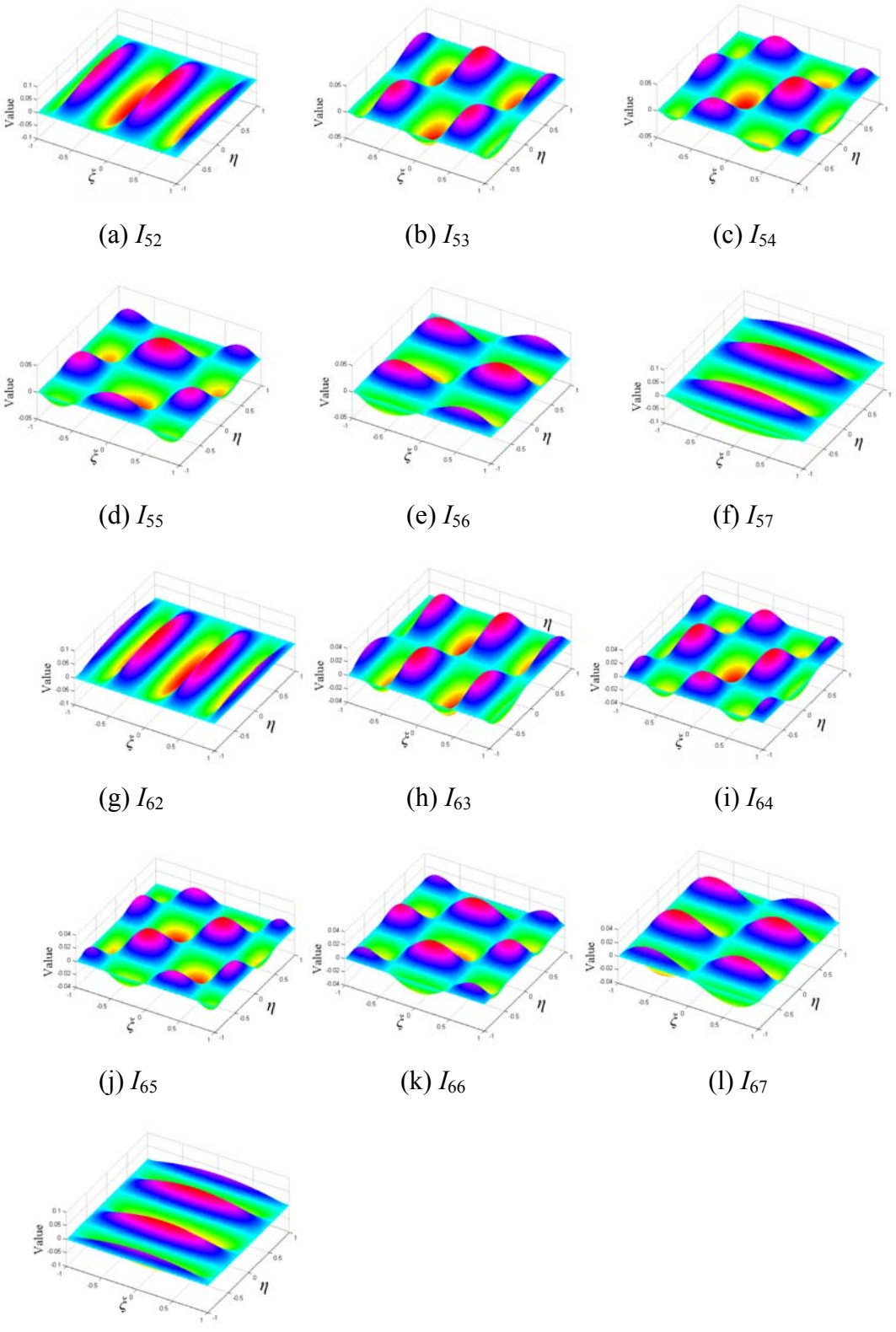

(a) I_{52} (b) I_{53} (c) I_{54}

(d) I_{55} (e) I_{56} (f) I_{57}

(g) I_{62} (h) I_{63} (i) I_{64}

(j) I_{65} (k) I_{66} (l) I_{67}

(m) I_{68}

Fig. 2.6 Internal modal shape functions in *p*-level=9 and 10

2.3 Full Discrete-Layer Model (FDLM)

In this approach for 3D modeling of laminated systems, each layup is treated discretely with deformation of a point in the layup in terms of three displacement components defined for each layer separately. Displacement fields at bottom and top surfaces within a layer are approximated by 2D shape functions (*V*, *E*, and *I*). Then the two surfaces are connected by 1D shape functions (*N* and *S*) which are of first-order or of higher variation across the thickness. Side modes of 1D shape functions connecting the two surfaces (bottom and top) can be called as thickness modes. Also, from the shape functions (*V*, *E*, *I*, *N*, and *S*) defined in terms of standard coordinate (ξ, η, or ζ) which were defined in section 2.2, shape functions with respect to local axes of a layer (x, y, and z) can be identified by the symbols $\widetilde{V}, \widetilde{E}, \widetilde{I}, \widetilde{N}, \text{and} \widetilde{S}$. First, the in-plane displacement filed (U^c; c=1 and 2) can be expressed as following Eq. 2.9.

$$U^c(x,y,z) = (\widetilde{V}_i(x,y) + \widetilde{E}_i(x,y) + \widetilde{I}_i(x,y))\,(\widetilde{N}_1(z)u_{i1}^c + \widetilde{N}_2(z)u_{i2}^c + \widetilde{S}_j(z)u_{ij}^c)$$
$$\text{in } i = 1,2,3,4,\ldots,M(p_{xy}) \text{ and } j = 3,\ldots,p_z+1 \tag{2.9}$$

where i and j follow regular summation convention. The function M refers to the number of total modes in 2D shape functions aforementioned in section 2.2. Also, p_{xy} and p_z indicate p-level with respect to xy-plane and z-axis, respectively. Similarly, out-of-plane displacement field (W) can be defined as follows.

$$W(x,y,z) = (\widetilde{V}_i(x,y) + \widetilde{E}_i(x,y) + \widetilde{I}_i(x,y))\,(\widetilde{N}_1(z)w_{i1} + \widetilde{N}_2(z)w_{i2} + \widetilde{S}_j(z)w_{ij})$$
$$\text{in } i = 1,2,3,4,\ldots,M(p_{xy}) \text{ and } j = 3,\ldots,\hat{p}_z+1 \tag{2.10}$$

where $\hat{p}_z$ represents p-level with respect to z-axis, p_z, used in planar displacement field. However, these need to be identical. That is, $p_z = \hat{p}_z$ or $p_z \neq \hat{p}_z$.

As the stress-strain relationships are based on 3D elasticity theory, all six strain components with respect to layer axes (x, y, and z) can be expressed as

$$\{\tilde{\varepsilon}\}_{x,y,z} = \left\lfloor \frac{\partial u}{\partial x} \quad \frac{\partial v}{\partial y} \quad \frac{\partial w}{\partial z} \quad \frac{\partial u}{\partial y} + \frac{\partial v}{\partial x} \quad \frac{\partial u}{\partial z} + \frac{\partial w}{\partial x} \quad \frac{\partial v}{\partial z} + \frac{\partial w}{\partial y} \right\rfloor^{\mathrm{T}} \tag{2.11}$$

Considering a state of anisotropy with three mutually orthogonal planes of symmetry, the following stress-strain relationships in any layer l can be defined.

$$\{\tilde{\sigma}\}^{l}_{x,y,z} = [X]^{\mathrm{T}}_{6\times6}\,[D]^{l}_{6\times6}[X]_{6\times6}\;\{\tilde{\varepsilon}\}^{l}_{x,y,z} \tag{2.12}$$

where

$$\begin{aligned} \{\tilde{\sigma}\}_{x,y,z} &= \left\lfloor \tilde{\sigma}_{xx} \quad \tilde{\sigma}_{yy} \quad \tilde{\sigma}_{zz} \quad \tilde{\tau}_{xy} \quad \tilde{\tau}_{xz} \quad \tilde{\tau}_{yz} \right\rfloor^{\mathrm{T}} \\ \{\tilde{\varepsilon}\}_{x,y,z} &= \left\lfloor \tilde{\varepsilon}_{xx} \quad \tilde{\varepsilon}_{yy} \quad \tilde{\varepsilon}_{zz} \quad \tilde{\gamma}_{xy} \quad \tilde{\gamma}_{xz} \quad \tilde{\gamma}_{yz} \right\rfloor^{\mathrm{T}} \end{aligned} \tag{2.13}$$

Also, $[D]_{6\times6}$ is a 3D elasticity matrix which is composed of engineering material constants with respect to principal material axes (1,2,3), and $[X]_{6\times6}$ is the transformation matrix based on the angle between layer axes (x, y) and principal axes of anisotropic material (1,2). The elasticity matrix can be written in the form

$$[D]_{6\times6} = \begin{bmatrix} [C]_{3\times3} & 0 \\ 0 & [G]_{3\times3} \end{bmatrix}_{6\times6} \tag{2.14}$$

where

$$\begin{aligned} [C]_{3\times3} &= \frac{1}{R}\begin{bmatrix} E_1(1-\nu_{23}\nu_{32}) & E_1(\nu_{23}\nu_{31}+\nu_{21}) & E_1(\nu_{21}\nu_{32}+\nu_{31}) \\ E_2(\nu_{13}\nu_{32}+\nu_{12}) & E_2(1-\nu_{13}\nu_{31}) & E_2(\nu_{12}\nu_{31}+\nu_{32}) \\ E_3(\nu_{12}\nu_{23}+\nu_{13}) & E_3(\nu_{13}\nu_{21}+\nu_{23}) & E_3(1-\nu_{12}\nu_{21}) \end{bmatrix}_{3\times3} \\ R &= 1-\nu_{12}\nu_{21}-\nu_{13}\nu_{31}-\nu_{23}\nu_{32}-2\nu_{12}\nu_{23}\nu_{31} \end{aligned} \tag{2.15}$$

and

$$[G]_{3\times3}=\begin{bmatrix} G_{12} & 0 & 0 \\ 0 & G_{13} & 0 \\ 0 & 0 & G_{23} \end{bmatrix} \tag{2.16}$$

Here E_1, E_2, and E_3 are Young's moduli in 1, 2, and 3 material directions, respectively. Moreover, v_{ij} are Poisson's ratios, defined as the ratio of transverse strain in the *j*th direction to the axial strain in the *i*th direction when stressed in the *i*th direction. G_{12}, G_{13}, and G_{23} are shear moduli in the 2-3, 1-3, and 1-2 planes, respectively. In addition, for the orthotropic material, the following reciprocity relations among the engineering constants hold

$$\frac{v_{12}}{E_1}=\frac{v_{21}}{E_2};\quad \frac{v_{13}}{E_1}=\frac{v_{31}}{E_3};\quad \frac{v_{23}}{E_2}=\frac{v_{32}}{E_3} \tag{2.17}$$

The aforementioned transformation matrix $[X]_{6\times6}$ can be shown to be

$$[X]_{6\times6}=\begin{bmatrix} r_x^2 & r_y^2 & r_z^2 & r_x r_y & r_x r_z & r_y r_z \\ s_x^2 & s_y^2 & s_z^2 & s_x s_y & s_x s_y & s_y s_z \\ t_x^2 & t_y^2 & t_z^2 & t_x t_y & t_x t_z & t_y t_z \\ 2r_x s_x & 2r_y s_y & 2r_z s_z & r_x s_y+r_y s_x & r_z s_x+r_x s_z & r_y s_z+r_z s_y \\ 2r_x t_x & 2r_y t_y & 2r_z t_z & t_x r_y+t_y r_x & t_z r_x+t_x r_z & t_y r_z+t_z r_y \\ 2s_x t_x & 2s_y t_y & 2s_z t_z & s_x x_y+s_y t_x & s_z t_x+s_x t_z & s_y t_z+s_z t_y \end{bmatrix} \tag{2.18}$$

Here *r*, *s*, and *t* refer to the principal axes (1, 2, and 3) of the layer material. The variable r_x means direction cosine of positive *x* direction with respect to the l-direction. To arrive at the elasticity matrix, $[\widetilde{D}]^l_{6\times6}$, with respect to layer reference axes (*x*, *y*, and *z*), the similar matrix, $[D]^l_{6\times6}$, defined in Eq. 2.14 with respect to the principal axes (1, 2, and 3) of the layer can be transformed as shown in Eq. 2.19.

$$[\widetilde{D}]^l_{6\times6}=[X]^{\mathrm{T}}_{6\times6}[D]^l_{6\times6}[X]_{6\times6} \tag{2.19}$$

Meanwhile, the displacement field $\{\Phi\}$ of a layer defined in Eqs. 2.9 and 2.10 can

be written by the following general form.

$$\{\Phi\} = [\widetilde{H}]\{d\} \tag{2.20}$$

where the matrix $[\widetilde{H}]$ indicates hierarchical shape functions with respect to layer reference axes (x, y, and z). All the elements of variables u^1, u^2, and w are included in the matrix $\{d\}$. The element equations for a layer can be expressed by using the principle of virtual work

$$\delta U_\varepsilon - \delta W = 0 \tag{2.21}$$

With the strain vector $\{\widetilde{\varepsilon}\}$ and the stress vector $\{\widetilde{\sigma}\}$ defined in (Eq. 2.13), the internal virtual strain energy can be written as

$$\delta U_\varepsilon = \int_V \delta\{\widetilde{\varepsilon}\}^{\mathrm{T}} \{\widetilde{\sigma}\}\, dV \tag{2.22}$$

If the virtual displacements are defined as

$$\delta\{\Phi\} = [\widetilde{H}]\ \delta\{d\} \tag{2.23}$$

The virtual strain can be written as

$$\delta\{\widetilde{\varepsilon}\} = [\widetilde{B}]\ \delta\{d\} \tag{2.24}$$

where $[\widetilde{B}]$ is the strain-displacement matrix with respect to layer reference axes (x, y, and z). In addition, the external virtual work takes following form.

$$\delta W = \delta\{d\}^{\mathrm{T}}\{F\}^p + \int_S \delta\{d\}^{\mathrm{T}}\{F\}^q\, dS + \int_A \delta\{d\}^{\mathrm{T}}\{F\}^r\, dA + \int_V \delta\{d\}^{\mathrm{T}}\{F\}^b\, dV \tag{2.25}$$

Here the superscripts p, q, r, and b signify point forces, side forces, surface forces, and body forces, respectively. Based on these definitions, the virtual work equation shown in Eq. 2.21 can be expressed as

$$\int_V \delta\{d\}^{\mathrm{T}}\,[\widetilde{B}]^{\mathrm{T}}\,[\widetilde{D}]_{6\times 6}\,[\widetilde{B}]\,\{d\}\,dV$$
$$= \delta\{d\}^{\mathrm{T}}\{F\}^{p} + \int_S \delta\{d\}^{\mathrm{T}}\{F\}^{q}\,dS + \int_A \delta\{d\}^{\mathrm{T}}\{F\}^{r}\,dA + \int_V \delta\{d\}^{\mathrm{T}}\{F\}^{b}\,dV \tag{2.26}$$

The element stiffness matrix of a layer can then be obtained from

$$[K]^{l} = \iiint_V [\widetilde{B}]^{\mathrm{T}}\,[\widetilde{D}]^{l}_{6\times 6}[\widetilde{B}]\,dx\,dy\,dz = \int_{-1}^{1}\int_{-1}^{1}\int_{-1}^{1} [B]^{\mathrm{T}}\,[\widetilde{D}]^{l}_{6\times 6}[B]\,|J|\,d\xi\,d\eta\,d\zeta \tag{2.27}$$

where $[B]$ is strain-displacement matrix with respect to the standard coordinate system (ξ. η, and ζ). $|J|$ is determinant of the Jacobian matrix. It is clear from Eq. 2.27 that FDLM can take into account any variation of material properties within a layer. Fig. 2.7 demonstrates the modeling scheme with FDLM for a laminated system with three layers. If there are no gaps and empty spaces between interfaces of layers, compatibility conditions can be applied at the layer interfaces.

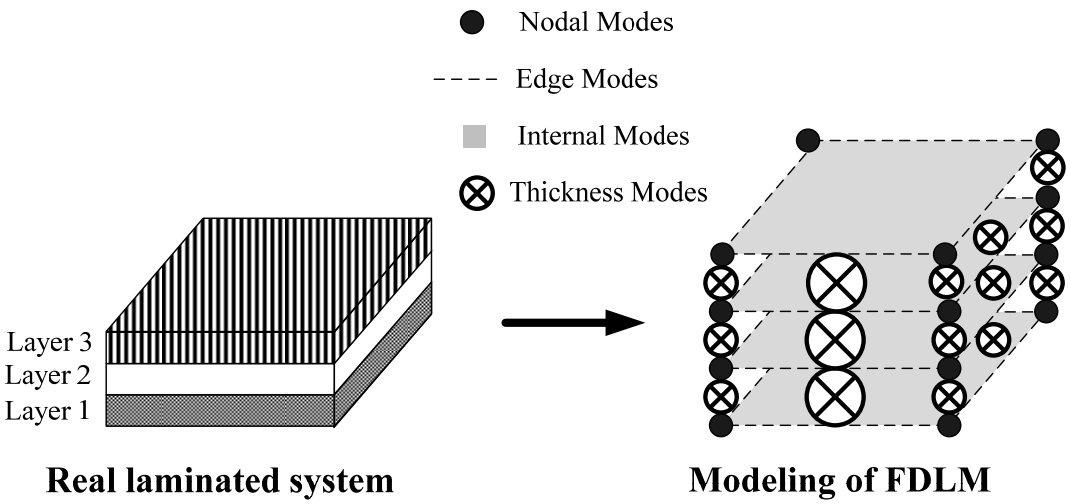

Fig. 2.7 Modeling scheme with full discrete-layer model

2.4 Partial Discrete-Layer Model (PDLM)

Another discrete-layer model which is somewhat simpler than FDLM can also be used for 3D modeling will be termed as the partial discrete-layer model. As in FDLM, in PDLM the two planar displacement components which have first or higher order variation across the thickness of lamina. On the other hand, the out-of-plane displacement is, however, assumed to be independent of the transverse coordinate z, invoking the condition of in-extensional theory in the thickness direction. Therefore, Eq. 2.9, developed for FDLM, can again be used to represent the in-plane displacement fields of a PDLM based layer. However, for the sake of reducing the required number of modal variables without significantly affecting the accuracy of the solution, a linear variation of the in-plane displacement field across the thickness is adopted. Thus the in-plane displacement field modified from Eq. 2.9 can be expressed in the following form.

$$\begin{aligned} &U^c(x,y,z) = (\ \widetilde{V}_i(x,y) + \widetilde{E}_i(x,y) + \widetilde{I}_i(x,y)\ )\ (\widetilde{N}_1(z)u^c_{i1} + \widetilde{N}_2(z)u^c_{i2}) \\ &\text{in } i = 1,2,3,4,\ldots,M(p_{xy}) \end{aligned} \tag{2.28}$$

Also, due to the assumption of in-extensional thickness, the out-of-plane displacement field is defined as

$$W(x,y,z) = (\ \widetilde{V}_i(x,y) + \widetilde{E}_i(x,y) + \widetilde{I}_i(x,y)\ )\ w_i \qquad \text{in } i = 1,2,3,4,\ldots,M(p_{xy}) \tag{2.29}$$

As a consequence to above, the strain components in a layer will reduce from the 3D ones used for FDLM to those shown in Eq. 2.30.

$$\{\widetilde{\varepsilon}\}_{x,y,z} = \left\lfloor \frac{\partial u}{\partial x} \quad \frac{\partial v}{\partial y} \quad \frac{\partial u}{\partial y} + \frac{\partial v}{\partial x} \quad \frac{\partial u}{\partial z} + \frac{\partial w}{\partial x} \quad \frac{\partial v}{\partial z} + \frac{\partial w}{\partial y} \right\rfloor^{\mathrm{T}} \tag{2.30}$$

Just as Eq. 2.12 used for FDLM, the stress-strain relationships of PDLM in any layer l can be re-written as Eq. 2.31.

$$\{\widetilde{\sigma}\}^{l}_{x,y,z} = [X]^{\mathrm{T}}_{5\times5}\,[D]^{l}_{5\times5}[X]_{5\times5}\;\{\widetilde{\varepsilon}\}^{l}_{x,y,z} \tag{2.31}$$

where

$$\begin{aligned}\{\widetilde{\sigma}\}_{x,y,z} &= \lfloor \widetilde{\sigma}_{xx} \quad \widetilde{\sigma}_{yy} \quad \widetilde{\tau}_{xy} \quad \widetilde{\tau}_{xz} \quad \widetilde{\tau}_{yz} \rfloor^{\mathrm{T}} \\ \{\widetilde{\varepsilon}\}_{x,y,z} &= \lfloor \widetilde{\varepsilon}_{xx} \quad \widetilde{\varepsilon}_{yy} \quad \widetilde{\gamma}_{xy} \quad \widetilde{\gamma}_{xz} \quad \widetilde{\gamma}_{yz} \rfloor^{\mathrm{T}}\end{aligned} \tag{2.32}$$

Based on the constitutive matrices Eq. 2.14 through Eq. 2.16 allowing for the state of anisotropy, the elasticity matrix of PDLM, accounting for the zero transversal normal stress assumption used in Eq. 2.31, takes the following modified form.

$$[D]_{5\times5} = \begin{bmatrix} [C]_{2\times2} & 0 \\ 0 & [G]_{3\times3} \end{bmatrix}_{5\times5} \tag{2.33}$$

where $[G]_{3\times3}$ matrix defined in Eq. 2.16 is still valid here. The zero transverse normal stress condition also allows the use of following assumptions.

$$E_3 = \nu_{13} = \nu_{31} = \nu_{23} = \nu_{32} = 0 \tag{2.34}$$

Thus, reciprocity relations among the engineering constants from Eq. 2.17 can be reduced to

$$\frac{\nu_{12}}{E_1} = \frac{\nu_{21}}{E_2} \tag{2.35}$$

From Eq. 2.34 and Eq. 2.35, the matrix $[C]_{2\times2}$ can be written more concisely as Eq. 2.36.

$$[C]_{2\times2} = \frac{1}{1-\nu_{12}\nu_{21}} \begin{bmatrix} E_1 & E_1\nu_{21} \\ E_2\nu_{12} & E_2 \end{bmatrix}_{2\times2} \tag{2.36}$$

Also, Transformation matrix $[X]_{5\times5}$ mentioned in Eq. 2.31 can be given the modified form based on Eq. 2.18 leading to Eq. 2.37.

$$[X]_{5\times5} = \begin{bmatrix} r_x^2 & r_y^2 & r_x r_y & r_x r_z & r_y r_z \\ s_x^2 & s_y^2 & s_x s_y & s_x s_y & s_y s_z \\ 2r_x s_x & 2r_y s_y & r_x s_y + r_y s_x & r_z s_x + r_x s_z & r_y s_z + r_z s_y \\ 2r_x t_x & 2r_y t_y & t_x r_y + t_y r_x & t_z r_x + t_x r_z & t_y r_z + t_z r_y \\ 2s_x t_x & 2s_y t_y & s_x x_y + s_y t_x & s_z t_x + s_x t_z & s_y t_z + s_z t_y \end{bmatrix} \tag{2.37}$$

The elasticity matrix with respect to the layer reference axes can be expressed as the triple product shown in Eq. 2.38.

$$[\widetilde{D}]^l_{5\times5} = [X]^{\mathrm{T}}_{5\times5}\,[D]^l_{5\times5}[X]_{5\times5} \tag{2.38}$$

Here again, for finite element formulation, the principle of virtual work can be used. Thus, Eqs. 2.20 through 2.25 are also valid for PDLM. The virtual work equations will now take the form

$$\begin{aligned} &\int_V \delta\{d\}^{\mathrm{T}}\,[\widetilde{B}]^{\mathrm{T}}\,[\widetilde{D}]_{5\times5}\,\,[\widetilde{B}]\,\{d\}\,dV \\ &\qquad = \delta\{d\}^{\mathrm{T}}\{F\}^p + \int_S \delta\{d\}^{\mathrm{T}}\{F\}^q\,dS + \int_A \delta\{d\}^{\mathrm{T}}\{F\}^r\,dA + \int_V \delta\{d\}^{\mathrm{T}}\{F\}^b\,dV \end{aligned} \tag{2.39}$$

Like Eq. 2.27 of FDLM, the element stiffness matrix of a PDLM based layer can be obtained from

$$[K]^l = \iiint_V [\widetilde{B}]^{\mathrm{T}}\,[\widetilde{D}]^l_{5\times5}[\widetilde{B}]\,dx\,dy\,dz = \int_{-1}^{1}\int_{-1}^{1}\int_{-1}^{1} [B]^{\mathrm{T}}\,[\widetilde{D}]^l_{5\times5}[B]\,|J|\,d\xi\,d\eta\,d\zeta \tag{2.40}$$

Fig. 2.8 defines the modeling scheme of PDLM for a three layered laminated system. The compatibility conditions at layer interfaces can be handled as with FDLM. Also, for out-of-plane displacements, 2D modeling is available as shown in Fig. 2.8.

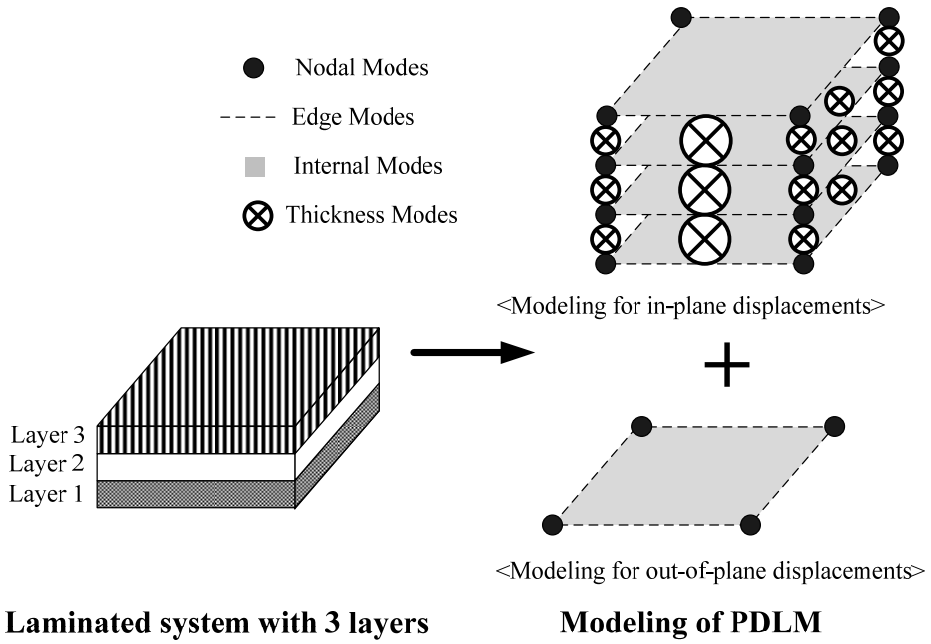

Fig. 2.8 Modeling scheme of partial discrete-layer model

2.5 Equivalent Single-Layer Model (ESLM)

In this C_z^1 function based model, dimensional reduction is effected by incorporating first-order shear deformation for bending behavior and plane stress condition for membrane action. In this case, the deformation at any point in the laminated plate is based on three displacement fields for a quadrilateral subparametric C_{xy}^0 element with three translational mode components (u^1,u^2 and w) and two rotational mode components (θ^1 and θ^2). The three displacement fields (U^c and W; c=1,2) can be defined as

$$\begin{aligned} U^c(x,y,z) &= (\widetilde{V}_i(x,y) + \widetilde{E}_i(x,y) + \widetilde{I}_i(x,y))\,(u_i^c + z\theta_i^c) \\ W(x,y,z) &= (\widetilde{V}_i(x,y) + \widetilde{E}_i(x,y) + \widetilde{I}_i(x,y))\,w_i \end{aligned} \qquad (2.41)$$

with $i = 1,2,3,4,\ldots,M(p_{xy})$

For strain components of the ESLM model, Eq. 2.30 used in the case of the PDLM model can still be used. As shown in Eq. 2.42, the strain vector can be partitioned into

membrane strains $\{\widetilde{\varepsilon}^m\}_{3\times1}$, bending strains $\{\widetilde{\varepsilon}^b\}_{3\times1}$, and transversal shear strains $\{\widetilde{\gamma}^t\}_{2\times1}$.

$$\{\widetilde{\varepsilon}\} = \begin{bmatrix} \widetilde{\varepsilon}_{xx} & \widetilde{\varepsilon}_{yy} & \widetilde{\gamma}_{xy} & \widetilde{\gamma}_{xz} & \widetilde{\gamma}_{yz} \end{bmatrix}^{\mathrm{T}} = \begin{Bmatrix} \{\widetilde{\varepsilon}^m\}_{3\times1} \\ \{\widetilde{\gamma}^t\}_{2\times1} \end{Bmatrix} + z \begin{Bmatrix} \{\widetilde{\varepsilon}^b\}_{3\times1} \\ \{0\}_{2\times1} \end{Bmatrix} \tag{2.42}$$

where

$$\{\widetilde{\varepsilon}^m\}_{3\times1} = \begin{bmatrix} \widetilde{\varepsilon}^m_{xx} & \widetilde{\varepsilon}^m_{xy} & \widetilde{\gamma}^m_{xy} \end{bmatrix}^{\mathrm{T}};\ \{\widetilde{\varepsilon}^b\}_{3\times1} = \begin{bmatrix} \widetilde{\varepsilon}^b_{xx} & \widetilde{\varepsilon}^b_{xy} & \widetilde{\gamma}^b_{xy} \end{bmatrix}^{\mathrm{T}};\ \{\widetilde{\gamma}^t\}_{3\times1} = \begin{bmatrix} \widetilde{\gamma}^t_{xz} & \widetilde{\gamma}^t_{yz} \end{bmatrix}^{\mathrm{T}} \tag{2.43}$$

Also, instead of using $\widetilde{N}_i(x,y)$, and $\widetilde{M}_j^{(h)}(x,y)$, the shape functions with respect to element axes (x and y) are denoted by $\widetilde{H}$. The strain-displacement matrix for five nodal (and modal) variables is then given by

$$[\widetilde{B}]_{8\times5} = \begin{bmatrix} [\widetilde{B}^m]_{3\times2} & [0]_{3\times3} \\ [0]_{3\times3} & [\widetilde{B}^b]_{3\times2} \\ [0]_{2\times2} & [\widetilde{B}^s]_{2\times3} \end{bmatrix}_{8\times5} \tag{2.44}$$

with

$$[\widetilde{B}^m]_{3\times2} = [\widetilde{B}^b]_{3\times2} = \begin{bmatrix} \dfrac{\partial\widetilde{H}}{\partial x} & 0 \\ 0 & \dfrac{\partial\widetilde{H}}{\partial y} \\ \dfrac{\partial\widetilde{H}}{\partial y} & \dfrac{\partial\widetilde{H}}{\partial x} \end{bmatrix};\ [\widetilde{B}^s]_{2\times3} = \begin{bmatrix} \dfrac{\partial\widetilde{H}}{\partial x} & -N & 0 \\ \dfrac{\partial\widetilde{H}}{\partial y} & 0 & -N \end{bmatrix} \tag{2.45}$$

For constitutive equations of stress resultants, it is assumed that each layer is orthotropic with respect to its material symmetry lines, like previously described partial discrete-layer models. The matrix $[G]_{3\times3}$ in Eq. 2.33 needs to be modified. Based on Eq. 2.3-8 used for FDLM and PDLM, $[G]_{3\times3}$ for ESLM takes the following form

$$[G]_{3\times3}=\begin{bmatrix} G_{12} & 0 & 0 \\ 0 & k_1 G_{13} & 0 \\ 0 & 0 & k_2 G_{23} \end{bmatrix} \tag{2.46}$$

where the terms k_1 and k_2 are shear correction factors in the 1-3 and 2-3 planes of material axes, respectively, to account for the actual presence of non-uniform transverse shear stress distribution across the thickness. The shear correction factor is equal to the ratio of the effective area resisting shear deformation to the actual cross-sectional area of the laminate plate. In general, the transverse shear continuity must be guaranteed at each layer interface. The equilibrium equations in *x*-direction (1-direction) and *y*-direction (2-direction) of layer reference coordinate axes (1≡*x*, 2≡*y*, 3≡*z*) can be written as

$$\frac{\partial \sigma_{xx}}{\partial x}+\frac{\partial \tau_{xy}}{\partial y}+\frac{\partial \tau_{xz}}{\partial z}=0\ ; \quad \frac{\partial \tau_{xy}}{\partial x}+\frac{\partial \sigma_{yy}}{\partial y}+\frac{\partial \tau_{yz}}{\partial z}=0 \tag{2.47}$$

Assuming cylindrical bending with $z=\pm h/2$ at top and bottom surfaces,

$$\begin{aligned} \tau_{xz} &= -\int_{-h/2}^{z}\frac{\partial \sigma_{xx}}{\partial x}dz=-\frac{Q_{xz}}{f_1}\int_{-h/2}^{z}D_1(z)zdz=\frac{Q_{xz}}{f_1}\ \Lambda_1(z) \\ \tau_{yz} &= -\int_{-h/2}^{z}\frac{\partial \sigma_{yy}}{\partial x}dz=-\frac{Q_{yz}}{f_2}\int_{-h/2}^{z}D_2(z)zdz=\frac{Q_{yz}}{f_2}\Lambda_2(z) \end{aligned} \tag{2.48}$$

where

· Q_{xz} and Q_{yz} are the shear forces in *xz*- and *yz*-planes.

· $f_1=\int_{-h/2}^{h/2}D_1(z)\,z^2dz$ and $f_2=\int_{-h/2}^{h/2}D_2(z)\,z^2dz$ are flexural plate stiffnesses in *x*- and *y*-directions.

· *z* is the coordinate in the thickness direction.

· $\Lambda_1(z)=-\int_{-h/2}^{z}D_1(z)zdz$ and $\Lambda_2(z)=-\int_{-h/2}^{z}D_2(z)zdz$ represent the transverse shear stress shape factors for *xz*-plane and *yz*-plane, respectively.

The functions $\Lambda(z)$ which determines the shape of the shear stress diagram is independent of the loadings for the conditions specified. The transverse shear strain energy components are given by

$$\Xi_1 = \int_{-h/2}^{h/2} \frac{\tau_{xz}^2}{G_{13}(z)} dz \; ; \quad \Xi_2 = \int_{-h/2}^{h/2} \frac{\tau_{yz}^2}{G_{23}(z)} dz \tag{2.49}$$

Here $G_{13}(z)$ and $G_{23}(z)$ are transverse shear modulus in *xz*- and *yz*-planes at a point *z* in the thickness direction. Substituting Eq. 2.48 into Eq. 2.49 leads to

$$\Xi_1 = \frac{Q_{xz}^2}{f_1^2} \int_{-h/2}^{h/2} \frac{\Lambda_1^2(z)}{G_{13}(z)} dz \; ; \quad \Xi I_2 = \frac{Q_{yz}^2}{f_2^2} \int_{-h/2}^{h/2} \frac{\Lambda_2^2(z)}{G_{23}(z)} dz \tag{2.50}$$

The strain energy components under the assumption of constant shear strain are

$$\begin{aligned} \hat{\Xi}_1 &= \int_{-h/2}^{h/2} \hat{\tau}_{xz}^2 G_{13}(z) dz = \frac{Q_{xz}^2}{\int_{-h/2}^{h/2} G_{13}(z) dz} \\ \hat{\Xi}_2 &= \int_{-h/2}^{h/2} \hat{\tau}_{yz}^2 G_{23}(z) dz = \frac{Q_{yz}^2}{\int_{-h/2}^{h/2} G_{23}(z) dz} \end{aligned} \tag{2.51}$$

Here $\hat{\tau}_{xz}$ and $\hat{\tau}_{yz}$ are the mean values of the shear strains. Using Eqs. 2.50 and 2.51, it is possible to obtain the shear correction factors k_1 and k_2 as

$$k_1 = \frac{\hat{\Xi}_1}{\Xi_1}; \quad k_2 = \frac{\hat{\Xi}_2}{\Xi_2} \tag{2.52}$$

Eq. 2.38, representing the elasticity matrix of each layer, can be rewritten in the following form.

$$[\widetilde{D}]_{5\times5}^l = [X]_{5\times5}^{\mathrm{T}} [D]_{5\times5}^l [X]_{5\times5} = \begin{bmatrix} [Q]_{3\times3}^l & [0]_{3\times2} \\ [0]_{2\times3} & [R]_{2\times2}^l \end{bmatrix} \tag{2.53}$$

Also, although the strains are continuous through the thickness of the laminated plate, stresses are not so because of change in material coefficients through the thickness. Thus,

the integration of stresses through the thickness of a laminated plate requires lamina-wise integration. Like the case of strain components, stress resultants are also classified into membrane force resultants, bending moment resultants, and transversal shear force resultants, respectively. In laminated plate with n layers, the stress resultants are as follows.

$$\{\widetilde{\sigma}\}_{8\times1} = \begin{Bmatrix} \{\widetilde{\sigma}^m\}_{3\times1} \\ \{\widetilde{\sigma}^b\}_{3\times1} \\ \{\widetilde{\tau}^t\}_{2\times1} \end{Bmatrix} \tag{2.54}$$

with

$$\begin{aligned}
\{\widetilde{\sigma}^m\}_{3\times1} &= \begin{Bmatrix} \widetilde{\sigma}^m_{xx} \\ \widetilde{\sigma}^m_{yy} \\ \widetilde{\tau}^m_{xy} \end{Bmatrix} = \sum_{l=1}^{n} \int_{z_l^\alpha}^{z_l^\beta} [Q]^l_{3\times3} \begin{Bmatrix} \widetilde{\varepsilon}^m_{xx} + z\widetilde{\varepsilon}^b_{xx} \\ \widetilde{\varepsilon}^m_{y} + z\widetilde{\varepsilon}^b_{y} \\ \widetilde{\gamma}^m_{xy} + z\widetilde{\gamma}^b_{xy} \end{Bmatrix} dz \\
\{\widetilde{\sigma}^b\}_{3\times1} &= \begin{Bmatrix} \widetilde{\sigma}^b_{xx} \\ \widetilde{\sigma}^b_{yy} \\ \widetilde{\tau}^b_{xy} \end{Bmatrix} = \sum_{l=1}^{n} \int_{z_l^\alpha}^{z_l^\beta} [Q]^l_{3\times3} \begin{Bmatrix} z\widetilde{\varepsilon}^m_{xx} + z^2\widetilde{\varepsilon}^b_{xx} \\ z\widetilde{\varepsilon}^m_{y} + z^2\widetilde{\varepsilon}^b_{y} \\ z\widetilde{\gamma}^m_{xy} + z^2\widetilde{\gamma}^b_{xy} \end{Bmatrix} dz \\
\{\widetilde{\tau}^t\}_{2\times1} &= \begin{Bmatrix} \widetilde{\tau}_{xz} \\ \widetilde{\tau}_{yz} \end{Bmatrix} \sum_{l=1}^{n} \int_{z_l^\alpha}^{z_l^\beta} [R]^l_{2\times2} \begin{Bmatrix} \widetilde{\gamma}^t_{xz} \\ \widetilde{\gamma}^t_{yz} \end{Bmatrix} dz
\end{aligned} \tag{2.55}$$

Here α and β refer to bottom and top indexes. The constitutive relationships for the laminated plate as a whole with respect to the reference surface of ESLM can then be expressed as

$$\{\widetilde{\sigma}\}_{8\times1} = [E]_{8\times8} \{\widetilde{\varepsilon}\}_{8\times1} \tag{2.56}$$

where $[E]_{8\times8}$ is the constitutive matrix linking membrane, bending, and transverse shear force resultants to reference surface strains and curvatures.

Meanwhile, like previous two models, principle of virtual work is applied for finite element formulation. Hence, Eq. 2.21 is also valid in process of formulation of present

ESLM. With strain components shown in Eq. 2.42 and stress resultants in Eq. 2.54, the internal virtual strain energy can be written as

$$\delta U_{\varepsilon} = \iint_{A} \delta\{\widetilde{\varepsilon}\}^{\mathrm{T}} \{\widetilde{\sigma}\}\, dA \tag{2.57}$$

The virtual displacements and strains defined in Eq. 2.23 and Eq. 2.24, respectively, are valid for ESLM as well. Here the external virtual work takes following form.

$$\delta W = \delta\{d\}^{\mathrm{T}} \{F\}^{p} + \int_{S} \delta\{d\}^{\mathrm{T}} \{F\}^{q}\, dS + \int_{A} \delta\{d\}^{\mathrm{T}} \{F\}^{r}\, dA \tag{2.58}$$

Based on above definitions, the virtual work equation shown in Eq. 2.21 is rewritten as

$$\begin{aligned} &\int_{A} \delta\{d\}^{\mathrm{T}}\, [\widetilde{B}]^{\mathrm{T}}\, [E]_{8\times 8}\, [\widetilde{B}]\, \{d\}\, dA \\ &\qquad = \delta\{d\}^{\mathrm{T}} \{F\}^{p} + \int_{S} \delta\{d\}^{\mathrm{T}} \{F\}^{q}\, dS + \int_{A} \delta\{d\}^{\mathrm{T}} \{F\}^{r}\, dA \end{aligned} \tag{2.59}$$

The stiffness matrix of the element with respect to the reference plane is then given by

$$[K] = \iint_{A} [\widetilde{B}]^{\mathrm{T}} [E]_{8\times 8} [\widetilde{B}]\, dx\, dy = \int_{-1}^{1}\int_{-1}^{1} [B]^{\mathrm{T}} [E]_{8\times 8} [B] \left|J\right| d\xi\, d\eta \tag{2.60}$$

where $[B]$ is strain-displacement matrix with respect to standard coordinate system (ξ. and ζ). Also, $\left|J\right|$ is determinant of the Jacobian matrix. Fig. 2.9 shows modeling strategy of FSLM for laminated system with three layers.

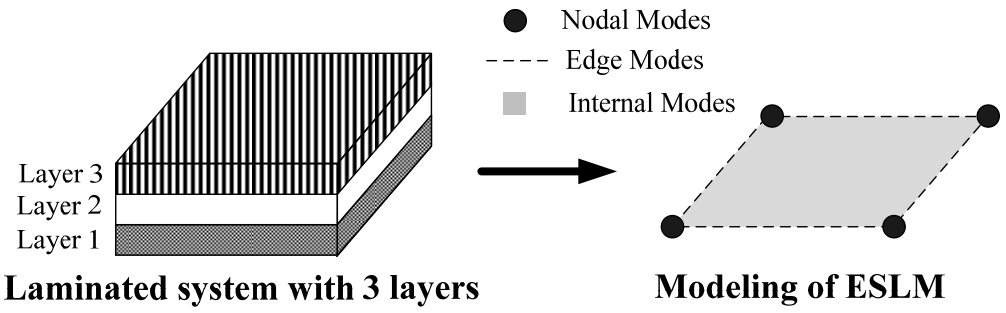

Fig. 2.9 Modeling scheme of equivalent single-layer model

2.6 Discrete-Layer Transition Model (DLTM)

Each of the three element models presented so far has its unique positive aspects as well as negative aspects characterized in terms of the accuracy of results obtained, relative degree of computational effort, and ease of modeling. No single model can be regarded to be best suited for all composite problems of practical importance. The choice of the most efficient model in a given situation will depend upon the characteristics of a given problems, the objectives of analysis, computational efficiency, the ease of modeling and so on. For example, if one tries to obtain maximum deflection or stress in a thin laminated plate, it is enough to use ESLM. Alternatively, if the objective is to determine the distribution of in-plane displacement or stresses across the thickness in a moderately thick-laminated plate, PDLM would be the reasonable choice. Furthermore, if the objective is to determine the accurate distribution of all stress components throughout the system, FDLM may be the logical choice in spite of being compute-intensive. However, if the objective is to study the effect of localized irregularity like delamination, it will be more efficient to use a mixed model involving a combination of FDLM in the delamination region and PDLM and/or ESLM, elsewhere. By a proper choice of models in such mixed modeling scheme, solutions of high accuracy with least computational effort can be obtained. Although this choice is conceptually simple, the actual implementation would be complicated and somewhat cumbersome due to the need of maintaining displacement continuity at interfaces of sub-domains modeled with different finite element models. In this study, for more efficient analysis, discrete-layer transition model (DLTM) is developed for joining sub-regions that use elements based on different types of mathematical models such as ESLM, PDLM, and FDLM. From Eq. 2.9 and Eq.

2.41, the assumed in-plane displacement fields (U^c; c=1,2) for DLTM can be expressed as

$$\begin{aligned} &U^c(x,y,z) = (\widetilde{V}_i(x,y) + \widetilde{E}_i(x,y) + \widetilde{I}_i(x,y))\ (A_i(z) + B_i(z)) \\ &\text{in } i = 1,2,3,4,\ldots, M(p_{xy}) \end{aligned} \tag{2.61}$$

where the functions A and B comprise of modal variables, depend on types of i-th mode of 2D shape functions in the xy-plane, and are defined as shown in the following.

$$A_i(z) = \begin{cases} \widetilde{N}_1(z)u_{i1}^c + \widetilde{N}_2(z)u_{i2}^c + \widetilde{S}_j(z)u_{ij}^c & \text{in FDLM or PDLM} \\ 0 & \text{in ESLM} \end{cases} \tag{2.62}$$

with

$$j = \begin{cases} 3,\ldots, p_z + 1 & \text{in FDLM} \\ 3,..., p_z' + 1 & \text{in PDLM} \end{cases} \tag{2.63}$$

where p_z and p_z' may or may not be identical.

$$B_i(z) = \begin{cases} 0 & \text{in FDLM or PDLM} \\ u_i^c + z\theta_i^c & \text{in ESLM} \end{cases} \tag{2.64}$$

Based on Eq. 2.10, Eq. 2.29 and Eq. 2.41, the out-of-plane displacement field, W, for DLTM is given by

$$\begin{aligned} &W(x,y,z) = (\widetilde{V}_i(x,y) + \widetilde{E}_i(x,y) + \widetilde{I}_i(x,y))\ (F_i(z) + G_i(z)) \\ &\text{in } i = 1,2,3,4,\ldots, M(p_{xy}) \end{aligned} \tag{2.65}$$

where the functions F and G comprise of modal variables, depend on types of i-th mode of 2D shape functions in the xy-plane, and defined as

$$F_i(z) = \begin{cases} \widetilde{N}_1(z)w_{i1} + \widetilde{N}_2(z)w_{i2} + \widetilde{S}_j(z)w_{ij} & \text{in FDLM}\,(j = 3,\ldots, \hat{p}_z + 1) \\ 0 & \text{in PDLM or ESLM} \end{cases} \tag{2.66}$$

and

$$G_i(z) = \begin{cases} 0 & \text{in FDLM} \\ w_i & \text{in PDLM or ESLM} \end{cases} \tag{2.67}$$

In DLTM, the need to include or neglect transverse normal strains and stresses, primarily, depends on the application. For instance, if the transition elements are located in a thick or moderately thick laminated system, transverse normal strains and stresses should be included in the derivation of the element properties. On the other hand, if DLTM belongs to a thin laminated system, these can be neglected in deriving the element properties. Formulation of finite element based on the DLTM can be undertaken in the same way as was shown in Sections 2.3 through 2.5. Fig. 2.10 illustrates simple connection of the DLTM when 3D elements (FDLM or PDLM) and ESLM-based element are simultaneously considered for modeling a laminate plate with three layers and Fig. 2.11 demonstrates another transitional link role of DLTM from FDLM-based elements to PDLM-based elements.

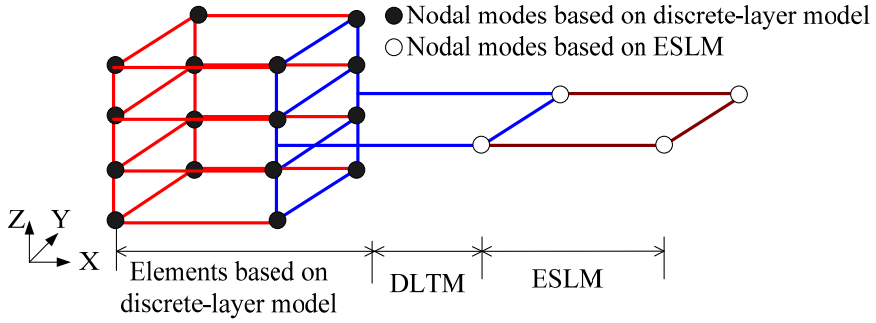

Fig. 2.10 Connection of 2D and 3D elements using DLTM

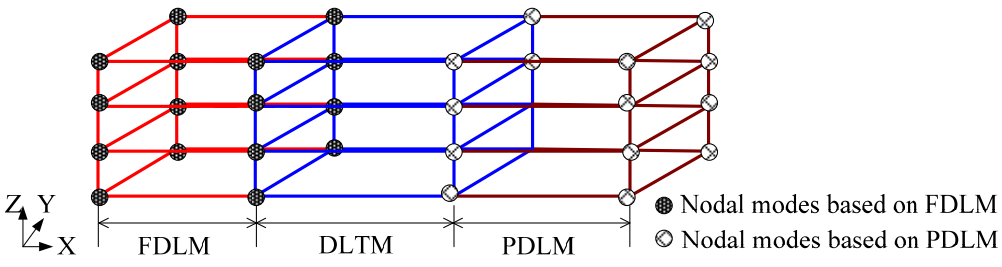

Fig. 2.11 Connection of full and partial discrete-layer elements using DLTM

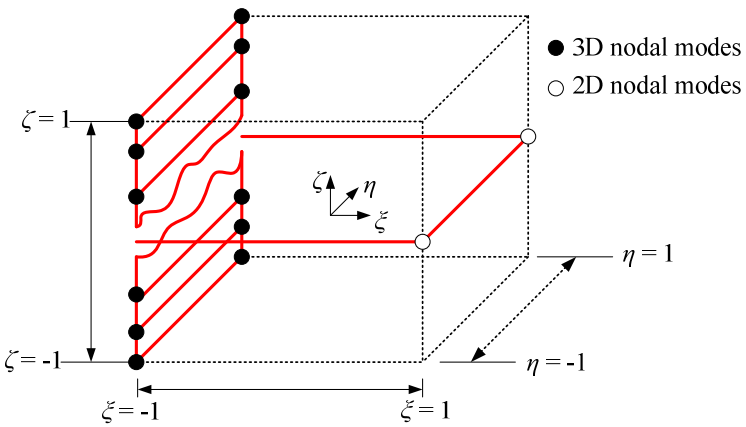

Fig. 2.12 Element based on DLTM with respect to standard coordinate system

Fig. 2.12 displays connection of one layer element with nodes in the 2D space and multi-layered element with nodes in the 3D space. It means that the larger the number of layers in a laminated plate is, the bigger the savings in computational effort required in this modeling technique using the proposed transition element. Fig. 2.13 shows an example finite element mesh in the 2D-plane for the application of transition elements when three element types are simultaneously used in the computational domain. The transition elements serve the purpose of preventing the violation of inter-element compatibilities in a heterogeneous modeling environment. Normally, FDLM-based elements should be used near regions where the stress field is likely to be three-dimensional. Such regions are characterized by the presence of various types of irregularities described in Chapter 1. On the other hand, PDLM-based elements can also be used in regions with less severe geometric irregularity in the thickness direction and the transverse stresses are not significant. ESLM-based elements can be used in regions free of irregularities where the stress field tends to be smooth. Finally, it is necessary to

use transition elements (DLTM) to allow smooth displacement variations between mixed pairs like FDLM-PDLM, FDLM-ESLM, PDLM-ESLM, etc., as shown in Fig. 2.13.

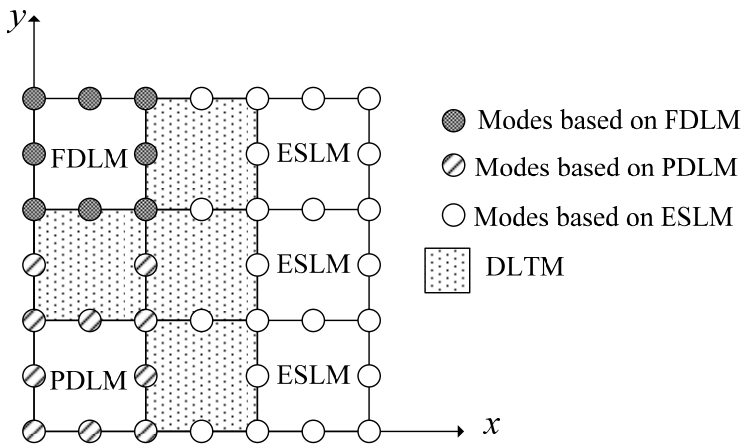

Fig. 2.13 Simple 2D mesh of a mixed model

2.7 Geometric Nonlinearity

In the formulation of the finite element models discussed in the preceding sections, the displacements and strains were assumed to be very small. In some applications of thin laminated plates, however, relatively large deflections may occur. In such cases, the laminated plate may undergo in-plane stretching giving rise to in-plane tensile stresses which tend to stiffen the plate. This may lead to considerable increase in the load capacity of laminated plates. This effect cannot be simulated by small-deflection bending theory used so far. For large deflection problems in solid mechanics, two formulations are possible - (a) Total Lagrangian approach, and (b) Updated Lagrangian approach. In this section, geometrically nonlinear finite element formulations are developed for FDLM, PDLM, ESLM, and DLTM based on the Total Lagrangian approach. It is assumed that deflections are large and rotations are still small or relatively moderate in the sense of

Von Karman hypothesis.

The problem is solved incrementally, and corresponding to *n*-th load increment, the following equilibrium equations must be satisfied.

$$[F]^n - [P]^n = 0 \tag{2.68}$$

where [*F*] are the summation vector of the external applied forces and the corresponding reaction forces, and [*P*] is the internal equivalent force vector. As the exact satisfaction of the equilibrium equations can not always be assured in s nonlinear analysis, a residual force vector [*R*] would exist such that

$$[R]^n = [F]^n - [P]^n \neq 0 \tag{2.69}$$

An iterative sequence can be preformed in order to eliminate the residual forces ($[R]^n \approx 0$). During the general stage of the iterative solution, the computed displacement vector at *i*–th iteration will be expressed as $[\delta]_i^n$. Therefore the iterative form of Eq. 2.69 will be

$$[R]_i^n = [F]^n - [P]_i^n \approx 0 \tag{2.70}$$

After each iteration cycle, the displacement vector is updated as below,

$$[\delta]_i^n = [\delta]_{i-1}^n + [\Delta\delta]_i^n \tag{2.71}$$

where $[\Delta\delta]_i^n$ denotes the change of displacements occurring during the current iteration. Also, in order to obtain the change of the displacements $[\Delta\delta]_i^n$, the tangent stiffness approach, which requires displacement search direction, can be used. The internal equivalent force vector $[P]_i^n$ in Eq. 2.70 can be written in following form

$$[P]_i^n = \int_V [B]_i^n [\sigma]_i^n \, dV \tag{2.72}$$

where [*B*] is the strain-displacement matrix, [σ] is the current stress field, and *V* denotes

the volume of considered domain. Taking the variation of Eq. 2.70 with respect to a displacement variation d[δ] and using Eq. 2.72, gives the tangent stiffness matrix for present geometrically nonlinear analysis as

$$[K]\ d[\delta]\ =\ d[P] = \int_V [B]^{\mathrm{T}}\, d[\sigma]dV + \int_V d[B]^{\mathrm{T}}\,[\sigma]dV \tag{2.73}$$

The strain-displacement matrix [B] may be separated into usual infinitesimal part $[\overline{B}]$ and nonlinear contribution $[\hat{B}]$ so that

$$[B] = [\overline{B}] + [\hat{B}] \tag{2.74}$$

Thus, the variation of the strain-displacement matrix may be written as

$$d[B] = d[\overline{B}] + d[\hat{B}] = d[\hat{B}] \tag{2.75}$$

Also, from Eq. 2.73, the following variational form is obtained.

$$[K]\ d[\delta] = \int_V [B]^{\mathrm{T}}\,[D][B]dV\, d[\delta] + \int_V d[B]^{\mathrm{T}}\,[\sigma]dV \tag{2.76}$$

where [D] is the elasticity matrix. Eq. 2.73 can now be written as

$$[K]\ d[\delta] = [\overline{K}]d[\delta] + \int_V d[B]^{\mathrm{T}}\,[\sigma]dV \tag{2.77}$$

Defining the stresses [σ] from results of previous iteration, the geometric stiffness matrix, being the second term in the right hand side of Eq. 2.77, can be obtained from

$$[\widetilde{K}]d[\delta] = \int_V d[B]^{\mathrm{T}}\,[\sigma]dV = \int_V d[\hat{B}]^{\mathrm{T}}\,[\sigma]dV \tag{2.78}$$

The substitution of Eq. 2.78 in Eq. 2.77 results in

$$[K] = [\overline{K}] + [\widetilde{K}] \tag{2.79}$$

Here, from Eqs. 2.76 and 2.77, $[\overline{K}]$ is given by

$$[\overline{K}] = \int_V [B]^{\mathrm{T}}\,[D][B]dV \tag{2.80}$$

As per one element of Von Karman assumption that derivatives of in-plane displacements with respect to three local coordinates are small, strain vector of FDLM expressed in Eq. 2.11 may be modified as

$$\begin{bmatrix} \varepsilon_{xx} \\ \varepsilon_{yy} \\ \varepsilon_{zz} \\ \gamma_{xy} \\ \gamma_{xz} \\ \gamma_{yz} \end{bmatrix} = \begin{bmatrix} \dfrac{\partial u}{\partial x} \\ \dfrac{\partial v}{\partial y} \\ \dfrac{\partial w}{\partial z} \\ \dfrac{\partial u}{\partial y}+\dfrac{\partial v}{\partial x} \\ \dfrac{\partial u}{\partial z}+\dfrac{\partial w}{\partial x} \\ \dfrac{\partial v}{\partial z}+\dfrac{\partial w}{\partial y} \end{bmatrix} + \begin{bmatrix} \dfrac{1}{2}\left(\dfrac{\partial w}{\partial x}\right)^2 \\ \dfrac{1}{2}\left(\dfrac{\partial w}{\partial y}\right)^2 \\ 0 \\ \left(\dfrac{\partial w}{\partial x}\right)\left(\dfrac{\partial w}{\partial x}\right) \\ 0 \\ 0 \end{bmatrix} = [\varepsilon]^{L}_{6\times1} + [\varepsilon]^{NL}_{6\times1} \tag{2.81}$$

Similarly, from Eq. 2.30, the nonlinear strain vector for PDLM, ESLM, and DLTM in which the variation of w with z may be neglected can be written by

$$\begin{bmatrix} \varepsilon_{xx} \\ \varepsilon_{yy} \\ \gamma_{xy} \\ \gamma_{xz} \\ \gamma_{yz} \end{bmatrix} = \begin{bmatrix} \dfrac{\partial u}{\partial x} \\ \dfrac{\partial v}{\partial y} \\ \dfrac{\partial u}{\partial y}+\dfrac{\partial v}{\partial x} \\ \dfrac{\partial u}{\partial z}+\dfrac{\partial w}{\partial x} \\ \dfrac{\partial v}{\partial z}+\dfrac{\partial w}{\partial y} \end{bmatrix} + \begin{bmatrix} \dfrac{1}{2}\left(\dfrac{\partial w}{\partial x}\right)^2 \\ \dfrac{1}{2}\left(\dfrac{\partial w}{\partial y}\right)^2 \\ \left(\dfrac{\partial w}{\partial x}\right)\left(\dfrac{\partial w}{\partial x}\right) \\ 0 \\ 0 \end{bmatrix} = [\varepsilon]^{L}_{5\times1} + [\varepsilon]^{NL}_{5\times1} \tag{2.82}$$

The components of the second-order Piola-Kirchhoff stress vector are given by usual stress-strain relations of linear elasticity like Eqs. 2.12, 2.31, and 2.5-55 in which the current strains are taken to be the nonlinear strains mentioned above. From Eqs. 2.81 and 2.82, the nonlinear contribution to the strain vector can be rxpressed as

$$[\varepsilon]^{NL} = \frac{1}{2}[A][S][\delta] \tag{2.83}$$

where [S] is a matrix with two rows and a number of columns equal to the total number of element nodal variables. This leads to the following

$$[S][\delta] = \begin{bmatrix} \dfrac{\partial w}{\partial x} \\ \dfrac{\partial w}{\partial y} \end{bmatrix} \tag{2.84}$$

Also, in FDLM-based elements, [A] in Eq. 2.83 is given by

$$[A] = \begin{bmatrix} \dfrac{\partial w}{\partial x} & 0 & \dfrac{\partial w}{\partial y} & 0 & 0 & 0 \\ 0 & \dfrac{\partial w}{\partial y} & \dfrac{\partial w}{\partial x} & 0 & 0 & 0 \end{bmatrix}^{\mathrm{T}} \tag{2.85}$$

In addition, for PDLM-based elements and DLTM-based elements with combination of only FDLM and PDLM, [A] can be expressed as

$$[A] = \begin{bmatrix} \dfrac{\partial w}{\partial x} & 0 & \dfrac{\partial w}{\partial y} & 0 & 0 \\ 0 & \dfrac{\partial w}{\partial y} & \dfrac{\partial w}{\partial x} & 0 & 0 \end{bmatrix}^{\mathrm{T}} \tag{2.86}$$

Also, for ESLM-based elements, and DLTM-based elements including ESLM, [A] can be written as

$$[A] = \begin{bmatrix} \dfrac{\partial w}{\partial x} & 0 & \dfrac{\partial w}{\partial y} & 0 & 0 & 0 & 0 & 0 \\ 0 & 0 & \dfrac{\partial w}{\partial x} & 0 & 0 & 0 & 0 & 0 \end{bmatrix}^{\mathrm{T}} \tag{2.87}$$

Now, the variation of Eq. 2.83 can be expressed as

$$d[\varepsilon]^{NL} = \frac{1}{2}d[A]\big([S][\delta]\big) + \frac{1}{2}[A]d\big([S][\delta]\big) = [A][S]\,d[\delta] \tag{2.88}$$

The nonlinear part of strain-displacement matrix, $[\hat{B}]$, used in Eq. 2.74 is given by

$$[\hat{B}] = [A][S] \tag{2.89}$$

Therefore, the incremental strain-displacement matrix $[B]$ can be calculated by summing the initially calculated matrix $[\overline{B}]$ and the matrix $[\hat{B}]$ evaluated at any iteration step. Also, to evaluate the geometric stiffness matrix appearing in Eq. 2.78, use of Eq. 2.89 results in

$$[\widetilde{K}]d[\delta] = \int_V d([A][S])^{\mathrm{T}}[\sigma]dV = \int_V [S]^{\mathrm{T}}\, d[A]^{\mathrm{T}}[\sigma]dV \tag{2.90}$$

$d[A]^{\mathrm{T}}[\sigma]$ in Eq. 2.90 can be expressed with the aid of Eq. 2.84 through Eq. 2.87 in following form.

$$d[A]^{\mathrm{T}}[\sigma] = [\sigma][S]d[\delta] \tag{2.91}$$

where $[\sigma]$ is composed of components of the current second-order Piola-Kirchhoff stress vector given by

$$[\sigma] = \begin{bmatrix} \sigma_{xx} & \tau_{xy} \\ \tau_{xy} & \sigma_{yy} \end{bmatrix} \tag{2.92}$$

In addition, the geometric stiffness matrix appearing in Eq. 2.90 can be expressed by

$$[\widetilde{K}] = \int_V [S]^{\mathrm{T}}[\sigma][S]dV \tag{2.93}$$

CHAPTER III

COMPUTER IMPLEMENTATION OF PROPOSED MODELING SCHEMES

3.1. Overview

Since the advent of electronic digital computers, a number of discrete numerical schemes have been put forward for solving the differential equations of the continua. Although the finite difference method predates the digital computer era, the schemes termed finite element method, boundary element method, mesh free method, wavelets method, etc., have advanced almost hand-in-hand with the ever increasing power of digital computers. Currently among the several numerical approaches, the finite element method, especially so-called *h*-FEM, is most widely used in all disciplines of engineering and sciences, primarily because commercial modeling and simulation software like ABAQUS, ADINA, ANSYS, LS-DYNA, and NASTRAN *etc*. almost exclusively utilize this scheme resulting from enhancements of available public domain software which essentially utilize *h*-FEM. The primary power of the stated commercial software lies in their excellent user-interface, and superior pre- & post-processing capabilities. In view of proven superiority of *p*-FEM, halfhearted attempts have been made to incorporate it as a secondary module in software like ANSYS and NASTRAN. A more comprehensive implementation of *p*-FEM can be found in the commercial software like StressCheck and ANSYS which is specifically designed for detailed local analysis. In spite of this welcome development, there is a glaring lack of capability in commercial software to deal with localized behavior of complex laminated composite systems. Since COMET-X,

the first implementation of *p*-FEM software, by Basu et al. (1977), *p*-FEM software tools described in some references (Hall and Merrill, 1987; Woo, 1988; Akhtar, 1989; Ahmed, 1989; Crull, 1989; Crim, 1992; Ghosh, 1996) have been basically meant for research work, but having limitations in efficient and accuracy in the modeling of complex and also the monitoring of the quality of predicted response. New efficient approach based on *p*-FEM can be considered as compelling reasons for developing a more accurate modeling scheme for complex composites materials and implemented for the purpose of the current investigation in the form of a set of software tools to be nicknamed as CTLAP (Computing Tools for Laminate Analysis based on *P*-version of finite element method). The CTLAP program is implemented using the M-file code of MATLAB 7, which is one of many technical computing languages and has recently become quite popular for research as well as for industrial applications. Formulations of laminate theories considered in present research are mentioned in previous Chapter 2. Here, additional numerical techniques built in CTLAP are discussed first.

3.2. Mapping of Curved Boundary Geometry Using Blending Functions

If edges of a quadrilateral or triangular element are straight, its geometry can be mapped uniquely from the standard element by defining the mapping function in terms of vertex node locations only. If one or more edges of the element is curved and the equation of such a curve can be defined in terms of a polynomial like: $y=f(x)$, or $x=\mathrm{f}(y)$, by introducing additional node(s) on such a curved edge (number of nodes should be one less than the degree of polynomial defining the curve) will allow exact one-to-one mapping of the geometry between the standard element and the actual element.

Alternatively, as normally done in *h*-FEM, the size of straight edged elements at a curved boundary can be made small enough to follow the curved side as closely as desired, irrespective of the shape of the curved edge. In *p*-FEM, this option is not acceptable and to avoid geometrical sources of error, exact mapping of a curved edge is necessary, because one of the sources of efficiency of *p*-FEM is the use of as large an element (or, as few) as it is possible. If the geometry of the curved edge of an element is defined in terms of conic sections like circle, ellipse, or hyperbola, a mapping based on the introduction of additional nodes in the curved edge will not allow exact mapping of the geometry. This calls for the use of more advanced scheme to enable exact mapping of such curved edges. Fig. 3.1 shows that 2D standard coordinates (ξ and η) is transformed into 2D actual coordinates (x and y) involving arbitrary curvilinear boundary with four reference points and sides. For this process, the general mapping functions with respect to the 2D-plane are derived from blending functions based on bilinear mapping expressions (Gordon and Hall, 1973) as shown below.

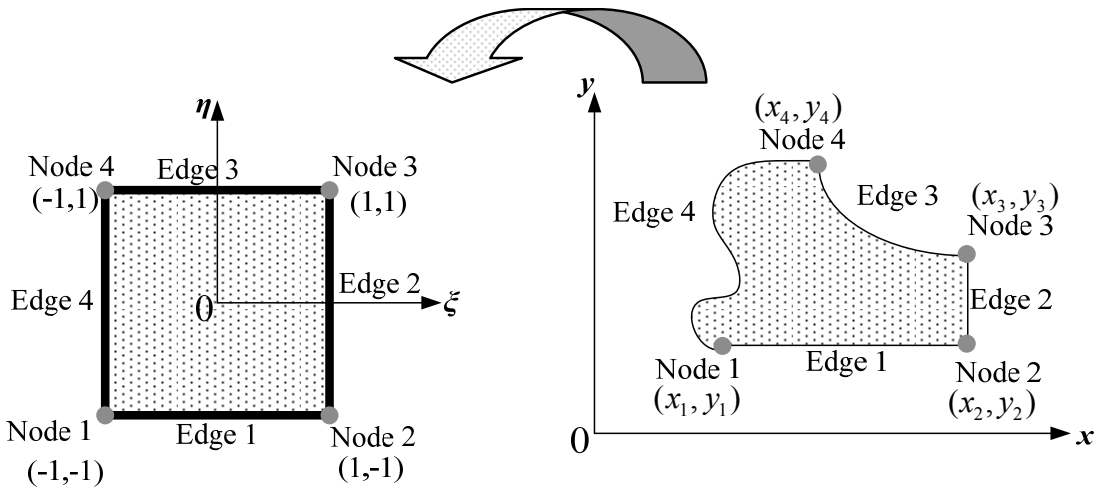

Fig. 3.1 Mapping concept for arbitrary curvilinear boundary

$$
\begin{aligned}
X = {} & H^1(x_1, x_2, \xi)S(\eta) + H^2(x_2, x_3, \eta)T(\xi) + H^3(x_4, x_3, \xi)T(\eta) + H^4(x_1, x_4, \eta)S(\xi) \\
& - x_1 S(\xi)\, S(\eta) - x_2 T(\xi)\, S(\eta) - x_3 T(\xi)\, T(\eta) - x_4 S(\xi)\, T(\eta) \\
Y = {} & H^1(y_1, y_2, \xi)S(\eta) + H^2(y_2, y_3, \eta)T(\xi) + H^3(y_4, y_3, \xi)T(\eta) + H^4(y_1, y_4, \eta)S(\xi) \\
& - y_1 S(\xi)\, S(\eta) - y_2 T(\xi)\, S(\eta) - y_3 T(\xi)\, T(\eta) - y_4 S(\xi)\, T(\eta)
\end{aligned}
\tag{3.1}
$$

in which S and T are given by

$$
S(\xi) = \frac{1-\xi}{2};\ T(\xi) = \frac{1+\xi}{2} \tag{3.2}
$$

Also, X and Y refer to mapping functions with respect to x and y. The four edges are treated independently. Then H^i is the function with respect to ξ or η describing the geometric property on Edge i. If the curved edge of an element is defined by a p-th degree polynomial, say, in the form $y=f(x)$, the functions H^i defining the geometry of any edge i (=1,2,3, and 4) can be expressed in terms of p-degree Lagrange interpolation polynomial. For example, if p-order equation defining the geometry of Edge i between any point a and b is in terms of the x coordinate in the xy-plane that is of the form $G(x)$, the functions H^i with respect to ξ to define the mapping function X in Eq. 3.1 is as follows.

$$
H^i(x_a, x_b, \xi) \begin{cases}
= S(\xi)\, x_a + T(\xi)\, x_b & \text{(Linear)} \\
= -\xi\, S(\xi)\, x_a + \xi\, T(\xi)\, x_b + 8\, S(\xi)\, T(\xi)\, (x_a + x_b) & \text{(Quadratic)} \\
= -\dfrac{1-9\xi^2}{8}\left(S(\xi)x_a + T(\xi)x_b\right) & \\
\quad + \dfrac{9}{12} S(\xi)\, T(\xi)\left[(1-3\xi)(2x_a + x_b) + (1+3\xi)(x_a + 2x_b)\right] & \text{(Cubic)}
\end{cases}
\tag{3.3}
$$

Also, the functions H^i with respect to ξ to define the vector function Y in Eq. 3.1 are as follows.

$$H^i(y_a, y_b, \xi)\begin{cases} = S(\xi)\, y_a + T(\xi)\, y_b & \text{(Linear)} \\ = -\xi\, S(\xi)\, y_a + \xi\, T(\xi)\, y_b + 4\, S(\xi) T(\xi) G\left(\dfrac{y_a + y_b}{2}\right) & \text{(Quadratic)} \\ = -\dfrac{1-9\xi^2}{8}\left(S(\xi)\ y_a + T(\xi) y_b\right) & \\ \quad + \dfrac{9}{4} S(\xi) T(\xi)\left[(1-3\xi) G\left(\dfrac{2y_a + y_b}{3}\right) + (1+3\xi) G\left(\dfrac{y_a + 2y_b}{3}\right)\right] & \text{(Cubic)} \end{cases} \tag{3.4}$$

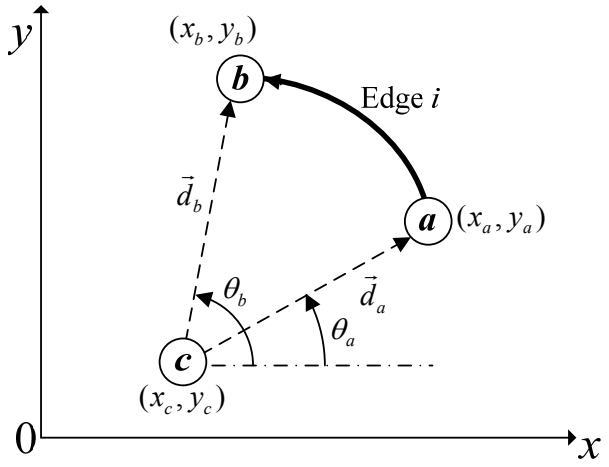

Fig. 3.2 Arc of circular as the boundary

Moreover, when shape of any edge is the arc of a circle, trigonometric functions are used to define the shape. Fig. 3.2 shows the edge *i* as an arc of a circle with the two referenced end points, *a* and *b*. The center of the arc is located at *c*. In Fig. 3.2, the actual coordinates of point *a* and *b* can be obtained from radial vectors:

$$\vec{d}_a = < x_a - x_c\,, y_a - y_c >;\ \vec{d}_b = < x_b - x_c\,, y_b - y_c > \tag{3.5}$$

Here the radius *d* is obtained from the norm of the vectors, so that

$$d = \left\|\vec{d}_a\right\| = \left\|\vec{d}_b\right\| \tag{3.6}$$

Also, θ_a and θ_b are the anticlockwise angles measured from the positive *x* direction to

the vector $\vec{d}_a$ and $\vec{d}_b$, respectively. The functions H^i for any edge i shown in Fig. 3.2 are of the form

$$H^i(\alpha,\beta,\xi)\begin{cases} = c_1 + d\cos\left(\theta_a \dfrac{1-\xi}{2} + \theta_b \dfrac{1+\xi}{2}\right) \text{when} \alpha \text{ and } \beta \text{ are } x-\text{coordinates} \\ = c_2 + d\sin\left(\theta_a \dfrac{1-\xi}{2} + \theta_b \dfrac{1+\xi}{2}\right) \text{when} \alpha \text{ and } \beta \text{ are } y-\text{coordinates} \end{cases} \tag{3.7}$$

with

$$\theta_a = \cos^{-1}\left(\frac{\vec{d}_a \bullet \vec{u}}{d}\right) \text{ and } \theta_b = \cos^{-1}\left(\frac{\vec{d}_b \bullet \vec{u}}{d}\right) \tag{3.8}$$

where $\vec{u}$ is the unit vector along the x-axis.

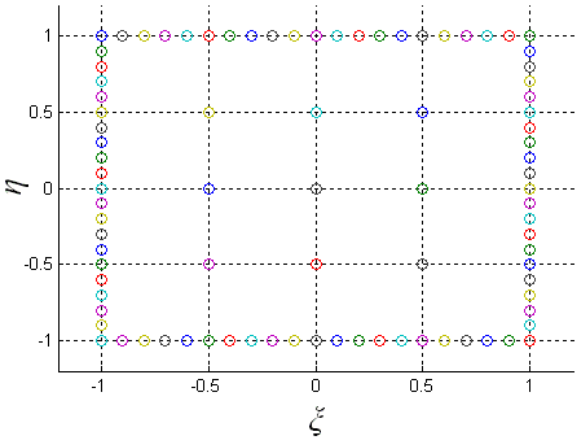

Fig. 3.3 Points in standard element (ξ and η)

Meanwhile, in order to verify the mapping technique defined above, at first, 80 and 9 sampling points on the boundaries and the interior on standard coordinate system, respectively, are considered as shown in Fig. 3.2. Using Eq. 3.1, all sampling point locations defined by standard coordinates can be transformed into those in actual

coordinates. The results of mapping of these points onto a series of domains of different shapes are shown in Fig. 3.4. The red-solid lines indicate the boundaries of real domain. It is noticed that the all the sampling points are exactly transformed into boundaries or inner parts of real domains.

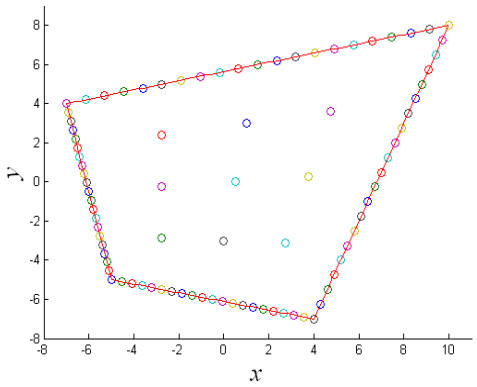

(a) Straight edges

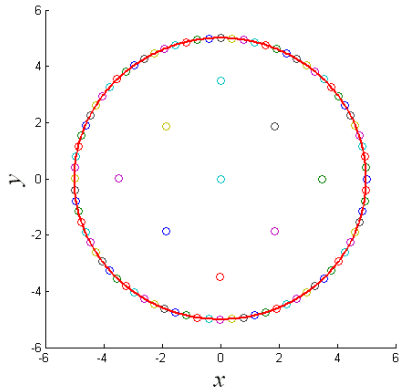

(b) Circular

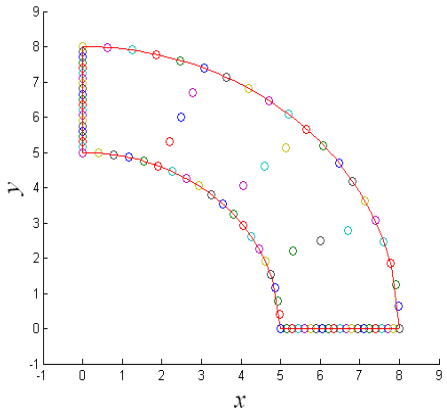

(c) Sector

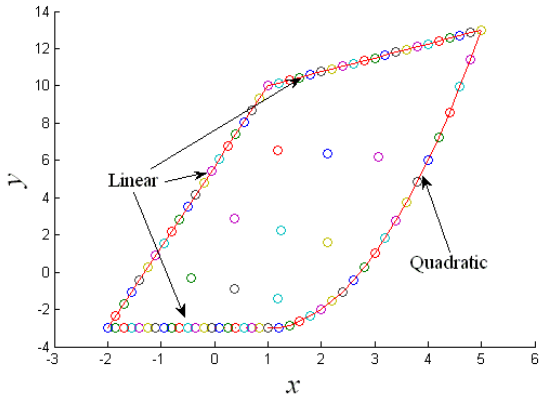

(d) One quadratic curved edge

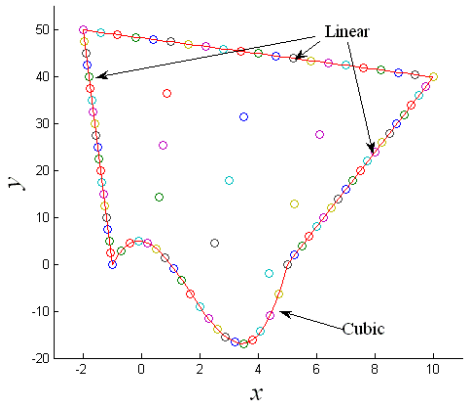

(e) One cubic curved edge

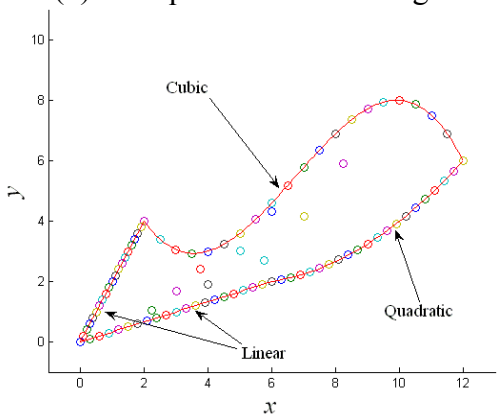

(f) Two curved edges

Fig. 3.4 Domains on actual coordinate system

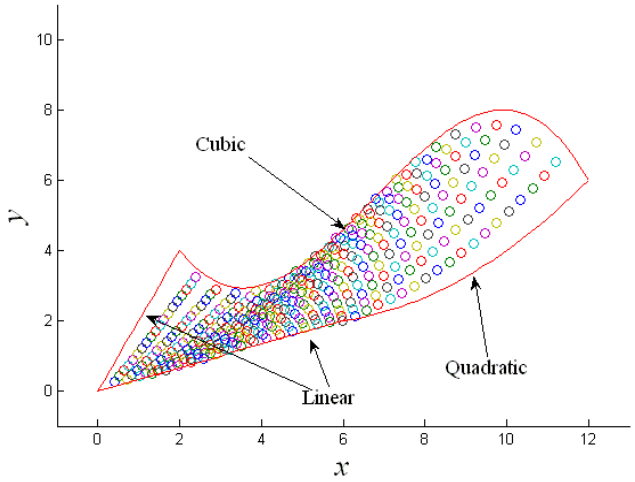

Fig. 3.5 Irregular sub-domain (361 sampling points)

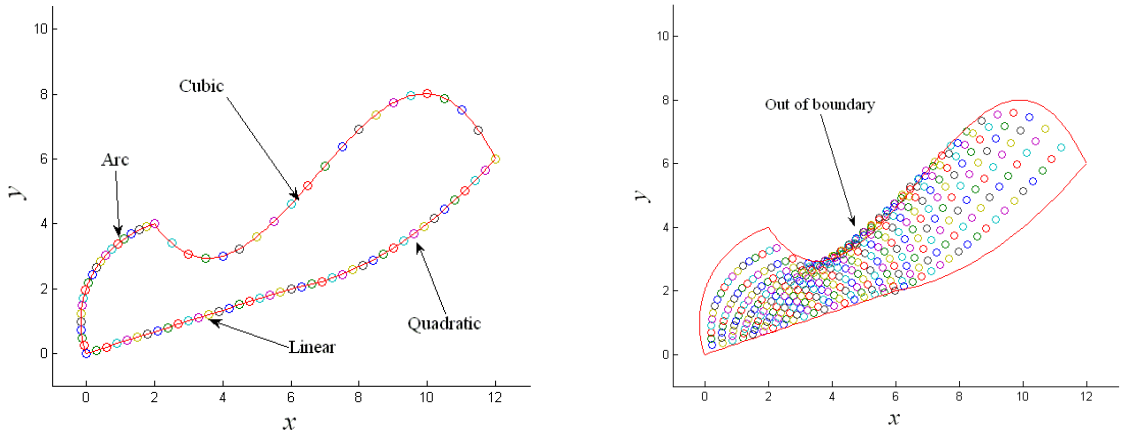

(a) Sampling points on the boundary (b) Inner sampling points

Fig 3.6 Irregular domain (Arc + Quadratic + Arc + Linear)

To further determine the accuracy of mapping the interior sampling points, 361 sampling points are considered for a grossly irregular domain. Fig. 3.5 shows that all interior points in the standard element are mapped inside the actual irregular sub-domain. However, Eq. 3.1 is not always valid for each and every irregular shape. For example, although Fig. 3.6

(a) shows that the sampling points on the boundaries of the standard element are mapped exactly on the boundaries of the real domain; a few interior sampling points have been mapped slightly outside at some edges of the real domain as shown in Fig. 3.6 (b). Therefore, in the case of actual problems, proper geometric discretization process of highly complex geometries will enable avoiding the situation shown in Fig. 3.6 (b).

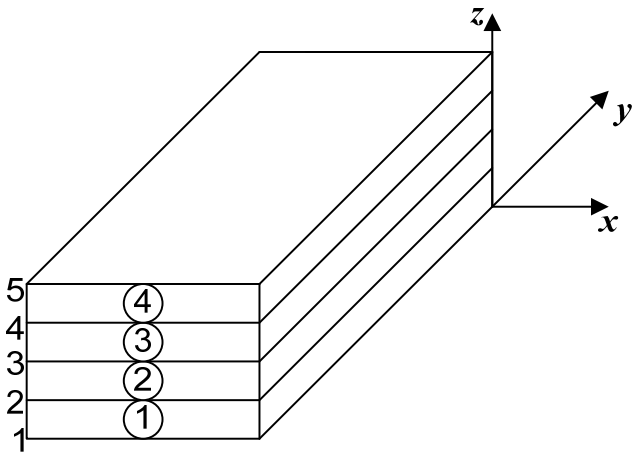

Fig. 3.7 Typical laminated system with four laminas

The mapping scheme defined in Eq. 3.1 is valid for purely 2D systems. In general, for 3D modeling, additionally *z*-axis needs to be considered. To account for geometry of the 3D elements, the standard element should be a cube with standard coordinates taken as (ξ, η, and ζ). In laminated system as shown in Fig. 3.7, however, top and bottom surfaces of layers are generally parallel. Therefore, from the characteristic of laminated systems and Eq. 3.1, the geometric mapping parameters for any layer *i* in 3D modeling of laminated systems can be expressed as follows

$$
\begin{aligned}
X &= H^1(x_1, x_2, \xi)S(\eta) + H^2(x_2, x_3, \eta)T(\xi) + H^3(x_4, x_3, \xi)T(\eta) + H^4(x_1, x_4, \eta)S(\xi) \\
&\quad - x_1 S(\xi)S(\eta) - x_2 T(\xi)S(\eta) - x_3 T(\xi)T(\eta) - x_4 S(\xi)T(\eta) \\
Y &= H^1(y_1, y_2, \xi)S(\eta) + H^2(y_2, y_3, \eta)T(\xi) + H^3(y_4, y_3, \xi)T(\eta) + H^4(y_1, y_4, \eta)S(\xi) \\
&\quad - y_1 S(\xi)S(\eta) - y_2 T(\xi)S(\eta) - y_3 T(\xi)T(\eta) - y_4 S(\xi)T(\eta) \\
Z &= S(\zeta)z^i + T(\zeta)z^{i+1}
\end{aligned}
\tag{3.9}
$$

where Z represents mapping function for z-coordinate, and z^i and z^{i+1} denote the positions of the bottom and top faces, respectively, on the z-axis.

3.3 Calculation of Energy Release Rate

In general, based on an energy approach proposed by Irwin (1956) for an elastic body containing a crack, a crack-extension force (or crack-driving force) G, so-called energy release rate (ERR), can be defined as

$$G = -\frac{\partial \Pi}{\partial A} \tag{3.10}$$

Here A is crack area and potential energy of an elastic body Π is defined as follows.

$$\Pi = E - W \tag{3.11}$$

where E is the strain energy stored in the body and W is the work done by external forces. According to linear elasticity theory, a body under constant applied loads obeys

$$W = 2E \tag{3.12}$$

Then Eq. 3.11 can be rewritten by following form

$$\Pi = E - 2E = -E \tag{3.13}$$

Therefore, Eq. 3.10 can be expressed as

$$G = \frac{\partial E}{\partial A} \tag{3.14}$$

3.3.1 Strain Energy Release Rate

A variety of methods have been used to compute ERR based on results obtained from finite element analysis. Among various methods, one of the simple techniques is *strain energy release rate* technique (Owen and Fawkes, 1983; SERR), often called *finite crack extension method* (Krueger, 2002). This SERR requires two complete analyses. In the first step with the actual crack length *a*, the strain energy is calculated as global forces on the structural level are multiplied with global deformations. Then the crack is extended for by an infinitesimal length (*da*) prior to the second analysis. In the second step, additional strain energy is calculated like in the first step. Thus, as shown in Fig. 3.8, the change in strain energy, *dE*, can be calculated as the difference between the values of two energies obtained from the two analyses Then the ERR can be obtained by applying Eq. 3.14. Although the SERR is very simple method, it is difficult to compute ERR locally at crack front because the method provides one global total energy release rate. Also, the process requiring two analyses is somewhat cumbersome.

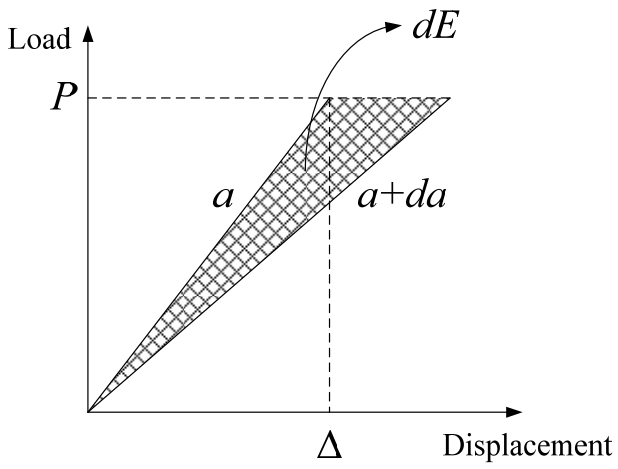

Fig. 3.8 Calculation of change in strain energy by constant load control

3.3.2 2D VCCT for ESLM

For fracture analysis for laminated plates with crack-like flaws and modeled with the proposed elements, 2D VCCT (virtual crack closure technique) is considered. This method is based on Irwin's original observation (Irwin, 1958) that the work required to extend a crack by an infinitesimal distance Δa is equal to the work required to close the crack to its original length. This procedure requires two calculations; whereas, the modified VCCT adapted below requires just one calculation. The VCCT procedure of calculating energy release rate for a model using the proposed ESL element is based on reference (Rybicki and Kanninen, 1977). Fig. 3.9 represents configurations for undeformed plate with a crack of length a (before analysis) and the deformed case (after analysis) applying the VCCT on ESLM-based element.

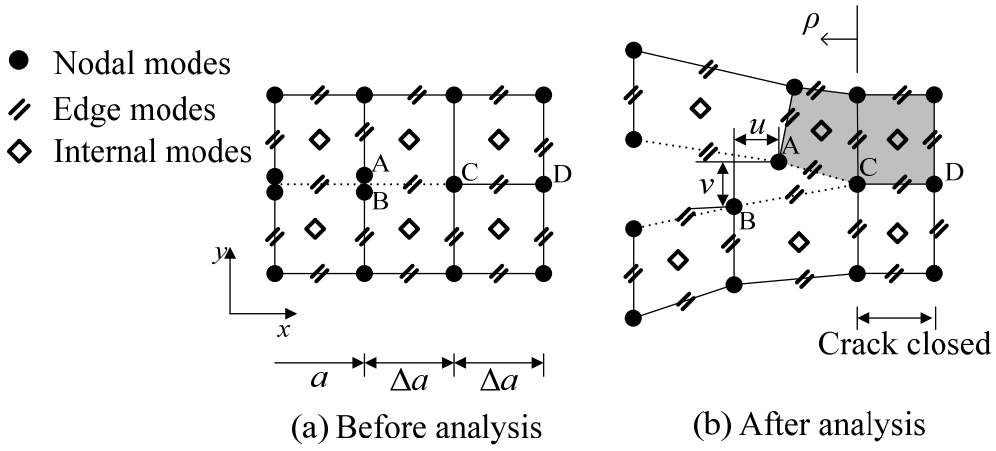

Fig. 3.9 Virtual crack closure technique for ESLM

The discontinuity caused by the presence of crack is shown by a dotted line between the vertex modes. In the same figure, the adjacent vertex modes within a crack are assigned

identical coordinates allowing independent deformations in adjacent vertex nodes and side modes enabling both Mode I and II deformations, as shown in Fig. 3.9 (b). Like Fig. 3.9, the basic premise of the method is that the energy ΔE released when the crack is extended by Δa from $a+\Delta a$ (point C) to $a+2\Delta a$ (point D) is same as the required work, W, to close the crack between points C and D. Another premise is that an additional crack extension of Δa from $a+\Delta a$ (point C) to $a+2\Delta a$ (point D) does not noticeably change the deformation state at the original crack tip, point A and B in Fig. 3.9 (a). The significance of this assumption is that for crack tip location point D, the deformations at point C will almost be same as those at point A, when the crack tip located at point C. The aforementioned premises lead to the following relationships.

$$W = \Delta E = E(a + \Delta a) - E(a) \tag{3.15}$$

The work W for crack extension can be expressed as

$$W = \frac{1}{2}\int_0^{\Delta a} U(\rho)\ \sigma_x(\rho - \Delta a) + V(\rho)\ \sigma_y(\rho - \Delta a)\, d\rho \tag{3.16}$$

where U and V relative displacement functions parallel to crack (x-direction) and normal to crack (y-direction), respectively. The stress components σ_x and σ_y also act parallel to the same axes. The variable ρ is the measure of distance of a point on the crack surface with the origin located at the crack tip. From Eq. 3.15 and Eq. 3.16, the total energy release rate can be expressed as

$$G_{total} = \lim_{\Delta a \to 0} \frac{\Delta E}{t\Delta a} = \lim_{\Delta a \to 0} \frac{W}{t\Delta a} = \lim_{\Delta a \to 0} \frac{1}{2t\Delta a}\int_0^{\Delta a} U(\rho)\sigma_x(\rho - \Delta a) + V(\rho)\sigma_y(\rho - \Delta a)d\rho \tag{3.17}$$

where t is thickness of a cracked plate. With nodal forces (F_C^x, F_C^y) at vertex node C and relative displacements (u, v) between vertex nodes A and B, the total energy release rate can be expressed as

$$G_{total} = \frac{F_C^x\, u + F_C^y\, v}{2t\Delta a} \tag{3.18}$$

In 2D crack problems, the total energy release rate can be calculated from individual component modes using the following uncoupled equations

$$G_I = \frac{F_C^y\, v}{2t\Delta a};\ G_{II} = \frac{F_C^x\, u}{2t\Delta a} \tag{3.19}$$

So, the energy release rate expressions take the form

$$G_{total} = G_I + G_{II} \tag{3.20}$$

The nodal forces F at vertex node C represent the summation of nodal forces for adjacent elements on one side of the crack and, say in the case of F_C^y, will be based on the two shaded elements shown in Fig 3.9 (b). To calculate an internal force F^* in any direction, say x or y, at a vertex node k of an ESLM-based element, the elasticity matrix $[L]_{8\times 8}$ and the strain vector $<\hat{\varepsilon}>_{1\times 8}^{T}$ (Eq. 2.56) are used, so that

$$F^* = \{B^*\}_{1\times 8}^{T}\ [L]_{8\times 8} <\hat{\varepsilon}>_{1\times 8}^{T} \tag{3.21}$$

where strain vector $\{B^*\}$ is a column vector of strain matrix $[B]_{8\times q}$ used in Eq. 2.24, corresponding to the degrees of freedom in the desired direction at vertex node k. Substituting Eq. 2.24 into Eq. 3.21, the internal forces are given by

$$F^* = <B^*>_{1\times 8}\ [L]_{8\times 8}\,[B]_{8\times q} <\delta>_{1\times q}^{T} \tag{3.22}$$

3.3.3 3D VCCT for PDLM and FDLM

In the case of 3D VCCT, the concept of 2D VCCT is extended in the z-direction. In doing so, the extension of the method from 2D to 3D requires adding displacement w and

stress σ_z in the *z*-direction. So, Eq. 3.17 is modified to

$$G_{total} = \lim_{\Delta a \to 0} \frac{1}{2t\Delta a} \int_0^{\Delta a} U(\rho)\ \sigma_x(\rho - \Delta a) + V(\rho)\ \sigma_y(\rho - \Delta a) + W(\rho)\sigma_z(\rho - \Delta a)\ \ d\rho \qquad (3.23)$$

The total energy release rate within any layer *i* applying 3D VCCT to elements based on discrete-layer models can be written as follows.

$$\begin{aligned} G_{total} = \frac{1}{2\,t_i\,\Delta a} [&(F_i^x)^{bot}\ u^{bot} + (F_i^x)^{top}\ u^{top} + (F_i^y)^{bot}\ v^{bot} + (F_i^y)^{top}\ v^{top} \\ &+ (F_i^z)^{bot}\ w^{bot} + (F_i^z)^{top}\ w^{top}\,] \end{aligned} \qquad (3.24)$$

In a 3D crack problem, Mode III of the total energy release rate needs to be added, so that.

$$G_{total} = G_{\mathrm{I}} + G_{\mathrm{II}} + G_{\mathrm{III}} \qquad (3.25)$$

Therefore, as in 2-D VCCT, the modal energy release rates will have the following forms.

$$\begin{aligned} G_{\mathrm{I}} &= \frac{(F_i^y)^{bot}\ v^{bot} + (F_i^y)^{top}\ v^{top}}{2\,t_i\,\Delta a}; \\ G_{\mathrm{II}} &= \frac{(F_i^x)^{bot}\ u^{bot} + (F_i^x)^{top}\ u^{top}}{2\,t_i\,\Delta a}; \\ G_{\mathrm{III}} &= \frac{(F_i^z)^{bot}\ w^{bot} + (F_i^z)^{top}\ w^{top}}{2\,t_i\,\Delta a} \end{aligned} \qquad (3.26)$$

Meanwhile, F_i^x, F_i^y, and F_i^z refer to crack-sliding, crack-opening, and crack-tearing forces. Also, *u*, *v*, and *w* are relative displacements corresponding to F_i^x, F_i^y, and F_i^z. Superscripts denoted by *bot* and *top* mean bottom and top surfaces. t_i is a thickness of layer *i*. Fig. 3.10 represents the 3D VCCT on the elements based on discrete-layer models graphically. From Fig. 3.10 (a) the relative displacements of layer 1 can be written as follows.

$$
\begin{aligned}
u^{bot} &= u_{\mathrm{A}} - u_{\mathrm{E}}; \quad u^{top} = u_{\mathrm{B}} - u_{\mathrm{F}};\\
v^{bot} &= v_{\mathrm{A}} - v_{\mathrm{E}}; \quad v^{top} = v_{\mathrm{B}} - v_{\mathrm{F}};\\
w^{bot} &= w_{\mathrm{A}} - w_{\mathrm{E}}; \quad w^{top} = w_{\mathrm{B}} - w_{\mathrm{F}}
\end{aligned}
\tag{3.27}
$$

In Fig. 3.10 (b), showing the three-layer laminated plate, for layer 1, the nodal forces are considered at vertex nodes I and J. These forces can be calculated by adding the internal forces obtained for elements 1 and 2.

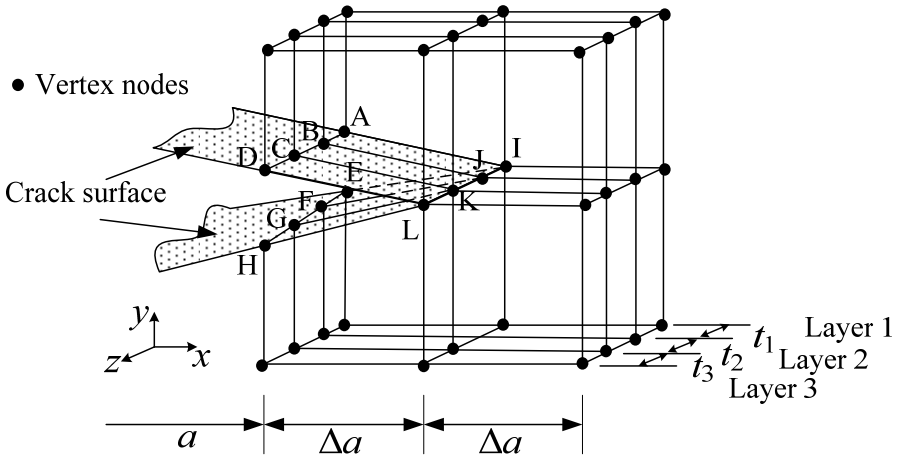

(a) 3D view after analysis

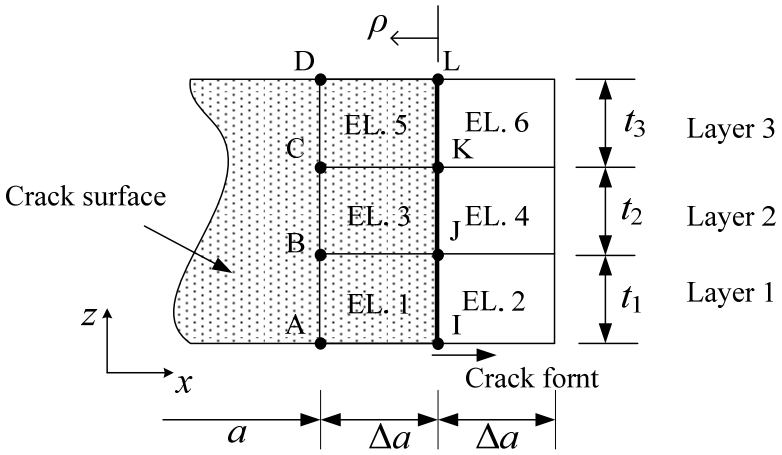

(b) Side view

Fig. 3.10 Virtual crack closure technique for elements based on discrete-layer model

Similar to the case of ESLM-based elements using 2D VCCT, in FDLM-based elements, the internal forces F^* with the elasticity matrix $[\widetilde{D}]^l_{6\times6}$ used in Eq. 2.19, and strain vector $\{\widetilde{\varepsilon}\}^l_{x,y,z}$ defined in Eq. 2.12 or Eq. 2.13 are considered.

$$F^* = \{\widetilde{B}^*\}^{\mathrm{T}}_{1\times6}\,[\widetilde{D}]^l_{6\times6}\,\{\widetilde{\varepsilon}\}^l_{x,y,z} \tag{3.28}$$

Here strain vector $\{\widetilde{B}^*\}$ is a column vector of strain matrix $[\widetilde{B}]_{6\times n}$ mentioned in Eq. 2.24, based on the applicable degrees of freedom. Therefore, the internal force F^* can be expressed as

$$F^* = \left\lfloor \widetilde{B}^* \right\rfloor_{1\times6}\,[\widetilde{D}]^l_{6\times6}\,[\widetilde{B}]_{6\times n} < \delta >^{\mathrm{T}}_{1\times n} \tag{3.29}$$

Additionally, in a similar way, the internal force of elements based on PDLM can be obtained from Eqs. 2.31, 2.32, and 2.38 in the following form.

$$F^* = \left\lfloor \widetilde{B}^* \right\rfloor_{1\times5}\,[\widetilde{D}]^l_{5\times5}\,[\widetilde{B}]_{5\times n} < \delta >^{\mathrm{T}}_{1\times n} \tag{3.30}$$

3.4 Adaptive Analysis Using Ordinary Kriging Interpolation

In general, the process of stress smoothening at interfaces between elements is often required for adaptive analysis. In this study, ordinary Kriging (OK) interpolation technique is considered for stress smoothening. The OK interpolation technique is a method which predicts unknown values at an arbitrary location based on known values with associated weight factors at specific locations. The weight factors are assigned by examining the spatial variation of data. For distribution of the spatial variation, variogram is used. From the references (Chen and Jiao, 2001; Lloyd and Atkinson, 2001; Pardo-Iguzquiza and Dowd, 2001), the semi-variogram $\gamma(h)$ can be defined as

$$\gamma(h) = \frac{1}{2} E\left[\{u(x+\Delta x, y+\Delta y) - u(x,y)\}^2\right] \tag{3.31}$$

where $u(x,y)$ is the value of the variable of interest at location (x,y), and E is the statistical expectation operator. The variogram, $2\gamma(h)$, is a function of the separation between points, $h\,(=\sqrt{\Delta x^2 + \Delta y^2})$. It is not a function of the specific location (x,y). The semi-variogram can also be expressed as

$$\gamma(h) = \frac{1}{2n} \sum_{i=1}^{n} \left[u(x_i + \Delta x, y+\Delta y) - u(x_i, y_i)\right]^2 \tag{3.32}$$

where n is equal to the number of pairs of values in which the separation distance is equal to h. Experimental semi-variogram by Eq. 3.32 can be approximated. Thus, for OK interpolation technique, one alike a theoretical variogram is usually chosen among some of the possibilities such as linear model, spherical model, exponential model and so on. In this study, to avoid manual selection of variogram model by trial-and-error, the third-order polynomial model has been adopted for theoretical variogram as shown in Fig. 3.11 by implementing it in a *p*-adaptive analysis using least square fitting.

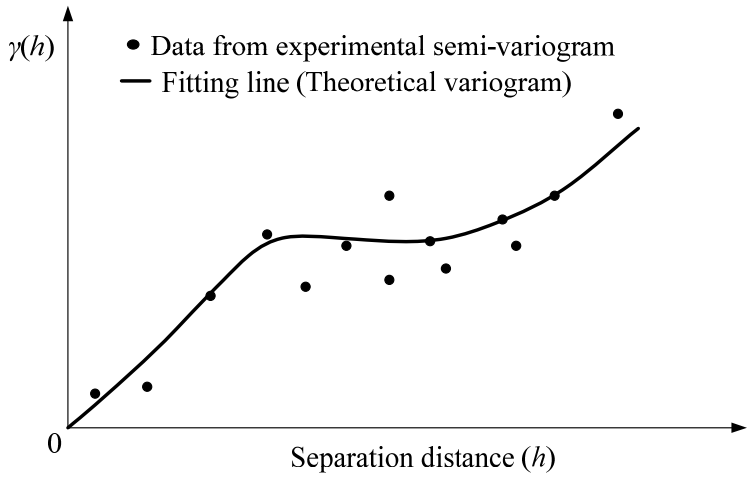

Fig. 3.11 Polynomial model for theoretical semi-variogram

In the Kriging technique, unknown value at any point *a* is calculated by multiplying the known values with the corresponding weight factors. The form is as follows

$$u^*(x_a, y_a) = \sum_{i=1}^{n} \lambda_i u(x_i, y_i) \tag{3.33}$$

where λ_i is weight factor assigned to the available data and neighbor data $u(x_i, y_i)$ in the proximity of the location (x_a, y_a) of unknown value. In OK, the weight factors add up to unity to ensure that the estimate is unbiased.

$$\sum_{i=1}^{n} \lambda_i = 1 \tag{3.34}$$

The Kriging variance associated to an OK estimate is called the minimum variance unbiased estimator or best linear unbiased estimator, since the constraint condition defined in Eq. 3.34 should be applied to minimize the variance of estimate errors. Thus the mathematical form can be expressed as

$$\text{Minimize} \quad \sigma_{OK}^2 = \sigma^2 - 2\sum_{i=1}^{n} \lambda_i \sigma_{ai}^2 + \sum_{i=1}^{n}\sum_{j=1}^{n} \lambda_i \lambda_j \sigma_{ij}^2 \tag{3.35}$$

$$\text{subjected to} \quad 1 - \sum_{i=1}^{n} \lambda_i = 0 \tag{3.36}$$

where σ_{OK}^2 is error variance of ordinary Kriging. σ is defined as

$$\begin{aligned} \sigma^2 &= \text{Var}(u_a) \\ \sigma_{0i}^2 &= \text{Cov}(u_a, u_i) \\ \sigma_{ij}^2 &= \text{Cov}(u_i, u_j) \end{aligned} \tag{3.37}$$

Here u_0 refers to the value to be determined. Using Lagrange multiplier, above formula can be expressed as

$$L(\lambda_1,\lambda_2,...,\lambda_n;\mu)=\sigma^2-2\sum_{i=1}^{n}\lambda_i\sigma_{ai}^2+\sum_{i=1}^{n}\sum_{j=1}^{n}\lambda_i\lambda_j\sigma_{ij}^2+2\mu\left[1-\sum_{i=1}^{n}\lambda_i\right] \tag{3.38}$$

where $L(\lambda_1,\lambda_2,...,\lambda_n;\mu)$ is Lagrange objective function, and μ is Lagrange multiplier. Minimization of the objective function can be carried out by finding the partial derivatives with respect to λ_i and μ such that

$$\begin{aligned}\frac{\partial L}{\partial\lambda_i}&=-2\sigma_{al}^2+2\sum_{i=1}^{n}\lambda_i\sigma_{il}^2-2\mu=0,\quad l=1,2,...,n\\ \frac{\partial L}{\partial\mu}&=2\left[1-\sum_{i=1}^{n}\lambda_i\right]=0\end{aligned} \tag{3.39}$$

Eq. 3.39 can be rearranged to the following form.

$$\begin{aligned}&\sum_{i=1}^{n}\lambda_i\sigma_{il}^2-\mu=\sigma_{al}^2,\quad l=1,2,...,n\\ &\sum_{i=1}^{n}\lambda_i=1\end{aligned} \tag{3.40}$$

From Eq. 3.40, weight factors for any unknown value are calculated by following form.

$$\begin{Bmatrix}\lambda_1\\ \lambda_2\\ \vdots\\ \lambda_n\\ \mu\end{Bmatrix}=\begin{bmatrix}\sigma_{11}^2 & \sigma_{12}^2 & \cdots & \sigma_{1n}^2 & -1\\ \sigma_{21}^2 & \sigma_{22}^2 & \cdots & \sigma_{2n}^2 & -1\\ \vdots & \vdots & \vdots & \vdots & \vdots\\ \sigma_{n1}^2 & \sigma_{n2}^2 & \cdots & \sigma_{nn}^2 & -1\\ 1 & 1 & \cdots & 1 & 0\end{bmatrix}^{-1}\begin{Bmatrix}\sigma_{a1}^2\\ \sigma_{a2}^2\\ \vdots\\ \sigma_{an}^2\\ 1\end{Bmatrix} \tag{3.41}$$

The unknown values for *m* points can, then, be obtained from.

$$\begin{Bmatrix}u_a\\ u_b\\ \vdots\\ u_m\end{Bmatrix}^{*}=\left(\underbrace{\begin{bmatrix}\sigma_{11}^2 & \sigma_{12}^2 & \cdots & \sigma_{1n}^2 & -1\\ \sigma_{21}^2 & \sigma_{22}^2 & \cdots & \sigma_{2n}^2 & -1\\ \vdots & \vdots & \vdots & \vdots & \vdots\\ \sigma_{n1}^2 & \sigma_{n2}^2 & \cdots & \sigma_{nn}^2 & -1\\ 1 & 1 & \cdots & 1 & 0\end{bmatrix}^{-1}}_{(n+1)\times(n+1)}\underbrace{\begin{bmatrix}\sigma_{a1}^2 & \sigma_{b1}^2 & \cdots & \sigma_{m1}^2\\ \sigma_{a1}^2 & \sigma_{b1}^2 & \cdots & \sigma_{m1}^2\\ \vdots & \vdots & \vdots & \vdots\\ \sigma_{an}^2 & \sigma_{b1}^2 & \cdots & \sigma_{m1}^2\\ 1 & 1 & 1 & 1\end{bmatrix}}_{(n+1)\times m}\right)^{\mathrm{T}}\underbrace{\begin{Bmatrix}u_1\\ u_2\\ \vdots\\ u_n\\ 0\end{Bmatrix}}_{(n+1)\times 1} \tag{3.42}$$

Meanwhile, for a posteriori error estimate for *p*-refinement, it is inevitable to slightly modify the existing superconvergent patch recovery (SPR) technique (Zienkiewicz and Zhu, 1992) because the number of Gauss points in each element is different when non-uniform *p*-distribution exists. The elemental error measure in SPR technique is quantified by computing the strain energy contained in the difference between the discontinuous *p*-FEM solution at the sampling points and the smoothened solution. The energy norm of the error in the displacement field proposed by SPR technique is given by

$$\|e_r\| = \sqrt{\int_\Omega \left(\sigma^* - \sigma^p\right)^{\mathrm{T}} [D]^{-1} \left(\sigma^* - \sigma^p\right) d\Omega} \tag{3.43}$$

where σ^* is the smoothed stress field by projection; σ^p the computed stress at Gauss points by non-uniform *p*-refinement; [*D*] the constitutive matrix; Ω the mesh domain. Thus the error in terms of stresses may be computed either exactly using the exact stress field, $\hat{\sigma}$, or it can be estimated using σ^*:

$$e_\sigma = \hat{\sigma} - \sigma^p \approx \sigma^* - \sigma^p \tag{3.44}$$

in which the smoothed continuous stress field, σ^*, is derived from the discontinuous finite element stresses σ^p. This means that the nodal values can be obtained by fitting surfaces to the sampling point values in a patch of elements by using OK interpolation, and then averaging the contributions from all element patches meeting at a node. The estimated stresses at the non-Gauss points can be computed by the weighted combination of stresses at Gauss points like Eq. 3.33. The energy norm of the displacement field can be expressed in terms of stresses as

$$\|\hat{r}\| = \sqrt{\int_\Omega \left(\sigma^p\right)^{\mathrm{T}} [D]^{-1} \left(\sigma^p\right) d\Omega} \tag{3.45}$$

The relative error can then be defined as

$$\eta_{\Omega} = \sqrt{\frac{\|e_r\|^2}{\|e_r\|^2 + \|\hat{r}\|^2}} \tag{3.46}$$

A typical patch normally consisting of four elements is adaptively refined by increasing the polynomial order uniformly. Gauss points are located symmetrically in a regular pattern. On the contrary, the distribution of the Gauss points will be irregular with non-uniform *p*-distribution. This raises the issue of effectively maintaining functional continuity across the inter-element boundary. In this study, the functional continuity between elements different polynomial orders sharing a common edge is achieved by constraining to zero the extra edge terms in the higher order element.

3.5 Numerical Integration

For the evaluation of some integrals like Eq. 2.27, Eq. 2.40, and Eq. 2.5-60, both *Gauss-Lobatto* quadrature and *Gauss-Legendre* quadrature are considered. Gauss-Legendre quadrature has widely been used in finite element analysis. The general form for 1D quadrature in standard coordinate system is as follows.

$$\int_{-1}^{1} f(x) \approx \sum_{i=1}^{n} c_i \, f(x_i) \tag{3.47}$$

where c is weight factor and n the number of sampling points. It is well know that in this quadrature technique, x_1 and x_n is not exactly in accordance with -1 and 1, respectively, which are position of end points in standard coordinate. It means that stresses of two end points, that is, nodes in an element, cannot directly be obtained. Thus the process of extrapolation is additionally required for obtaining stresses at nodes in present models. In order to avoid this additional calculation, Gauss-Lobatto quadrature which can directly

obtain stresses at nodes can be chosen to evaluate some of the integrals. The general form for one dimensional quadrature with n sampling points in standard coordinate system is given by

$$\int_{-1}^{1} f(x) \approx \alpha[f(-1)+f(1)] + \sum_{i=2}^{n-1} \omega_i f(x_i) \tag{3.48}$$

where α and ω are weight factors which are determined by following forms.

$$\alpha = \frac{2}{n(n-1)}; \quad \omega_i = \frac{2}{n(n-1)[P_{n-1}(x_i)]^2} \tag{3.49}$$

The abscissas x_i are the roots of the $P'_{n-1}(x)$ where $P(x)$ is a Legendre polynomial. In the application of Gauss-Legendre and Gauss-Lobatto for numerical evaluation of integrals, the required number of optimally located sampling points within an element depends on the p-level, and is given by

$$n_{optimal} \begin{cases} = (p_{xy} + \beta)^2 & \text{for ESLM} \\ = (p_{xy} + \beta)^2 \times (p_z + \beta) & \text{for discrete} - \text{layer models} \end{cases} \tag{3.50}$$

where β = 1 for Gauss-Legendre quadrature and 2 for Gauss-Lobatto quadrature, In addition, p_{xy} and p_z are p-level chosen for two- and one- dimensional shape functions, separately.

The weight factors and Gauss points for the application of these techniques are calculated in CTLAP. The possible numbers of sampling points within the interval of standard coordinates, (-1, 1), are nearly unrestricted because about 8000 sampling points within an interval were tested using MATLAB programming. Actually, 2~15 sampling points with respect to one axis are approximately used according to the order of shape functions used in the model.

CHAPTER IV

VERIFICATION AND VALIDATION OF PROPOSED MODELING SCHEMES

4.1 Overview

In order to validate and evaluate the developed simulation tools, some basic examples such as isotropic and anisotropic single-layer and multi-layer plates are analyzed. The results of the developed tools are compared with analytical solutions available in the published literature, and with values based on commercial software.

4.2 Isotropic Single-Layer Plates under Tensile Loading

As the first example, a 30 in × 10 in cantilever plate (E=3×10^7 psi, ν=0.0 or 0.3) subjected to uniaxial tension, shown in Fig. 4.1 (a), is considered. The thickness of the plate is 2 in. A three-element model of the computational domain shown in Fig. 4.1 (b) is subjected to applicable essential (constrained in all three directions at the fixed end and constrained in the y-direction on the boundary corresponding to the line of symmetry) and the natural boundary condition (at the free end).

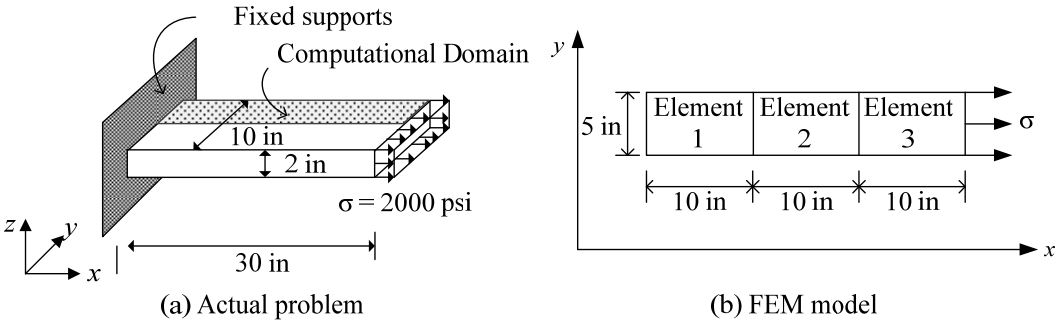

Fig. 4.1 Cantilever plate under tensile loading

The combination of element types assigned to three elements in each model is shown in Table 4.1. Model A~C are composed of only one of the element three developed types, namely, ESLM, PDLM and FDLM. The meshes in Model D~F consist of elements based on DLTM to allow transition between different element types. In Model D~F, transition elements are introduced to allow modeling with different element types in the same model. To compare the results from these models with those of commercial finite element code, this example problem is also analyzed by ANSYS. The ANSYS models are based on linear isoparametric elements Plane42 for 2-D modeling and Solid45 for 3D modeling. The results from these analyses are shown in Table 4.2.

Table 4.1 Models assigned to each element

Model Types	Element 1	Element 2	Element 3
Model A	ESLM	ESLM	ESLM
Model B	PDLM	PDLM	PDLM
Model C	FDLM	FDLM	FDLM
Model D	FDLM	PDLM	ESLM
Model E	ESLM	FDLM	PDLM
Model F	PDLM	ESLM	FDLM

Table 4.2 Maximum displacements (unit: inch) and stresses (unit: psi)

Type	Poisson's ratio = 0.0		Poisson's ratio = 0.3	
	Maximum displacement	Maximum stresses	Maximum displacement	Maximum stresses
2D elements of ANSYS	0.20000×10^{-2}	2000.0	0.19874×10^{-2}	2062.1
3D elements of ANSYS	0.20000×10^{-2}	2000.0	0.19564×10^{-2}	2073.7
Model A	0.20000×10^{-2}	2000.0	0.19805×10^{-2}	2143.2
Mode B	0.20000×10^{-2}	2000.0	0.19805×10^{-2}	2143.2
Model C	0.20000×10^{-2}	2000.0	0.19407×10^{-2}	2439.3
Model D	0.20000×10^{-2}	2000.0	0.19805×10^{-2}	2143.2
Model E	0.20000×10^{-2}	2000.0	0.19805×10^{-2}	2143.2
Model F	0.20000×10^{-2}	2000.0	0.19805×10^{-2}	2143.2

It is evident from this table that with a zero value for Poisson's ratio, the maximum displacements and stresses for all the models are same as those with ANSYS regardless of whether 2D or 3D elements are used. However, when the Poisson's ratio equals 0.3, displacement and stress values shown in Table 4.2 are not exact agreement due the effect of non-zero Poisson's ratio in the presence of fixed support condition. To verify the accuracy of the results obtained by the proposed analysis tools, convergence test is implemented by increasing the NDF by *p*-refinement in the developed scheme, and *h*-refinement in ANSYS. As expected, Fig. 4.2 illustrates that the convergence characteristics of ESLM and PDLM are similar to that of 2D model of ANSYS, and the converged value of FDLM agree with the 3D model of ANSYS. In addition, it is seen that PDLM has more rapid rate of convergence ANSYS 3D model based on *h*-refinement.

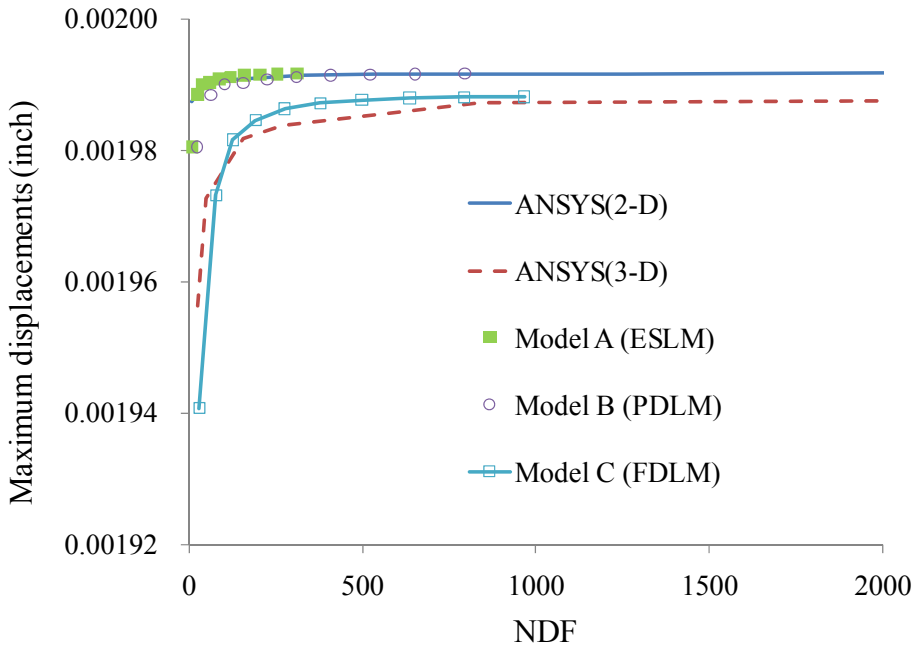

Fig. 4.2 Maximum displacements with variation of NDF

Fig. 4.3 shows comparison of maximum stresses (σ_{xx}) by Model A~C and ANSYS with variation of NDF. It is noticed that maximum stress continues to go up with an increase of NDF at the corner points in the supported end, where stress singularity is expected. Also, it is shown that with increasing NDF, the proposed models using *p*-refinement approach the peak stress value more rapidly than ANSYS models.

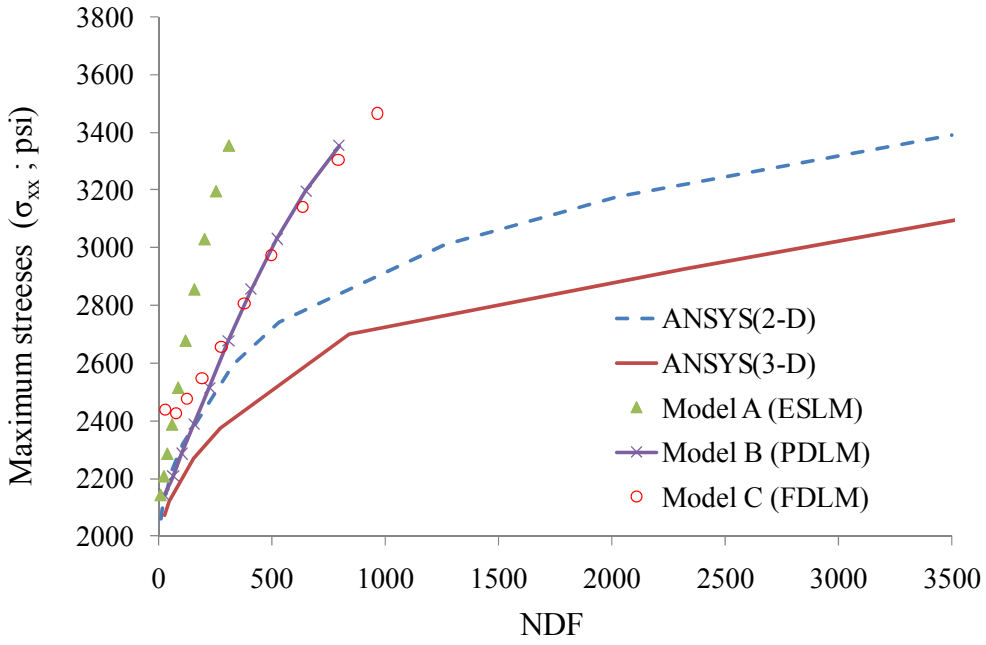

Fig. 4.3 Variation of maximum stresses with NDF

Fringe plot of stresses (σ_{xx}) are shown in Fig. 4.4 (a) for the case with ν=0 and in Fig. 4.4 (b) when ν=0.3. The existence of stress singularity at the corner of fixed support is evident from Fig. 4.4 (b). The stress fringes shown in Fig. 4.4 are typical for all the models including models using DLTM and ANSYS models. To further examine the accuracy of the proposed DLTM-based elements for problem with stress singularity, Fig. 4.5 shows the variation of displacement with the *p*-level of shape functions in the *xy*-

plane for the case with ν=0.3. It is evident from Fig. 4.5 that the converged characteristics of Models D~F with DLTM is identical with that of Models A and B in which just one element type such as ESLM and PDLM is used. On the other hand, Fig. 4.6 shows the variation of maximum stress with *p*-level. In this case also, the results of Model A, B, D, E, and F are same, except in the case of Model C simulating 3D behavior shows some difference. Therefore, the proposed elements are capable of modeling planar problems of elasticity quite accurately.

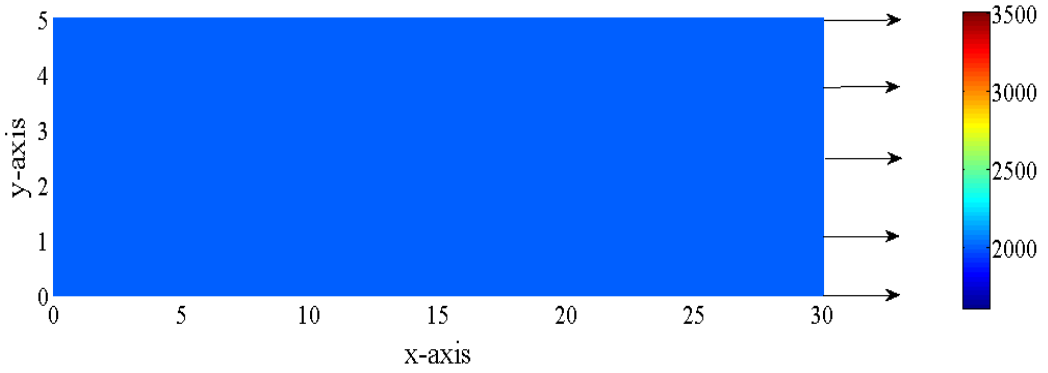

(a) Stress fringes without stress singularity

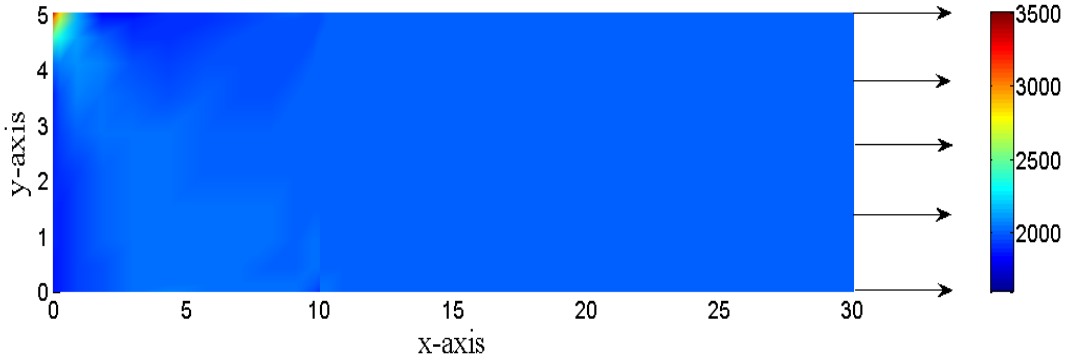

(b) Stress fringes with stress singularity

Fig. 4.4 Stress fringes for normal stresses (σ_{xx}, psi)

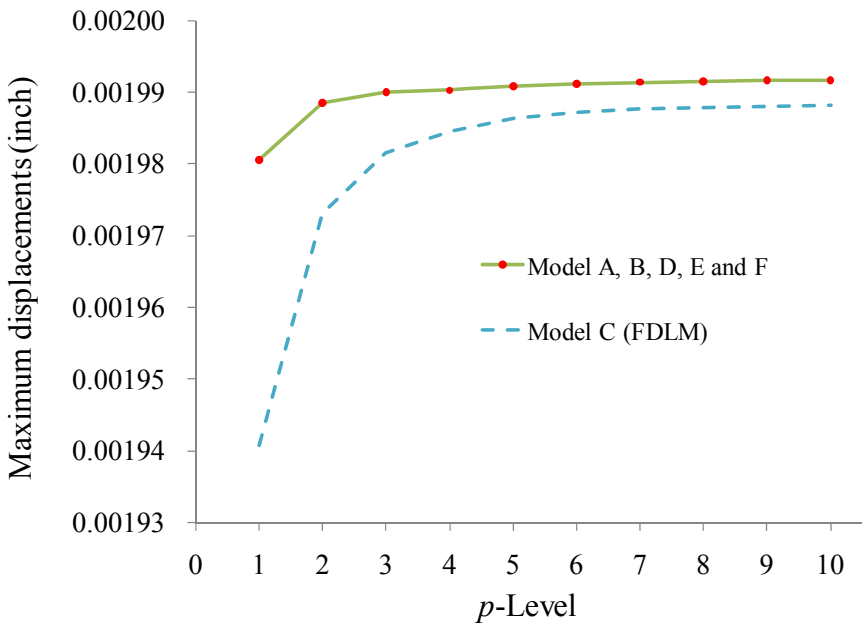

Fig. 4.5 Variation of maximum displacement with *p*-level

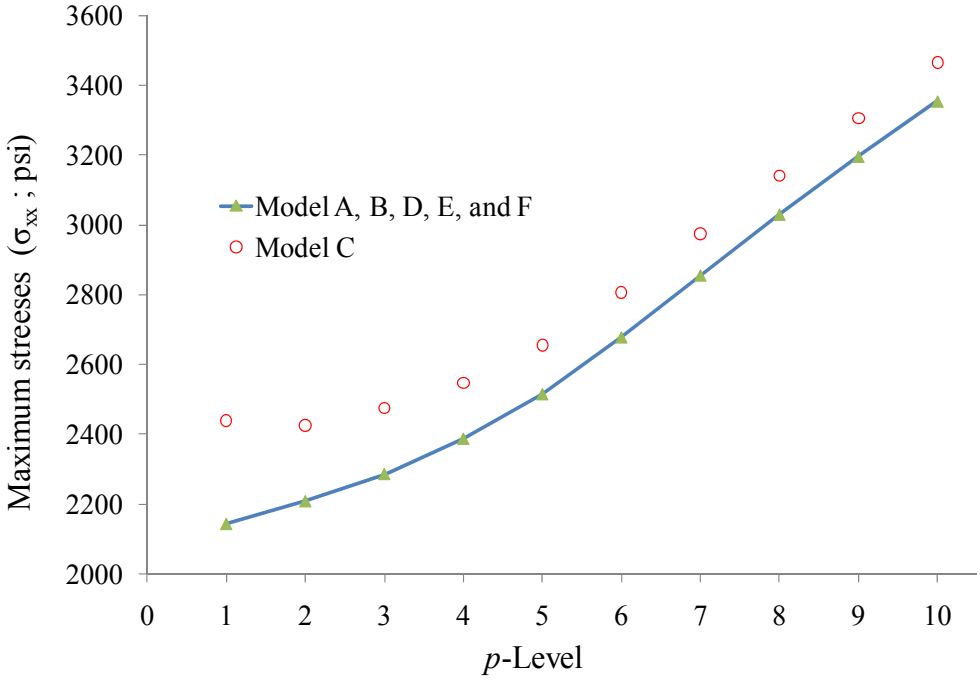

Fig. 4.6 Variation of maximum stresses (σ_{xx}) with *p*-level

4.3 Isotropic Single-Layer Plates under Uniformly Distributed Transverse Loading

In this example, the simple problem of a simply supported isotropic (ν = 0.25) plate under uniformly distributed transverse loading, q_0, is solved to evaluate the accuracy and efficiency of the developed modeling schemes in 2D and 3D modeling of plate bending problems. The geometry and coordinate system used for the plate are shown in Fig. 4.7. The direction of z-coordinate is obtained by the right-hand rule with the limits defined as $-h/2 \le z \le h/2$, where h is the thickness of the plate. Taking advantage of two-way symmetry, only one quadrant of the plate is modeled by a single element using ESLM, PDLM, and FDLM, respectively. The boundary conditions for ESLM, PDLM and FDLM are presented in Table 4.3 and the identical boundary conditions are applied across the thickness. For ESLM solution, the shear correction factor is assumed as 5/6. The deflections and stresses are normalized as

$$\bar{w} = \frac{100\,E\,h^3}{q_0\,a^4}\,w\left(\frac{a}{2},\frac{a}{2},0\right), \qquad \bar{\sigma}_{xx} = \frac{h^2}{q_0\,a^2}\,\sigma_{xx}\left(\frac{a}{2},\frac{a}{2},\frac{h}{2}\right) \tag{4.1}$$

where E is Young's modulus.

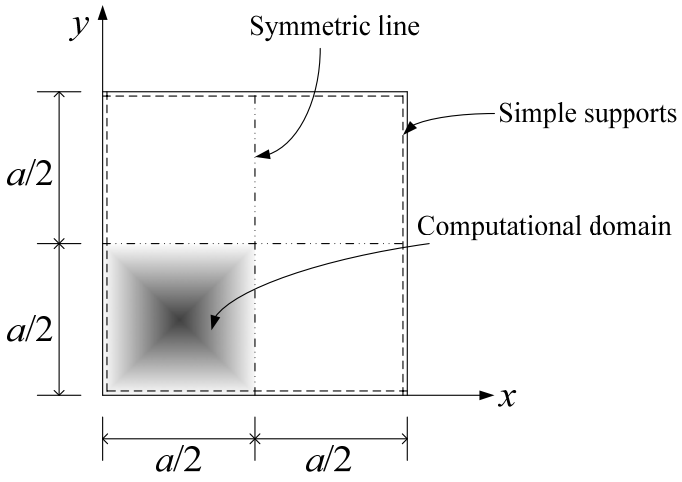

Fig. 4.7 Geometry and coordinate system

Table 4.3 Boundary conditions

Types	$(x, 0)$ and (x, a)	$(0, y)$ and (a, y)
ESLM	$u = 0,\ \theta_x = 0, w = 0$	$v = 0,\ \theta_y = 0, w = 0$
PDLM	$u = 0, w = 0$	$v = 0, w = 0$
FDLM	$u = 0, w = 0$	$v = 0, w = 0$

Figs. 4.8 and 4.9 show the convergence of maximum deflections and normal stresses for plates with different aspect ratios when PDLM-based elements are used. The sequence of markers on each line represents the sequence of *p*-levels. From the Figs. 4.8 and 4.9, it is noted that the deflection converges at *p*-level=5 for all thickness ratios and the stress at *p*-level=6. Similar convergence characteristics were also observed with ESLM and FDLM elements.

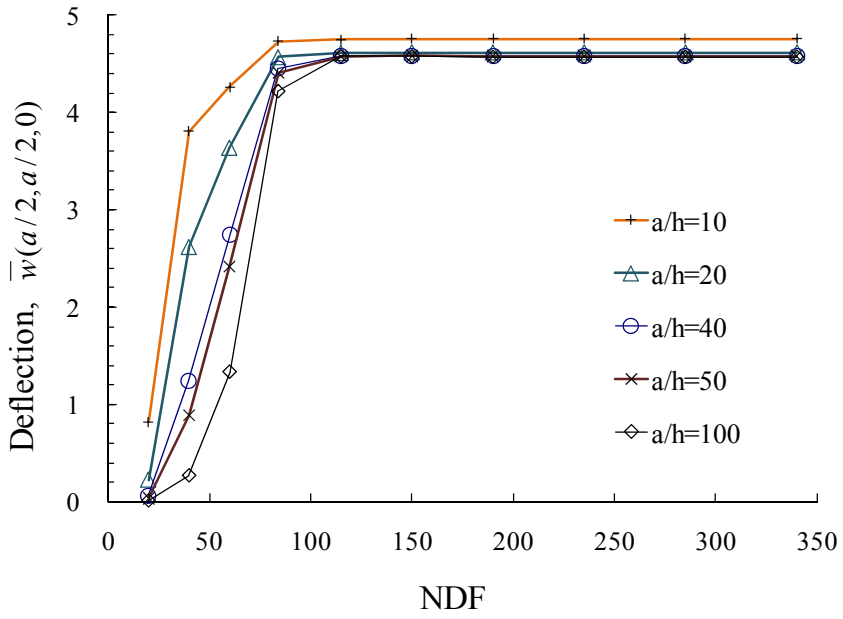

Fig. 4.8 Central deflections with variation of NDF in PDLM

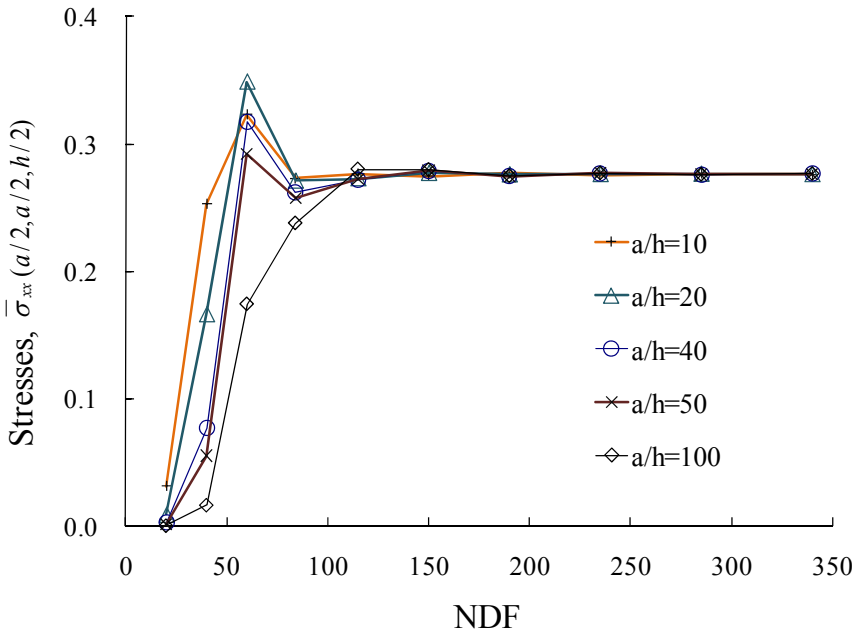

Fig. 4.9 Normal stresses with variation of NDF in PDLM

Table 4.4 Ratio of the required NDF of each approach to NDF of ESLM [1×1×1]

	Mesh [1×1×1]	Mesh [1×1×2]	Mesh [1×1×3]
ESLM	1.0	1.0	1.0
PDLM	1.0	1.4	1.8
FDLM {1,1}	1.2	1.8	2.4
FDLM {1,2}	1.4	2.2	3.0
FDLM {2,1}	1.6	2.6	3.6
FDLM {2,2}	1.8	3.0	4.2

Table 4.4 gives the ratio of the required NDF for each model as multiple of that for single layer ESLM [1×1×1]. The columns designated as Mesh [1×1×2] and Mesh [1×1×3] signify that the plate is treated as two- and three-layered, respectively. Also, the bracketed numbers of FDLM in Table 4.4 represent the degrees of 1D polynomial approximation

for in-plane and out-of-plane displacements of the plate, respectively. In the case of single layer representation, ESLM and PDLM agree at all *p*-levels. This is, however, not true in the case of multiple layer representations of the plate. It may also be noted from Table 4.4 that to achieve convergence the required NDF with FDLM is significantly more than ESLM and PDLM. The comparisons of central deflection and maximum stress analyzed by ESLM and the reference values (Reddy, 2006) based on *h*-FEM are shown in Tables 4.5 and 4.6, respectively.

Table 4.5 Comparison of displacements

a/h		*h*-FEM (Reddy, 2006)		ESLM	
		4×4 Linear [NDF=69]	2×2 Quadratic [NDF=64]	*p* = 4 [NDF=51]	*p* = 5 [NDF=69]
10	*F*	0.8105	0.9956	0.9943	0.9996
	M	0.9962	1.0017		
20	*F*	0.5109	0.9881	0.9905	0.9989
	M	0.9952	1.0017		
40	*F*	0.2059	0.9828	0.9757	0.9983
	M	0.9948	1.0017		
50	*F*	0.1424	0.9818	0.9670	0.9983
	M	0.9948	1.0017		
100	*F*	0.0398	0.9803	0.9674	1.0002
	M	0.9948	1.0017		

Table 4.6 Comparison of stresses

a/h		*h*-FEM (Reddy, 2006)		*p*-FEM (1×1)	
		4×4 Linear [NDF=69]	2×2 Quadratic [NDF=64]	*p* = 4 [NDF=51]	*p* = 5 [NDF=69]
10	*F*	0.7826	1.0507	0.9891	1.0036
	M	0.9638	0.9855		
20	*F*	0.5000	0.9710	0.9855	0.9928
	M	0.9638	0.9855		
40	*F*	0.2029	0.9783	0.9601	0.9855
	M	0.9638	0.9819		
50	*F*	0.1413	0.9819	0.9457	0.9891
	M	0.9638	0.9638		
100	*F*	0.0399	0.9638	0.8732	1.0109
	M	0.9638	0.9855		

The tabulated values represent the ratios of finite element solutions to the analytical solutions based on 2D elasticity theory. Both finite element models are based on first-order shear deformation (or, Mindlin) theory and plane stress theory, and thus have the same NDF per node. The analytical solution is also based on the Mindlin plate theory. In the case of ESLM, full numerical integration is used whereas two types, full (*F*) and mixed (*M*) integration, are chosen in the *h*-FEM. It is noted that for comparable values of NDF, *p*-FEM results are invariably better than those by *h*-FEM for both displacement and stress values. The results based on ESLM are unaffected at p=5 or more. It is noticed that the better ratio of convergence can be obtained and special numerical integration techniques do not need to be considered in ESLM with higher-order shape functions.

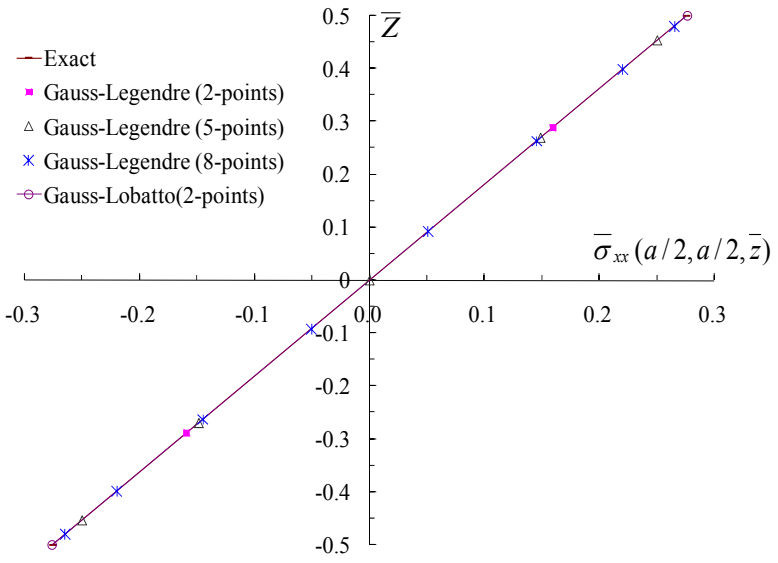

Fig. 4.10 Normal stresses at center across the thickness of the plate

Fig. 4.10 shows the stress distribution across the thickness of the plate using Gauss-Lobatto quadrature and Gauss-Legendre quadrature, respectively. It is seen that there is

hardly any difference between the results obtained by the two quadrature rules. It is noticed from the Fig. 4.10 that the advantage of Gauss-Lobatto quadrature in terms of ability to directly compute accurate stresses at boundary points of an element can be somewhat offset by the need for more sampling points and, hence, increased computational effort to achieve the same degree of accuracy as Gauss-Legendre quadrature, which is almost exclusively used as the numerical quadrature tool in finite element analysis.

Table 4.7 Comparison of deflections and stresses for various span-to-thickness ratios

a/h	Type	$\overline{w}$ (*a*/2, *a*/2, 0)	$\overline{\sigma}_x$ (*a*/2, *a*/2, ±1/2)
10	ESLM	4.791	± 0.276
	PDLM	4.754	± 0.276
	FDLM	4.770	0.279 - 0.278
	Analytical Solution	4.791	± 0.276
20	ESLM	4.625	± 0.276
	PDLM	4.616	± 0.276
	FDLM	4.620	0.277 - 0.276
	Analytical Solution	4.625	± 0.276
40	ESLM	4.584	± 0.276
	PDLM	4.582	± 0.276
	FDLM	4.583	0.277 - 0.276
	Analytical Solution	4.584	± 0.276
50	ESLM	4.579	± 0.276
	PDLM	4.577	± 0.276
	FDLM	4.578	0.277 - 0.276
	Analytical Solution	4.579	± 0.276
100	ESLM	4.572	± 0.276
	PDLM	4.572	± 0.276
	FDLM	4.572	± 0.276
	Analytical Solution	4.572	± 0.276

The maximum lateral displacements and stresses calculated by ESLM, PDLM, and FDLM for different aspect (span-to-thickness) ratios are presented in Table 4.7, to compare with analytical solutions based on Mindlin plate theory. The finite element results are obtained based on *p*-levels allowing convergence up to four and three significant digits for displacements and stresses, respectively. It is shown that stresses and displacements by ESLM agree mostly with the analytical solutions, for all aspect ratios. Therefore, it can be concluded that ESLM-based results converge with increase of NDF to those of analytical solution in the single-layer plate regardless of being thin or thick. It can also be noted that the results of FDLM are similar to those of analytical solution in thin plate. However, it appears that the differences between the two solutions become pronounced larger with increase in plate thickness.

In FDLM, the differences between magnitudes of stresses at bottom and top surfaces also become larger with increase in plate thickness; whereas, these are same for ESLM and PDLM models. This behavior can be attributed to the fact that FDLM contains full three-dimensional kinematics and constitutive relations. The stresses of PDLM in Table 4.7 are found to be mostly similar to those of analytical solutions for all aspect ratios. However, the differences in displacement values between PDLM and analytical solution become more pronounced with increasing plate thickness. Indeed, in the case of thicker plates, the displacement discrepancy between PDLM and analytical solutions are more pronounced than that between FDLM and analytical solution. In order to understand the cause of this discrepancy, layer thickness based weighted averages of lateral displacements across thickness by FDLM were calculated. These results are compared with PDLM results in Table 4.8. It is noticed that weighted average results of FDLM are

identical to the lateral displacements by PDLM, for all span-to-thickness ratios. Therefore it is inferred that the lateral displacements of PDLM can be characterized as the average of the lateral displacement distribution across the thickness.

Table 4.8 Central deflections of the plate

a/h	PDLM	Midpoint across thickness in FDLM	Weighted average across thickness in FDLM
10	4.754	4.770	4.754
20	4.616	4.620	4.616
40	4.582	4.583	4.582
50	4.577	4.578	4.577
100	4.572	4.572	4.572

4.4 Simply Supported Square Plate with a Central Square Cutout

A square plate of side length, a=1m with a concentric square cutout of side length 0.5a, shown in Fig. 4.11, is considered. The plate is assumed to have a thickness to length ratio h/a=0.01 and is subjected to a uniformly distributed load of intensity, q=1 kPa. For material properties, Young's modulus, E, is taken as 210 GPa, and Poisson's ratio, ν, as 0.3. This example is characterized by the existence of singular moments at the four re-entrant corners. For boundary conditions, the plate is considered as simply supported at outer edges, while the cutout boundaries are free. In order to validate the proposed element models, three element types, such as FDLM, PDLM, and ESLM, are considered. Taking advantage of four-way symmetry, only the eighth quadrant of the plate, shown shaded in Fig. 4.11, is considered. The selected computational domain is modeled with just one finite element of the types mentioned.

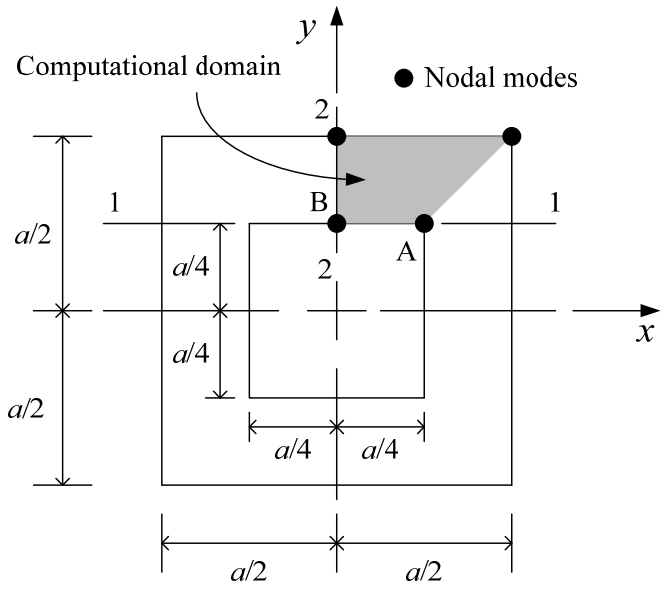

Fig. 4.11 Geometry and modeling scheme for a square plate with a central square cutout

The results of analysis based on the three models are shown in Figs.4.12 through 4.17. The convergence of the normalized displacements (at points A and B in Fig. 4.11) with respect to *p*-level is shown in Figs. 4.12 and 4.13. These figures indicate that for *p*-levels equal to 5 or greater the results for all three cases converge to the reference value (Hrudey, 1986). The singular nature of the moment field is evident from the results of the models based on *p*=8, as evidenced in Figs. 4.14 and 4.15. These figures show the distributions of M_x and M_y along Line 1-1, passing through the re-entrant corner. The closeness of the results with the reference values (Morley, 1970) is clearly demonstrated. In addition, Figs 4.16 and 4.17 show the distributions of M_x and M_y along Line 2-2 lying on the *y*-*y* axis and away from the singular point corners. It may be noted that a single element model is able to model both smooth and singular responses of the problem without the need for supplementing with any especial function.

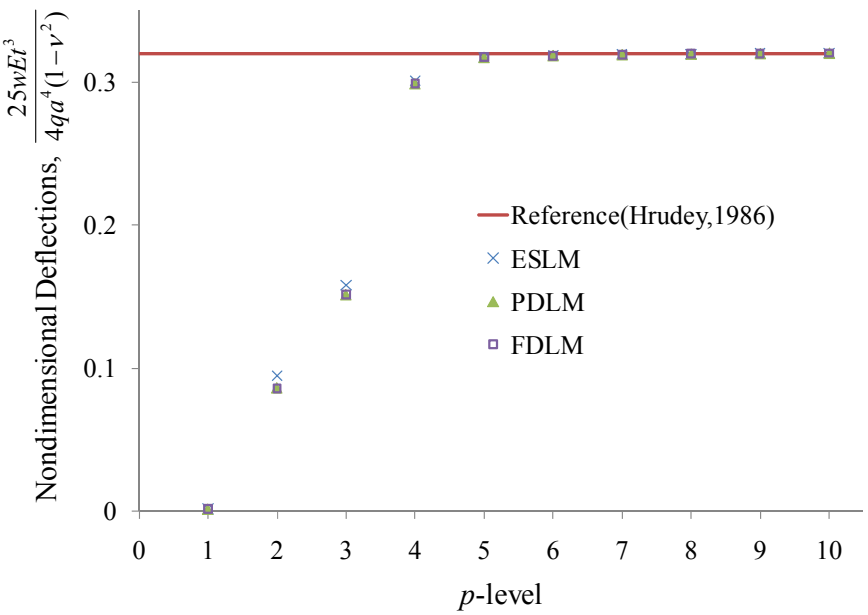

Fig. 4.12 Convergence of displacements with different *p*-levels at Point A

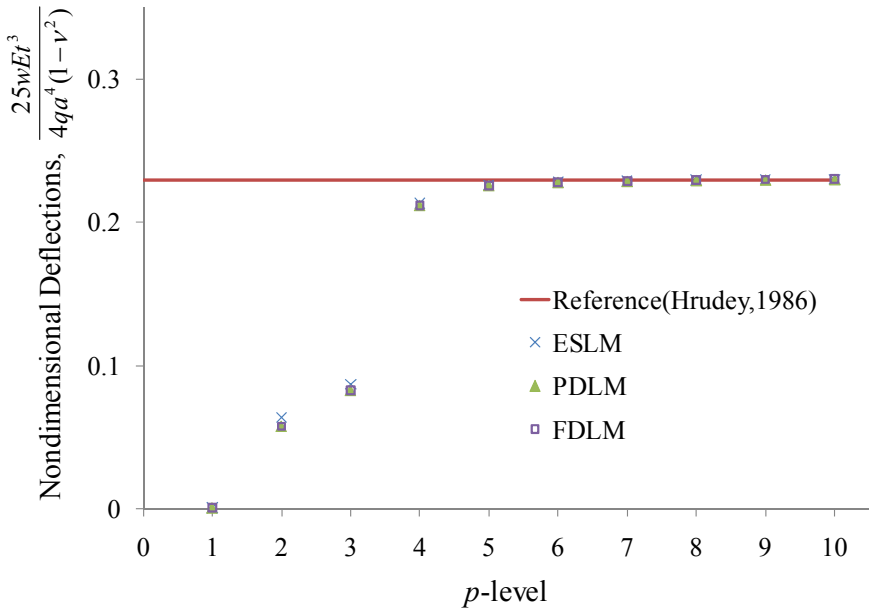

Fig. 4.13 Convergence of displacements with different *p*-levels at Point B

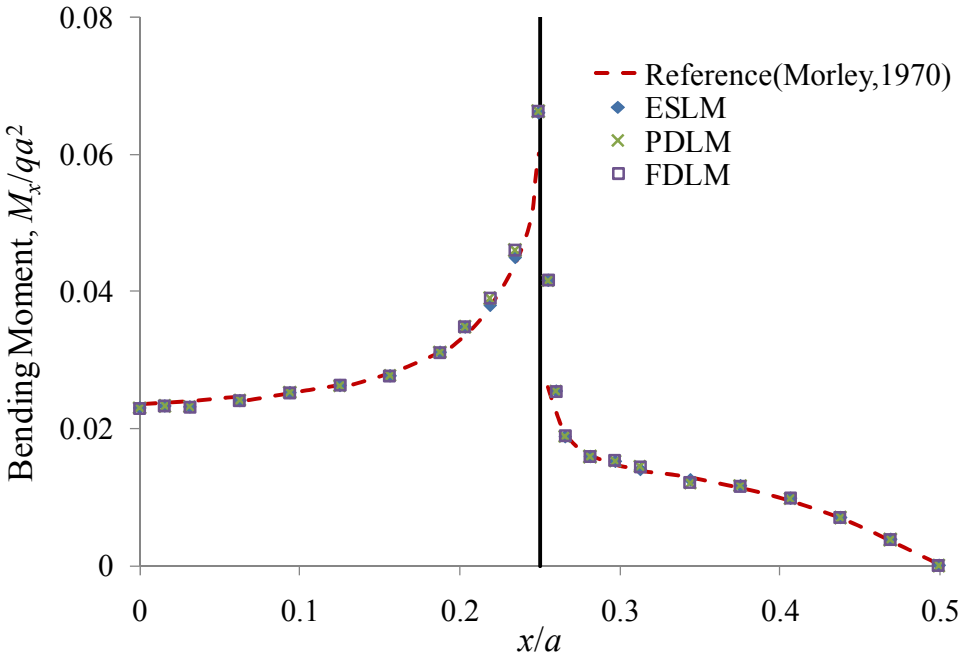

Fig. 4.14 Bending Moment M_x across Line 1-1

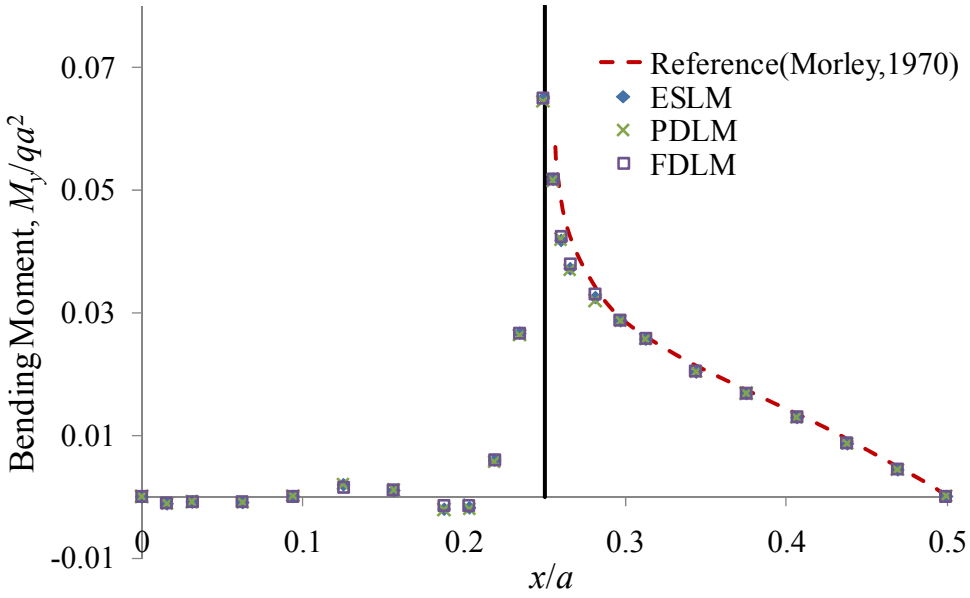

Fig. 4.15 Bending Moment M_y across Line 1-1

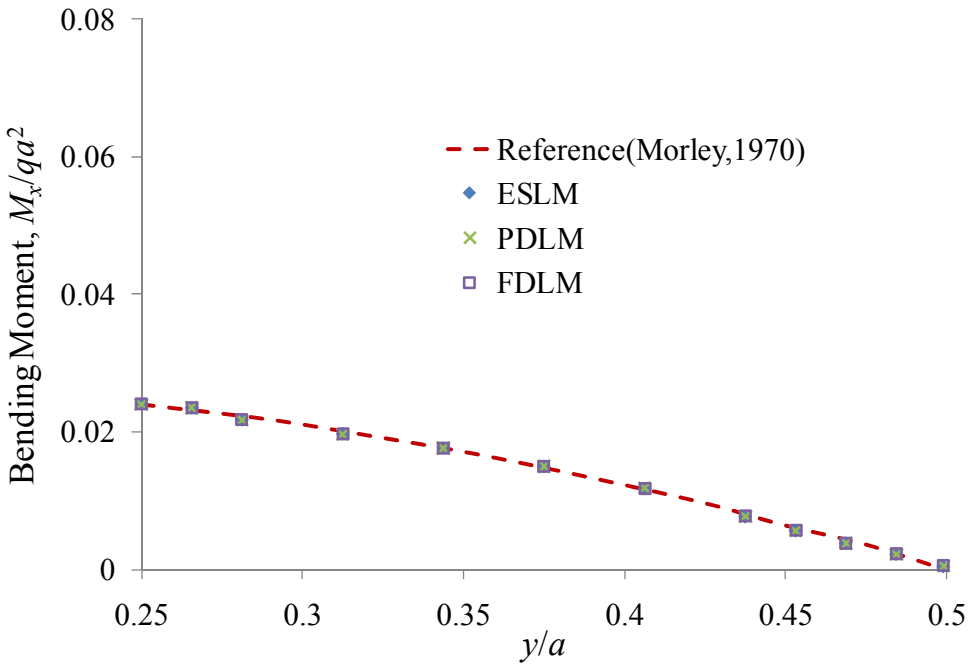

Fig. 4.16 Bending Moment M_x across Line 2-2

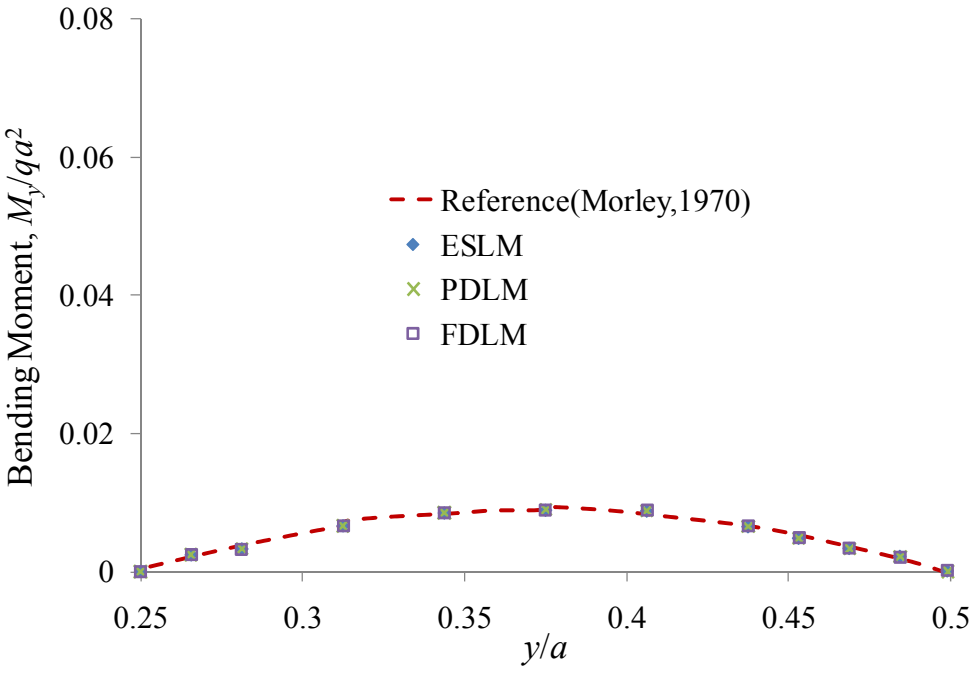

Fig. 4.17 Bending Moment M_y across Line 2-2

4.5 Anisotropic-Multi-Layer Plates under Sinusoidal Loading

In order to evaluate the performance of the developed models (ESLM, PDLM, and FDLM) in the case of laminated systems, a series of simply supported (Table 4.3) bidirectional square-symmetric laminated composite plates under sinusoidal loading are considered. Each unidirectional fiber reinforced composite layer has the following material constants.

$$E_L = 25E_T \qquad G_{LT} = 0.5E_T \qquad G_{TT} = 0.2E_T \qquad \nu_{LT} = \nu_{TT} = 0.25 \tag{4.2}$$

where L signifies the direction parallel to the fibers, T the transverse direction, ν_{LT} is the Poisson's ratio for T-direction with respect to L-direction. The following three cases of square laminates with edge dimension a and thickness h having the material properties given in Eq. 4.2.

Case 1: A three-ply symmetric laminate; the layups are of equal thickness with ply angles 0/90/0º.

Case 2: A five-ply symmetric laminate, with fiber orientations alternating between 0º and 90 º with respect to the x axis, and the 0º layups are at the outer surfaces of the laminate. The total thickness of 0º and 90 º layups are same, with layups in the same orientation having equal thickness.

Case 3: A nine-ply symmetric laminate of same construction as case 2.

The distributed sinusoidal transverse load (Fig. 4.18) in all cases is defined as

$$q(x,y) = q_0 \sin\left(\frac{\pi x}{a}\right)\sin\left(\frac{\pi y}{a}\right) \tag{4.3}$$

where constant q_0 is the amplitude.

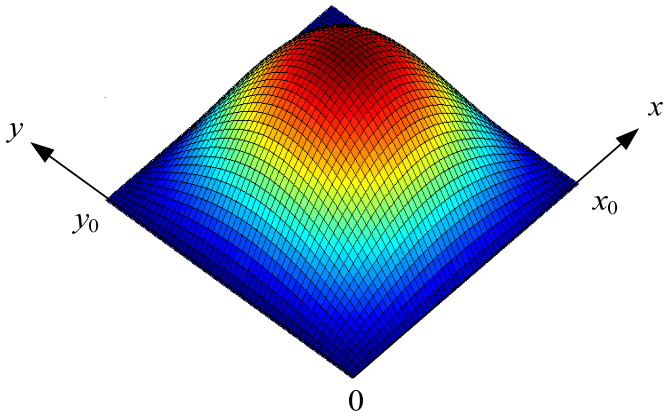

Fig. 4.18 3D view in sinusoidal loading

Other conditions of modeling and analysis for the three models used are similar to the cases of the previously considered single-layer plates. However, the normalized quantities of interest are defined as follows

$$\overline{u} = \frac{E_T\, h^2}{q_0\, a} u^x \tag{4.4}$$

$$\overline{w}_c = \frac{\pi^4\, h^3\, w}{12\, q_0\, a^4}\left[4G_{LT} + \frac{E_L + E_T\,(1+2\nu_{TT})}{1-\nu_{LT}^2\left(E_T / E_L\right)}\right] \tag{4.5}$$

$$\left(\overline{\sigma}_x, \overline{\sigma}_y, \overline{\tau}_{xy}\right) = \frac{h^2}{q_0\, a^2}\left(\sigma_x, \sigma_y, \tau_{xy}\right) \tag{4.6}$$

$$\left(\overline{\tau}_{xz}, \overline{\tau}_{yz}\right) = \frac{h}{q_0\, a}\left(\tau_{xz}, \tau_{yz}\right) \tag{4.7}$$

$$\overline{z} = \frac{z}{h} \tag{4.8}$$

It is well known that the thicker the thickness of a laminated plate means more disagreement will appear in the results by 2D and 3D modeling. So, in Case 1, for a thick laminated plate with a/h=4, the sufficiently converged stress and displacement

distributions using p-level≥6 as obtained for ESLM, PDLM and FDLM models are shown in Figs. 4.19 through 4.21, and are compared with 3D elasticity solution (Pagano, 1970) and CLT solution (Reddy, 2004b). It is seen that although the results by ESLM show large discrepancy with those based on PDLM and FDLM, the latter models show good agreement with 3D elasticity solution. Especially, the FDLM based results are almost identical to the exact three-dimensional elasticity solution. It is, thus, obvious that with the ESLM model, the through the thickness behavior of laminated plates with a large aspect ratio like a/h=4 cannot be represented well.

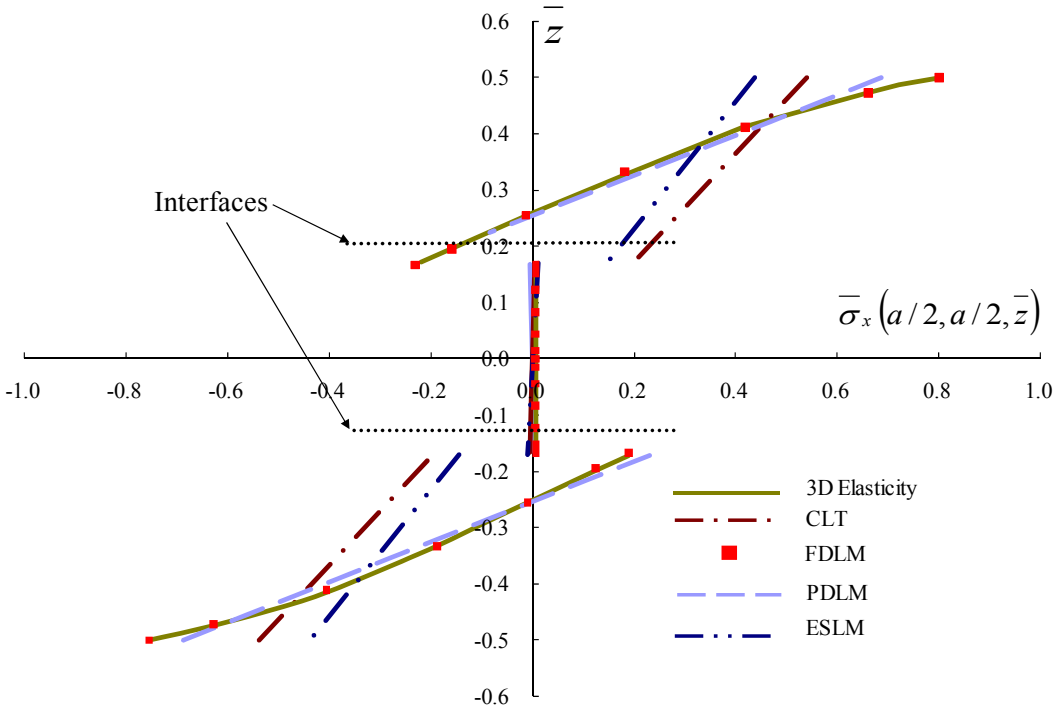

Fig. 4.19 In-plane normal stress distribution in three-ply laminated plates

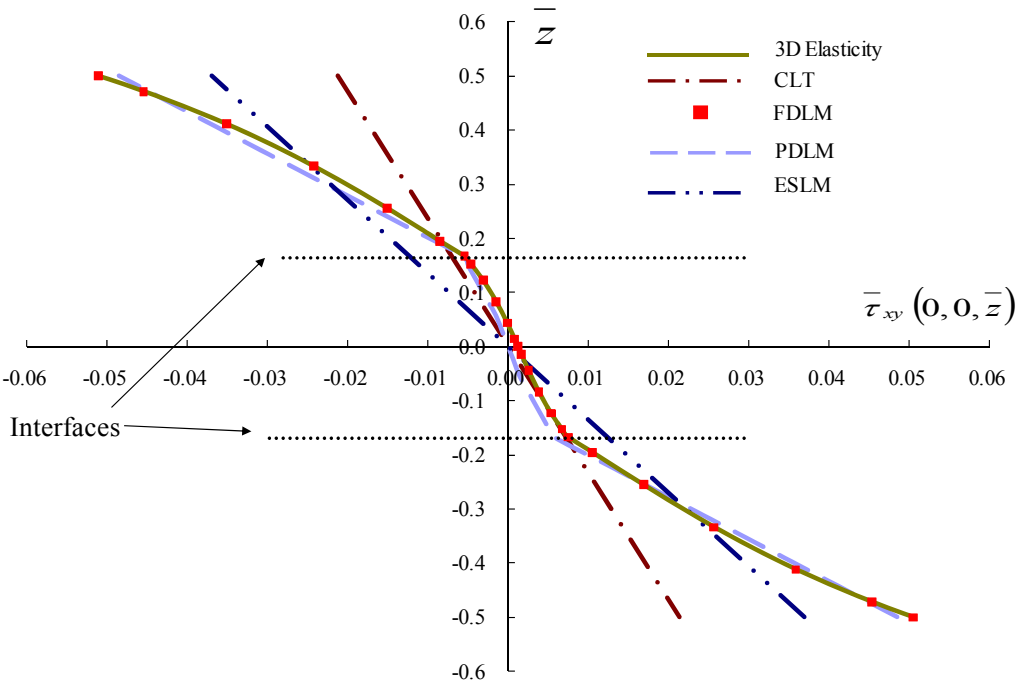

Fig. 4.20 In-plane shear stress distribution in three-ply laminated plates

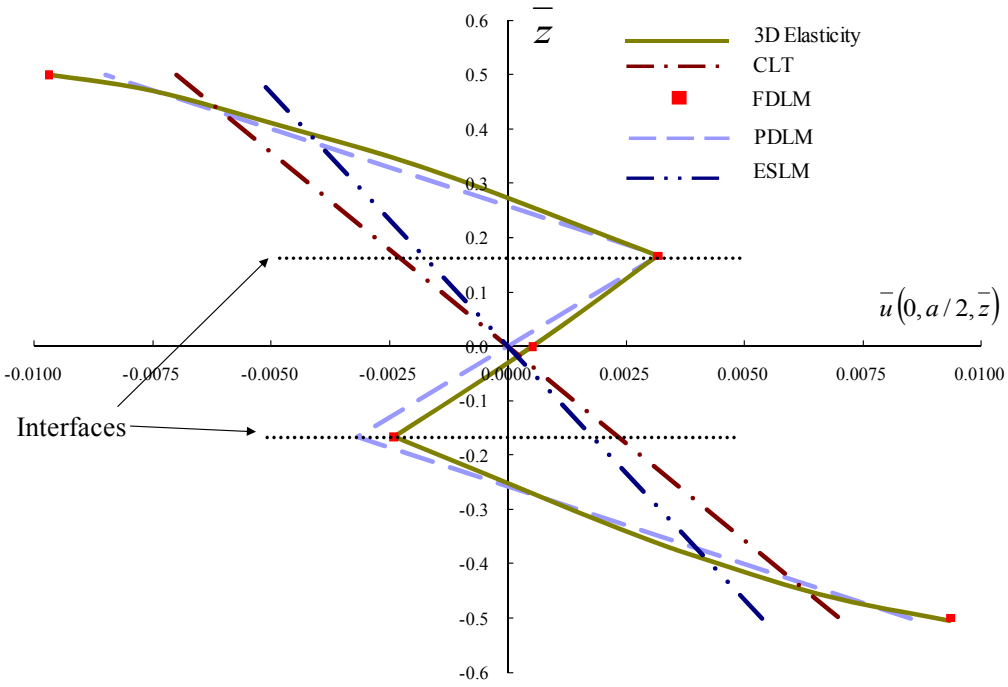

Fig. 4.21 In-plane displacement in three-ply laminated plates

Table 4.9 Ratios of computed deflections to exact values

		p-level for two-dimensional shape functions					
		3	4	5	6	8	10
PDLM		0.939	0.975	0.982	0.982	0.982	0.982
FDLM	{1,1}	0.922	0.957	0.964	0.964	0.964	0.964
	{1,2}	0.922	0.957	0.964	0.965	0.964	0.964
	{1,3}	0.922	0.957	0.964	0.965	0.964	0.964
	{2,1}	0.950	0.986	0.993	0.993	0.993	0.993
	{2,2}	0.950	0.986	0.993	0.994	0.993	0.994
	{2,3}	0.950	0.986	0.993	0.994	0.994	0.994
	{3,1}	0.957	0.992	0.999	1.000	1.000	1.000
	{3,2}	0.957	0.992	1.000	1.000	1.000	1.000
	{3,3}	0.957	0.992	1.000	1.000	1.000	1.000

Table 4.10 Ratios of computed normal stress (σ_x) to exact values

		p-level for two-dimensional shape function					
		3	4	5	6	8	10
PDLM		0.946	0.847	0.850	0.857	0.857	0.857
FDLM	{1,1}	0.963	0.865	0.868	0.875	0.875	0.875
	{1,2}	0.962	0.864	0.867	0.875	0.875	0.875
	{1,3}	0.962	0.864	0.868	0.875	0.875	0.875
	{2,1}	1.088	0.976	0.978	0.986	0.986	0.986
	{2,2}	1.087	0.976	0.977	0.986	0.986	0.986
	{2,3}	1.086	0.974	0.976	0.985	0.985	0.985
	{3,1}	1.113	0.995	0.993	1.001	1.002	1.002
	{3,2}	1.112	0.994	0.992	1.001	1.001	1.001
	{3,3}	1.111	0.993	0.991	1.001	1.000	1.000

Tables 4.9 through 4.10 show the values of deflections and normal stresses (σ_x) for PDLM and FDLM models with different *p*-levels. In these tables, the two numbers, separated by a comma, appearing within parentheses for FDLM refer to degrees of 1D polynomial approximation for in-plane and out-of-plane displacements in each layer. In

the case of FDLM results, the increasing degree of in-plane variation of displacements shows noticeable improvement. However, no such striking improvement is noticed as the polynomial degree for across-the-thickness variation is increased. In the case of PDLM, it is seen that the results do not quite converge to exact values. This is especially true in the cases of stresses. Unlike PDLM, it is found that the results of FDLM for displacement and stresses converge to exact solutions as higher *p*-levels are used. For Case 1, Table 4.11 shows the ratio of the required NDF for various *p*-level of PDLM and FDLM to the required NDF for PDLM with *p*-level = 1. Although FDLM leads to better accuracy than PDLM, the latter is found to be computationally much less intensive.

Table 4.11 Ratios of the required NDF to NDF of PDLM when *p*-level=1

		p-level for two-dimensional shape functions									
		1	2	3	4	5	6	7	8	9	10
PDLM		1.00	2.00	3.00	4.25	5.75	7.50	9.50	11.75	14.25	17.00
FDLM	{1,1}	1.09	2.18	3.27	4.64	6.27	8.18	10.36	12.82	15.55	18.55
	{1,2}	1.36	2.73	4.09	5.80	7.84	10.23	12.95	16.02	19.43	23.18
	{1,3}	1.64	3.27	4.91	6.95	9.41	12.27	15.55	19.23	23.32	27.82
	{2,1}	1.64	3.27	4.91	6.95	9.41	12.27	15.55	19.23	23.32	27.82
	{2,2}	1.91	3.82	5.73	8.11	10.98	14.32	18.14	22.43	27.20	32.45
	{2,3}	2.18	4.36	6.55	9.27	12.55	16.36	20.73	25.64	31.09	37.09
	{3,1}	2.18	4.36	6.55	9.27	12.55	16.36	20.73	25.64	31.09	37.09
	{3,2}	2.45	4.91	7.36	10.43	14.11	18.41	23.32	28.84	34.98	41.73
	{3,3}	2.73	5.45	8.18	11.59	15.68	20.45	25.91	32.05	38.86	46.36

In Table 4.12, the maximum deflection and stress values calculated by PDLM are compared with the exact solutions when a/h = 10 and 50. With the 1×1×3 mesh, the results are, in general, in good agreement with reference values except that relatively lager errors are noted in $\bar{\tau}_{yz}$-values. With the 90º-ply equally assigned to two or three

layers across the thickness, the results appear in the categories, 1×1×4 mesh and 1×1×5 mesh, respectively. With1×1×4 mesh, there is no change in the values. However, with 1×1×5 mesh, it is seen that the $\bar{\tau}_{yz}$ -values are improve without any noticeable change in other results. Owen and Li (1987a) emphasized the need for artificially introducing more layers when partially layer-wise theory, which is similar with PDLM, is applied. Therefore, to achieve accuracy of the transverse shear stress values in thin as well as thick laminated plates with a PDLM model, discretization into more layers is needed in the thickness direction than the actual number of laminated plies, especially when this number is small.

Table 4.12 Maximum stresses and deflections by PDLM approaches

a/h	Source (Mesh)	$\bar{w}_c$ ($a/2,a/2,0$)	$\bar{\sigma}_x$ ($a/2,a/2,\pm h/2$)	$\bar{\sigma}_y$ ($a/2,a/2,\pm h/6$)	$\bar{\tau}_{xy}$ ($0,0,\mp h/2$)	$\bar{\tau}_{xz}$ ($0,a/2,0$)	$\bar{\tau}_{yz}$ ($a/2,0,0$)
10	Analytical Sol. [3D Elasticity]	1.746	±0.590	0.285 -0.288	±0.0289	0.357	0.1228
	PDLM (1×1×3)	1.716	±0.572	±0.281	±0.0283	0.358	0.0958
	PDLM (1×1×4)	1.716	±0.572	±0.281	±0.0283	0.358	0.0958
	PDLM (1×1×5)	1.717	±0.572	±0.281	±0.0283	0.359	0.1177
50	Analytical Sol. [3D Elasticity]	1.032	±0.541	±0.185	±0.0216	0.393	0.0842
	PDLM (1×1×3)	1.031	±0.540	±0.184	±0.0216	0.392	0.0674
	PDLM (1×1×4)	1.031	±0.540	±0.184	±0.0216	0.392	0.0674
	PDLM (1×1×5)	1.031	±0.540	±0.184	±0.0216	0.393	0.0823

Table 4.13 Maximum deflections and stresses in five-ply plates (a/h=2 and 4)

a/h	Source (Mesh)	$\bar{w}_c$ ($a/2,a/2,0$)	$\bar{\sigma}_x$ ($a/2,a/2,\pm h/2$)	$\bar{\sigma}_y$ ($a/2,a/2,\pm h/3$)	$\bar{\tau}_{xy}$ ($0,0,\mp h/2$)	$\bar{\tau}_{xz}$ ($0,a/2,0$)	$\bar{\tau}_{yz}$ ($a/2,0,0$)
2	Analytical Sol. [3D Elasticity]	12.278	1.332 -0.903	1.001 -0.848	0.0634 -0.0836	0.227 0.229 (0.02)	0.186 0.268 (0.18)
	Analytical Sol. [Closed Form]	11.211	±0.402	±0.552	±0.0243	0.284	0.262
	h-refinement ESLM (4×4)	11.209	±0.399	±0.548	±0.0241	0.282	0.260
	p-refinement ESLM (1×1)	11.211	±0.402	±0.552	±0.0243	0.284	0.262
	p-refinement PDLM (1×1×5)	12.665	±0.944	±0.819	±0.0684	0.211	0.211
	p-refinement FDLM (1×1×5)	12.278	1.332 -0.903	1.001 -0.848	0.0634 -0.0836	0.227 0.229 (0.014)	0.186 0.269 (0.21)
4	Analytical Sol. [3D Elasticity]	4.291	0.685 -0.651	0.633 -0.626	0.0384 -0.0394	0.238 0.238 (0.02)	0.229 0.233 (-0.11)
	Analytical Sol. [Closed Form]	3.623	±0.437	±0.503	±0.0235	0.305	0.240
	h-refinement ESLM (4×4)	3.622	±0.434	±0.499	±0.0233	0.303	0.228
	p-refinement ESLM (1×1)	3.623	±0.437	±0.503	±0.0235	0.305	0.240
	h-refinement PDLM (4×4×5)	4.249	±0.642	±0.601	±0.0382	0.233	0.240
	p-refinement PDLM (1×1×5)	4.269	±0.634	±0.593	±0.0377	0.227	0.235
	p-refinement FDLM (1×1×6)	4.291	0.685 -0.651	0.633 -0.626	0.0384 -0.0394	0.238 0.238 (0.014)	0.229 0.233 (0.13)

Table 4.14 Maximum deflections and stresses in five-ply plates (a/h=10 and 20)

a/h	Source (Mesh)	$\bar{w}_c$ ($a/2,a/2,0$)	$\bar{\sigma}_x$ ($a/2,a/2,\pm h/2$)	$\bar{\sigma}_y$ ($a/2,a/2,\pm h/3$)	$\bar{\tau}_{xy}$ ($0,0,\mp h/2$)	$\bar{\tau}_{xz}$ ($0,a/2,0$)	$\bar{\tau}_{yz}$ ($a/2,0,0$)
10	Analytical Sol. [3D Elasticity]	1.570	±0.545	0.430 -0.432	0.0247 -0.0246	0.258	0.223 0.223 (-0.02)
	Analytical Sol. [Closed Form]	1.441	±0.502	±0.411	±0.0221	0.346	0.200
	h-refinement ESLM (4×4)	1.440	±0.499	±0.408	±0.0219	0.344	0.198
	p-refinement ESLM (1×1)	1.441	±0.502	±0.411	±0.0221	0.346	0.200
	h-refinement PDLM (4×4×5)	1.553	±0.547	±0.431	±0.0247	0.259	0.230
	p-refinement PDLM (1×1×5)	1.561	±0.540	±0.426	±0.0244	0.253	0.225
	p-refinement FDLM (1×1×5)	1.570	±0.546	0.430 -0.432	0.0247 -0.0246	0.258	0.223 0.223 (-0.014)
20	Analytical Sol. [3D Elasticity]	1.145	±0.539	±0.380	±0.0222	0.268	0.212
	Analytical Sol. [Closed Form]	1.112	±0.528	±0.375	±0.0215	0.362	0.184
	h-refinement ESLM (4×4)	1.112	±0.524	±0.372	±0.0214	0.359	0.183
	p-refinement ESLM (1×1)	1.112	±0.528	±0.375	±0.0215	0.362	0.184
	h-refinement PDLM (4×4×5)	1.137	±0.544	±0.384	±0.0224	0.270	0.217
	p-refinement PDLM (1×1×5)	1.143	±0.537	±0.379	±0.0221	0.263	0.212
	p-refinement FDLM (1×1×6)	1.146	0.538 -0.539	±0.380	0.0222 -0.0221	0.268	0.212

Table 4.15 Maximum deflections and stresses in five-ply plates (a/h=50 and 100)

a/h	Source (Mesh)	$\bar{w}_c$ ($a/2,a/2,0$)	$\bar{\sigma}_x$ ($a/2,a/2,\pm h/2$)	$\bar{\sigma}_y$ ($a/2,a/2,\pm h/3$)	$\bar{\tau}_{xy}$ ($0,0,\mp h/2$)	$\bar{\tau}_{xz}$ ($0,a/2,0$)	$\bar{\tau}_{yz}$ ($a/2,0,0$)
50	Analytical Sol. [3D Elasticity]	1.023	±0.539	±0.363	±0.0214	0.271	0.206
	Analytical Sol. [Closed Form]	1.018	±0.537	±0.362	±0.0213	0.367	0.178
	h-refinement ESLM (4×4)	1.018	±0.533	±0.359	±0.0212	0.365	0.177
	p-refinement ESLM (1×1)	1.018	±0.537	±0.362	±0.0213	0.367	0.178
	h-refinement PDLM (4×4×5)	1.018	±0.544	±0.367	±0.0216	0.274	0.211
	p-refinement PDLM (1×1×5)	1.023	±0.538	±0.363	±0.0214	0.267	0.206
	p-refinement FDLM (1×1×5)	1.023	±0.539	±0.363	±0.0214	0.271	0.206
100	Analytical Sol. [3D Elasticity]	1.006	±0.539	±0.360	±0.0213	0.272	0.205
	Analytical Sol. [Closed Form]	1.005	±0.538	±0.360	±0.0213	0.368	0.177
	h-refinement ESLM (4×4)	1.004	±0.535	±0.357	±0.0211	0.366	0.176
	p-refinement ESLM (1×1)	1.005	±0.538	±0.360	±0.0213	0.368	0.177
	h-refinement PDLM (4×4×5)	1.001	±0.544	±0.384	±0.0213	0.275	0.211
	p-refinement PDLM (1×1×5)	1.006	±0.539	±0.360	±0.0213	0.268	0.205
	p-refinement FDLM (1×1×6)	1.006	±0.539	±0.360	±0.0213	0.272	0.205
	CLPT	1.005	±0.539	±0.359	±0.0213	0.272	0.205

In Tables 4.13 through 4.15, the maximum deflections and stresses obtained by different models in the laminated plate with five layers (Case 2) are compared with those of 3D elasticity solution (Pagano, 1970) and the closed-form solution (Reddy, 2004b) for five side-to-thickness ratios, namely, a/h=2,4,10,20,50,100. The h-refinement results from references (Reddy, 2004b; Owen and Li, 1987a) are based on selective integration and/or extrapolation technique, for better prediction of nodal stress values. The current results based on p-refinement converged satisfactorily only when higher p-levels were used, without any mesh refinement, but with regular integration. In the Tables 4.13 through 4.15, although p-refinement invariably shows better accuracy than h-refinement, the NDF required with the two numerical models are quite different. In order to examine performance of ESLM, PDLM and FDLM based p-FEM models, a range of thin to thick laminated plates are considered. It can be seen that for the full range of thicknesses considered, FDLM based results converge exactly to solutions based on 3D elasticity. It is also noted that the displacements and stresses based on ESLM tend to converge to the closed form solutions for all the values of side-to-thickness ratios considered. PDLM based results has been found to have relatively smaller error than those by ESLM. Especially, the thicker the laminated plate is, the closer the PDLM based results are to exact solutions, which is contrary to the performance of ESLM based model.

In Figs. 4.22 through 4.24, the distribution of in-plane displacements, normal stresses, and transverse shear stress, which are calculated by FDLM, are shown for nine-ply laminated plates (Case 3) with different values of a/h. All the results are found to be almost identical with the results from reference (Pagano and Hatfield, 1972), considered to be exact solution.

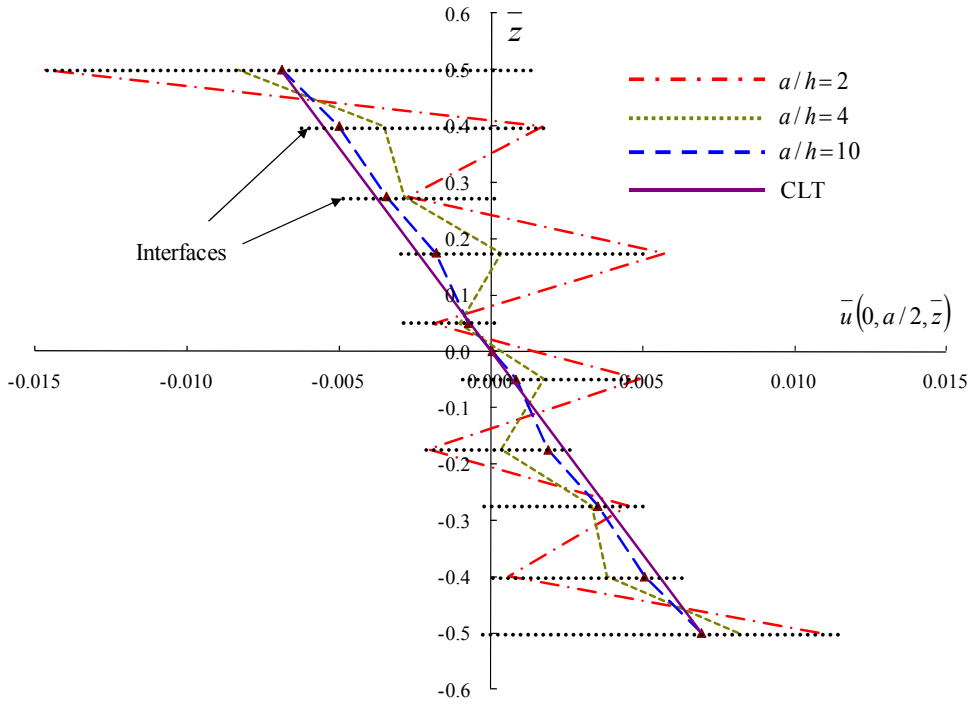

Fig. 4.22 In-plane displacement in nine-ply laminated plates

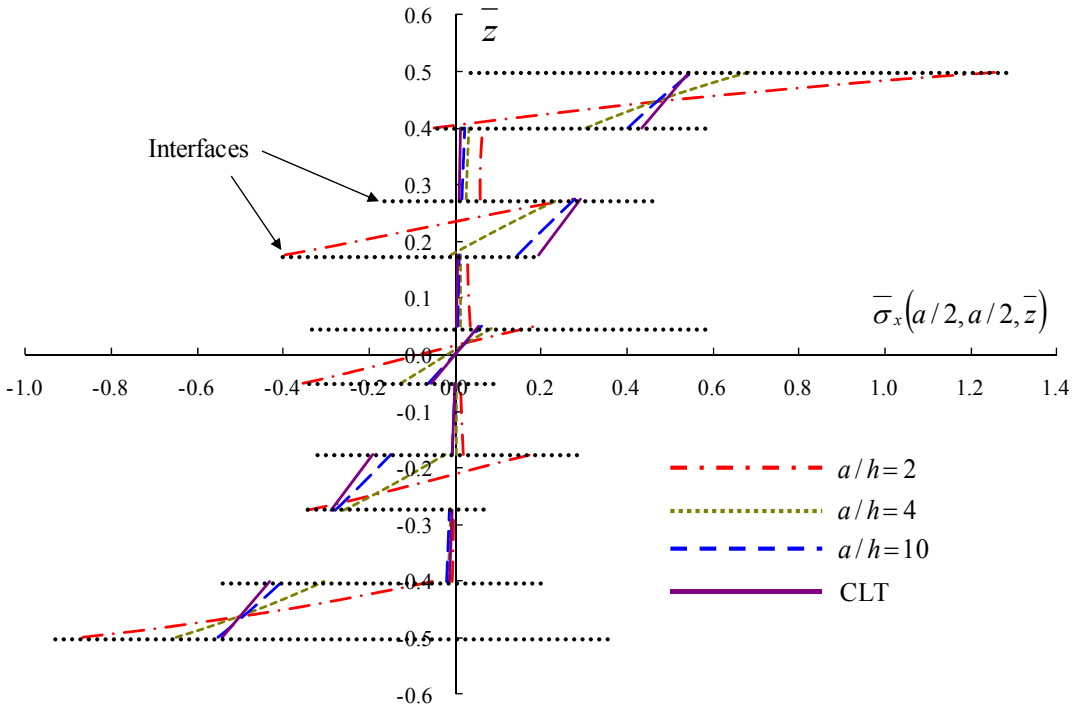

Fig. 4.23 Normal stress distribution in nine-ply laminated plates

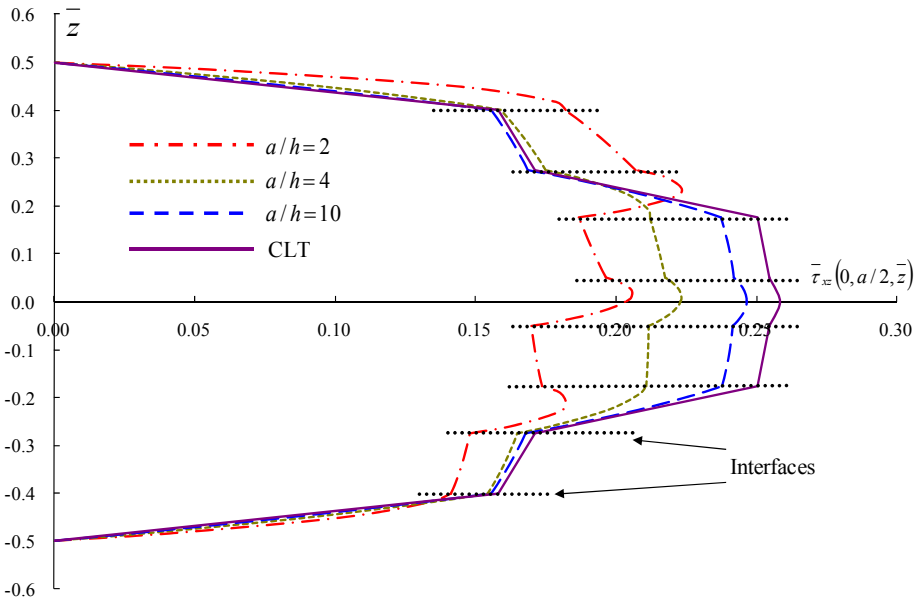

Fig. 4.24 Transverse shear stress distribution in nine-ply laminated plates

The across the thickness variations of the in-plane displacement u (in Figs. 4.25 through 4.27) and normal stress σ_{xx} (in Figs. 4.28 through 4.30) based on ESLM, PDLM and FDLM based models are for aspect ratios of a/h=2, 4, and 10. As the thickness is reduced (or, the plate aspect ratio is increased), the discrepancy in the results by the different models is found to reduce, converging eventually to CLT results which in turn are independent of the aspect ratio of the plate. Fig. 4.31 shows the transverse shear stress distribution by each model when a/h=10. Although the real behavior of transverse stresses follow continuity condition at interface of adjacent layers, PDLM and ESLM shown discontinuity in transverse shear stresses at ply interfaces. As with ESLM, the transverse shear stresses by PDLM are same within a layer. In addition, it is noted that the representative value of the transverse shear stresses within one layer by PDLM is approximately average of the values across the thickness of the layer obtained by FDLM.

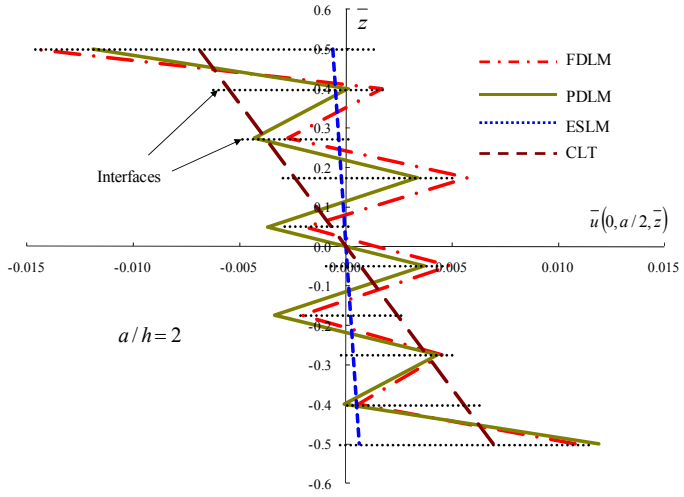

Fig. 4.25 In-plane displacement in nine-ply laminated plates (a/h=2)

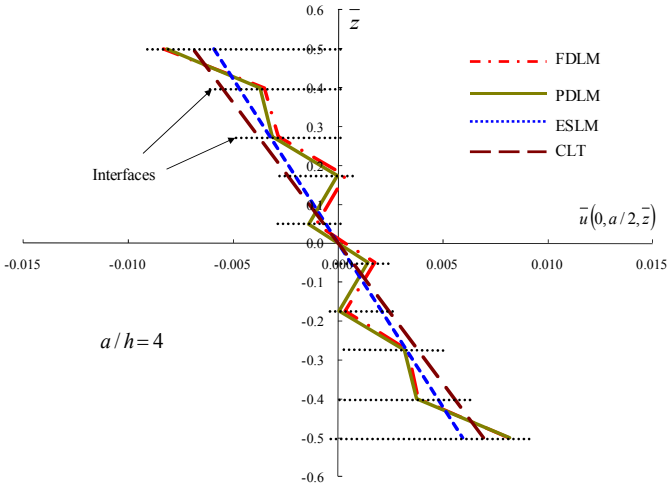

Fig. 4.26 In-plane displacement in nine-ply laminated plates (a/h=4)

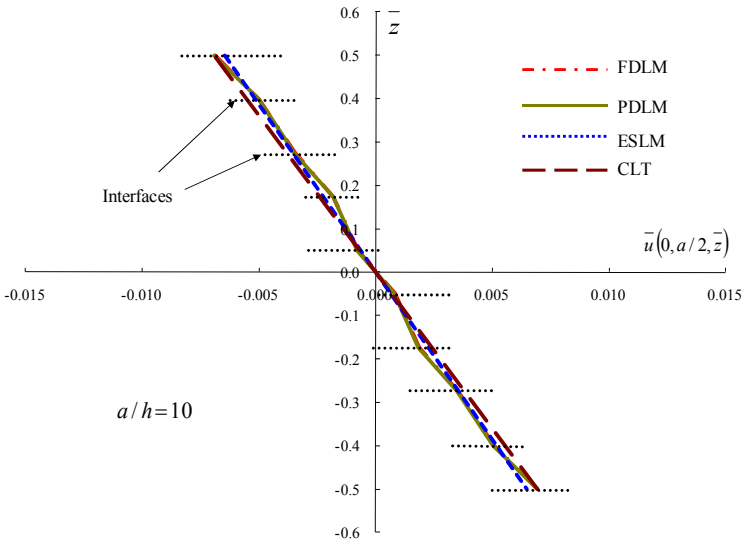

Fig. 4.27 In-plane displacement in nine-ply laminated plates (a/h=10)

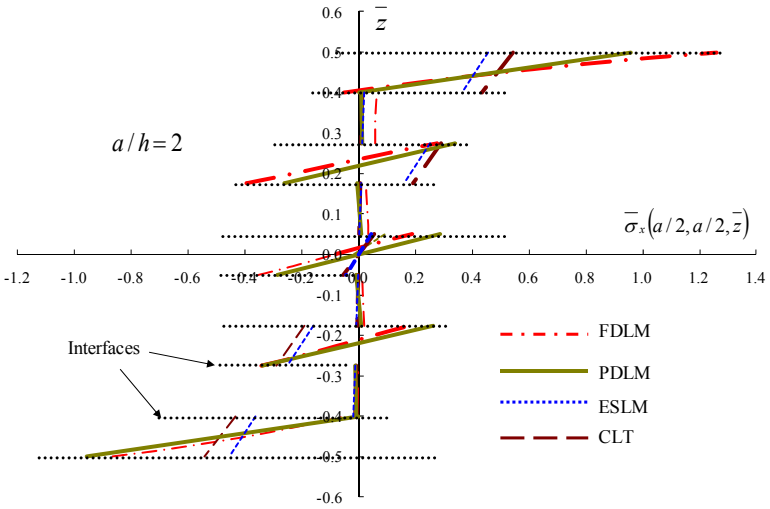

Fig. 4.28 Normal stress distribution in nine-ply laminated plates (a/h=2)

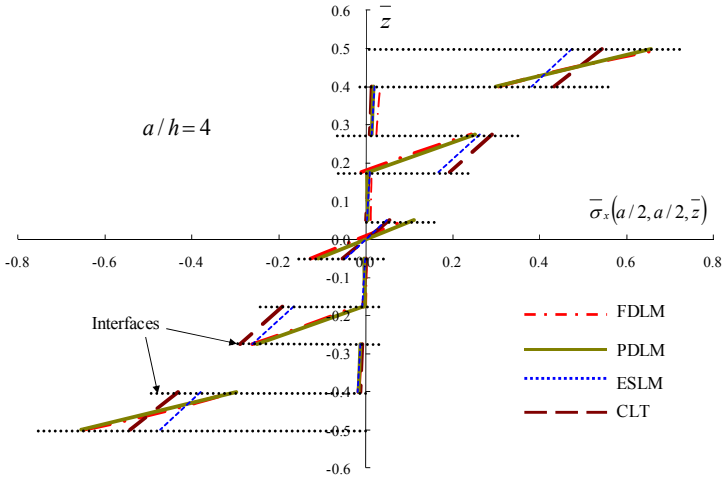

Fig. 4.29 Normal stress distribution in nine-ply laminated plates (a/h=4)

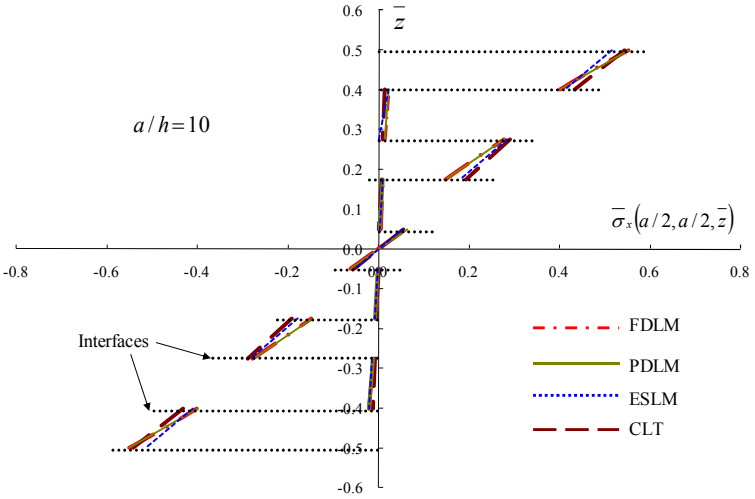

Fig. 4.30 Normal stress distribution in nine-ply laminated plates (a/h=10)

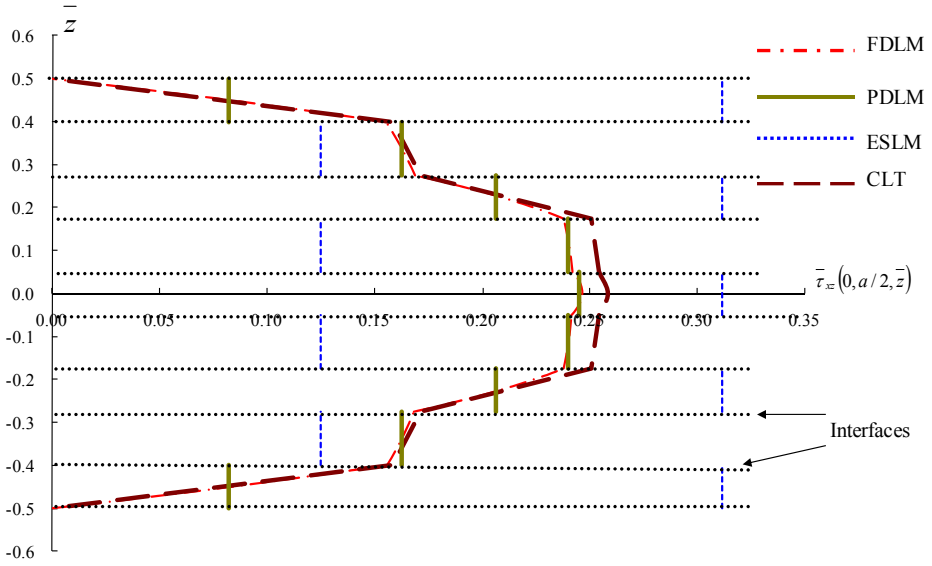

Fig. 4.31 Transverse shear stress distribution in nine-ply laminated plates in a/h=10

4.6 Geometrically Nonlinear Analysis for Bending Problems

To investigate application of developed models using geometrically nonlinear analysis, several examples of isotropic and orthotropic rectangular plates are considered. For all examples considered, 1×1 mesh on xy-plane is adopted and the number of modeling layers through thickness is equal to the number of physical layers.

As the first example, an isotropic square plate subjected to uniformly distributed transverse loading q_0, shown in Fig. 4.7, is considered with a=10 in and the thickness h is taken as 1 in. The boundary conditions are defined as in Table 4.3. The material properties are taken as

$$E = 7.8\times10^6 \text{ psi}; \qquad \nu = 0.3 \tag{4.9}$$

Only one quadrant of the plate in the xy-plane is modeled by only one element taking advantage of two-way symmetry. The loading, deflection and in-plane normal stress are normalized as

$$\overline{P} = \frac{q_0 a^4}{Eh^4}; \quad \overline{w} = \frac{w(5,5,0)}{h}; \quad \overline{\sigma} = \frac{a^2 \sigma_{xx}(4.375,4.375,0.5)}{Eh^4} \tag{4.10}$$

Fig. 4.32 shows variation of deflection at center of plate with increase of loading. In the presence of tensile stresses caused by support constraints, deflections based on a geometrically nonlinear analysis will tend to be smaller due to stiffening effect of these forces. The nonlinear results based on FDLM, PDLM, and ESLM based models show good agreement with reference (Reddy, 2004a) using 16 elements (4×4 mesh) and first-order shear deformation theory. Although, in the case of linear analysis, the results of ESLM based model and reference values are exactly same, in the case of nonlinear analysis, slight discrepancy (about 3%) is noted between current and reference values. This can be attributed to the fact that, unlike the reference nonlinear model, the present model applies geometric nonlinearity appropriate by using total Lagrangian formulation to appropriately reflect the changes in plate geometry.

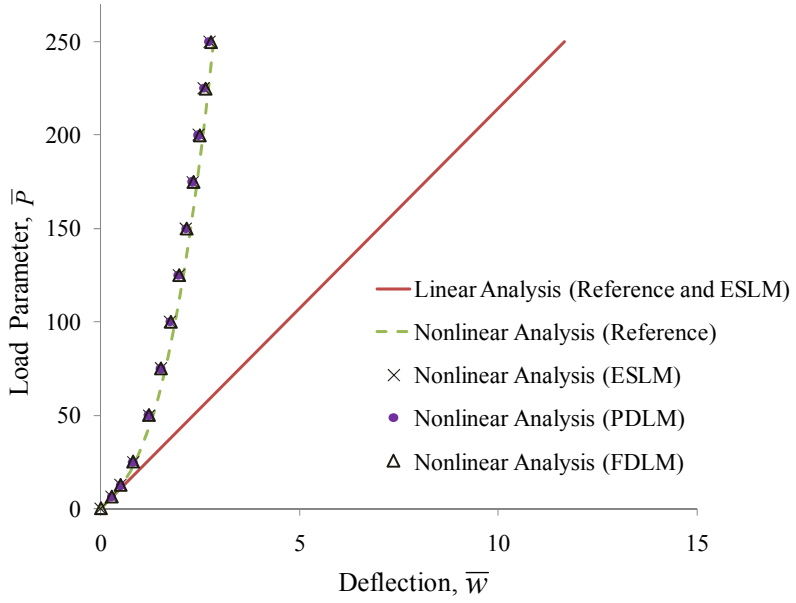

Fig. 4.32 Plot of load versus center deflection

Fig. 4.33 shows variation of in-plane normal stresses with increasing load. Like displacement behavior, the effect of geometric nonlinearity on in-plane normal stresses obtained by the current models is well represented, showing good agreement with reference values. Also, good agreement is shown between present models and reference. However, slight discrepancy (within 5%) is noted between the values based on 2D elasticity theory models and those by FDLM model utilizing 3D elasticity theory.

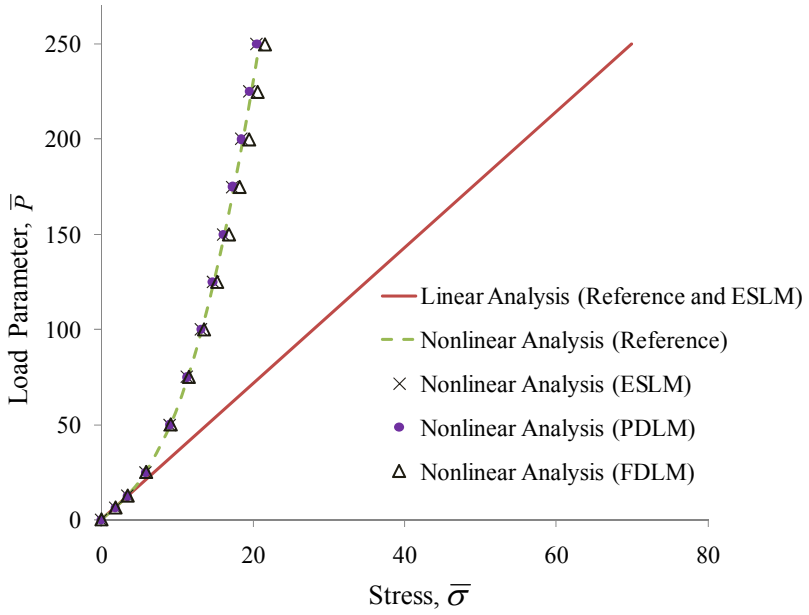

Fig. 4.33 Plot of load versus in-plane normal stress

The second problem considered consists of a simply-supported orthotropic plate under uniform load. As in Fig. 4.7, plate size, a, is 12 in and the thickness, h, is 0.138 in. The finite element models used are same as in the first example. The orthotropic material properties used are as follows

$$E_L = 3\times10^6 \text{ psi};\ E_T = 1.28\times10^6 \text{ psi};$$
$$G_{LT} = G_{TT} = 0.37\times10^6 \text{ psi};\ \nu_{LT} = \nu_{TT} = 0.32 \tag{4.11}$$

where subscript L denotes the fiber direction, and T denotes a direction which is orthogonal to L. The results of current models are shown in Fig. 4.34 and compared with references (Zaghloul and Kennedy, 1975; Reddy, 2004a). The values from Zaghloul and Kennedy (1975) are experimental results, and (Reddy, 2004a) uses *h*-FEM 2D elements and first-order shear deformation theory. In geometrically nonlinear analysis of *h*-FEM, the total Lagrangian formulation was used, like the current models. For this simply-supported plate, results from current models are in good agreement with all reference values.

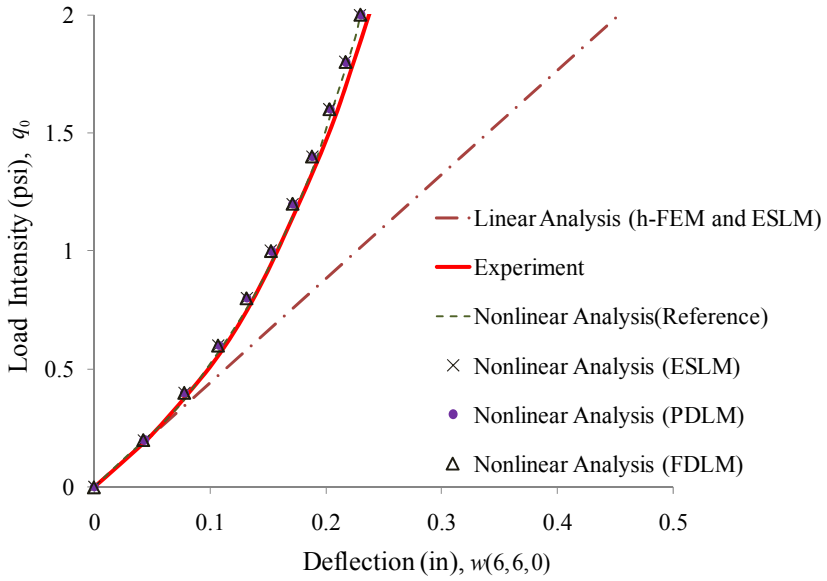

Fig. 4.34 Geometrically nonlinear response of an orthotropic plate

Finally, a four-layer (0°/90°/90°/0°) clamped plate under uniform load is considered as the third example. The material properties of a typical layer are given by

$$\begin{aligned} &E_L = 1.8282\times10^6 \text{ psi};\ E_T = 1.8315\times10^6 \text{ psi};\\ &G_{LT} = G_{TT} = 0.3125\times10^6 \text{ psi};\ \nu_{LT} = \nu_{TT} = 0.2395 \end{aligned} \tag{4.12}$$

Total thickness, h, is 0.096 in, and thickness of all the layers is same. Any data not mentioned for this problem is taken to be same as those for the second example. The variation of deflection for the current models with loading is shown in Fig. 4.35. Just like the last example, in this example the current models represent geometrically nonlinear behavior quite well. However, some discrepancy is noted between the results for current models and experiment; whereas, the same results are very similar to numerical results implemented by Reddy (2004a). The discrepancy with the experimental data can be attributed to differences between the assumptions made in the numerical models and the actual conditions present in the experimental setup.

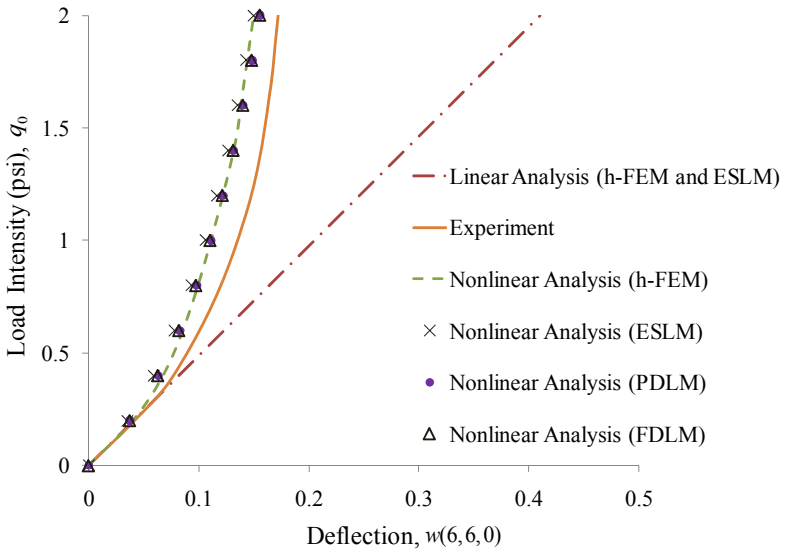

Fig. 4.35 Nonlinear response of a laminated plate with clamped boundary conditions

4.7 Remarks

Some basic examples with in-plane and bending behaviors were solved to examine the validity and performance of current developed models (ESLM, PDLM, FDLM, and DLTM) based on p-FEM, and the results were compared with published results and in

some instances with results obtained by using commercial tools. On the basis of the numerical studies, the following preliminary observations can be made.

1. While ESLM based on first-order shear deformation theory is inherently simple and computationally efficient due to the relatively small number of dependent variables that must be solved for, the solution accuracy and the capability of modeling laminated system with irregularities is questionable. In short, this model is inadequate for problems having 3D stress fields at the ply level or in relatively thick plates.

2. In order to overcome these deficiencies of the ESLM, FDLM can be used with the assumption of separating displacement field expansions within each material layer. Therefore, the variation of the displacements through the thickness can be represented to any desired level of accuracy by independently increasing *p*-level with respect to planar shape function and shape functions in the thickness direction. Due to the presence of a large NDF associated a FDLM element, but its accuracy is comparable to a conventional 3-D and is computationally more efficient than a full-blown 3D analysis.

3. PDLM is computationally more efficient than FDLM, and at the same time provides more accurate representations of displacements and stresses than ESLM. However, because of the assumption of inextensibility of transverse normal, it is limited in accurately representing the 3D stress field.

4. Considering the aforementioned advantages and disadvantages of each model, 3D and 2D mathematical models are concurrently analyzed with DLTM combining 3D and 2D models in terms of solution accuracy, solution efficiency, and ease of implementation.

5. Application of developed models using geometrically nonlinear analysis based on total Lagrangian approach is represented for isotropic, orthotropic and laminated plates.

CHAPTER V

NUMERICAL ANALYSIS OF SYSTEMS WITH IRREGULARITIES

5.1 Plates with Stepped Thickness

In the presence of irregularities sudden change in thickness or section is generally characterized by the occurrence of stress singularity of unknown strength at such a location. In order to evaluate this condition, a cantilever plate with stepped thickness, as shown in Fig. 5.1, and subjected to in-plane and bending loads is considered.

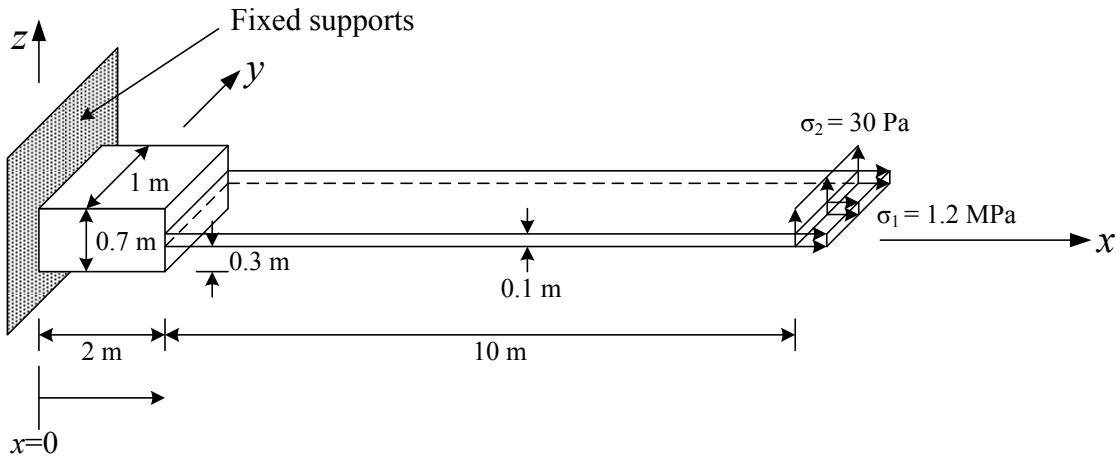

Fig. 5.1 Cantilever system with different sections

For the plate material the Young's modulus is assumed as 30 MPa and Poisson's ratio as zero. As shown in Fig. 5.2, the cantilever is partitioned into four regions in the *xy*-plane, and the finite element model is selected as shown in Table 5.1 which shows five finite element models designated as Model A~E. Of these, first three uses identical elements in a system while later two types are composed of a combination of different element types,

along with appropriately located compatible transition elements. When 3D element is used in the thick section, discretization into three layers is considered.

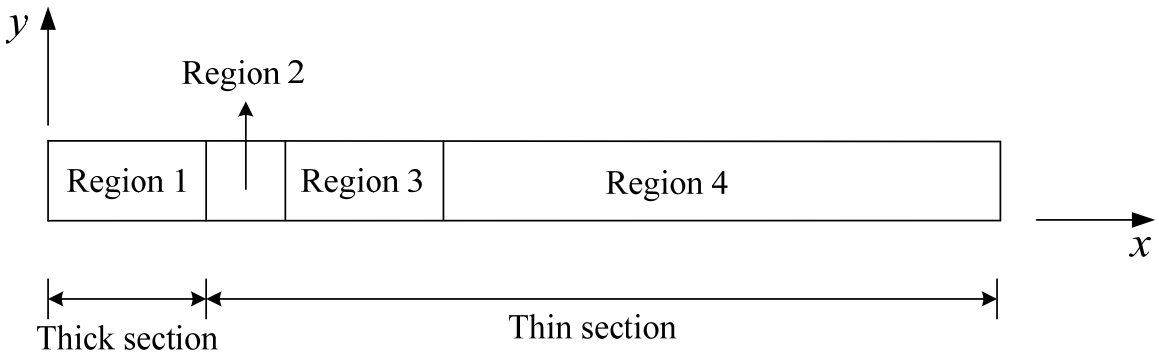

Fig. 5.2 Partition in *xy*-plane for finite element modeling

Table 5.1 Models assigned to each region

	Region 1	Region 2	Region 3	Region 4
Model A	FDLM (3 layers)	FDLM (1 layer)	FDLM (1 layer)	FDLM (1 layer)
Model B	PDLM (3 layers)	PDLM (1 layer)	PDLM (1 layer)	PDLM (1 layer)
Model C	ESLM	ESLM	ESLM	ESLM
Model D	FDLM (3 layers)	FDLM (1 layer)	DLTM	ESLM
Model E	PDLM (3 layers)	PDLM (1 layer)	DLTM	ESLM

5.1.1 Case of In-Plane Loading

Stepped plate subjected to in-plane loading (σ_1) shown in Fig. 5.1 is analyzed. The variation of axial displacement along the longitudinal centerline of the plate by Models A~C is shown in Fig. 5.3, showing seemingly identical values for all the models. Also,

using exaggerated scale, the plot of the same displacement for $0 \le x \le 2.5$ is shown in Fig. 5.4. The plot of Fig. 5.4 displays noticeable difference in displacements in regions near the step and beyond. It is seen that the displacements by Model C with only 2D elements are somewhat smaller than those by the 3D elements. Also, Model A and Model D which are composed of identical FDLM elements near the step region give identical results. The same is also true for Model B and Model E.

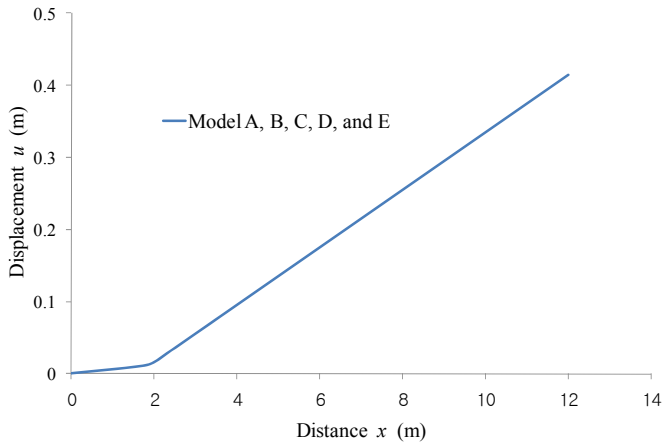

Fig. 5.3 Variation of displacement u along the length of the plate

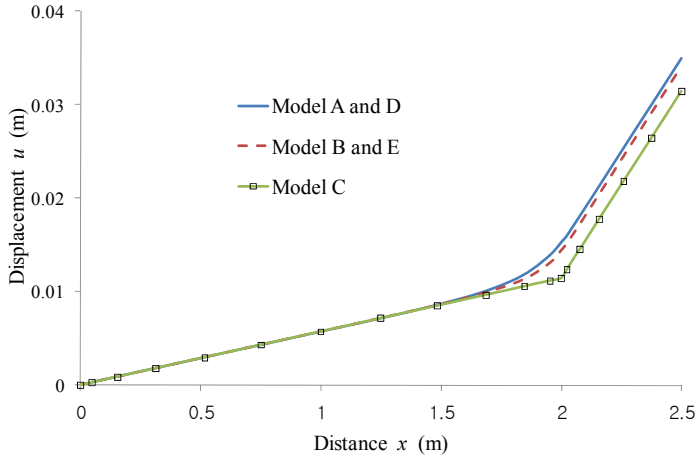

Fig. 5.4 Variation of displacement u near region with step change in thickness

Figs. 5.5 through 5.7 show variation of displacements along the thickness of the plate at x=2 m, 1.85 m, and 1.69 m, respectively. It is seen from those figures that Model C with only 2D elements shows constant deflection across the thickness and thus fails to capture the correct pattern, especially near the step change in thickness region.

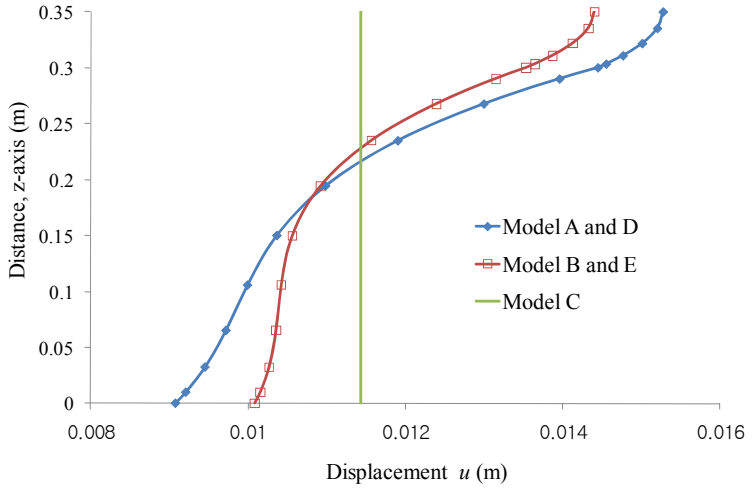

Fig. 5.5 Variation of displacement u along the thickness of the plate (x=2 m)

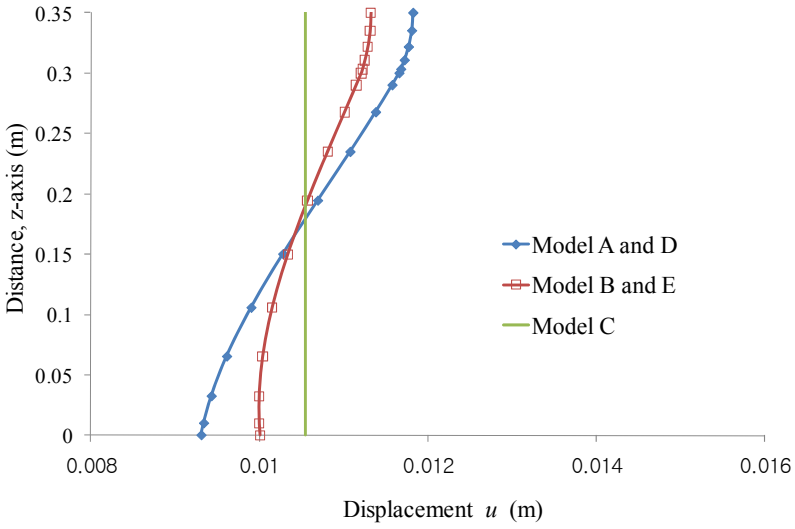

Fig. 5.6 Variation of displacement u along the thickness of the plate (x=1.85 m)

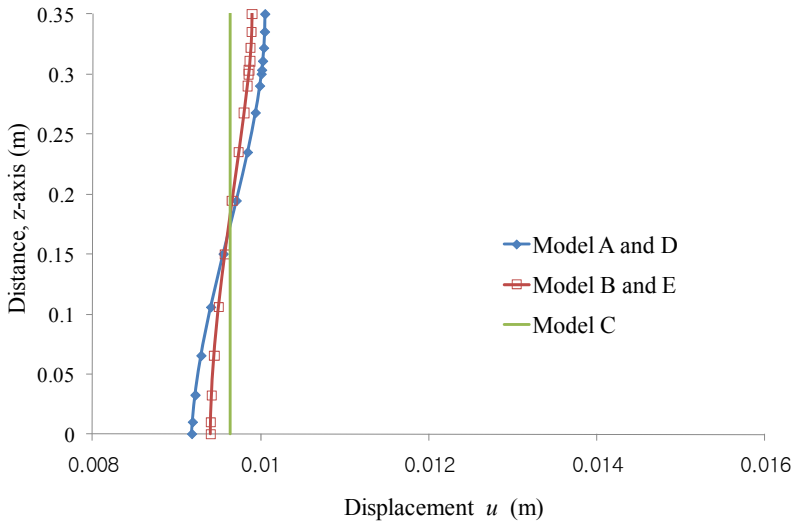

Fig. 5.7 Variation of displacement u along the thickness of the plate (x=1.69 m)

Fig. 5.8 shows the variation of normal stress (σ_{xx}) along the thickness of the thinner part of the plate at the step location (x=2.0 m). From the results of 3D models, it is noticed that considerably high stresses occur at the corners; whereas, can not simulate such behavior.

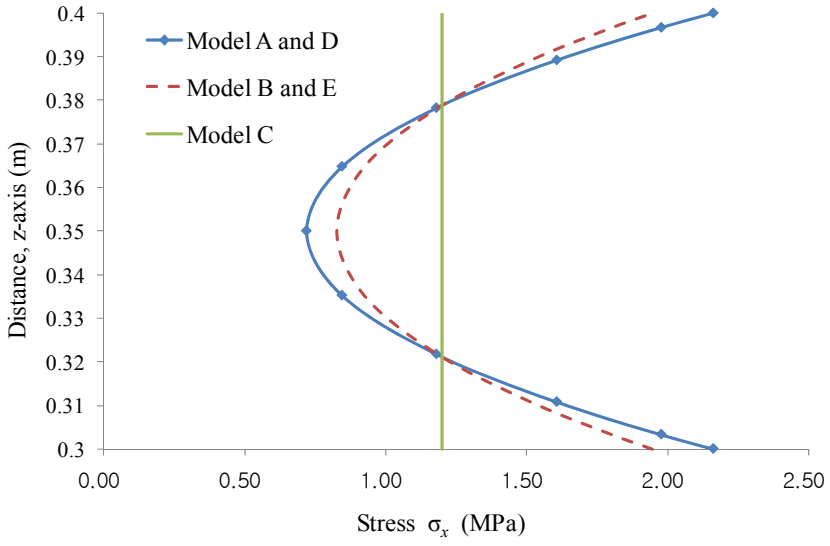

Fig. 5.8 Variation of stress σ_{xx} along the thickness of the plate (x=2.0 m)

In Fig. 5.9, the contour of normal stresses is shown near the region with stepped change in thickness from analysis based on Model A. The remaining models also show similar behavior, except Model C.

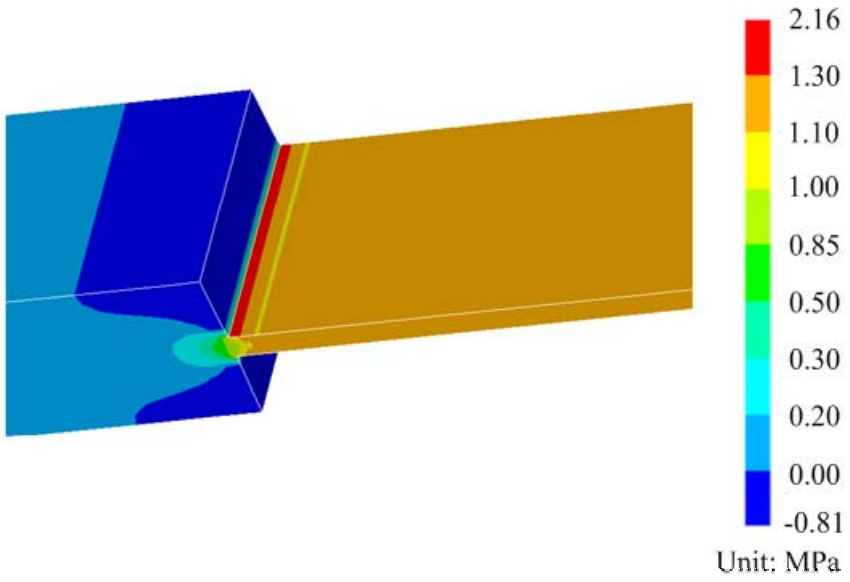

Fig. 5.9 Stress (σ_{xx}) fringes near the region with step change of thickness

From the results presented above, it can be told that in the case of the problem considered there is hardly any difference in 3D based models, whether transition element is used or not. The primary difference amongst the four models is that the required degrees of freedom in Model A (NDF=3762) is more than that for Model D (NDF=2964). The same is true between Model B (NDF=2736) and Model E (NDF=2280). However, although the least number of degrees of freedom is associated with Model C (NDF=1140), the corresponding results are gross erroneous in region of step change in thickness. It can therefore be stated that models with transition elements are more efficient than the rest.

5.1.2 Case of Transverse Loading

Here the stepped plate with transverse loading σ_2 at its tip, as shown in Fig. 5.1, is under consideration. Fig. 5.10 shows the variation of transverse deflection w along the length of the plate, and Fig. 5.11 shows an exaggerated view of the same plot over the region $0 \leq x \leq 2.26$. The sharp change in the slope deflection curve near the step in the plate is as expected. In this case the results for all the models tend to agree closely.

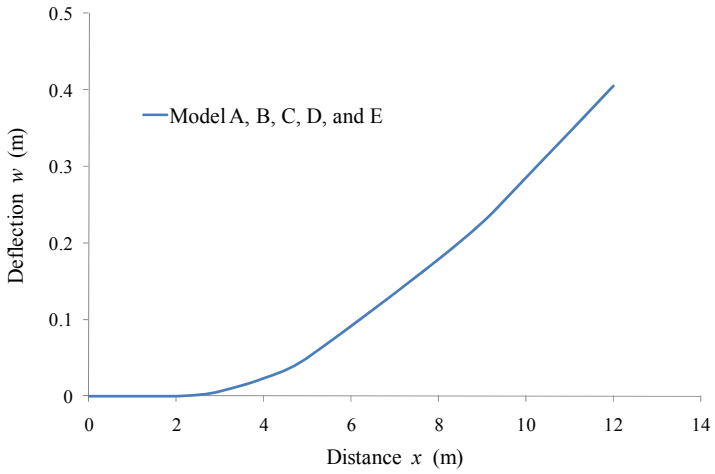

Fig. 5.10 Variation of displacement w along the length of the plate

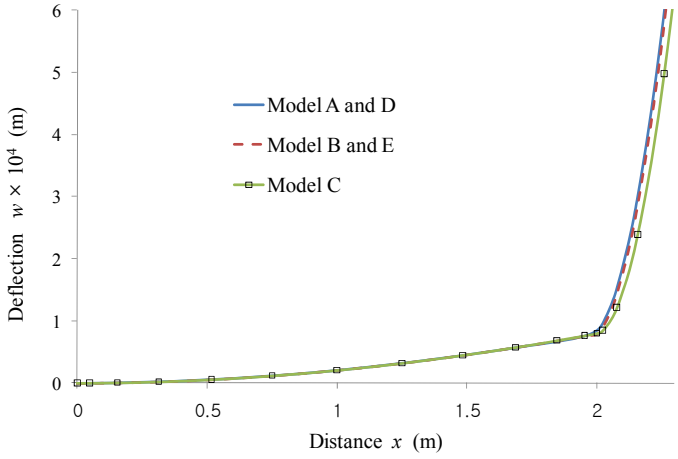

Fig. 5.11 Variation of displacement w in the region near the step in the plate

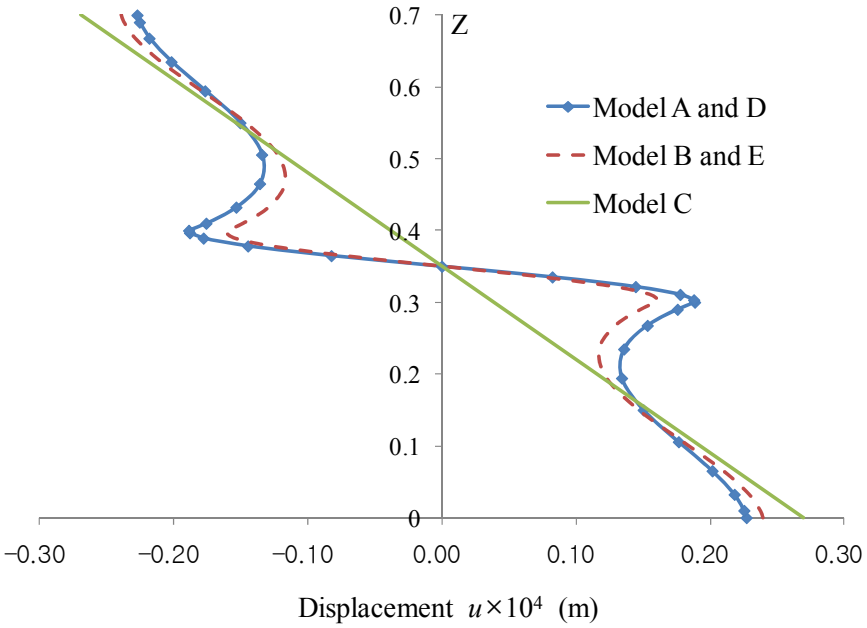

Fig. 5.12 Variation of displacement u along the thickness of the plate (x=2 m)

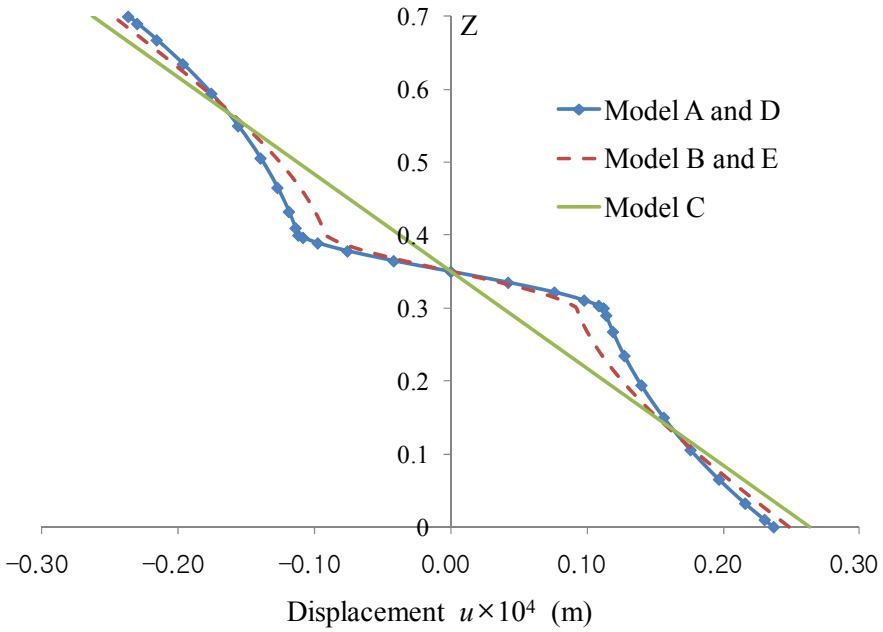

Fig. 5.13 variation of displacement u along the thickness of the plate (x=1.95 m)

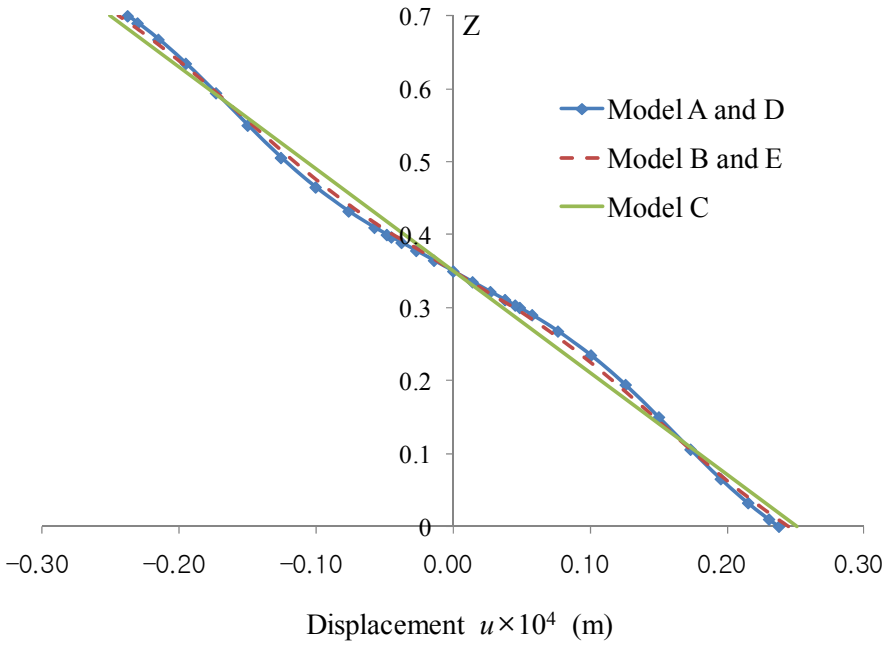

Fig. 5.14 Variation of displacement u along the thickness of the plate (x=1.85 m)

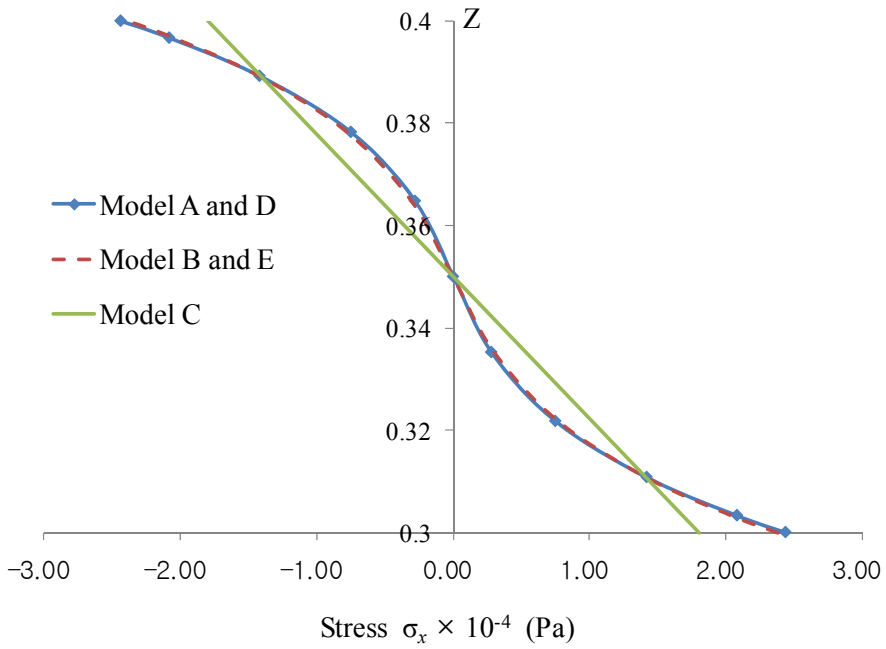

Fig. 5.15 Variation of stress σ_{xx} along the thickness of the plate (x=2.0 m)

Figs. 5.12 through 5.14 show the variation of in-plane displacement u along the thickness of the plate at x=2 m, x=1.95 m, and x=1.85 m, respectively. It is seen that only Model C with 2D elements fails to capture the correct deformation pattern, while the results of Models D and E containing transition elements have no difference with those by Models A and B, respectively. The effect of modeling with FDLM, PDLM, ESLM, or suitable combinations thereof is most significant at x=2 m. In regions away from the step, the increasing correlation between the results of the models with 3-D elements and that with 2D elements is obvious from the plots shown in Figs. 5.12 through 5.14. Fig. 5.15 shows the variation of normal stress, σ_{xx}, along the thickness of the thinner plate at x=2.0 m. The results of Models A, B, D and E agree, but Model C fails to represent this true behavior. Fig. 5.16 shows normal stress fringes for the same problem. The extremely large stress values at step location appears to be unrealistically high and in reality the material will fail at this point well before reaching this stress level. This unrealistic stress value can be attributed to the presence of elastic stress singularity at the location, which is clearly revealed as the p-level of the approximation is increased.

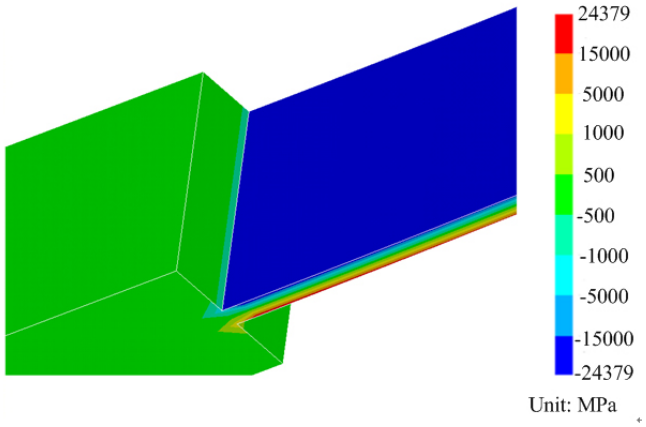

Fig. 5.16 Stress fringes (σ_{xx}) of the plate in the step region

5.2 Skew Plates

5.2.1 Single-Layer Isotropic Rhombic Plate

A simply supported rhombic plate under uniformly distributed transverse load, q = 0.7 kPa, with skew angle, α = 60º, as shown in Fig. 5.17, is known to possess a strong moment singularity of the type $r^{-0.8}$, at obtuse corners B and D.

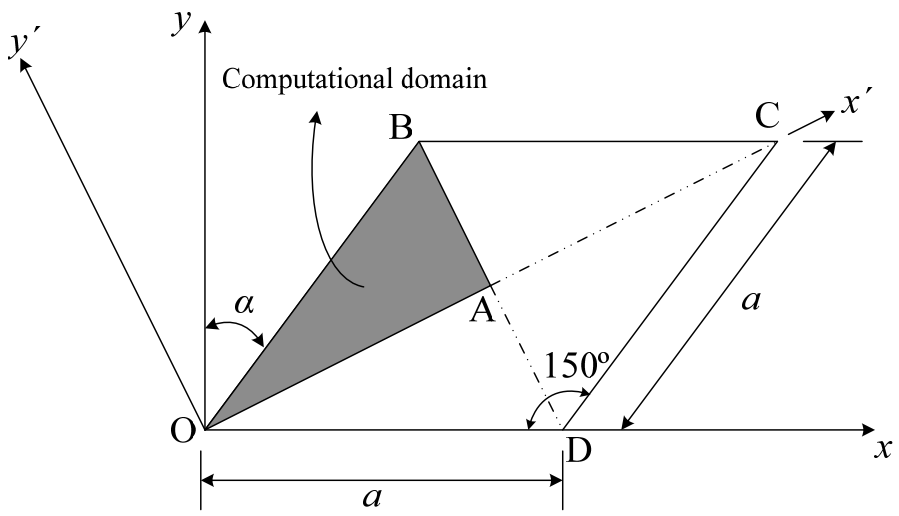

Fig. 5.17 Skew simply supported plate under uniformly distributed load

Although no exact solution is available for the problem, Morley (1962) tried to address the problem by 2D elasticity approximation and finite difference solution and was able to give accurate estimates of deflection and bending moment at plate center. Here, the plate is separately discretized with FDLM-, PDLM-, and ESLM-based elements. For convenience in defining the model, the reference axes are rotated counter-clockwise by 15 degrees, as shown in Fig. 5.17. With x'-, and y'-axis as the reference axes, the quarter plate area is discretized into five elements, by strongly grading the element sizes towards

the singular corner, as shown in Fig. 5.18. The material and geometrical properties are taken as: Young's modulus, E = 210 GPa, Poisson's ratio, v = 0.3, the side length, a = 1 m, and plate thickness, t = 10 mm.

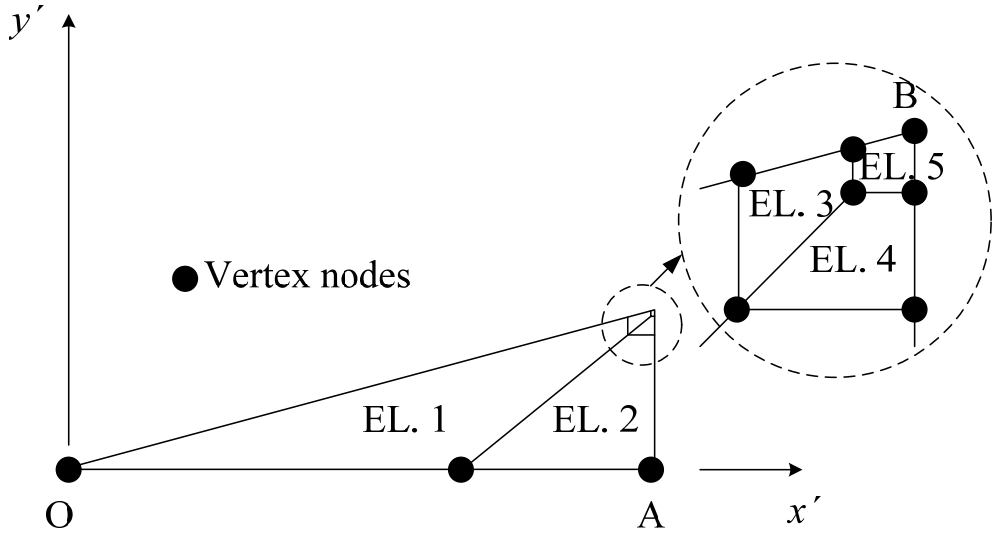

Fig. 5.18 Finite element mesh for skew plate

Figs. 5.19 and 5.20 show the convergence characteristics of lateral displacement w, and principal bending moment M_1, both at the central point A, obtained by the three element types, as the in-plane p-levels are varied. From the results, it is seen that displacements by all the proposed element models converged at p-level = 5 and principal bending moments converged at p-level = 6, agreeing with Morley (1962) results. Table 5.2 gives a comparison of the present numerical results with those from the reference (Morley, 1962), showing excellent agreement. As the plate is very, all the computed results, based on ESLM, PDLM, and FDLM, are found to be almost the same.

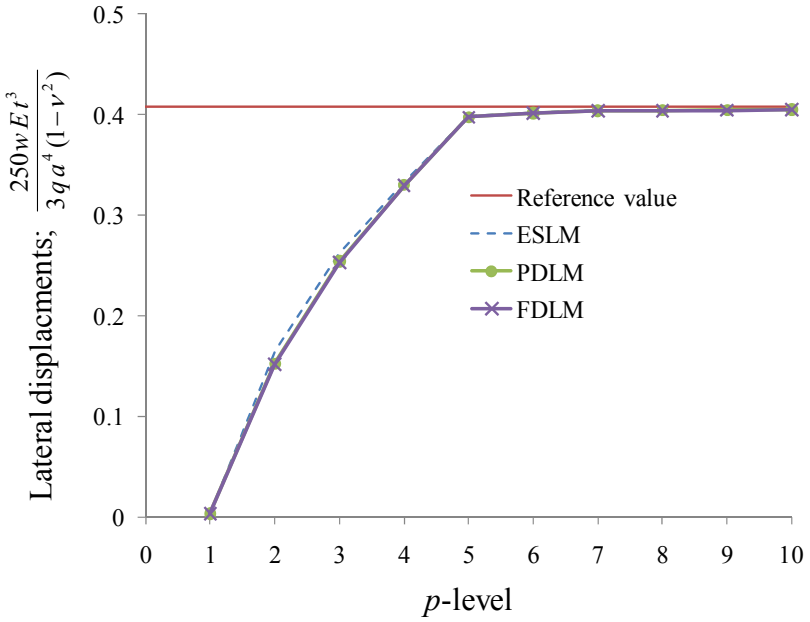

Fig. 5.19 Convergence test of lateral displacement with *p*-level

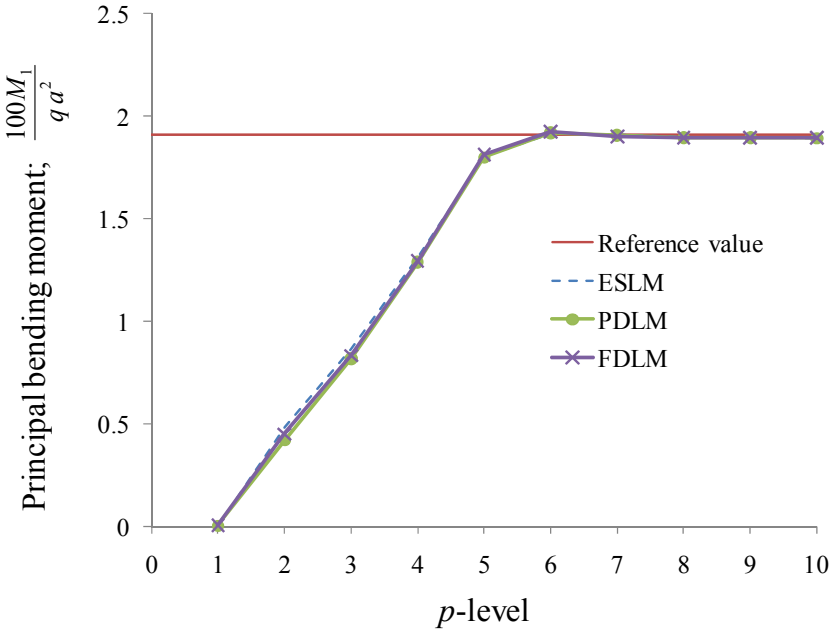

Fig. 5.20 Convergence test of bending moment with *p*-level

Table 5.2 Comparison of lateral displacements and principal bending moments

Types		$\frac{250wEt^3}{3qa^4(1-\nu^2)}$	$\frac{100M_1}{qa^2}$	$\frac{100M_2}{qa^2}$
Reference	2-D approximate solution	0.408	1.91	1.08
	Finite difference method	0.384	1.92	0.98
Present models	ESLM	0.4051	1.894	1.072
	PDLM	0.4049	1.894	1.072
	FDLM	0.4048	1.895	1.072

In Figs. 5.21 and 5.22 are shown the variation of bending moments, $M_{x'x'}$ and $M_{y'y'}$ along the line AB. With *p*-level = 10, the computed results closely follow those by Morley (1962), accurately representing singular behavior near Point B in the obtuse corner of the plate.

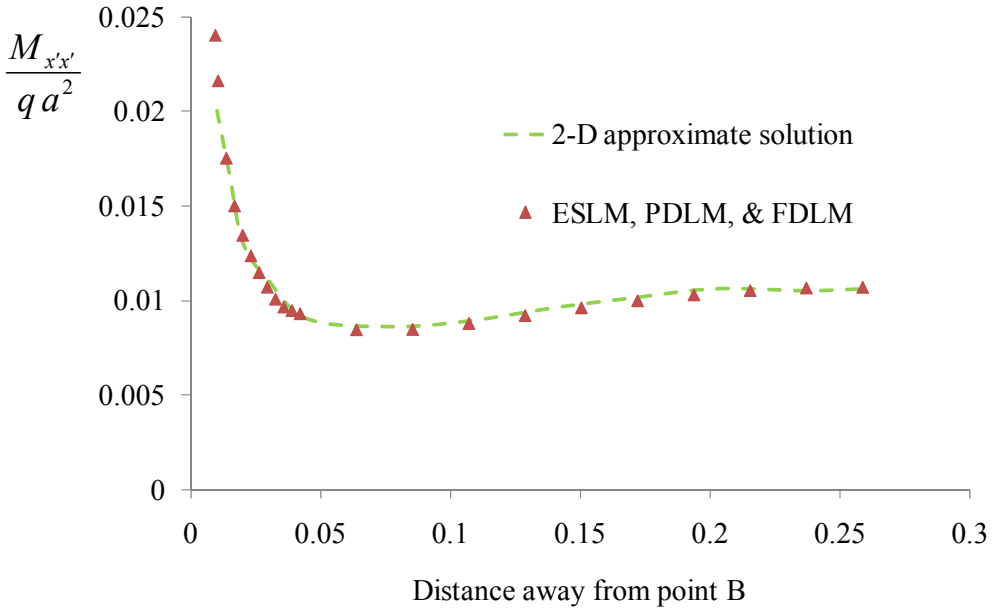

Fig. 5.21 Stress resultants of bending moment $M_{x'x'}$ along line AB

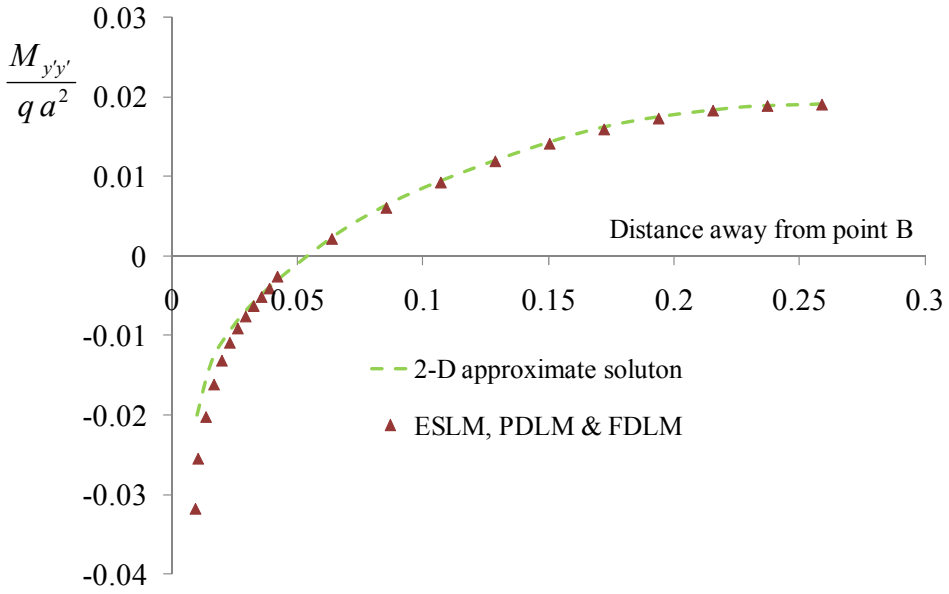

Fig. 5.22 Stress resultants of bending moment $M_{y'y'}$ along line AB

Table 5.3 gives maximum normal and shear stress values based on the three element types. It was noticed that model refinement near the obtuse corner, based on the *hp*-version, led to unbounded increase in the stress values near the obtuse corner. The numerical values of maximum normal stresses occurring at the obtuse corner B are compared in Table 5.3. It can be seen that the results of PDLM and FDLM based models, however, are slightly smaller than those of ESLM.

Table 5.3 Maximum normal stresses for *p*-level = 10 (unit: MPa)

Types	$\sigma_{x'x'}$	$\sigma_{y'y'}$	$\tau_{x'y'}$
ESLM	7.39	41.27	20.49
PDLM	6.72	37.62	18.67
FDLM	6.16	40.62	19.50

In order to examine the efficacy of mixed element types along with transition element DLTM, the mixed models shown in Table 5.4 are used. Table 5.5 shows the resulting values of lateral displacements and two principal bending moments. The results obtained by all the models are found to be same. So, the use of mixed models along with DLTM did not make any difference, as far as the quality of the results is concerned. The results obtained from all modeling types are similar.

Table 5.4 Comparison of lateral displacements and principal bending moments

Model types	Element 1 and 2	Element 3 and 4	Element 5
Model A	ESLM	DLTM	FDLM
Model B	FDLM	DLTM	ESLM
Model C	ESLM	DLTM	PDLM
Model D	PDLM	DLTM	ESLM
Model E	FDLM	DLTM	PDLM
Model F	PDLM	DLTM	FDLM

Table 5.5 Lateral displacements and principal bending moments

Types	$\frac{250wEt^3}{3qa^4(1-\nu^2)}$	$\frac{100M_1}{qa^2}$	$\frac{100M_2}{qa^2}$
Model A	0.4049	1.893	1.071
Model B	0.4050	1.895	1.072
Model C	0.4050	1.894	1.072
Model D	0.4050	1.894	1.072
Model E	0.4048	1.893	1.071
Model F	0.4050	1.895	1.072

The maximum normal and shear stresses at corner B, for all the models considered, are shown in Table 5.6. Square brackets represent the element type used in Element 5 located

at point B. As in Table 5.3, the value of maximum stress is dependent upon the type of model used for Element 5. The advantage of using mixed models along with DLTM is obvious from these results.

Table 5.6 Maximum stresses in modeling types of using DLTM (unit: MPa)

Types	$\sigma_{x'x'}$	$\sigma_{y'y'}$	$\tau_{x'y'}$
Model A [FDLM]	6.16	40.65	19.51
Model B [ESLM]	7.39	41.27	20.49
Model C [PDLM]	6.72	37.62	18.67
Model D [ESLM]	7.39	41.29	20.50
Model E [FDLM]	6.16	40.67	19.52
Model F [PDLM]	6.72	37.62	18.68

5.2.2 Laminated Skew Plates

A simply supported laminated skew plates (0°/90°/0°) with total thickness h subjected to uniformly distributed loads is considered. In the absence of any analytical solution for skew laminated plates, the results based on present models (with FDLM-, PDLM-, and ESLM-based elements) are compared with the numerical results available in references (Sheikh and Chakrabarti, 2003; Kulkarni and Kapuria, 2007) using 2D finite element models based on first-order and third-order shear deformation. The example problems considered in the references are thin (a/h=100) and moderately thick (a/h=10) laminated plates with skew angle α = 30 º, 45 º, and 60º. Unidirectional fiber reinforced composite laminas of equal thickness with materials constants like those characterized in Eq. 4.2 are used. As shown in Fig. 5.23, the whole plate is discretized by a (3×3) mesh. The

deflection and the in-plane normal stresses at the center of the plate as obtained with proposed element models are compared in Table 5.7 along with the reference values. All results are normalized as below.

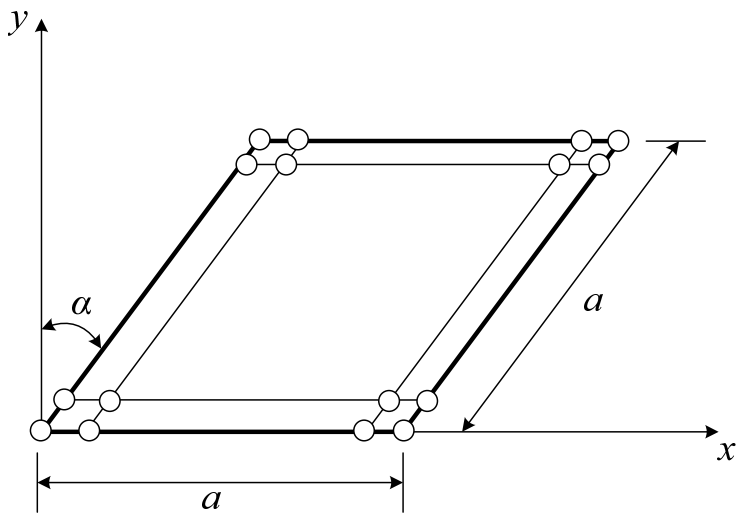

Fig. 5.23 Simply-supported composite skew plate with 3×3 mesh

$$\begin{aligned}
\overline{w} &= \left(\frac{h^3 E_2}{qa^4}\right) w\left(\frac{a(1+\sin\alpha)}{2}, \frac{b\cos\alpha}{2}, \frac{h}{2}\right) \\
\overline{\sigma}_{xx} &= \left(\frac{h^2}{qa^2}\right) \sigma_{xx}\left(\frac{a(1+\sin\alpha)}{2}, \frac{b\cos\alpha}{2}, h\right) \\
\overline{\sigma}_{yy} &= \left(\frac{h^2}{qa^2}\right) \sigma_{yy}\left(\frac{a(1+\sin\alpha)}{2}, \frac{b\cos\alpha}{2}, \frac{2h}{3}\right)
\end{aligned} \tag{5.1}$$

It is obvious from Table 5.7 that the results with all the proposed element models are similar to the reference values. The ESLM results are closer to the reference values; whereas, the PDLM and FDLM values are somewhat larger. Also, it is not surprising that the discrepancy between the results increase as the plate aspect ratio increases from the thin case (say, a/h=10) to the moderately thick case (say, a/h=100). To further explore the

effect of increasing plate thickness, plates with aspect ratio, *a*/*h,* of 10 and 5 were considered.

Table 5.7 Deflections and normal stresses for laminated skew plates

a/*h*	Skew angle (α)	Types	$\overline{w}$	$\overline{\sigma}_{xx}$	$\overline{\sigma}_{yy}$
10	30°	ESLM	0.8195	0.6226	0.3701
		PDLM	0.8838	0.6794	0.4031
		FDLM	0.9011	0.6970	0.4092
		Reference 1	0.8199	0.6098	0.3527
		Reference 2	0.8665	0.6775	0.3901
	45°	ESLM	0.5514	0.4209	0.3869
		PDLM	0.5794	0.4621	0.4067
		FDLM	0.5927	0.4752	0.4150
		Reference 1	0.5512	0.4143	0.3684
		Reference 2	0.5725	0.4583	0.3961
	60°	ESLM	0.2452	0.1822	0.3134
		PDLM	0.2517	0.2061	0.3165
		FDLM	0.2572	0.2145	0.3252
		Reference 1	0.2454	0.1808	0.3008
		Reference 2	0.2461	0.1976	0.3005
100	30°	ESLM	0.5459	0.6587	0.2792
		PDLM	0.5469	0.6592	0.2796
		FDLM	0.5471	0.6595	0.2797
		Reference 1	0.5447	0.6439	0.2626
		Reference 2	0.5516	0.6622	0.2816
	45°	ESLM	0.3629	0.4494	0.3174
		PDLM	0.3637	0.4500	0.3178
		FDLM	0.3642	0.4504	0.3182
		Reference 1	0.3628	0.4417	0.3006
		Reference 2	0.3679	0.4493	0.3211
	60°	ESLM	0.1463	0.2063	0.2688
		PDLM	0.1469	0.2069	0.2697
		FDLM	0.1471	0.2071	0.2700
		Reference 1	0.1453	0.2008	0.2570
		Reference 2	0.1467	0.1985	0.2693

Reference 1: FEM based on first-order shear deformation (Sheikh and chakrabarti, 2003)
Reference 2: FEM based on third-order shear deformation (Kulkarni and kapuria, 2007)

To normalize transverse shear stresses, the following expression is used.

$$\overline{\sigma}_{yz}^{1} = \left(\frac{h^2}{qa^2}\right)\sigma_{yz}(0, \frac{b\cos\alpha}{2}, \frac{h}{2}) \tag{5.2}$$

It can be seen in Table 5.8 that the results obtained by FDLM-based elements are reasonably close to those by layer-wise formulation based triangular elements (Ramesh et al., 2009). In addition, the results for ESLM, PDLM, and FDLM based models show increasing discrepancy as the thickness is increase and/or the skew angle is decreased.

Table 5.8 Deflections and stresses for thick (a/h=5) laminated skew plates

Skew angle (α)	Types	$\overline{w}$	$\overline{\sigma}_{xx}$	$\overline{\sigma}_{yz}$
30°	ESLM	1.5601	0.5442	0.3048
	PDLM	1.6870	0.7329	0.4699
	FDLM	1.7346	0.7929	0.4738
	Reference	1.7350	0.7932	0.4957
45°	ESLM	1.0587	0.3616	0.3313
	PDLM	1.0856	0.4921	0.4262
	FDLM	1.1217	0.5345	0.4339
	Reference	1.1248	0.5361	0.4389
60°	ESLM	0.5148	0.1569	0.2535
	PDLM	0.5015	0.2276	0.2732
	FDLM	0.5160	0.2541	0.2792
	Reference	0.5210	0.2576	0.2898

Reference: Finite Elements based on 3D elasticity theory (Ramesh et al., 2009)

Fig. 5.24 shows the variation of deflection at the center of plate with skew angle for different aspect ratios, a/h = 5, 10 and 100, representing thick, moderately thick and thin plates. In the case of thin plate, there is little difference in the results for ESLM, PDLM, and FDLM based models. Also, in the case moderately thick and thick plates, however, the discrepancy among these results appear when skew angles are small. However, it become smaller as the skew angle is increased.

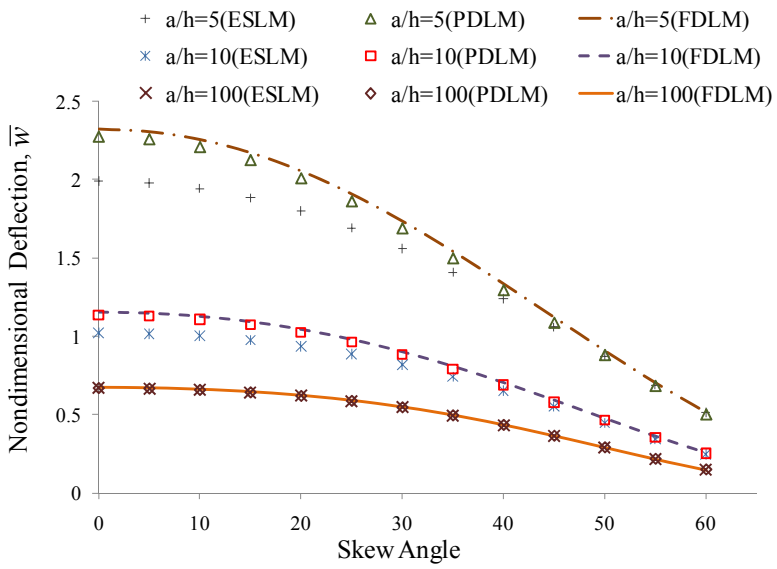

Fig. 5.24 Variation of central deflection with skew angle

Figs. 5.25 through 5.28 represent the influence of skew angle and plate aspect ratio (a/h) on the variation of transverse shear stresses ($\overline{\sigma}_{yz}$) through thickness of the plate at the location ($a/2$,0). It was found that only FDLM-based elements can show continuity of interlaminar transverse shear stresses. So, in order to study effect of degree of polynomial approximation in the thickness direction on transverse shear stress distribution, FDLM based model was considered and the p-level (P_z) was varied from 1 to 5, at the same time the in-plane polynomial degree, P_{xy}, was kept fixed at 10. From these plots, it is evident that distribution of transverse shear stress tend to converge at P_z=3. However, minor stress oscillations are observed in the vicinity of the loaded surface for large skew angle and thicker plate. As is evident from Fig. 5.29, with higher p-level these oscillations can be reduced significantly and with high enough refinement (P_z=8), it can be eliminated completely. In Fig. 5.30 is shown the transverse shear stress distributions for different in-plane p-levels (P_{xy}=3, 4,…, 10) when P_z=8, when a/h=5 and α=60°. It can be seen that for

$P_{xy} > 3$, the discrepancy between shear stress distributions is small and gets smaller as P_{xy} is increased, maintaining continuity in the shear stress distribution. It is evident from the above results that *p*-refinement in in-plane and out-of-plane directions is essential in order to accurately represent transverse shear stresses in laminated plates with large skew angle and thickness.

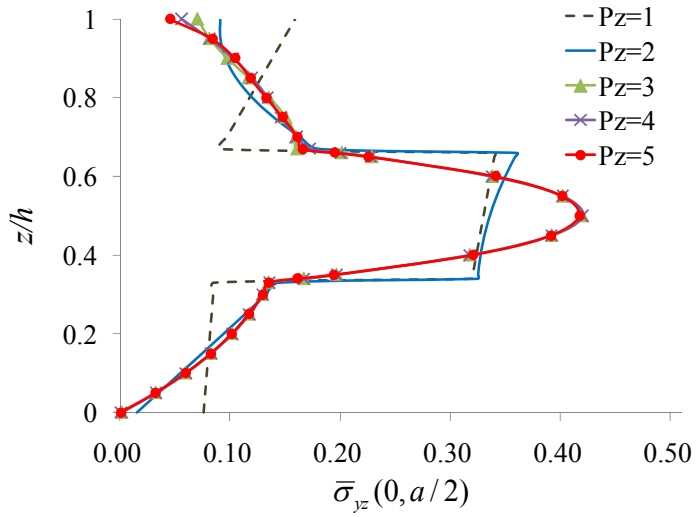

Fig. 5.25 Transverse shear stress distribution across thickness for a/h=10 and α = 15°

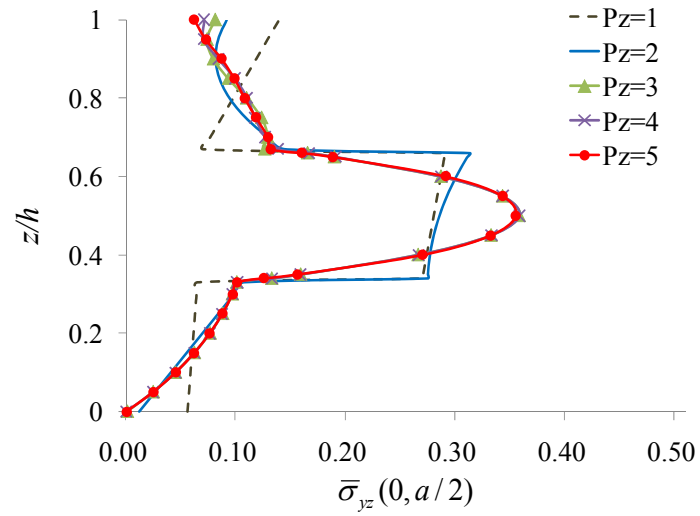

Fig. 5.26 Transverse shear stress distribution across thickness for a/h=10 and α = 60°

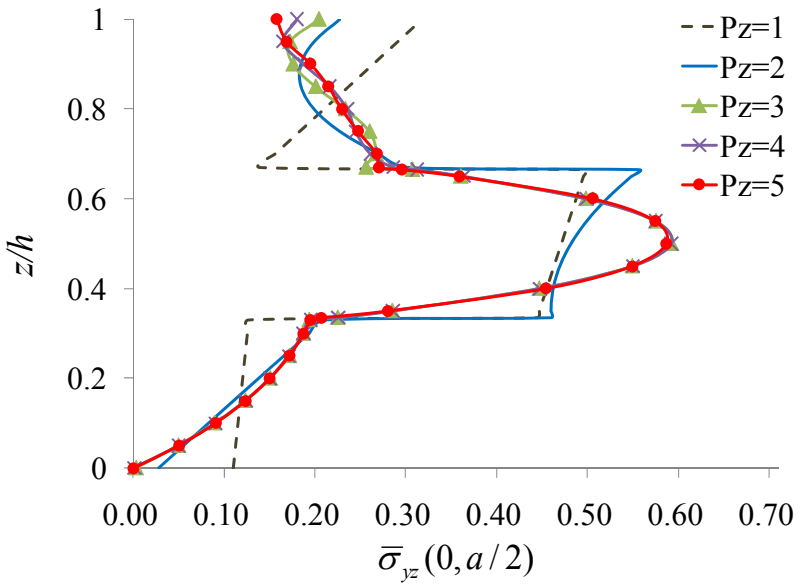

Fig. 5.27 Transverse shear stress distribution across thickness for a/h=5 and α = 15°

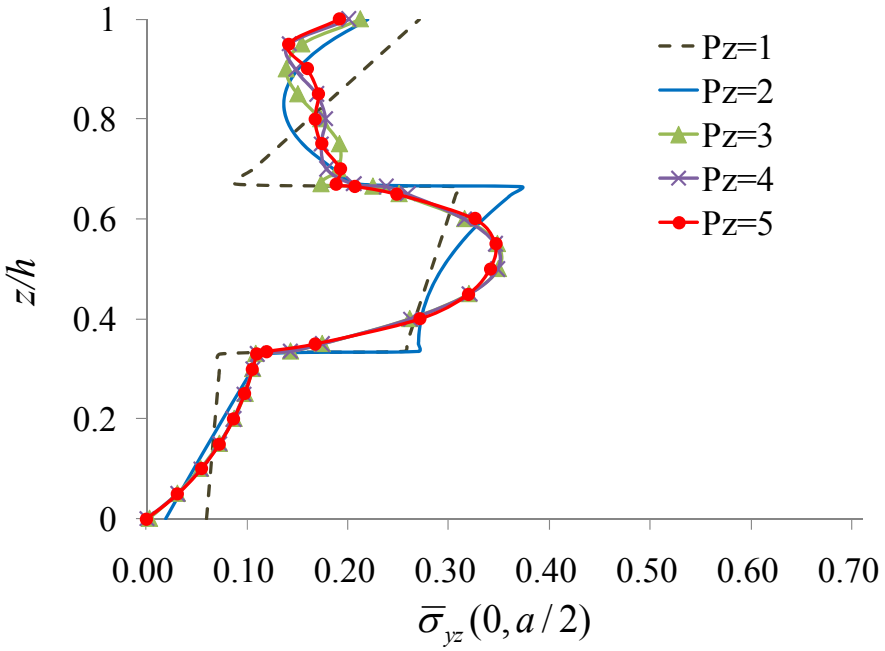

Fig. 5.28 Transverse shear stress distribution across thickness for a/h=5 and α = 60°

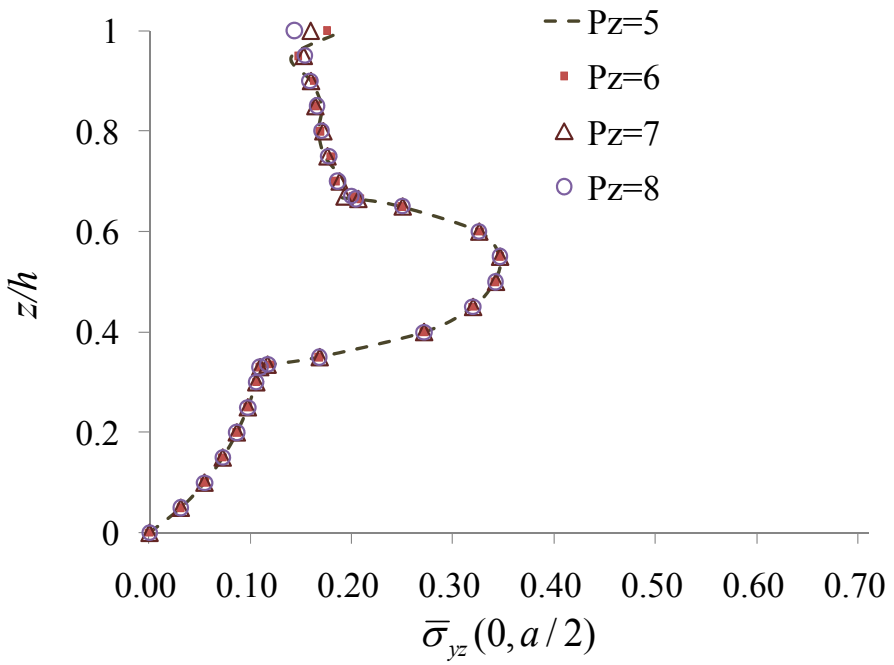

Fig. 5.29 Variation of transverse shear stress distribution with *p*-refinement in the thickness direction for a/h=5 and α = 60°

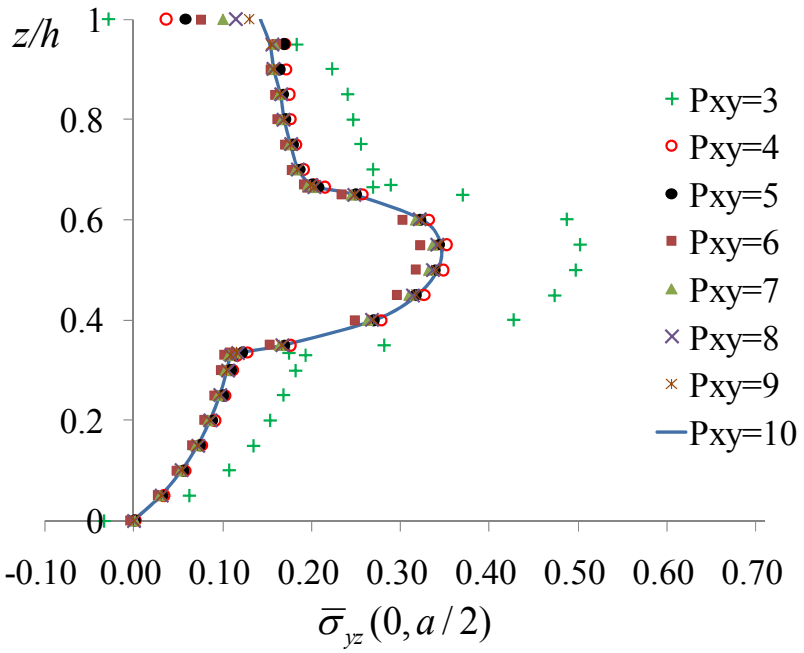

Fig. 5.30 Variation of normalized transverse shear stress distribution with *p*-refinement in the *xy*-plane for a/h=5 and α = 60°

For laminated plates with small skew angle but large thickness, 3D elements are needed for properly representing shear deformations. In 3D elements, however, much computational resources are required. So more efficient modeling needs to be employed. For computational efficiency, the mixed models like Models A, B, and C shown in Fig. 5.31 (a) ~ (c) are suggested. Model A consists of FDLM and DLTM-based elements. In Models B and C, PDLM-based elements and FDLM-based elements are considered in obtuse corner region, unlike Model A where ESLM based elements are used instead. The comparison of results for different mesh configurations comprising of both single and mixed element models are shown in Table 5.9. The discrepancies between the results by different models are found to be very small, except that the mixed models were found to be computationally more efficient.

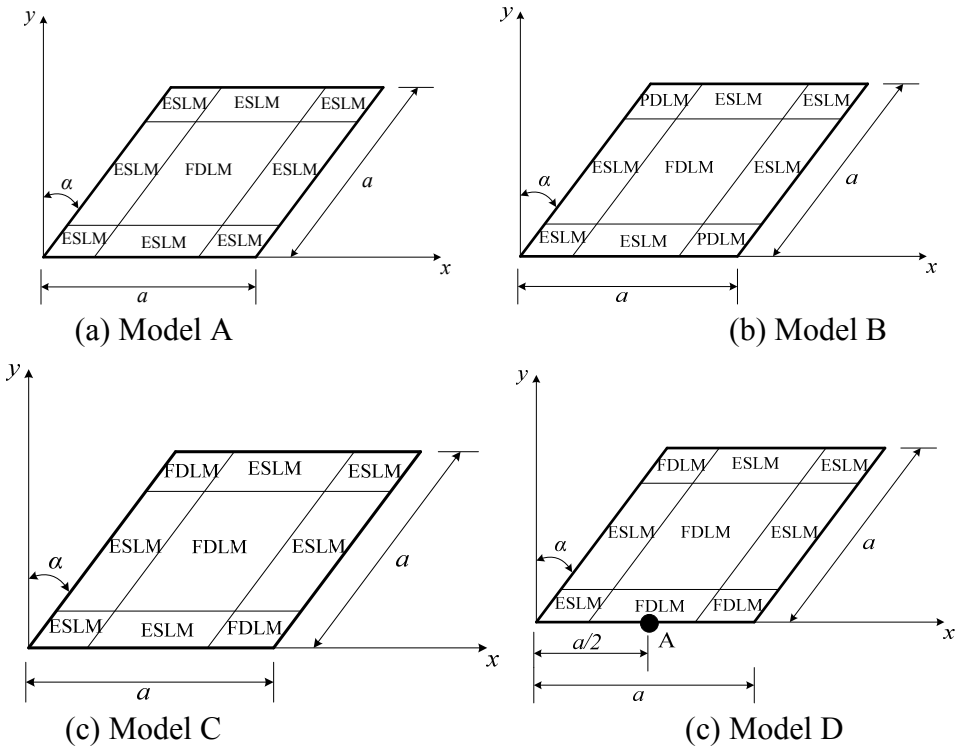

Fig. 5.31 Various models for efficient modeling

Table 5.9 Comparison of deflections and stresses for efficient modeling

a/h	Skew angle (α)	Types	NDF	$\overline{w}$	$\overline{\sigma}_{xx}$	$\overline{\sigma}_{yy}$
5	10°	FDLM	12080	2.2549	0.9954	0.6472
		PDLM	3740	2.2053	0.9230	0.6439
		ESLM	2052	1.9425	0.6772	0.5486
		Model A	3752	2.0213	0.9525	0.5800
		Model B	4200	2.1715	0.9853	0.6217
		Model C	6372	2.1836	1.0022	0.6261
	30°	FDLM	12080	1.7346	0.7929	0.6266
		PDLM	3740	1.6870	0.7329	0.6155
		ESLM	2052	1.5601	0.5442	0.5610
		Model A	3752	1.6024	0.7641	0.5842
		Model B	4200	1.6810	0.7856	0.6092
		Model C	6372	1.700	0.8021	0.6123
	50°	FDLM	12080	0.9089	0.4382	0.4921
		PDLM	3740	0.8800	0.4020	0.4674
		ESLM	2052	0.8726	0.2914	0.4745
		Model A	3752	0.8675	0.4165	0.4762
		Model B	4200	0.8857	0.4288	0.4823
		Model C	6372	0.9006	0.4407	0.4830
10	10°	FDLM	12080	1.1274	0.8515	0.3660
		PDLM	3740	1.1084	0.8303	0.3621
		ESLM	2052	1.0011	0.7566	0.3166
		Model A	3752	1.0753	0.8553	0.3465
		Model B	4200	1.1107	0.8574	0.3572
		Model C	6372	1.1132	0.8585	0.3606
	30°	FDLM	12080	0.9011	0.6970	0.4092
		PDLM	3740	0.8838	0.6794	0.4031
		ESLM	2052	0.8195	0.6226	0.3701
		Model A	3752	0.8711	0.6998	0.3964
		Model B	4200	0.8894	0.7013	0.4022
		Model C	6372	0.8949	0.7028	0.4056
	50°	FDLM	12080	0.4768	0.3873	0.3988
		PDLM	3740	0.4662	0.3758	0.3904
		ESLM	2052	0.4467	0.3400	0.3752
		Model A	3752	0.4656	0.3841	0.3906
		Model B	4200	0.4694	0.3864	0.3931
		Model C	6372	0.4735	0.3874	0.3964

Thickness-wise transverse shear stress distributions at point A (in Fig. 5.31 (d)) of the skew plates with a/h=5 and α=15° and 60° based on Model D in Fig. 5.31 (d) and a

model based on FDLM only (P_{xy} = 10 and P_z = 8) are shown in Figs. 5.32 and 5.33. Although the required number of degrees of freedom for Model D is 34% of the FDLM based model, accuracy of the results is almost same.

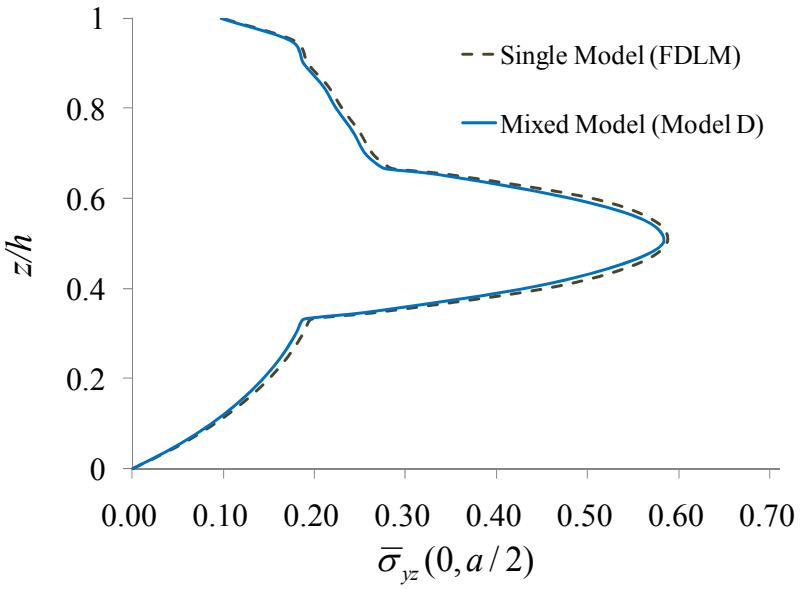

Fig. 5.32 Variation of normalized transverse shear stress for α = 15°

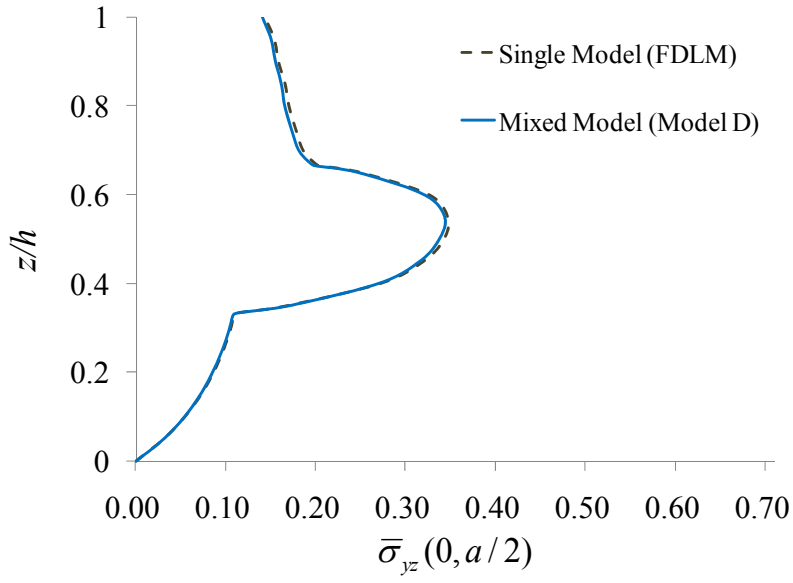

Fig. 5.33 Variation of normalized transverse shear stress for α = 60°

5.3 Free Edge Stresses in Laminates

In this section, free edge stresses are considered as examples of laminate systems with irregularities. At free edges of laminates, a singular point exists at the intersection of the bi-material ply interface and the free surface, where the numerically computed stresses tend to be large, decaying rapidly to the stress plateau away from the free edge. Such effect is often termed as 'boundary layer effect' or, more commonly, as 'free edge effect'. Such an effect is the result of the stress transfer between laminate through the action of interlaminar shearing stresses caused by the presence of discontinuities in material properties between layers, particularly the mismatch in Poisson's ratios and shear coupling terms. Thus the edge effects in laminated composite may result in edge delamination and transverse cracking even when the applied loading is much lower than the failure strength predicted. The stress distributions near the free edges are of 3D nature even though the laminates are only subjected to in-plane loading and it is difficult to conceive that conventional 2D elements alone can predict all the stress components of interest.

5.3.1 Laminates in Extension

At first, free edge stress problems with cross-ply or angle-ply lamination with four layers under uniform constant axial strain ε_o are considered. FDLM-based elements capturing 3D stress states are used to investigate the free edge effect. The laminated plate is shown in Fig. 5.34. Each of the four material layers is of equal thickness (h) and the laminate length and width are a=80h and b=8h, respectively. The overall thickness is 4h. The xy-plane is taken to be the middle surface of the laminate with the origin of the

coordinate system located at the centroid of the 3D laminate. Since the geometry and loading are symmetric about the *xy*-plane, only upper half of the laminate is modeled. Thus the computational domain is defined by

$$-a \le x \le a;\ -b \le y \le b;\ 0 \le z \le 2h \tag{5.3}$$

Also, displacement boundary conditions for the laminate are

$$u(a, y, z) = u_0;\ \ u(-a, y, z) = v(-a,0,0) = w(x, y,0) = 0 \tag{5.4}$$

Fig. 5.35 shows the modeling configuration with 3×3 mesh composed of FDLM-based elements. Due to symmetry in the layers, only two layers are required to be considered across the thickness. The material properties of the layers are taken to be those of a high-modulus graphite/epoxy lamina idealized as homogeneous, orthotropic material with the following properties

$$\begin{aligned} &E_1 = 137.9\,\text{GPa};\ E_2 = E_3 = 14.48\,\text{GPa};\\ &G_{12} = G_{13} = G_{23} = 5.861\,\text{GPa};\ \nu_{12} = \nu_{13} = \nu_{23} = 0.21 \end{aligned} \tag{5.5}$$

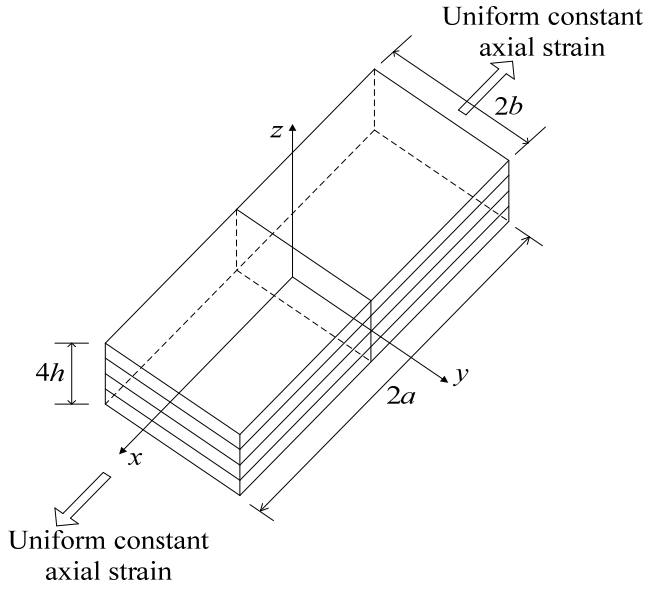

Fig. 5.34 Coordinates and geometry of composite laminate in extension

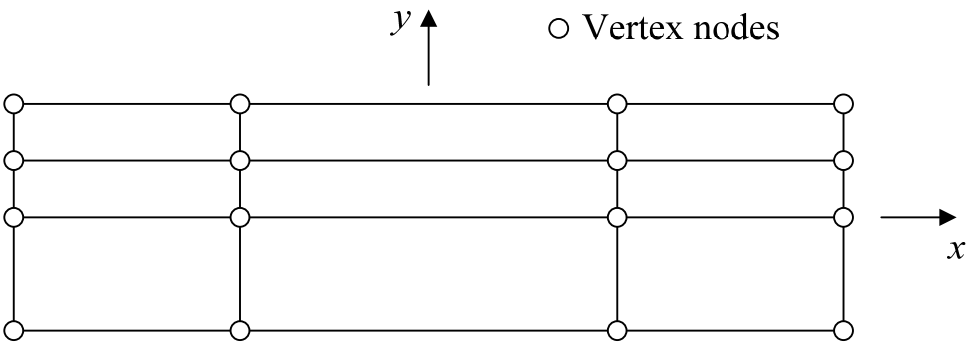

Fig. 5.35 Mesh configuration on *xy*-plane for free edge problems

Convergence of the transverse normal stresses at free edge ($y = b$) are investigate in Tables 5.10 and 5.11 for $(0/90)_s$ and $(90/0)_s$ problems, respectively. The results are compared with the values of reference (Tahani and Nosier, 2003b) which used *h*-refinement for in-plane and out-of-plane behavior. It is seen that difference between current values with higher order shape functions and reference values with the considerable number of numerical layers is within 1%. It is also seen that the numerical value of σ_z at 0°/90° interfaces is noticeably dependent on the *p*-refinement, not only P_{xy} for in-plane behavior but also P_z for out-of-plane. Moreover, it can be stated that the transverse normal stress component grows monotonically as the order of shape functions is increased, which suggests that a stress singularity may exist at two materials interface with different fiber angles (0°/90°). In contrast, the value of σ_z at the middle plane ($z=0$) is seen to converge to a constant value with increasing *p*-level. This is true because there can be no stress singularity at the interface of two layers with same fiber orientations. It is alos noted that the results are practically identical for $P_{xy} \geq 6$ and $P_z \geq 4$. In addition, both σ_{xy} and σ_{xz} are approximately close to zero as expected due to the symmetric nature of the cross-ply laminates.

Table 5.10 Convergence of interlaminar normal stresses for a $(0/90)_s$ laminated plate

Location		P_z							
		1	2	3	4	5	6	7	8
$z = 0$	$P_{xy} = 5$	1.543	1.638	1.750	1.865	1.865	1.865	2.001	2.001
	$P_{xy} = 6$	1.890	1.912	1.965	1.990	2.001	2.001	2.002	2.003
	$P_{xy} = 7$	1.890	1.963	1.980	2.010	2.012	2.012	2.012	2.012
	$P_{xy} = 8$	1.890	1.963	2.012	2.012	2.013	2.013	2.013	2.013
	$P_{xy} = 9$	1.890	1.967	2.012	2.015	2.013	2.013	2.013	2.013
	$P_{xy} = 10$	1.890	1.968	2.012	2.015	2.013	2.013	2.013	2.013
	Reference	1.937 <4>	2.008 <8>	2.000 <12>	2.000 <16>	2.001 <20>	2.002 <24	2.002 <24>	2.002 <24>
$z = h$	$P_{xy} = 5$	1.754	1.960	2.113	2.259	2.359	2.458	2.557	2.558
	$P_{xy} = 6$	1.800	2.008	2.114	2.271	2.344	2.449	2.550	2.559
	$P_{xy} = 7$	1.892	2.017	2.117	2.275	2.350	2.465	2.558	2.560
	$P_{xy} = 8$	1.892	2.024	2.120	2.280	2.378	2.495	2.560	2.561
	$P_{xy} = 9$	1.892	2.028	2.126	2.285	2.416	2.512	2.562	2.566
	$P_{xy} = 10$	1.892	2.030	2.128	2.286	2.426	2.586	2.563	2.569
	Reference	1.462 <4>	1.790 <8>	2.017 <12>	2.180 <16>	2.307 <20>	2.411 <24	2.568 <28>	2.579 <32>

< >: The number of modeling layers

Table 5.11 Convergence of interlaminar normal stresses for a $(90/0)_s$ laminated plate

Location		P_z							
		1	2	3	4	5	6	7	8
$z = 0$	$P_{xy} = 5$	-2.112	-2.223	-2.308	-2.572	-2.527	-2.572	-2.572	-2.572
	$P_{xy} = 6$	-2.114	-2.321	-2.362	-2.573	-2.574	-2.575	-2.573	-2.575
	$P_{xy} = 7$	-2.114	-2.328	-2.371	-2.573	-2.574	-2.575	-2.575	-2.576
	$P_{xy} = 8$	-2.116	-2.331	-2.389	-2.573	-2.574	-2.575	-2.575	-2.577
	$P_{xy} = 9$	-2.119	-2.334	-2.447	-2.574	-2.575	-2.576	-2.576	-2.578
	$P_{xy} = 10$	-2.119	-2.335	-2.449	-2.576	-2.576	-2.577	-2.578	-2.578
	Reference	-3.288 <4>	-2.683 <8>	-2.588 <12>	-2.576 <16>	-2.574 <20>	-2.574 <24	-2.574 <24>	-2.574 <24>
$z = h$	$P_{xy} = 5$	-1.387	-0.904	-0.627	0.132	0.412	0.660	0.745	0.796
	$P_{xy} = 6$	-1.322	-0.887	-0.742	0.230	0.440	0.678	0.751	0.799
	$P_{xy} = 7$	-1.318	-0.836	-0.697	0.232	0.448	0.680	0.758	0.802
	$P_{xy} = 8$	-1.314	-0.795	-0.587	0.334	0.452	0.682	0.762	0.807
	$P_{xy} = 9$	-1.303	-0.775	-0.456	0.238	0.456	0.687	0.768	0.808
	$P_{xy} = 10$	-1.258	-0.768	-0.316	0.240	0.458	0.690	0.774	0.809
	Reference	-0.242 <4>	0.170 <8>	0.377 <12>	0.523 <16>	0.637 <20>	0.730 <24	0.809 <28>	0.880 <32>

< >: The number of modeling layers

Fig. 5.36 shows distribution for σ_{yz} vs. y at $z = h$ at the mid cross-section for $(0°/90°)_s$ and (90°/0°) laminates. It is seen that the peak values of transverse shear stresses occur in the close vicinity of the free edge and then rather suddenly drop to zero at the free edge(y=b). This behavior is suspected due to the presence of interfacial singularity at the free edge. Some authors (Tahani and Nosier, 2003b) argued that stress singularity may not exist at all because of nonlinearity in the matrix material and the fact that real laminates do not exhibit distinct interfaces between layers as assumed in a macroscopic analysis. However, it is still believed by many researchers (Pipes and Pagano, 1970; Wang and Crossman, 1977; Wang and Choi, 1982a, 1982b; Nguyen and Caron, 2006) that mathematically there is a stress singularity at the free edge at the interface of different materials. It is to be remembered that no exact elasticity solution to the free edge problems is yet known to exist. Thus the results of present analysis are compared with the numerical solutions by Wang and Crossman (1977) and excellent agreement is noted between present solutions and reference values.

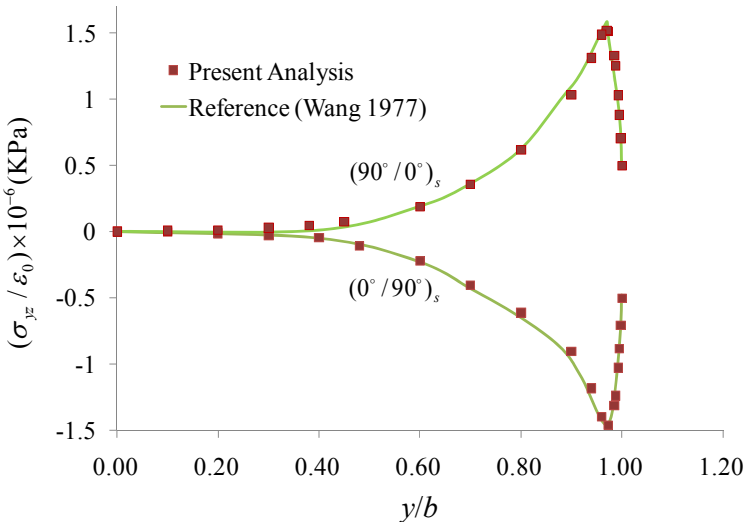

Fig. 5.36 Distribution of interlaminar shear stresses σ_{yz} at the 0°/90° interfaces

Next, the prediction of free edge stresses for (45°/-45°) angle-ply laminate is considered. The finite element mesh, boundary conditions, and material properties are identical with those of the cross-ply laminate considered last. In order to verify the present analysis for in-plane behavior, in Fig. 5.37 is shown the axial displacement distribution across the width of the top surface. Good agreement is noted between the present analysis and the references (Wang and Crossman, 1977; Pagano, 1978a).

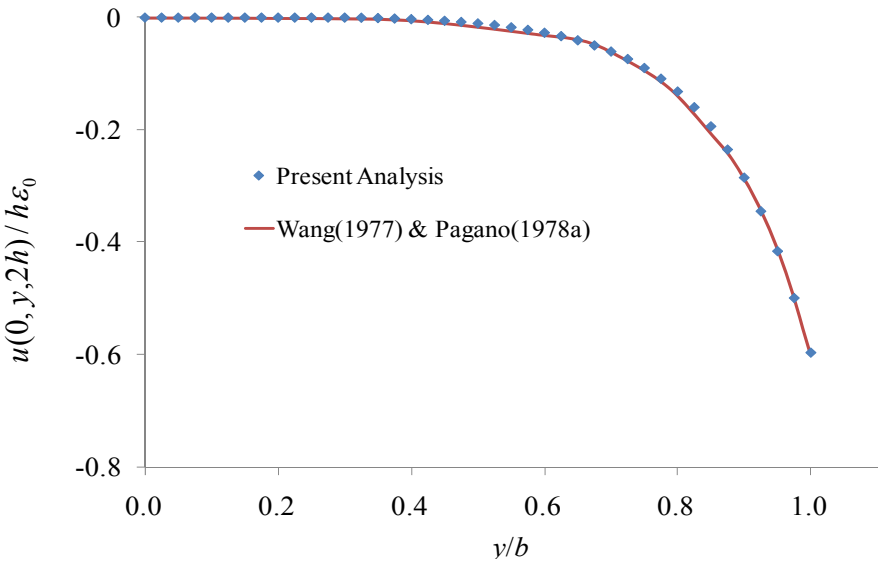

Fig. 5.37 Axial displacement across top surface

Figs. 5.38 and 5.39 show the distribution of displacement, σ_{xx} and τ_{xy} along the width of the laminate at the center of the top layer. The results of present analysis and those given in the references are found to be nearly coincident for all values of y. Fig. 5.40 shows the distribution of τ_{xz} along -45°/45° interface. Contrary to behavior noted in the case of in-plane stresses (σ_{xx} and τ_{xy}), absolute values of τ_{xz} suddenly increase near edge of laminate, supposedly, due to free-edge effect. Moreover it is seen that the results

of present analysis for τ_{xz} is closer to those of Pagano (1978a) than those of Wang and Crossman (1977).

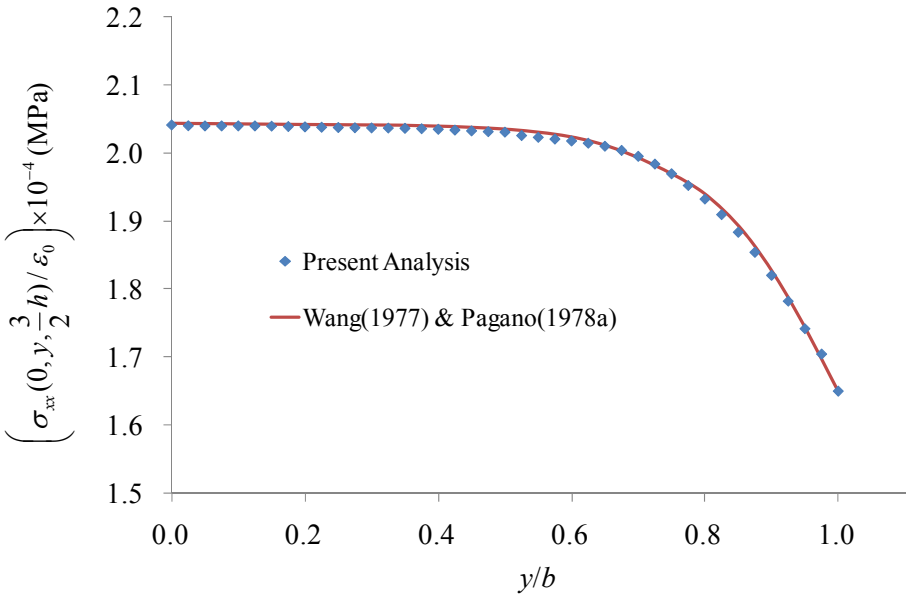

Fig. 5.38 Distribution of σ_{xx} along center of top layer

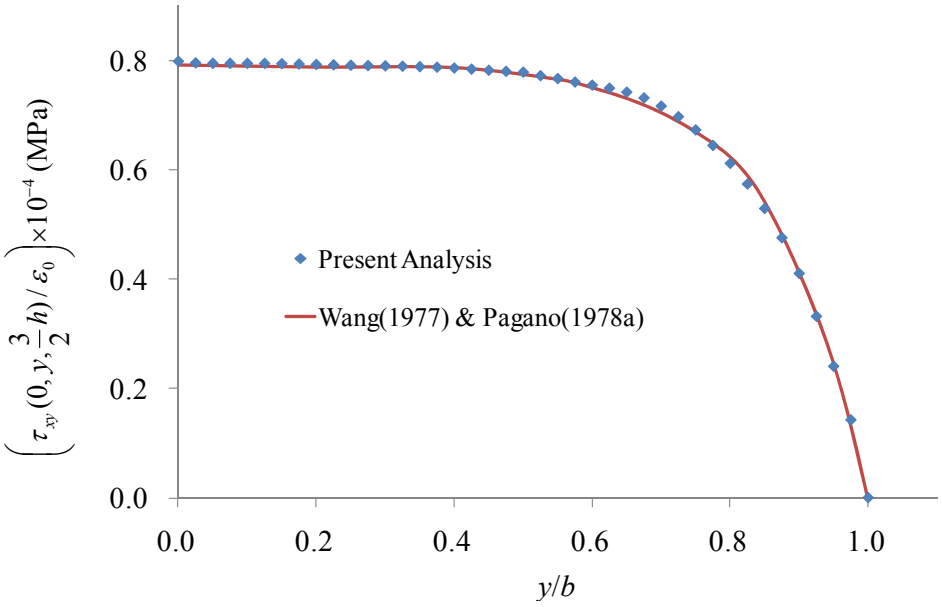

Fig. 5.39 Distribution of τ_{xy} along center of top layer

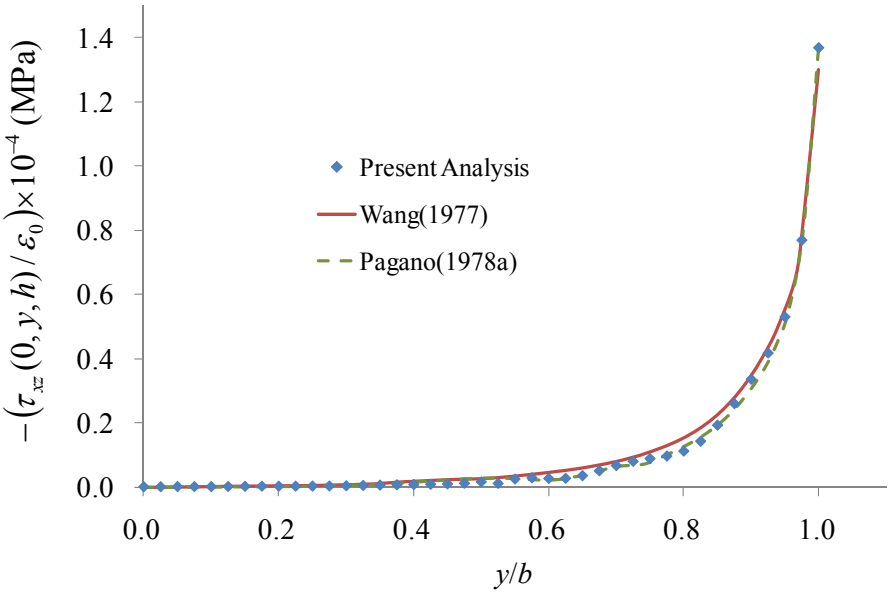

Fig. 5.40 Distribution of τ_{xz} along -45°/45° interfaces

Figs. 5.41 and 5.42 show that the distributions of transverse normal stresses near the free edge (x = -0.115a and y = 0.998b) computed by 1×1 and 2×2 mesh of FDLM-based elements, respectively, and compared with the results of h-FEM (15×5 mesh) (Reddy, 2004b). Here, the fourth-order shape functions for out-of-plane displacement approximation were kept unchanged. It can be seen that considerable transverse normal stress develops near the interfaces with different fiber angles. It is also noticed that, in both cases, the computed results become closer to those of h-FEM with increasing p-level. Moreover, as one will expect, the 2×2 mesh shows more rapid convergence and better qualitative agreement with h-FEM.

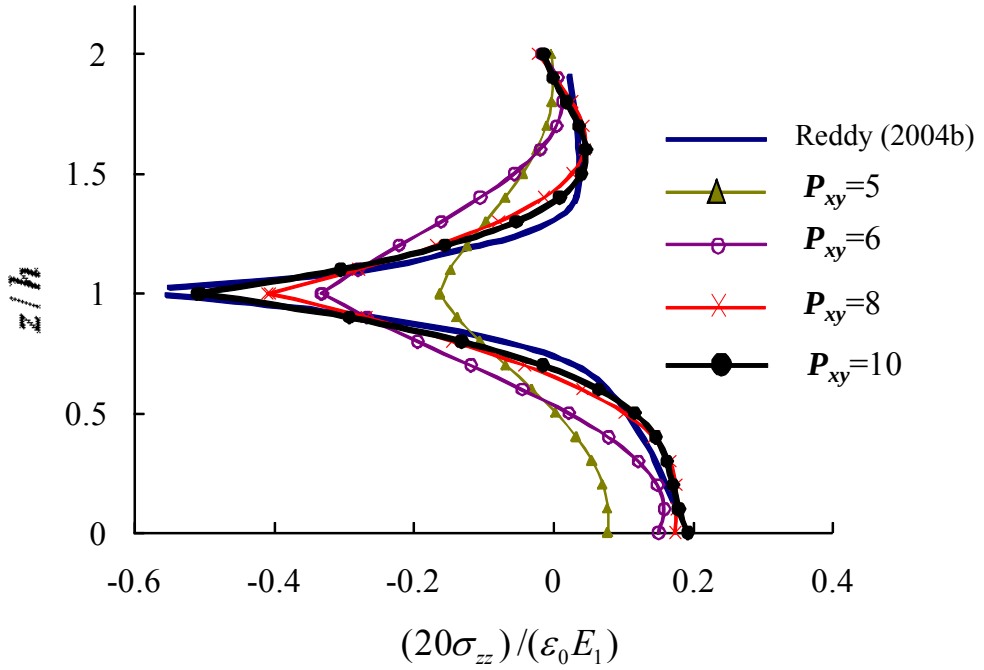

Fig. 5.41 Transverse normal stresses across the thickness (1×1 mesh)

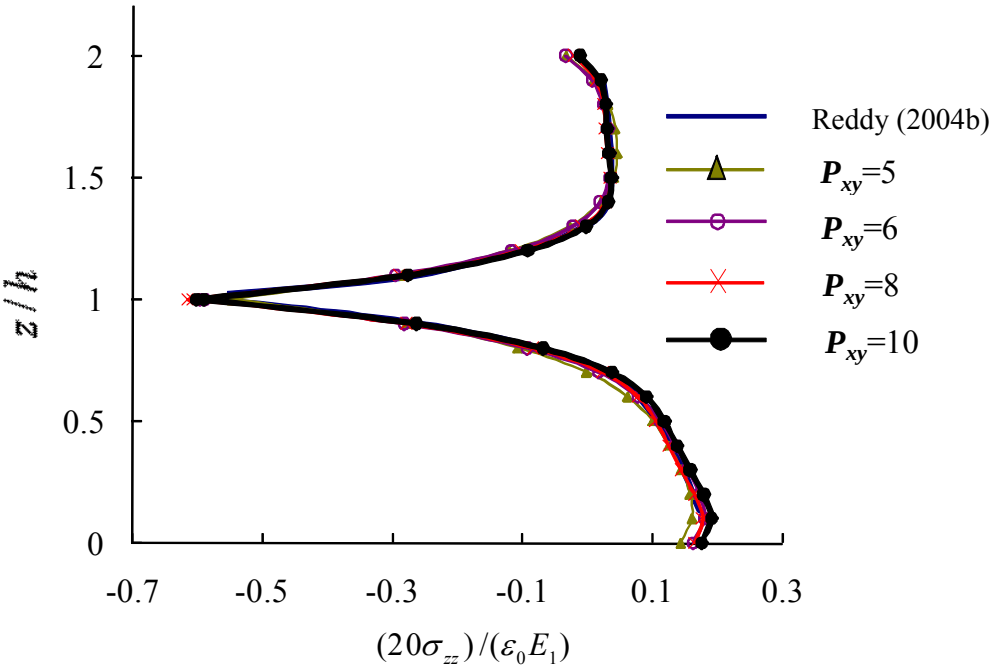

Fig. 5.42 Transverse normal stresses across the thickness (2×2 mesh)

To achieve computational efficiency, mixed-element models along with FDTM-based single models were also considered. Fig. 5.43 shows 2D in-plane discretization (3×3 mesh) to assess the performance of the proposed DLTM model.

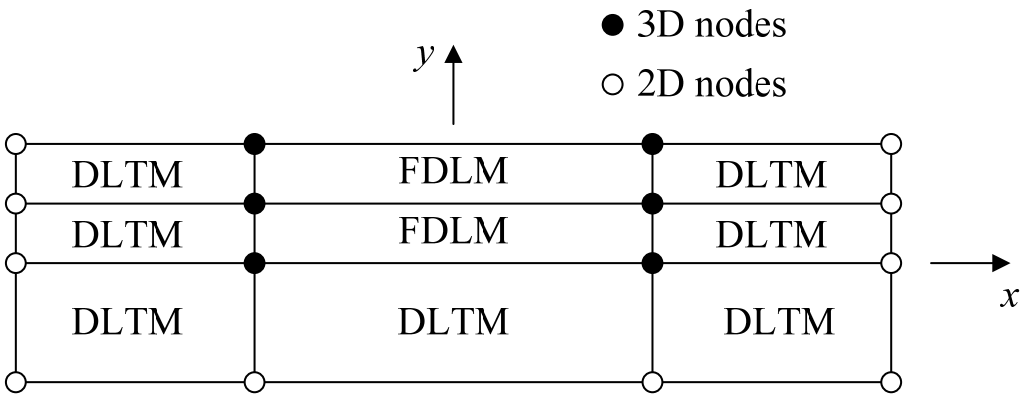

Fig. 5.43 2D mesh of finite elements using simultaneously 2D & 3D models

The results (namely, axial displacements u, normal stresses σ_{xx}, and shear stresses τ_{xy}) for in-plane behavior based on DLTM model were found to be identical with the results previously shown in Figs. 5.37 through 5.39. Also, the transverse normal and shear stresses from the mixed model are presented and compared with the results from single model composed of only FDLM-based elements and the *h*-FEM based ones from reference (Reddy, 2004b). These results are shown in Figs. 5.44 and 5.45. No difference is detected between the mixed model and single model based results. It may also that the required NDF of *p*-FEM based single model is invariably less than that with *h*-FEM model. Moreover, the required NDF is further reduced when mixed model is used.

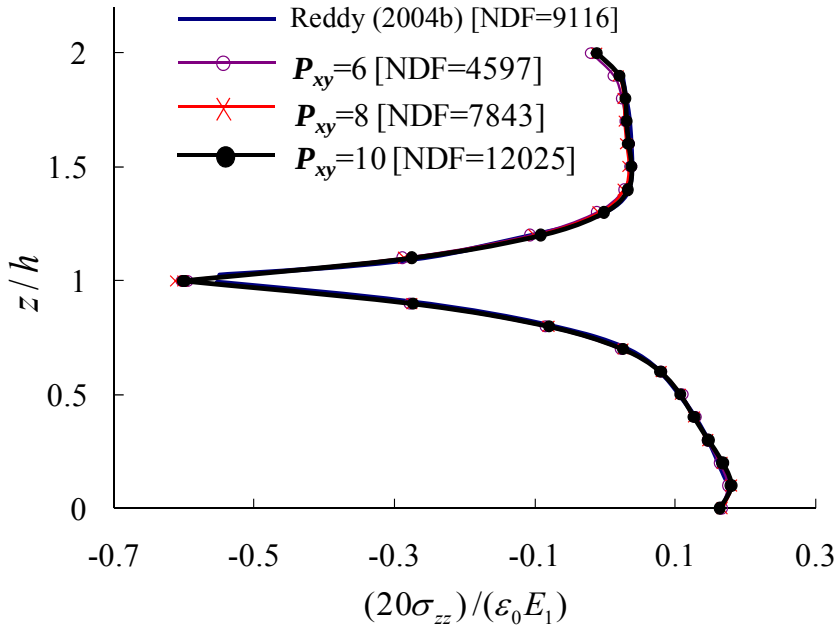

(a) Single Model (only FDLM-based elements)

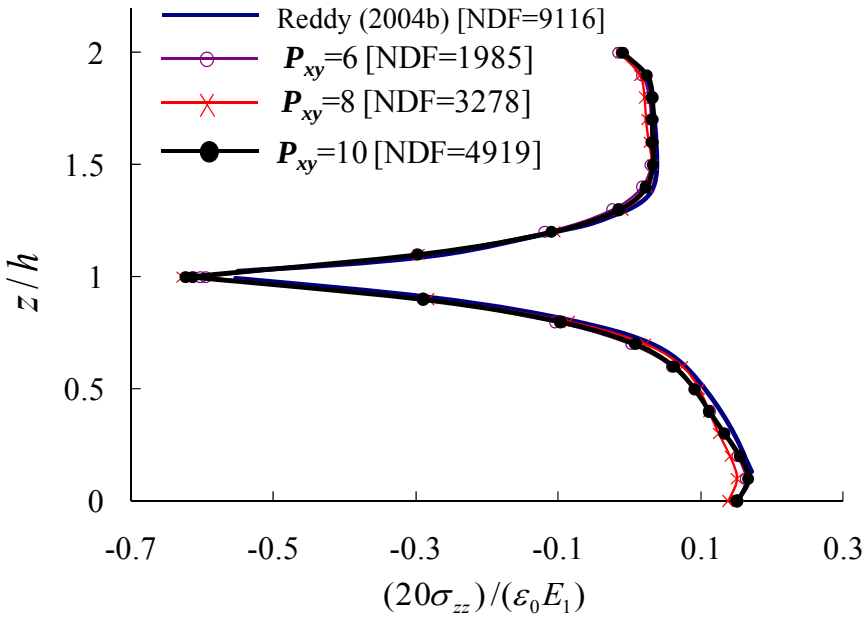

(b) Multiple Model using FDLM-based and DLTM-based elements

Fig. 5.44 Transverse normal stresses across the thickness (3×3 mesh)

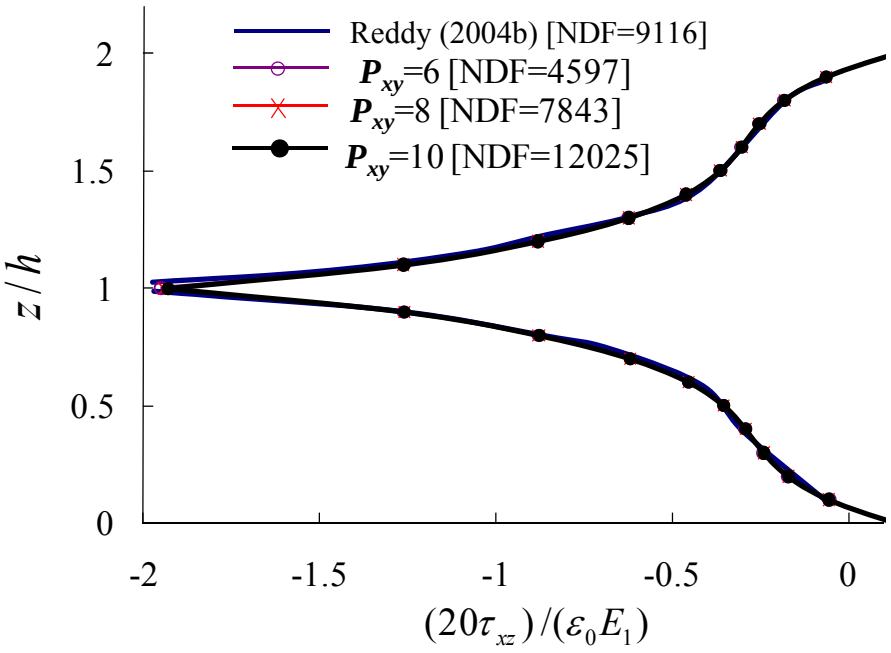

(a) Single Model (only FDLM-based elements)

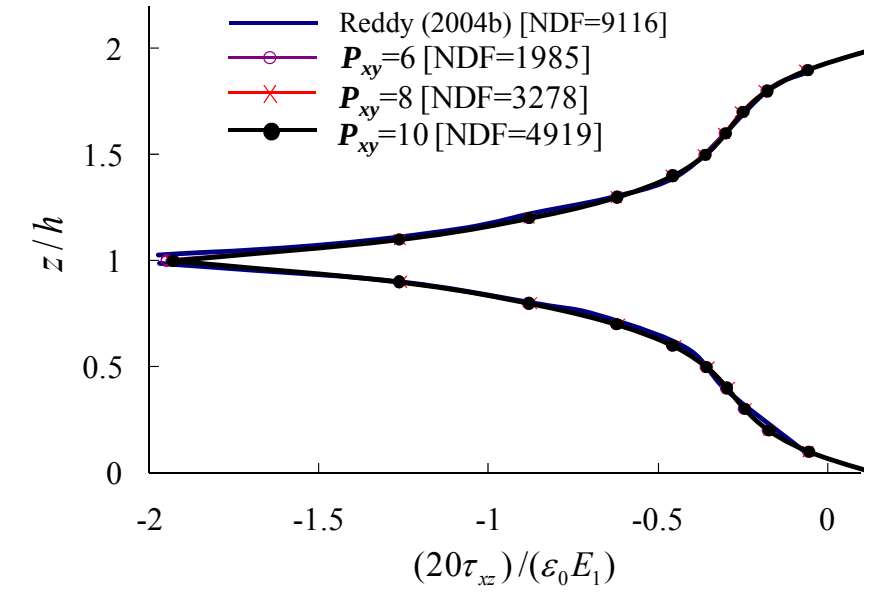

(b) Mixed Model using FDLM-based and DLTM-based elements

Fig. 5.45 Transverse shear stresses across the thickness (3×3 mesh)

5.3.2 Laminates Undergoing Flexure

To demonstrate the effectiveness of developed finite elements for determining free-edge stresses in laminates under flexure, a simply supported (45°/-45°) laminated plate subjected to uniform transverse load is considered. The physical dimensions and material properties of the considered laminate are the same as in the previous axial extension example defined in Fig. 5.34 and Eq. 5.3, respectively. The uniform transverse load q_0 is applied to the upper surface of the laminate and acts in the negative z direction. Unlike symmetric conditions about mid-surface in the previous axial extension example, there are no planes of symmetry in this problem. Thus the computational domain covers the entire laminate, such that

$$-a \le x \le a;\ -b \le y \le b;\ -2h \le z \le 2h \tag{5.6}$$

The displacement boundary conditions are given by Eq. 5.7.

$$\begin{aligned} &u(0,-b,-2h) = 0 \\ &v(-a,y,z) = v(a,y,z) = 0 \\ &w(-a,y,-2h) = w(a,y,-2h) = 0 \end{aligned} \tag{5.7}$$

In h-FEM model, it is necessary to use highly refined mesh near free edges of interest, both in-plane and out-of-plane or thickness directions. The analysis uses single model comprising of FDLM with a 4×3 mesh in the xy-plane, as shown in Fig. 5.46. As in previous examples, the number of modeling layers is taken to be the same as the number of physical layers. But with h-FEM, significantly more number of discretized layers than the number of physical layers is needed. In the present analysis, however, only four discretized layers are used. As discussed in the following, the results of present analysis are compared with those from reference (Reddy, 2004b) based on h-FEM.

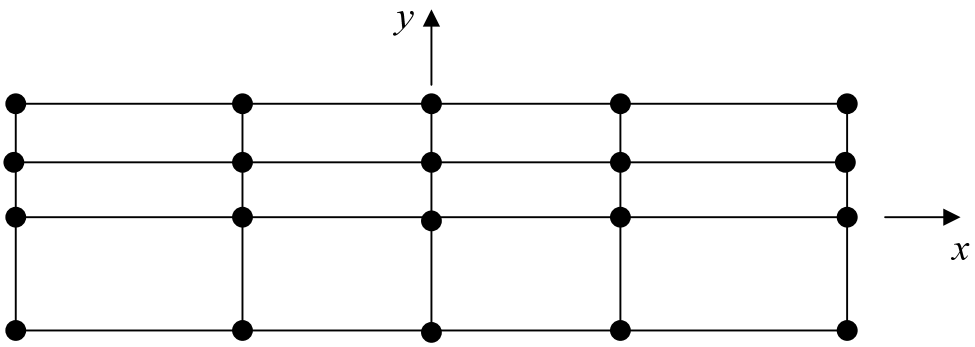

Fig. 5.46 2D mesh for free edge problems under bending

To investigate the convergence of transverse stresses, in Fig. 5.47 is shown the distribution of transverse normal stresses across the thickness at the free edge (x=0, y=b), for increasing values of in-plane p-levels (P_{xy}) while the out-of-plane p-level, P_z, is kept unchanged at 4. In the two middle layers, both with -45° fiber angle, the responses obtained by using different P_{xy} are almost the same, whereas, in top and bottom layers, the nature of distribution and magnitude of transverse normal stresses across the thickness is dependent on P_{xy}. It is, also, evident from the results that the transverse normal stresses in the top and bottom layers reach a converged value with increasing $P_{xy,}$ except at their interfaces with the inner layers where the values tend to increase indefinitely with P_{xy}. Based on the results obtained, all stress values converged with $P_{\mathrm{xy}} \geq$ 7, except at layer interfaces with different fiber angles. Fig. 5.48 shows distribution of transverse normal stress across the thickness with variation of p-level for out-of-plane behavior (P_z), when the p-level for in-plane behavior (P_{xy}) is kept fixed at 4. It may be noted from the results that there little difference in transverse normal stress profile when $P_{\mathrm{z}} \geq 4$. The results in Figs. 5.47 and 5.48 are based on P_{xy}=8 and P_z=4. Figs. 5.49 and 5.50 show distributions of transverse normal stresses and transverse shear stresses across the thickness. In the two figures, the results of present analysis are compared with those

of reference. It can be noted from the results that the responses by the present analysis and reference are almost same, although there is small quantitative difference in the two responses. Distribution of transverse normal stresses and transverse share stresses, at upper interfaces, across the width of the plate, for different fiber angles are shown in Figs. 5.51 and 5.52, respectively. It is seen that the results of present analysis agree well with the reference values. It may be noted that the transverse normal stress is almost zero over the segment $0 \le y/b < 0.7$, and then it rises suddenly near the free edge of the laminate. Moreover, it can be seen that considerably high transverse shear stresses also occur over the same region, near the free edge. Thus, the results of Figs. 5.49 through 5.52, confirm the existence of singular stress field at the free edge of laminated plate under flexure.

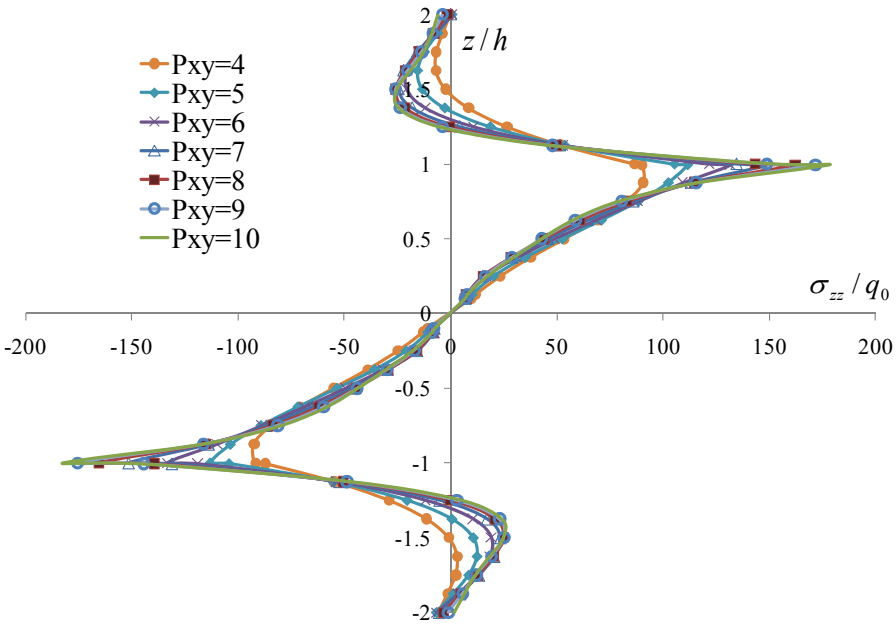

Fig. 5.47 Convergence of transverse normal stresses with increase of p-levels P_{xy}

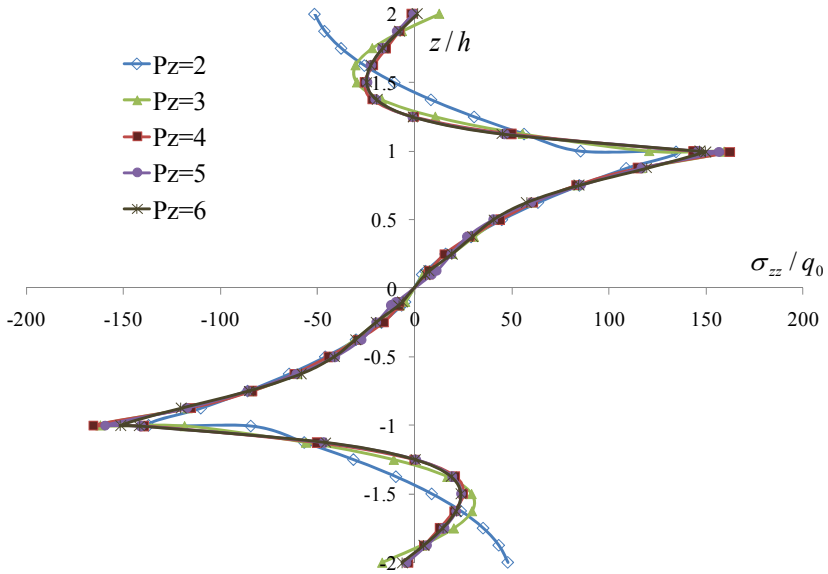

Fig. 5.48 Convergence of transverse normal stresses with increase of p-levels P_z

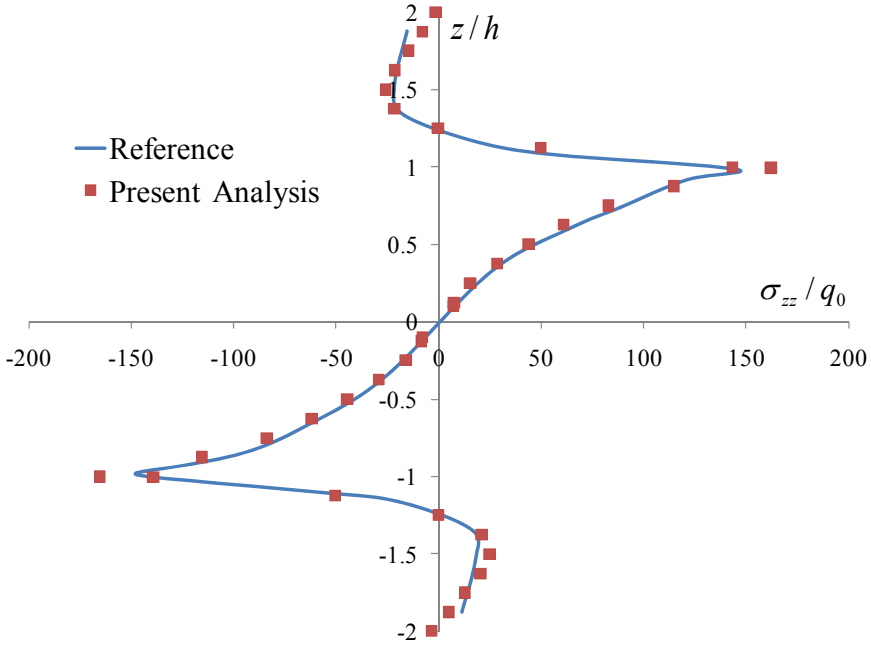

Fig. 5.49 Distribution of transverse normal stresses (σ_{zz}) across the thickness

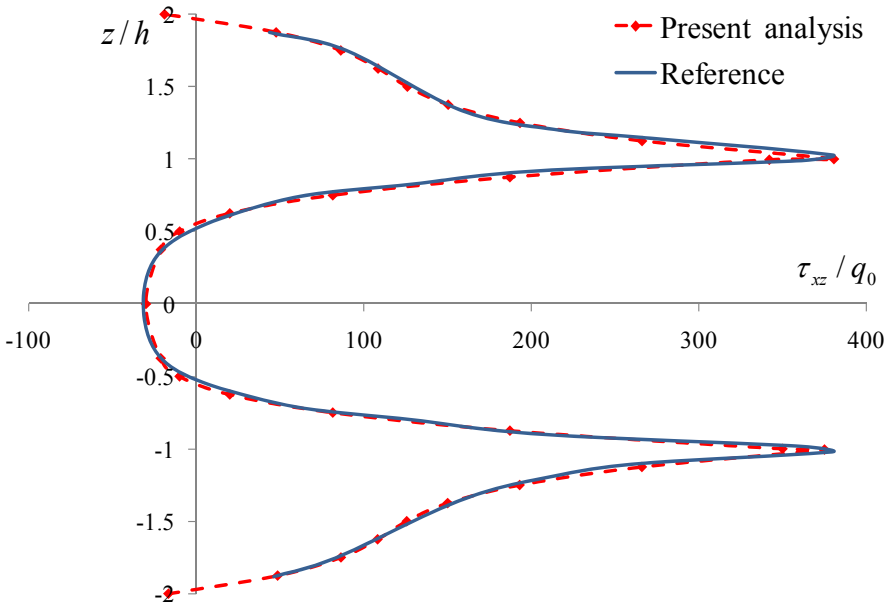

Fig. 5.50 Distribution of transverse shear stresses (τ_{xz}) across the thickness

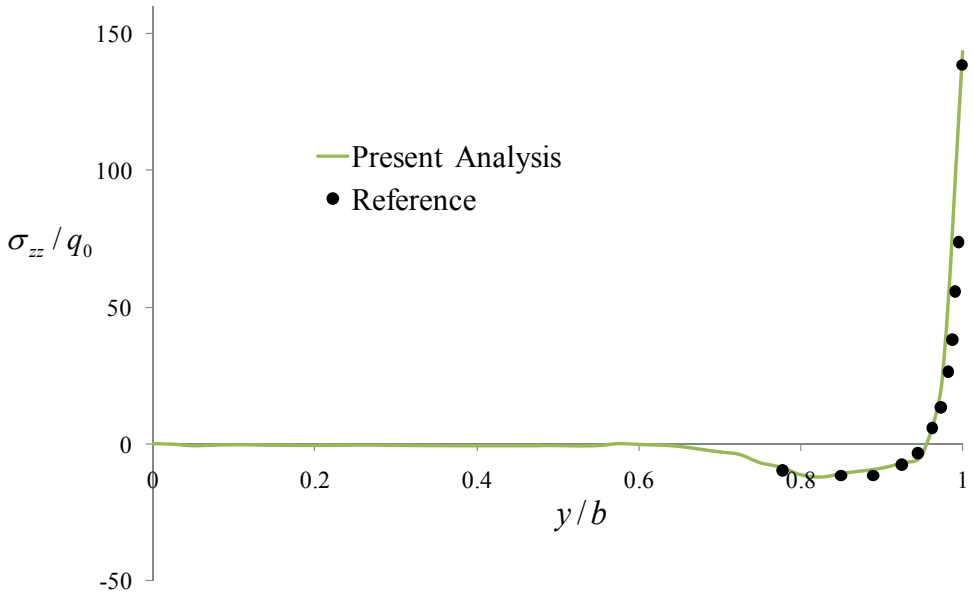

Fig. 5.51 Distribution of transverse normal stresses (σ_{zz}) across the width

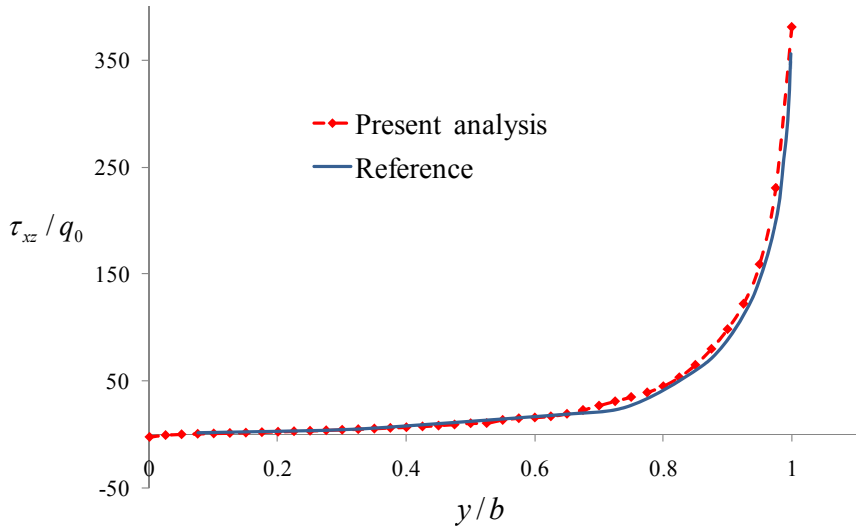

Fig. 5.52 Distribution of transverse shear stresses (τ_{xz}) across the width

As in the case of free edge problem with in-plane stress, the mixed model analysis was undertaken in the case of flexure problem as well. The 4×3 mixed model mesh is shown in Fig. 5.53. All other conditions of present mixed model analysis are identical to those of single model analysis using only FDLM-based elements. Also, the *p*-levels are taken as P_{xy}=8 and P_z=4. NDF of single model using only FDLM-based elements is 20,366; whereas, NDF for mixed model analysis is 9,013. Thus the reduction in computational resources with mixed model is almost 50% of that for single model.

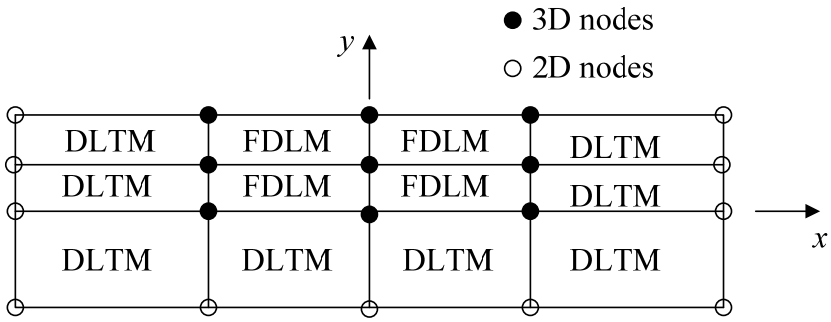

Fig. 5.53 Modeling configuration on *xy*-plane using simultaneously 2D & 3D models

The transverse normal stress distribution obtained with the single model and mixed model are shown in Figs. 5.54 through 5.57. It is noted that the mixed model analysis captures the local 3D stress field quite accurately. However, there exists a small discrepancy between the single and mixed model results. In addition, it is noted from Fig. 5.57 that small stress oscillations occur in mixed model results in transverse normal stress values over the segment where the single model values are close to zero.

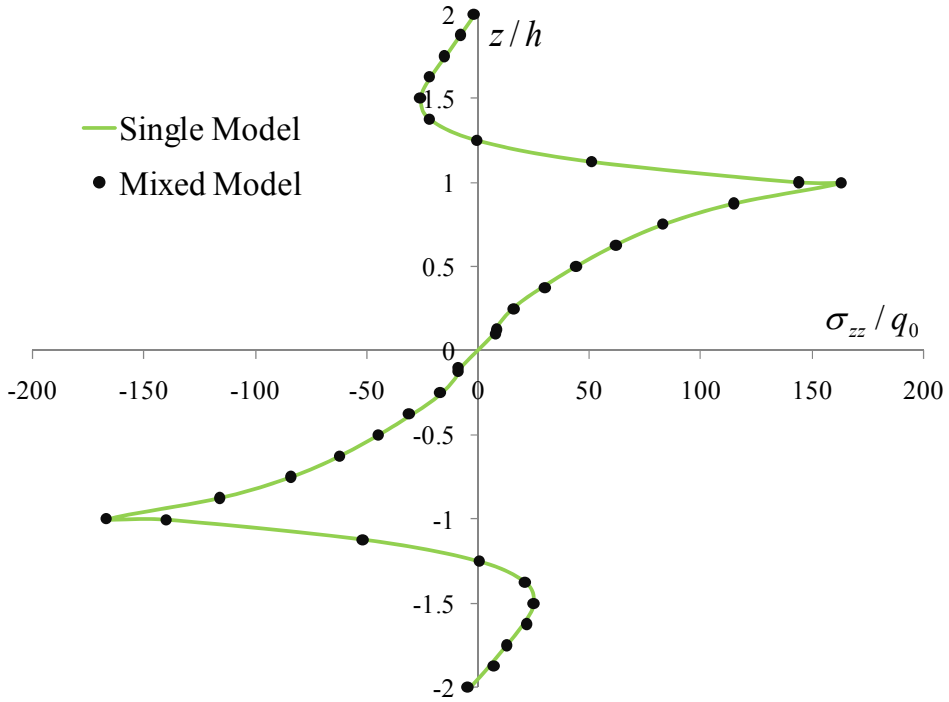

Fig. 5.54 Distribution of transverse normal stresses (σ_{zz}) across thickness at the free edge (x=0 and y=b)

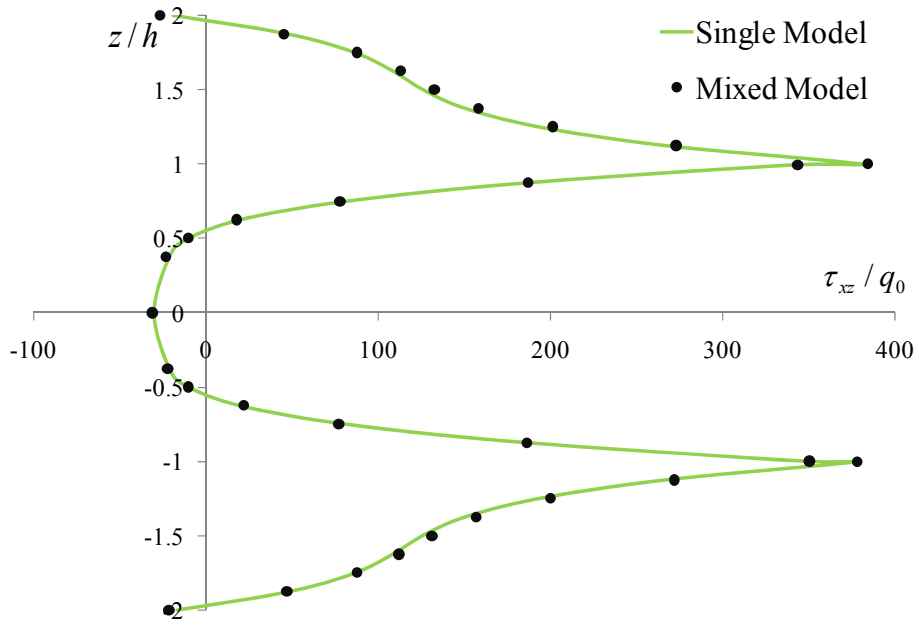

Fig. 5.55 Distribution of transverse shear stresses (τ_{xz}) across thickness at the free edge (x=0 and y=b)

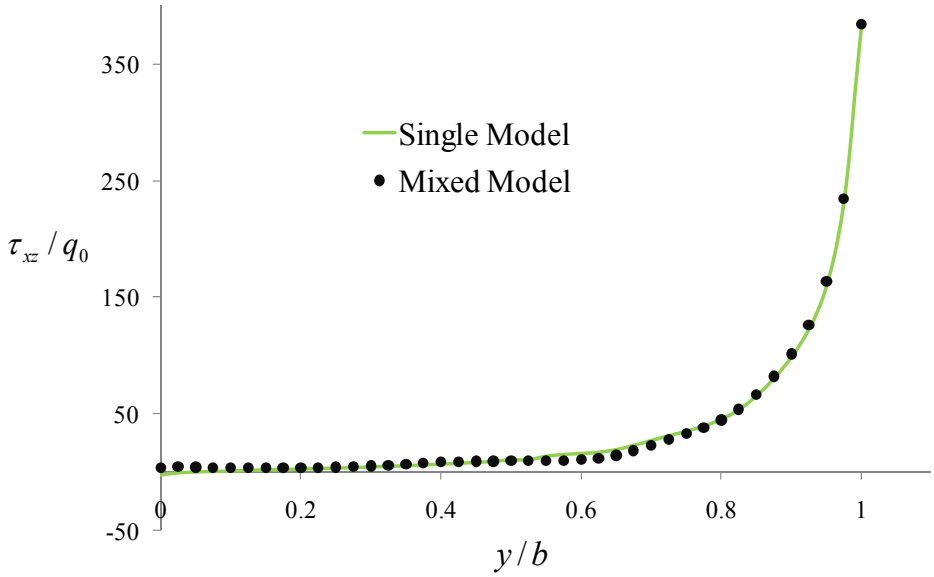

Fig. 5.56 Distribution of transverse shear stresses (τ_{xz}) across the width at upper interfaces for single and mixed models

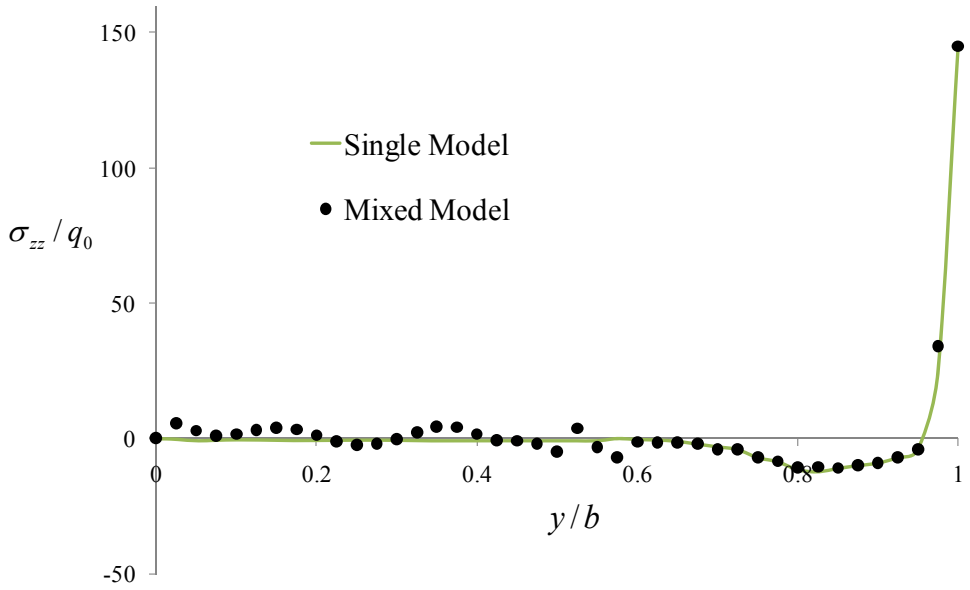

Fig. 5.57 Distribution of transverse normal stresses (σ_{zz}) across the width at upper interfaces for single and mixed models

5.4. Plates with Cutout

5.4.1 Unpatched Plates with Circular Cutout

The purpose of this section is to study the effectiveness of patch repair of damage in the form of a cutout. For the sake of simplicity a circular cutout is considered first. With a circular cutout the finite element model will involve elements with one edge in the shape of the arc of a circle with radius equal to that of the cutout. In the context of a *p*-refined model, the elements will be large with the size being kept fixed as the model is refined. In this situation, in order to avoid geometrical errors at the curved boundary caused by linear mapping, elements with mapping of curved boundary using blending functions will be used. As shown in Fig. 5.58 (a), the plate with a hole and subjected to tensile loading is considered first to verify the applicability of the present model to such plates.

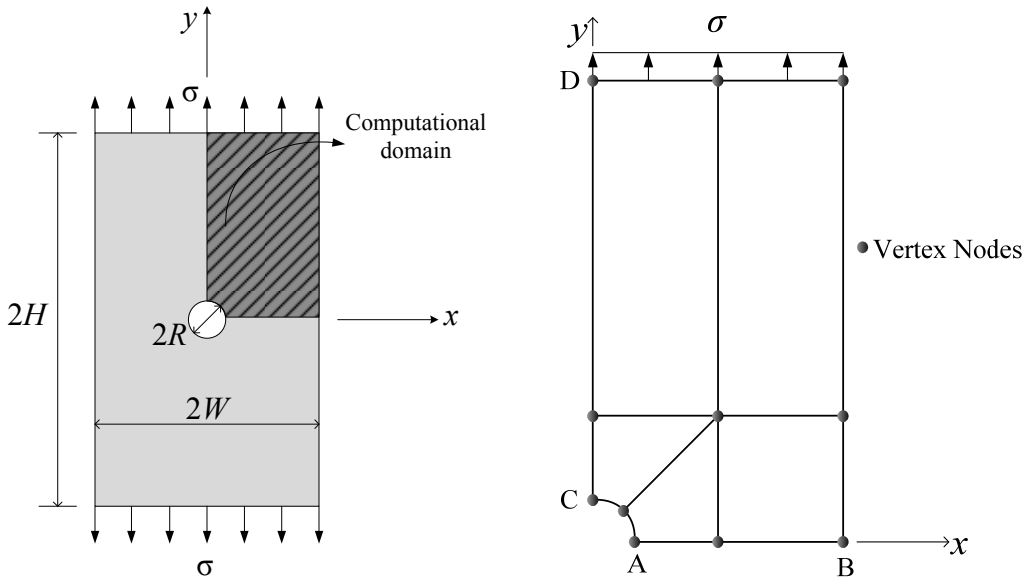

(a) Real configuration of plate (b) Finite element mesh

Fig. 5.58 Plate with circular hole

It is well established that the maximum stress in an infinite elastic thin plate, subjected to uniaxial in-plane tension stress σ, is three times the average stress, occurring at the edges of the hole. The, corresponding stress concentration factor, K_t, is thus given by

$$K_t = \frac{\sigma_{\max}}{\sigma} = 3 \tag{5.8}$$

However, when the plate is finite, Eq. 5.8 is not valid any more. For a thin plate of finite width with centrally located hole, the stress concentration factors can be calculated from (Pilkey and Pilkey, 2008)

$$K_{tg} = 0.284 + \frac{2}{1 - R/W} - 0.6\left(1 - \frac{R}{W}\right) + 1.32\left(1 - \frac{R}{W}\right)^2 \tag{5.9}$$

$$K_{tn} = 2 + 0.284\left(1 - \frac{R}{W}\right) - 0.6\left(1 - \frac{R}{W}\right)^2 + 1.32\left(1 - \frac{R}{W}\right)^3 \tag{5.10}$$

where K_{tg} and K_{tn} are the stress concentration factors based on nominal stress defined over gross and net areas, respectively. Also, R refers to radius of the circular hole and W is half plate width. For numerical simulation, a quarter of the plate is considered by applying appropriate symmetry conditions. Fig. 5.58 (b) shows the configuration of the used mesh on xy-plane, which is composed of five FDLM-based elements.

In Table 5.12 is shown a comparison of the reference values (Pilkey and Pilkey, 2008) of K_{tg} and K_{kn}, and the values calculated by present analysis, with $W = 2$ in., $H = 5$ in., $R =$ 0.375 in., and thickness = 0.1 in. Also, Young's modulus and Poisson's ratio values for the plate material are taken as $E = 10.2\times10^6$ psi, and $\nu = 0.33$. The results by present analysis are found to agree well with the reference values. Figs. 5.59 and 5.60 show the variation of normal stresses (σ_{xx} and σ_{yy}) along the lines of symmetry A-B and C-D, respectively, based on present analysis in comparison with the analytical solutions based on elasticity theory for an infinite plate (Ugural and Fenster, 2003), showing good agreement. As the stress concentration factors K_{tg} and K_{tn} are different, both are plotted in Fig. 5.61, showing little difference between present analysis and reference values. As R/W is increased from 0 to 1, K_{tg} increases from 3 to ∞; whereas, K_{tn} decreases from 3 to 2. Although both the factors can be used to calculate the maximum stress, K_{tn} is the most commonly used factor, since the stress of interest is usually in the net cross section.

Table 5.12 Comparison of stress intensity factors

K_{tg}		K_{tn}	
Reference value	Present analysis	Reference value	Present analysis
3.129	3.132	2.543	2.545

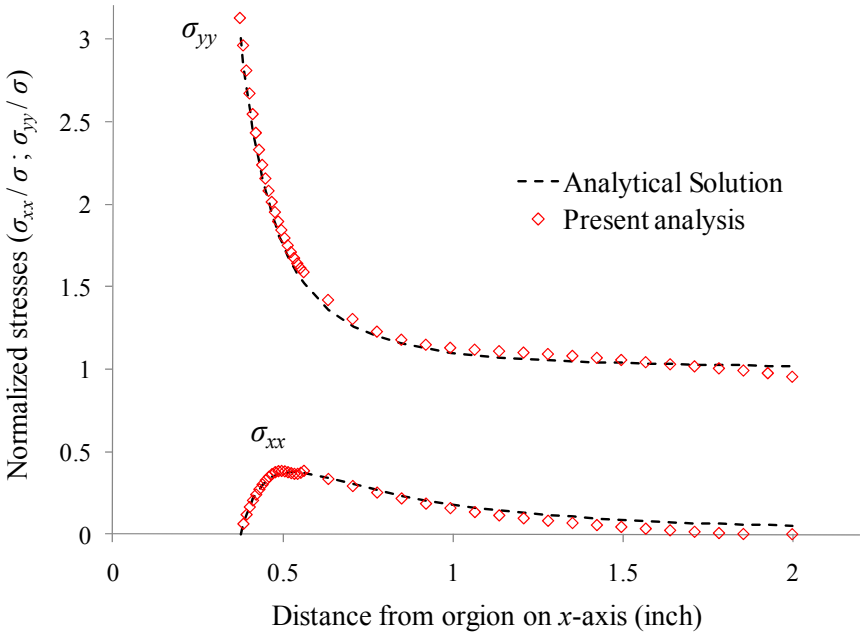

Fig. 5.59 Distribution of stresses on section A-B

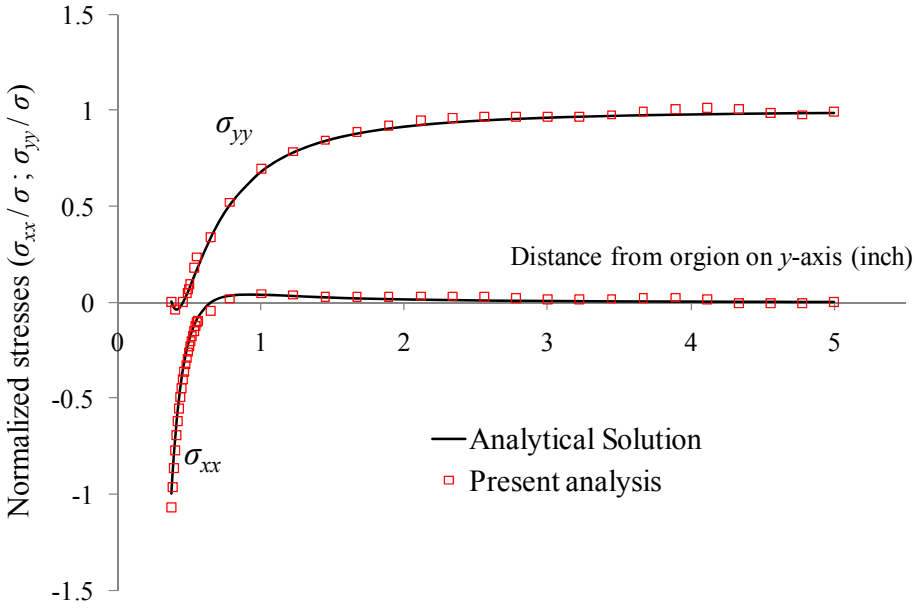

Fig. 5.60 Distribution of stresses on section C-D

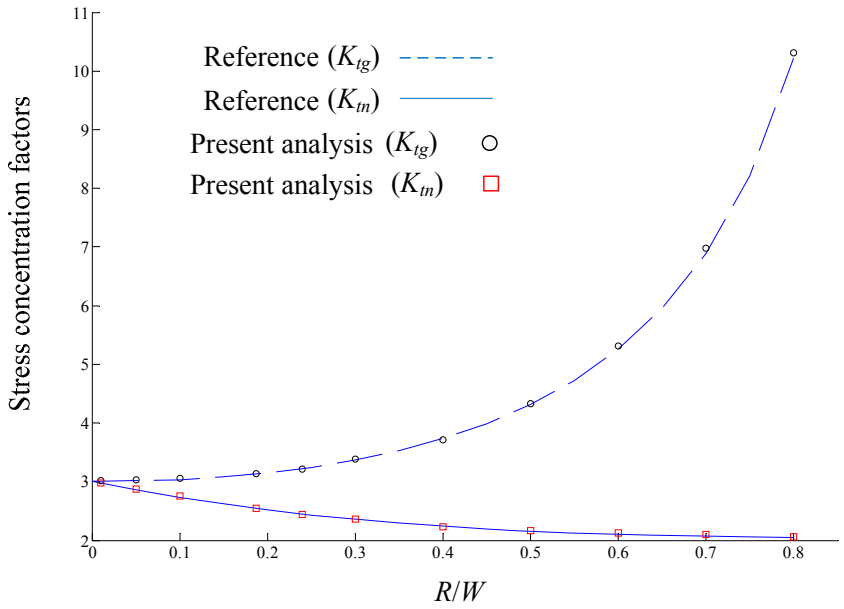

Fig. 5.61 Stress concentration factors for a plate of finite-width with a circular cutout

5.4.2 Modeling of Patched Plates with a Circular Cutout

As the next problem concerning patch repair of components with irregularities, the behavior of bonded patch repair of an aluminum plate with circular cutout, subjected to uniform tensile loading, is considered. Fig. 5.62 shows the basic geometry of a single-side patched plate with circular cutout. Here the single patch is shown to be placed symmetrically with respect to the center of the hole and glued with an intervening layer of adhesive. The planar dimension of the aluminum plate are specified as W_{al} = 2 in., and H_{al} = 5 in., and the radius of circular hole, R, as 0.375 in. Also, the size of the square patch and adhesive is given by H_p=W_p = 0.5625 in.. Young's modulus and Poisson's ratio of aluminum are E_{al}=10.2×10^6 psi, v_{al}=0.33, respectively. The patch material is taken to be identical with the material of the parent plate. Material properties of adhesive are specified as E_{ad}=160.8×10^6 psi, and v_{ad}=0.34, respectively.

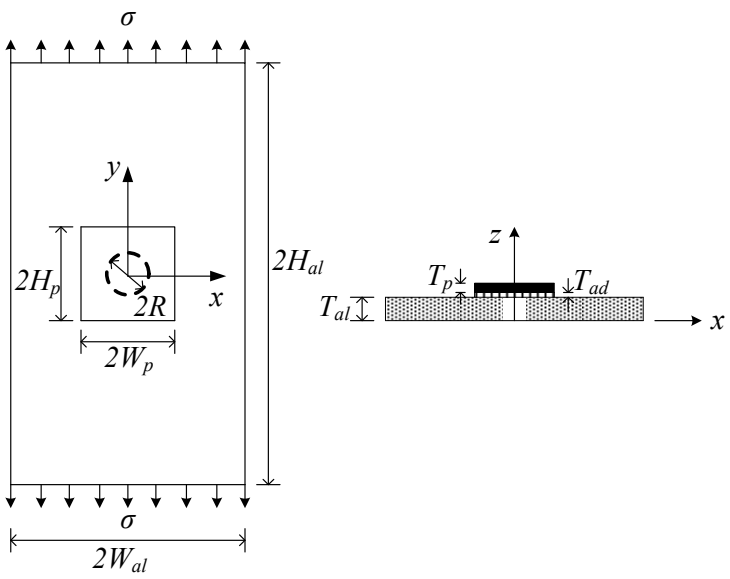

Fig. 5.62 Geometric configuration of patch-repaired aluminum specimen

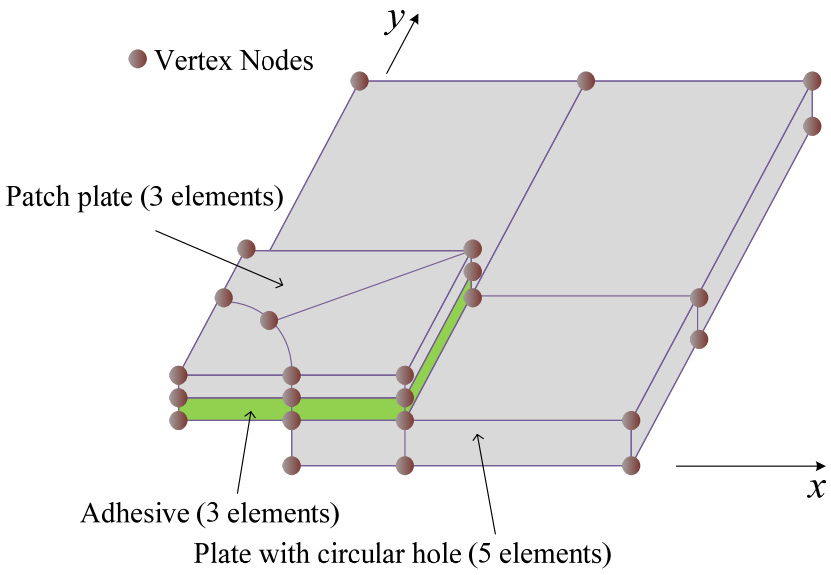

Fig. 5.63 Finite element mesh of patched plate

As shown in Fig. 5.63, a quarter of the patch-repaired plate is discretized with 11 FDLM elements (5 for parent plate and 3 each for patch and adhesive, when symmetry

conditions with respect to x- and y- axes are used. Also, additional boundary conditions used for referenced experimental studies (Barut et al., 2002) are applied as follows

$$u_z(x, H_{al}, z) = 0 \tag{5.11}$$

This problem was also analyzed by Barut et al. (2002) using a h-version mesh with over about 20,000 solid elements involving a NDF of over 70,000. These numbers are significantly more than those for the present model. Actually, for the 11 element model with $P_{xy} = 7$ and $P_z = 3$ used herein, the total required total NDF is just 3,145.

5.4.3 Effect of Relative Thickness in Patched Plates

For studying the effect of relative patch thickness (T_{al}/T_p), two cases (Model A and B) are considered. The thickness of damaged plate, adhesive, and repair plate for these cases are given in Table 5.13.

Table 5.13 Thickness in Model A and B

	Model A	Model B
Damaged Plate (T_{al})	0.088 in.	0.0635 in.
Patch Plate (T_p)	0.024 in.	0.049 in.
Thickness ratio(T_{al}/T_p)	3.67	1.30
Adhesive (T_{ad})	0.0025 in.	0.0025 in.

In order to examine the accuracy of the 11-element mesh shown in Fig. 5.63 is considered. The response of the plate is computed by both linear and geometrically nonlinear analysis with increasing applied load. For both the cases, the strain component, ε_{yy}, near the hole of the damaged plate, at the location where $x = 0.46875$ in., $y = 0.0$ in., z

= 0.0 in, versus the applied load are plotted in Figs. 5.64 and 5.65.

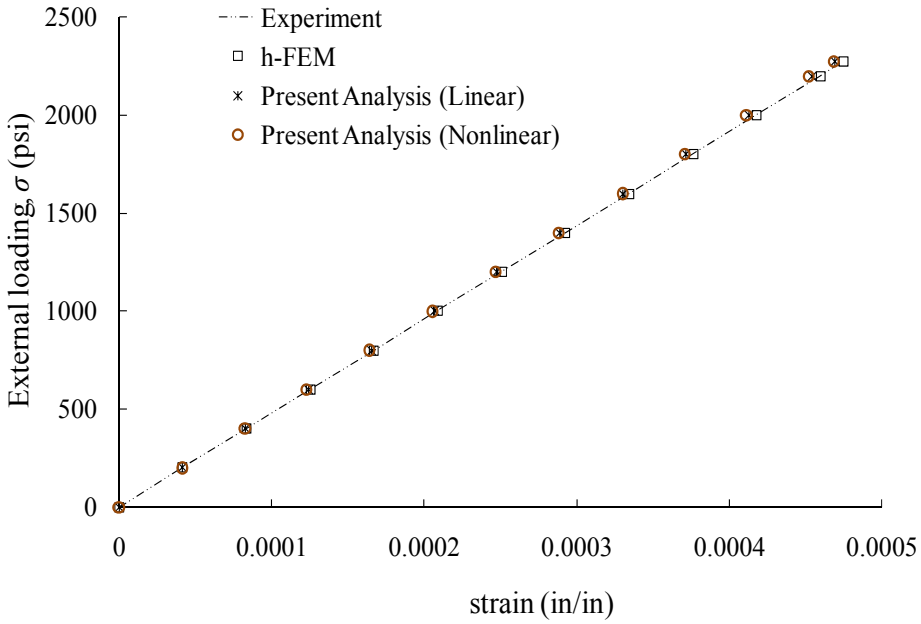

Fig. 5.64 Comparison of strain values with variation of external loading (Model A)

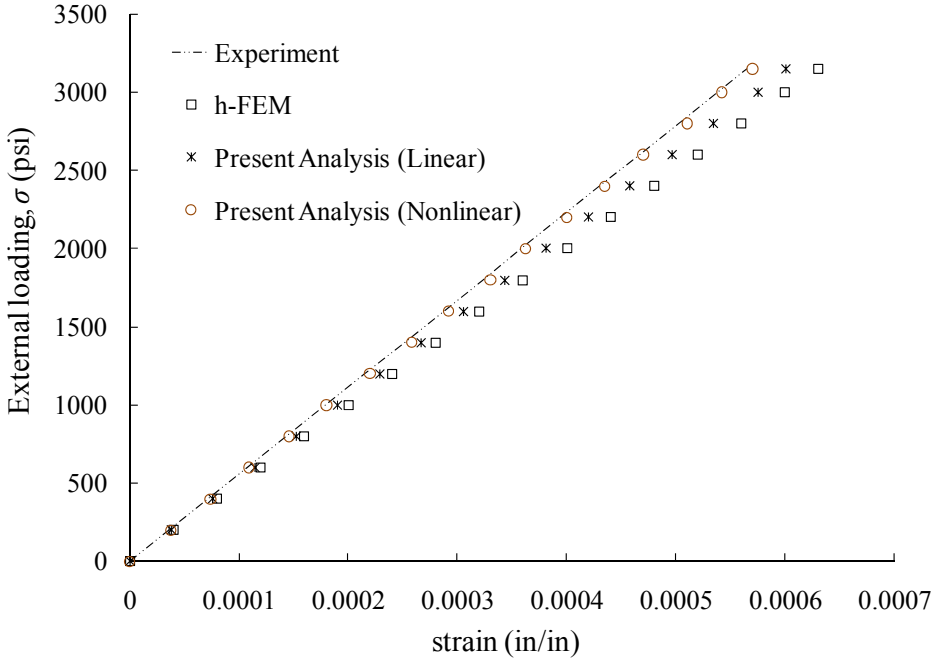

Fig. 5.65 Comparison of strain values with variation of external loading (Model B)

It can be observed that the results of Model A are nearly identical with the reference values (Barut et al., 2002). Also, it is seen that there is little difference between the linear and geometrically nonlinear analysis results. In the case of Model B, there is small discrepancy between experiment and linear numerical analysis results. The values of present analysis reflecting geometrical nonlinearity are closest to the experimental values; whereas, the *h*-FEM results show maximum discrepancy with present linear analysis results lying between the other two numerical results. In other words, the present non-linear and linear results are closer to the experimental values than the reference *h*-FEM values. Based on these findings, it can be stated that the inclusion of geometric nonlinearity is important when the ratio of damaged material thickness and the patch thickness (T_{al}/T_p) is small. Table 5.14 shows the lateral displacements at top surface of patch plate (Point A; x = 0.15625 in. y = 0.00 in.) and also at the bottom surface of the parent plate (Point B; x = 0.71875 in. y = 0.00 in.), for a tensile loading of 800 lb giving σ =2272.73 psi in Model A and σ =3149.61 psi in Model B. It is evident from the table that the present analysis shows better agreement with experiment than the results of Barut et al. (2002) using *h*-FEM.

Table 5.14 Comparison of lateral displacements at specified locations (unit: inch)

Model Type	Locations	Experiment	Reference (Barut et al., 2002)	Present analysis	
				Linear	Nonlinear
Model A	Point A	-0.00613	-0.00425	-0.00615	-0.00613
	Point B	-0.00520	-0.00409	-0.00558	-0.00547
Model B	Point A	-0.01315	-0.01025	-0.01405	-0.01350
	Point B	-0.01125	-0.01021	-0.01196	-0.01150

Fig. 5.66 shows the variation of normalized normal stress resultants along *x*-axis beginning with the center of hole, for unpatched and patch cases (for Models A and B). It is evident from Fig. 5.66 that the patch reduces maximum normal forces by about 35~40% from that of unpatched plate. Likewise, Fig. 5.67 shows normalized moment stress resultants for the same cases.

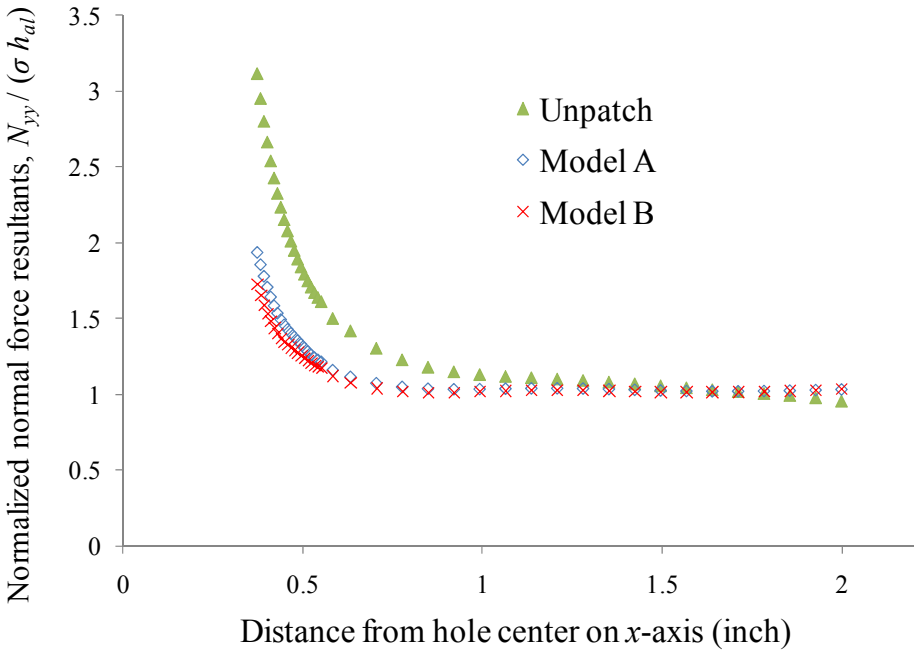

Fig. 5.66 Normalized normal force resultants along *x* axis

Fig. 5.67 represents the bending response with patch. It is well known that out-of-plane deflection arises in the single-side-patched plate under tensile loading because of the local eccentricity effect of the asymmetric patch. Especially, in Model B which has relatively thinner damaged plate and thicker patch, this effect is much more prominent. Although the normal stress resultant in Model A is somewhat larger than that for Model B, the former case with smaller relative patch thickness is preferred. In the strain curves of

previous Figs. 5.64 and 5.65, Model B showed more discrepancy between experiment values and numerical analysis with increasing external loading. This may be attributed to more pronounced effect in Model B than in Model A, confirming the need for geometrically non-linear analysis. Figs. 5.68 (a) and (b) show the variation of normal stress at bottom, middle and top surfaces with distance from the edge of hole along *x*-axis, for Models A and B.

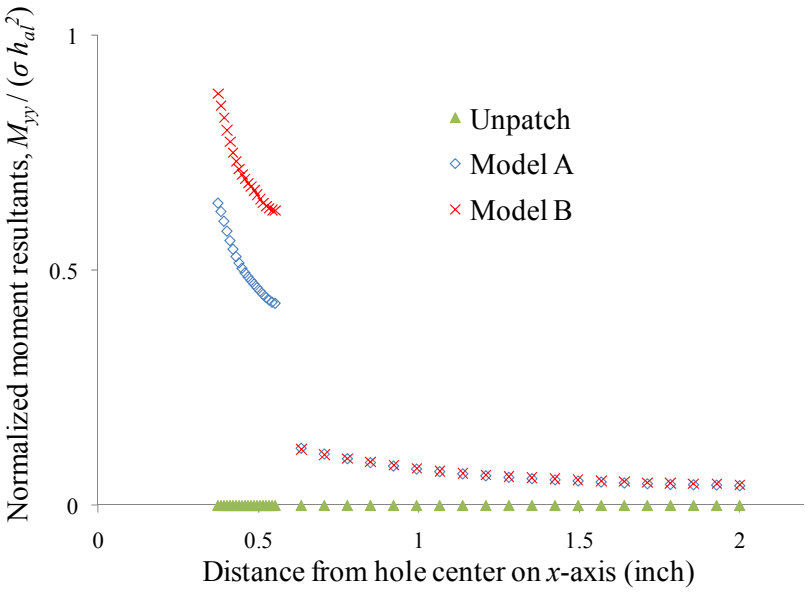

Fig. 5.67 Normalized moment resultants along *x* axis

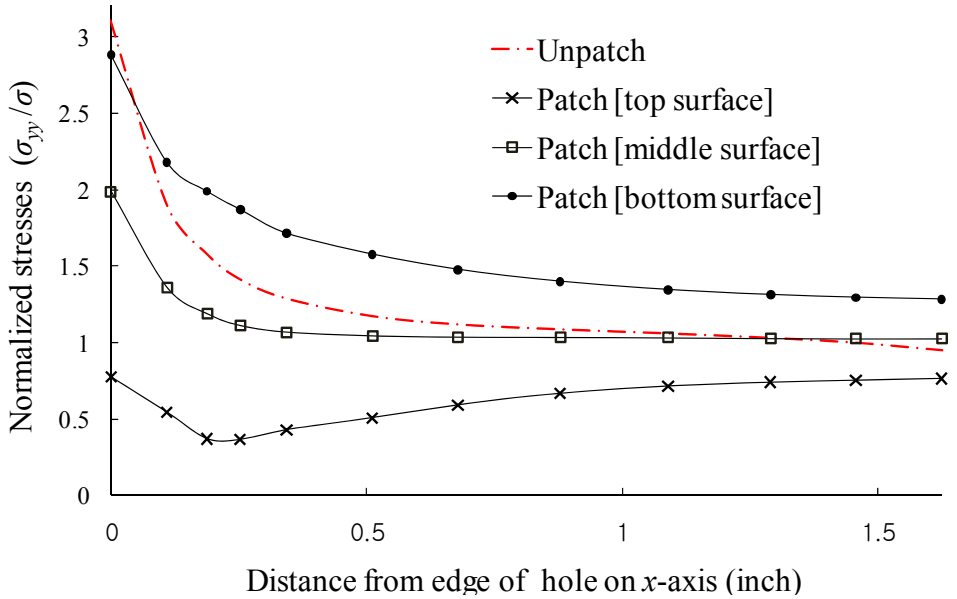

(a) Model A

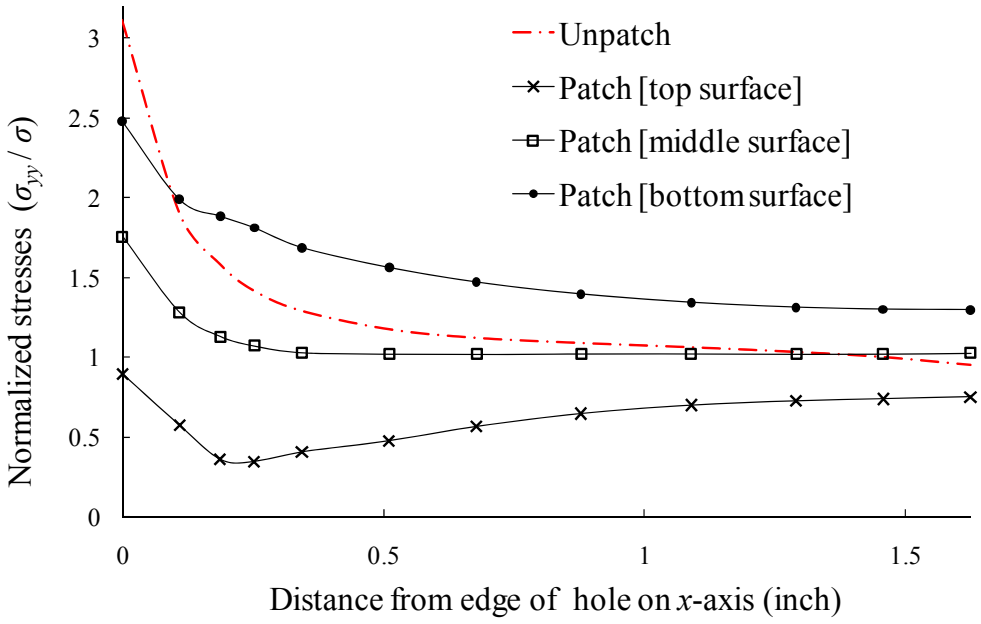

(b) Model B

Fig. 5.68 Stress distributions at different surfaces of damaged plate

5.4.4 Effect of Adhesive in Patched Plates

In general, the debonding of adhesive in externally bonded repaired system has an important effect on stiffness loss of total system and can create a local instability that leads to failure. Thus, for study of free edge effect in patch-repaired plates, some transverse stresses with singular behavior, which would cause debonding at local region, are investigated in Model A, the first of two models used in the preceding example. For comparison of absolute values of transverse stresses, the variation of stresses over the segment $-2 \leq y \leq 10$ on the y-axis is considered in the following plots.

Figs. 5.69 through 5.71 show the distribution of stresses, τ_{xz}, τ_{yz}, and σ_{zz}, in the adhesive across its thickness at the edge of the patch, for which x = 0.5625 in. and $0 \leq y \leq 0.5625$ in. It is noted that the transverse shear stresses, τ_{yz}, grow slightly near the corner of the patch area, while the other two stress components are mostly constant along the patch edge. Also, the transverse stresses at interfaces between original plate and adhesive are relatively larger than those at other locations within the adhesive.

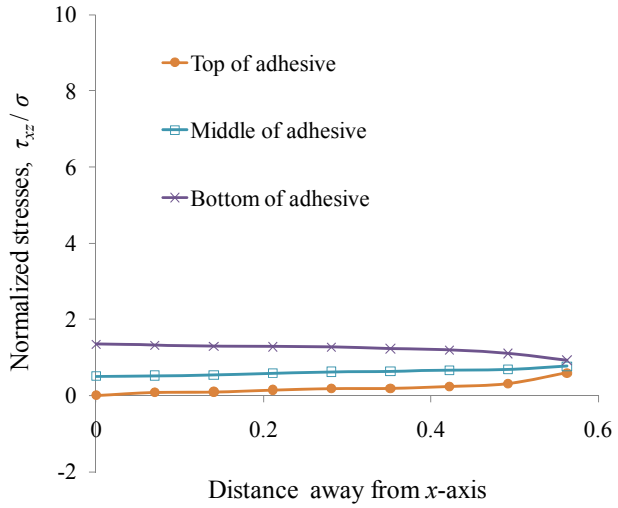

Fig. 5.69 Distribution of shear stresses τ_{xz} along y-direction at adhesive edge

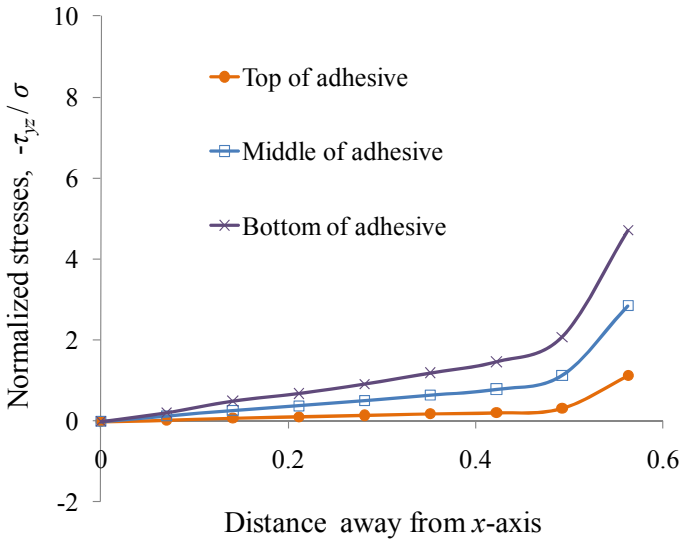

Fig. 5.70 Distribution of shear stresses τ_{yz} along y-direction at adhesive edge

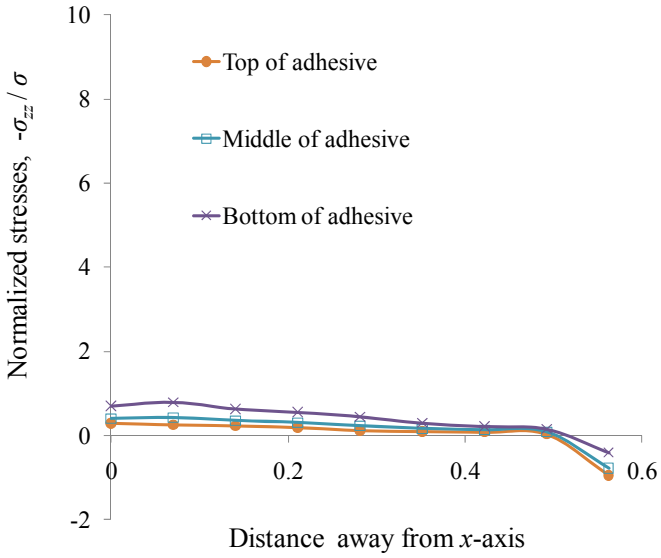

Fig. 5.71 Distribution of shear stresses σ_{zz} along y-direction at adhesive edge

Likewise, Figs. 5.72 through 5.74 show the distribution of stresses, τ_{xz}, τ_{yz}, σ_{zz}, at an edge of patch area where $0 \leq x \leq 0.5625$ in. and $y = 0.5625$ in. It is to be noted that in this case the edge stresses are mostly larger than for the edge parallel to the y-axis. It can then

be arrived at that the transverse shear stresses τ_{yz} at the patch edge parallel to x-direction (y = 0.5625 in.) are considerably larger than other stress components, especially, in the bottom surface of the adhesive layer. This signifies that the potential for delamination between the adhesive and the parent plate mobilized by high values of τ_{yz} is quite high. The existence such high values of τ_{yz} is amply clear from Fig. 5.75.

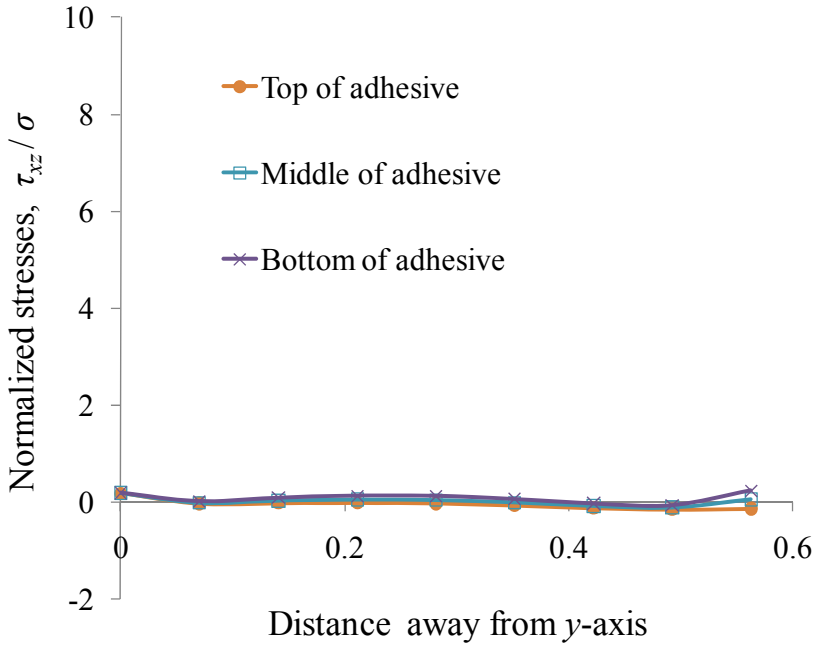

Fig. 5.72 Distribution of shear stresses τ_{xz} along y-direction at adhesive edge

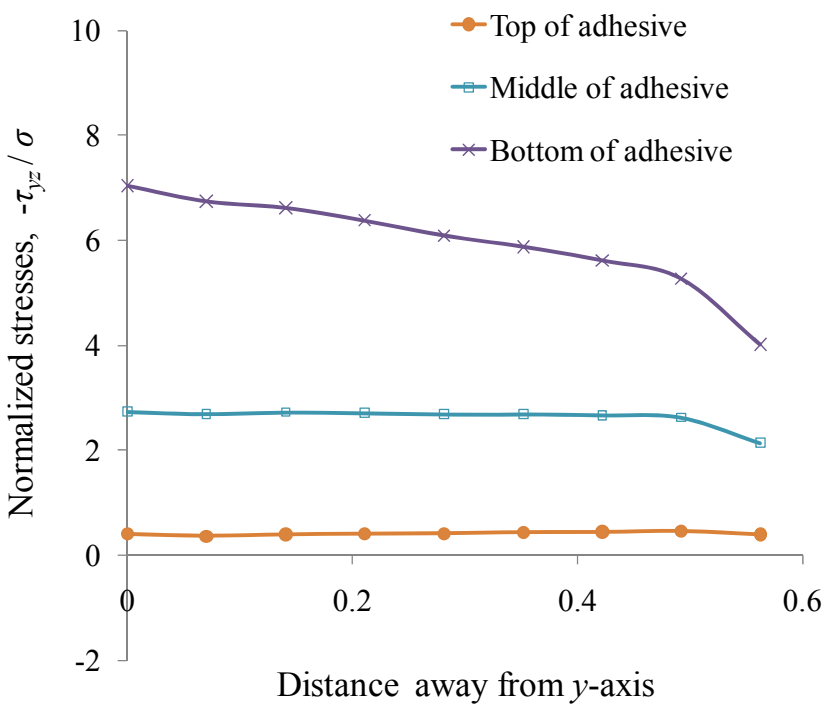

Fig. 5.73 Distribution of shear stresses τ_{yz} along x-direction at adhesive edge

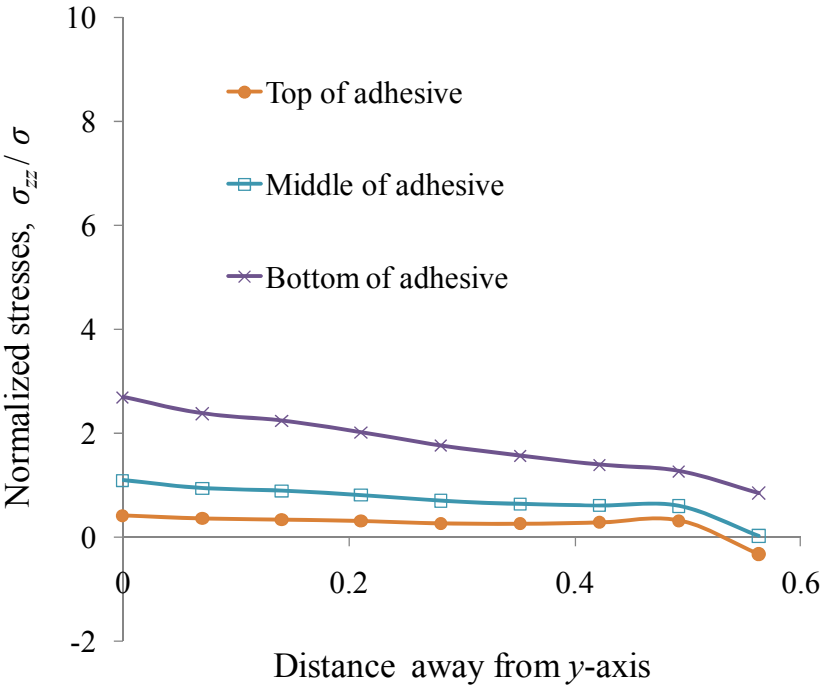

Fig. 5.74 Distribution of shear stresses σ_{zz} along y-direction at adhesive edge

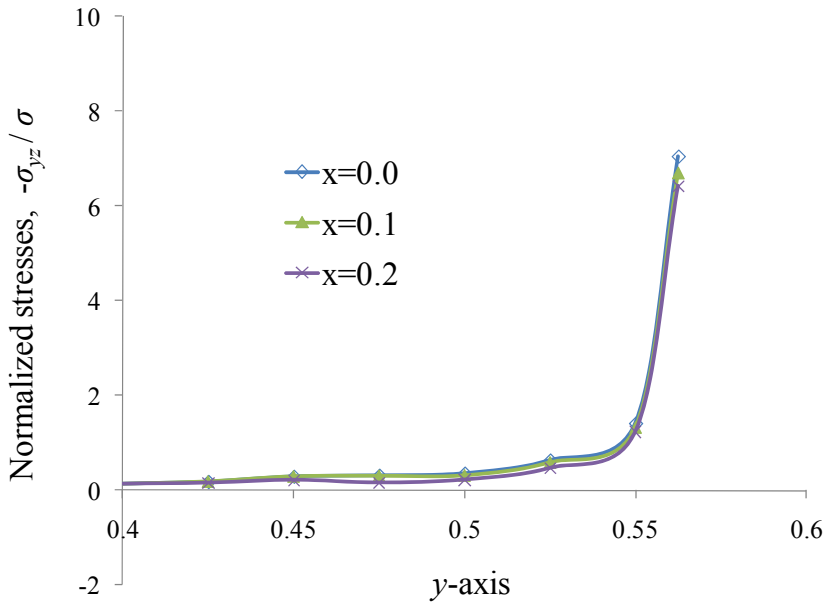

Fig. 5.75 Distribution of transverse shear stresses, σ_{yz}, on bottom surface of layer

For studying the influence of effective of adhesive area, the four cases shown in Fig. 5.76 are considered. First case refers to full bonding of patch area and the other three represent partial bonding of patch area, meaning that in the grey shaded areas no bond is allowed. All conditions except *xy*-plane area of adhesive are identical in four cases. For the analysis, modeling of present analysis needs to be changed. Figs. 5.77 (a), (b), and (c) show three modeling configurations of the analysis for partial bonding A, B, and C, respectively. Fig. 5.78 shows stresses distributions through the thickness of the plate at the point of maximum stress in the damaged plate for the four cases considered. The results are compared with those for the unpatched plate. It is seen from Fig. 5.78 that partial bonding reduces the effectiveness of a patch. Also, behavior of Part Bonding Case A, with un-bonded area smaller than the area of the circular hole, is similar with that of Full Bonding. In other cases, the trend is similar but show discrepancy with the fully bonded case, especially at the patched surface of the plate.

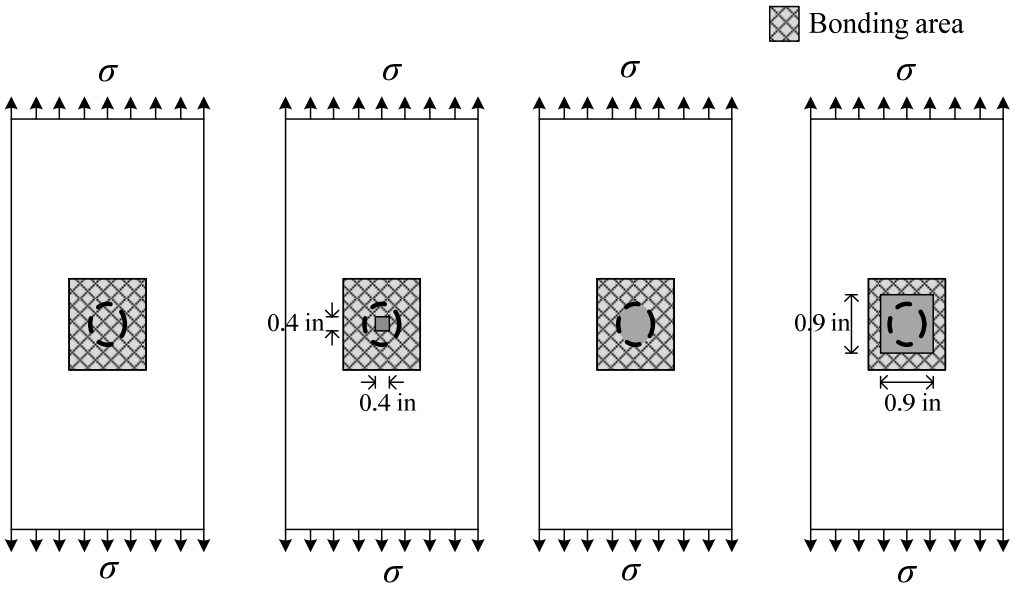

(a) Full bonding (b) Part Bonding A (b) Part Bonding B (b) Part Bonding C

Fig. 5.76 Four cases according to area of adhesive

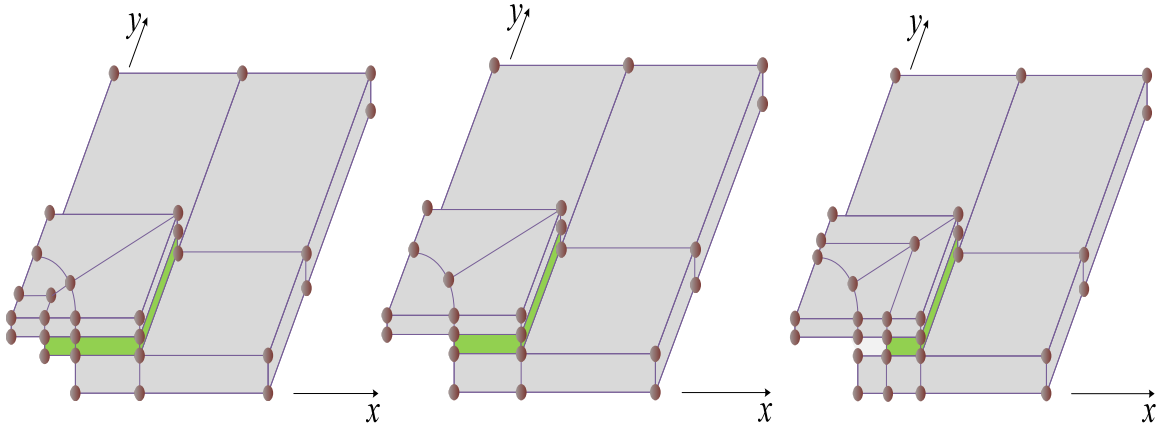

(a) Part Bonding A (b) Part Bonding B (c) Part Bonding C

Fig. 5.77 Modeling configurations for analysis of part bonding

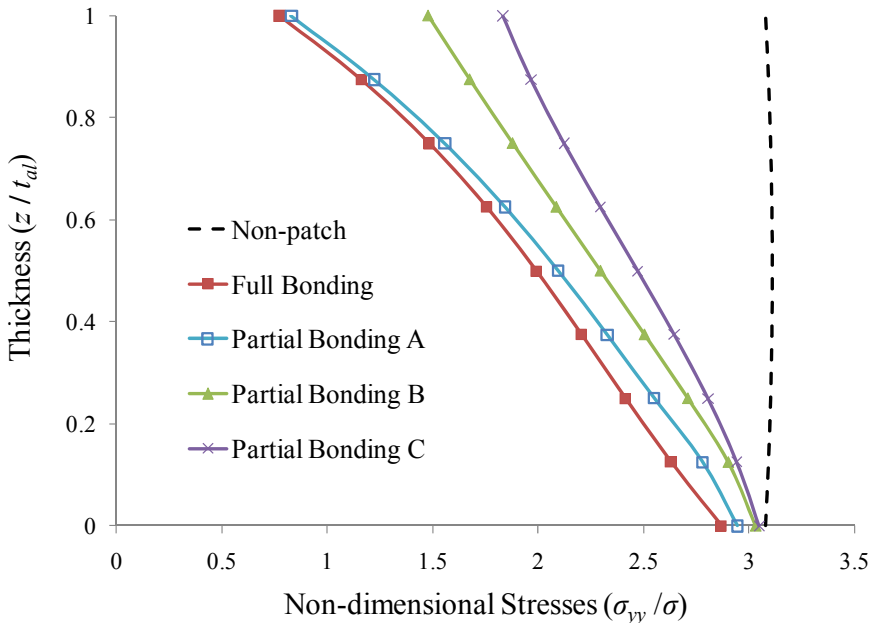

Fig. 5.78 Non-dimensional stresses on effect of bonding area

5.4.5 Effect of Patch Shape and Size

Patch shape and patch size with respect to the size of damage can play a significant role in the behavior of patch-repaired systems. In order to investigate this aspect, two patch shapes (rectangular and circular) shown in Fig. 5.79 are considered. All data not mentioned here are identical with those of Model A, considered in the previous section. In Fig. 5.79, the normal stresses in the parent plate at Pont A are calculated to examine reduction, if any, of the stress concentration factor in the parent plate. Also, from the analysis results in the previous section and reference (Soutis and Hu, 1997), it is known that maximum stresses in the adhesive, like σ_{yy}, τ_{yz}, and σ_{zz}, can develop near Point B, giving rise to the possibility of delamination. Based on the results of stress analysis of these two cases of rectangular and circular patch repairs, the influence of patch shape and size on performance is critically examined.

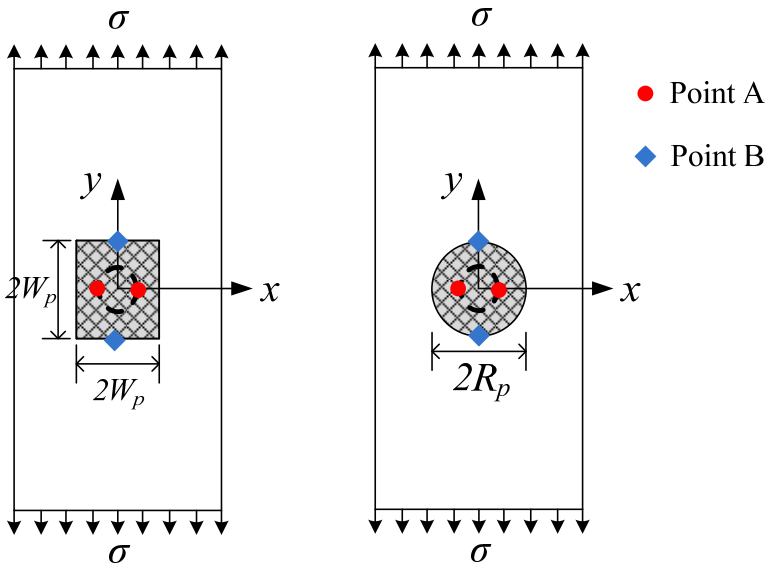

(*a*) Rectangular Patch (*b*) Circular Patch

Fig. 5.79 External patch repair configurations

Figs. 5.80 through 5.82 present the variation of each of these stress components with the planar area of the patch. For the two shapes, the area of a quadrant, A, is given by

$$A = W_p^{\,2}, \text{ or } 0.25\pi R_p^{\,2} \tag{5.12}$$

Fig. 5.80 shows the variation of in-plane normal stresses, σ_{yy}, in the parent plate at bottom and top surfaces. It is noticed that in-plane normal stresses at bottom surface are mostly constant regardless of patch area while the stress at patched top surface is dependent on patch area for $A \leq 0.3$. In addition, in the case of small values of area A, the stress reduction in the top surface with circular patch is greater than that with rectangular patch. But for $A \geq 0.3$, there is almost no difference in stress reduction for the two patch shapes. The shear and normal stresses, τ_{yz} and σ_{zz}, at the interface between the parent plate and the adhesive are shown in Figs. 5.81 and 5.82. In these cases, also, the performance of circular patch seems to be slightly better than the rectangular patch for

smaller values of area A.

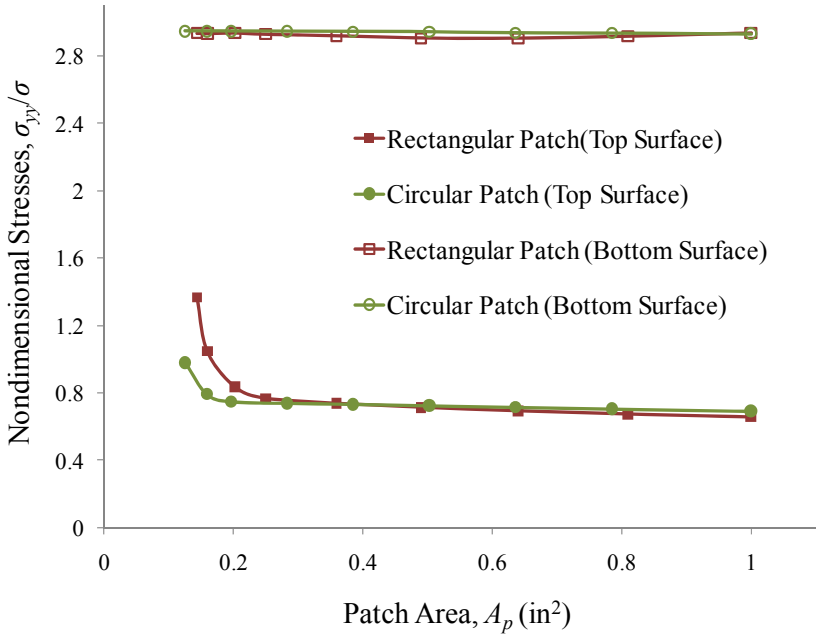

Fig. 5.80 Normal stresses of parent plate with variation of patch area

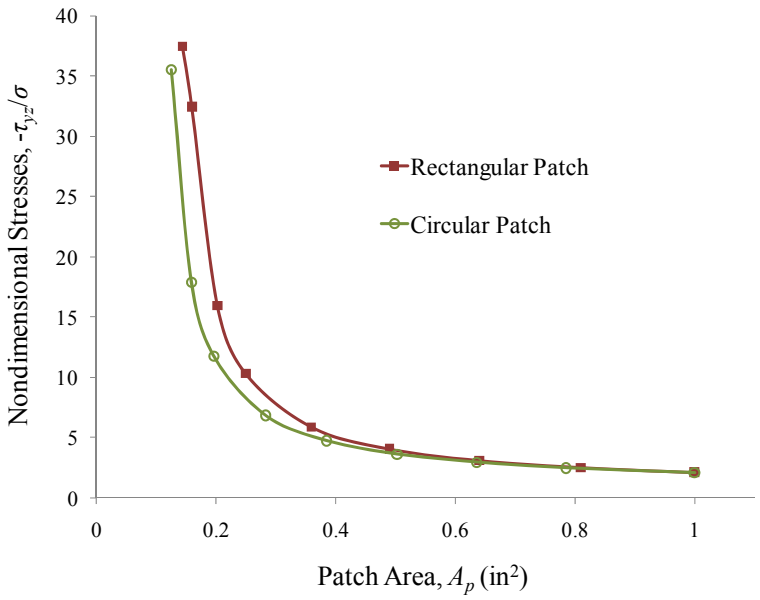

Fig. 5.81 Transverse shear stresses of adhesive with variation of patch area

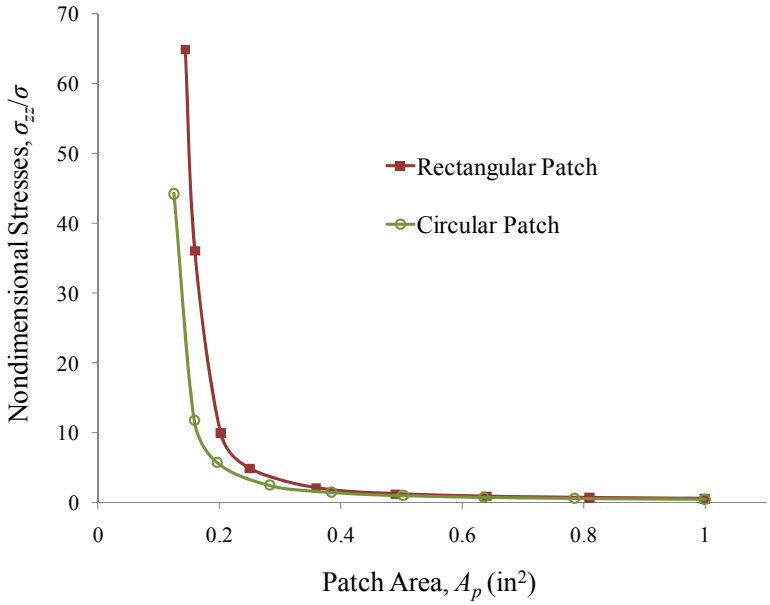

Fig. 5.82 Transverse normal stresses of adhesive with variation of patch area

Figs. 5.83 through 5.85 illustrate the variation of same three stress components with patch thickness, for both rectangular and circular patches. These patches are assumed to the same values of A=0.6 in^2. From Fig. 5.83 it is evident that the reduction of in-plane normal stress, σ_{yy}, is practically independent of the patch thickness, although some difference in stress reduction at top surface is evident when $t_p/t_{al} < 0.1$. In addition, there is no difference between rectangular patch and circular patch in the reduction of this stress component. Figs. 5.84 and 5.85 show variation of transverse shear and normal stresses, τ_{yz} and σ_{zz}, at the interface of parent plate and the adhesive layer. These two figures, however, emphasize that with a circular patch the possibility of delamination is lower than that with a rectangular patch. It is also evident that these transverse stress components at the interface are affected by the choice of path thickness, the values tending to increase with increase in patch, irrespective of the shape of the patch. Such

increase seems to be steeper in the case of transverse normal stresses, as shown in Fig. 5.85. Based on these results, it can be deducted that circular patch repairs are superior to rectangular but patch thickness should not be more what is needed.

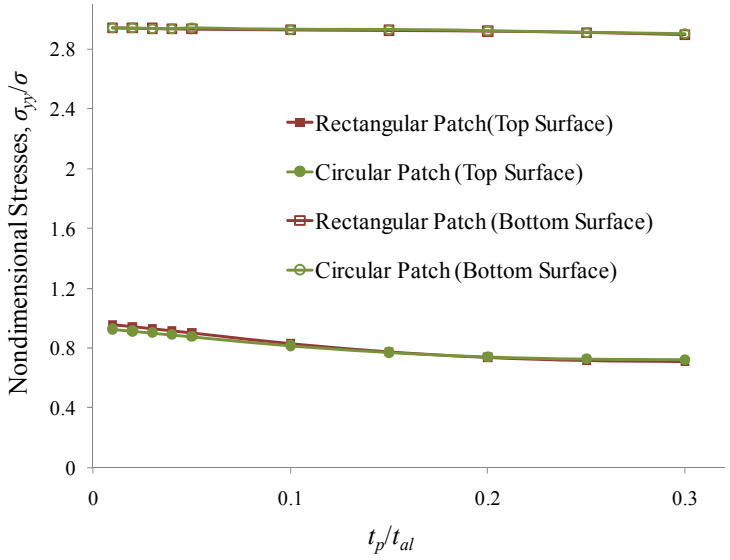

Fig. 5.83 Normal stresses of adhesive with variation of thickness

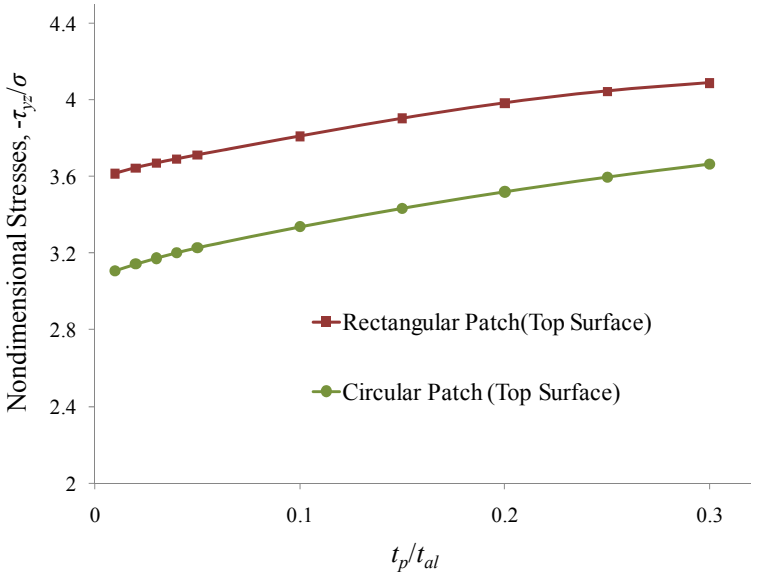

Fig. 5.84 Transverse shear stresses of adhesive with variation of thickness

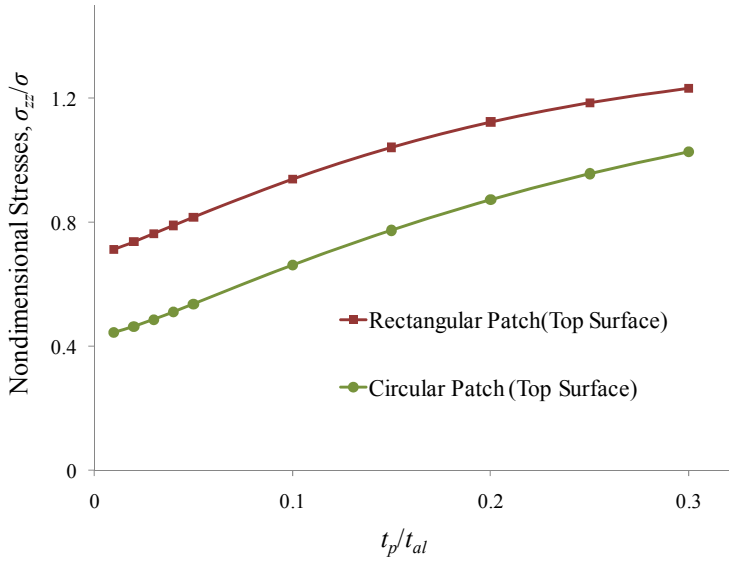

Fig. 5.85 Transverse normal stresses of adhesive with variation of thickness

5.5 Cracked Plates

5.5.1 *P*-Adaptive Analysis Using Ordinary Kriging Technique

In a *p*-adaptive procedure, the optimal mesh allowing least possible solution error is chosen on the basis of some error measures. In this section, the Kriging procedure is used for the prediction of an improved solution based on the current numerically computed solution. The improved solution can then be used in the local error prediction process required in the adaptive mesh refinement leading to optimal adjustment of *p*-levels of selected elements in the mesh.

The validation of *p*-adaptive procedure based on ordinary Kriging technique is demonstrated with the example of a two-dimensional plate with a central crack. The geometry of the plate under remote tensile loading σ is shown in Fig. 5.86. Due to symmetry, only a quarter of the plate is considered. The *p*-adaptive mesh in the modeled

region is composed of ESLM-based elements. The plate under consideration with height denoted by $2H$, width by $2W$, and crack length by $2a$ has an aspect ratio (H/W) of 2 and crack size is one-half the plate width ($a/W = 0.5$). The quadrant of the plate is discretized with eight elements. The applied tensile loading σ is taken as 10 MPa, Young's Modulus E is 70 GPa, and Poisson's ratio v is 0.3.

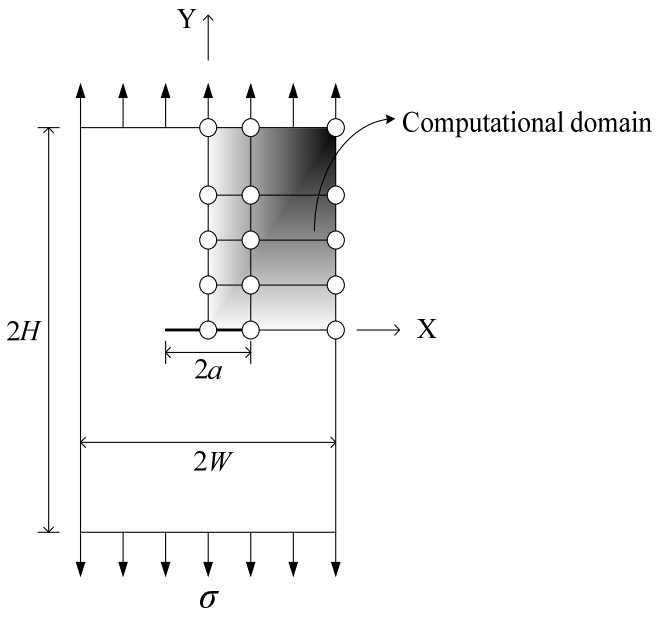

Fig. 5.86 Geometric configuration of a centrally cracked plate and finite element model

The final adaptive meshes are shown in Fig. 5.87, comparing the results of ordinary Kriging technique with those of least square method, which is one of the widely used techniques in adaptive analysis. Ordinary Kriging technique and least square method were used to calculate the estimated exact solution and smoothened stress field by projection. It is noted that the distribution of p-levels by the least square method based adaptive mesh in the vicinity of the crack tip is slightly higher than those required by the p-adaptive mesh using ordinary Kriging technique.

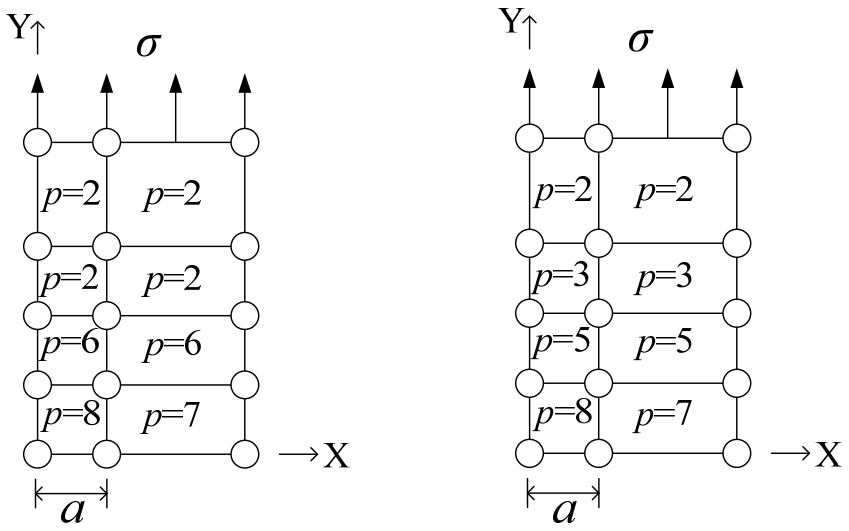

(a) Least square method (b) Ordinary Kriging technique

Fig. 5.87 Final adaptive meshes for $a/W = 0.5$

Table 5.15 gives the comparison of Mode I stress intensity factor for different crack lengths based on ordinary Kriging technique, least square method and other reference values based on global total energy release rate calculated by the finite crack extension method. The non-dimensional form, F, of Mode I stress intensity factor, K_I, is obtained from

$$F = \frac{K_I}{\sigma\sqrt{\pi a}} \tag{5.13}$$

The finite crack extension method was based on a crack length increment Δa equal to $a\times10^{-6}$, arrived at by sensitivity tests. In Table 5.15, the results of ordinary Kriging technique shows good agreement with p-adaptive analysis based on least square method as well as other reference values. The relative percentage error based on the modified super-convergent patch recovery technique is listed in Table 5.16, when a/W=0.5. In Table 5.17, a comparison of the least square method with the ordinary Kriging technique is presented in terms of the number of the required iteration and the corresponding NDF

for optimal *p*-adaptive mesh. The comparison is undertaken for a/W = 0.1 to 0.9, incremented by 0.1.

Table 5.15 Non-dimensional stress intensity factors of cracked plates with respect to a/W

a/W	Irwin	Brown	Feddersen	Dixon	Uniform *p*-level (*p*=8)	*p*-adaptive mesh	
						Least square method	Ordinary Kriging
0.1	1.004	1.011	1.006	1.005	0.977	0.950	0.931
0.2	1.017	1.026	1.025	1.0211	1.001	0.994	0.984
0.3	1.040	1.054	1.059	1.048	1.035	1.033	1.007
0.4	1.075	1.103	1.112	1.091	1.085	1.086	1.054
0.5	1.128	1.183	1.189	1.155	1.158	1.162	1.123
0.6	1.208	1.303	1.304	1.250	1.267	1.274	1.251
0.7	1.336	1.473	1.484	1.400	1.437	1.448	1.420
0.8	1.565	1.670	1.799	1.667	1.729	1.748	1.700
0.9	2.114	1.994	2.528	2.294	2.384	2.420	2.331

Table 5.16 Required NDF and percentile errors through *p*-adaptive analysis in $a/W = 0.5$

The numbers of iteration	Least square method		Ordinary Kriging technique	
	NDF	Percentile errors	NDF	Percentile errors
1	23	10.77	23	11.99
2	49	13.34	49	9.58
3	66	11.35	79	5.66
4	83	10.91	104	4.06
5	113	10.73	135	2.73
6	140	10.92	-	-
7	168	10.39	-	-
8	203	10.10	-	-
9	215	9.92	-	-

As per Table 5.5-3, the *p*-adaptive procedure based on ordinary Kriging technique needs mostly 5~6 iterations as the crack length is varied; whereas, the *p*-adaptive procedure based on least square method requires more iterations and a larger number of NDF.

Table 5.17 Comparison of the number of iterations and NDF with variation of crack length

a / *W*	Least square method		Ordinary Kriging technique	
	No. of iteration	NDF	No. of iteration	NDF
0.1	11	210	5	86
0.2	10	198	5	95
0.3	9	182	6	118
0.4	10	191	6	111
0.5	9	215	5	135
0.6	10	223	6	141
0.7	10	231	6	113
0.8	9	231	6	107
0.9	9	223	6	146

Fig. 5.88 show stress fringes by interpolations based on ordinary Kriging technique and least square method in *p*=5, respectively. It is noticed that the stress distribution based on ordinary Kriging interpolation appear smoother than those by least square method, when same *p*-levels are used.

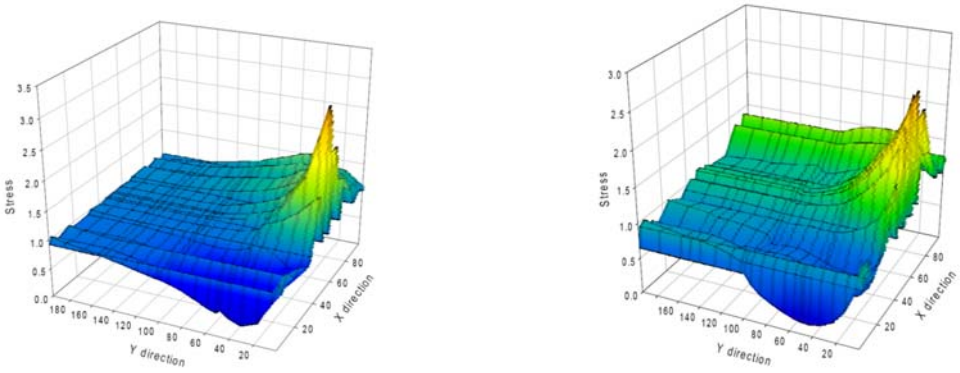

(a) Ordinary Kriging technique (b) Least square method

Fig. 5.88 Stress distributions by OK technique and least square method in *p*=5

5.5.2 Analysis of Cracked Plates with Bonded Patch using PDLM

In laminated systems like bonded patch repaired plates with crack, the use of 2D ESLM based elements will not be advisable due to the problem of satisfying continuity conditions at the boundary between patched region and the unpatched region. Although conventional fully fledged 3D modeling would easily overcome this difficulty, entailing excessive computational effort. Also, because of the extreme thinness of the adhesive layer relative to plate and patch thicknesses, the use of 3D elements with high aspect ratio cannot be avoided, otherwise the required number of elements will be exorbitant. A better solution to the stated modeling problems will be to use PDLM based elements, which are more economical than conventional 3D elements and have characteristic of 2D elements with respect to thickness direction.

In this analysis, in using the PDLM based model, it is assumed that the composite patch is perfectly bonded to the cracked plate by the adhesive film without the possibility of debonding. The stress intensity factors K_{I} with respect to opening mode are calculated from total strain energy release rate using finite crack extension method (Owen, 1983). Fig. 5.89 shows various configurations of the three different cracked plates subjected to uniaxial tensile loading. The plate has the following dimensions: height $2H_{al}$ = 480 mm, width $2W_{al}$ = 240 mm and thickness t_{al} =3 mm. The length of patch, $2H_{p,}$ is 90 mm and the width, $2W_{p,}$ is 90 mm. The thicknesses of composite patch and adhesive film are 1 mm and 0.2 mm, respectively. Graphite epoxy and boron epoxy, a pair of popular composites, are considered as patch material. The properties of the materials used are given in Table 5.18. Taking advantage of symmetry in loading and geometric conditions, only one-quarter of center crack and double-edge crack panels and one half of the single-

edge crack panel are modeled. The analyzed parts are shaded as shown in Fig. 5.89. Fig. 5.90 shows the mesh used for analysis, when the quarter-plate is discretized with six elements. In the process, the composite patch and adhesive film are modeled with two elements each.

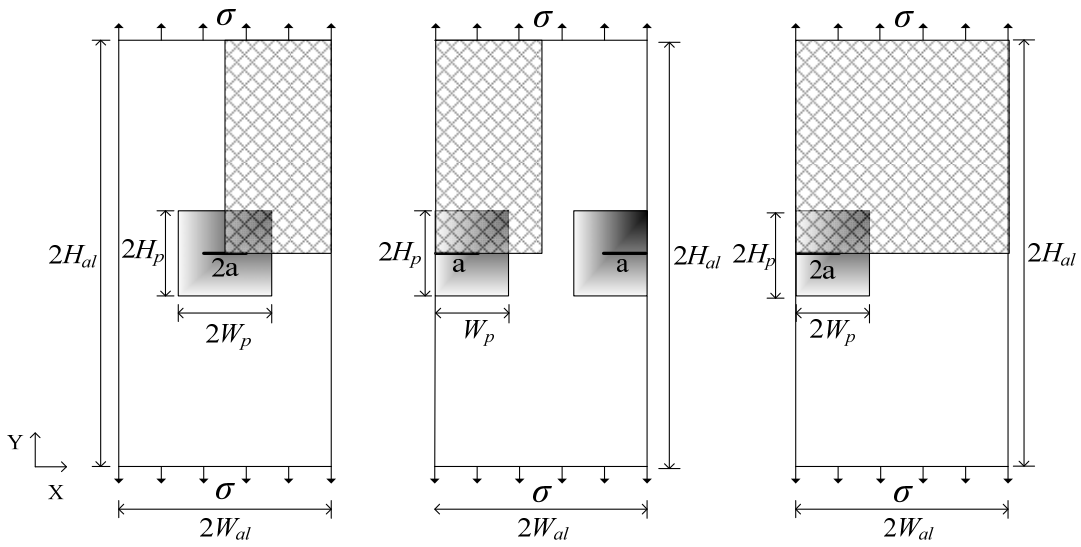

(a) Center crack (b) Double edge crack (c) Single edge crack

Fig. 5.89 Three configurations of cracked aluminum plates with patch repair

Table 5.18 Material properties (unit: GPa)

	E_1	E_2	v_{12}	G_{12}	G_{13}	G_{23}
Plate material	72	-	0.33	-	-	-
Graphite Epoxy	172.4	10.34	0.3	4.82	4.82	3.1
Boron Epoxy	208	25.4	0.17	7.24	7.24	4.94
Adhesive film	0.97	-	0.32	-	-	-

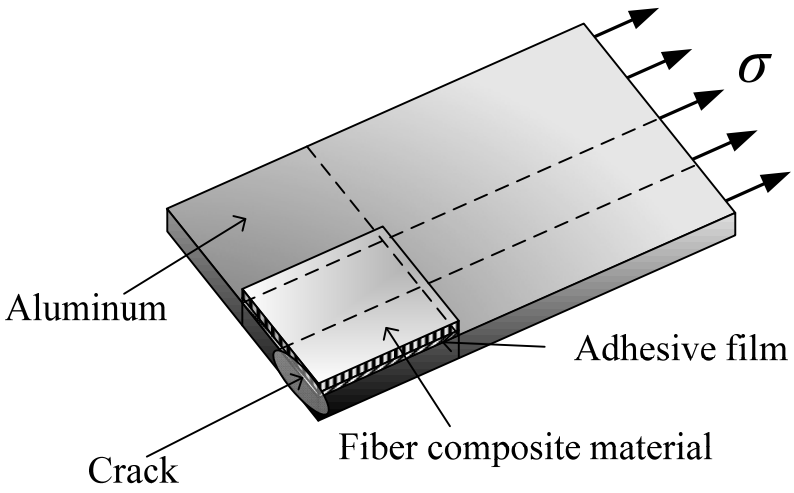

Fig. 5.90 Mesh using PDLM-based elements

First, the unpatched cracked plates are analyzed using PDLM-based elements. Non-dimensional stress intensity factors, F, defined in Eq. 5.13, are calculated by finite crack extension method and the results are assessed by comparing with some referenced values (Isida, 1971; Bowie, 1972; Tada et al., 1985; Yugawa and Nishioka, 1979) as shown in Fig. 5.91 for the plates with center, double-edge, and single-edge cracks. The values predicted by present analysis show reasonably good agreement with the reference values.

Figs. 5.92 through 5.94 show the normal stress fringes for σ_{yy} in the middle plane of the un-patched plate for $a/W_{al} = 0.3$ and $a/W_{al} = 0.6$ corresponding to the three plates. It can be seen that that the magnitude of the maximum stress increased with crack length. Also, it is demonstrated well in all the stress fringe plots that the stresses at crack surfaces drop to zero, in conformity with the expected behavior (Anderson, 2004).

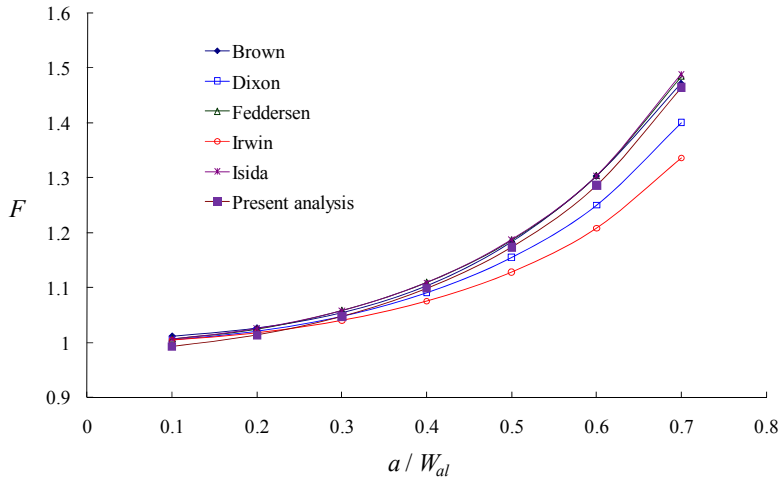

(a) Center crack

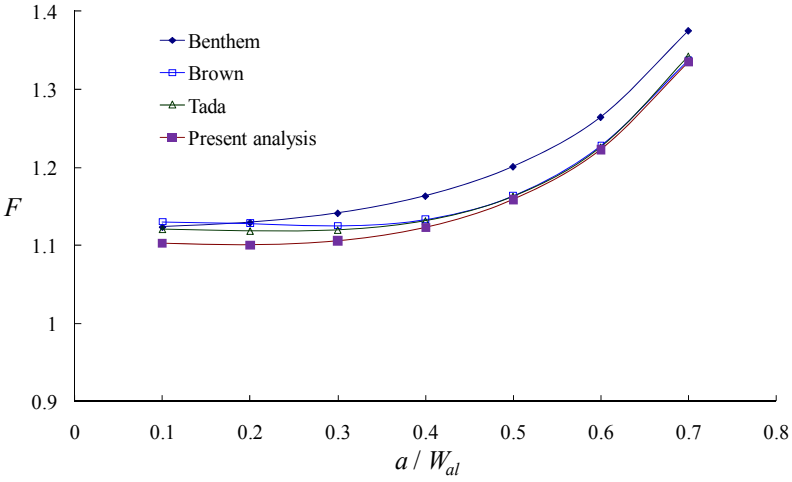

(b) Double-edge crack

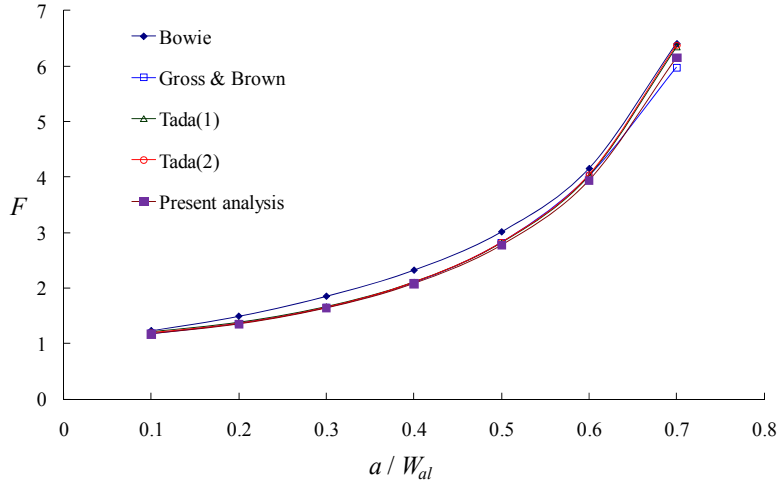

(c) Single-edge crack

Fig. 5.91 Non-dimensional stress intensity factors for un-patched plates

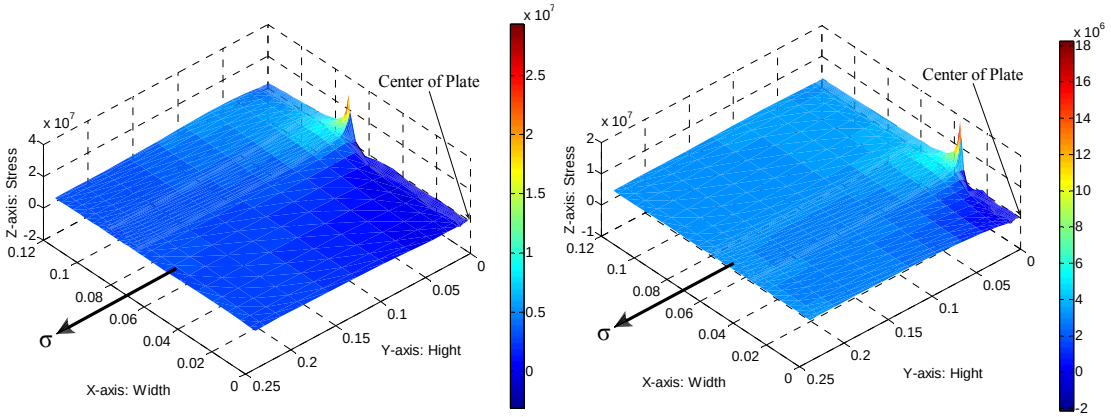

(a) $a/W_{al} = 0.3$ (b) $a/W_{al} = 0.6$

Fig. 5.92 Stresses (σ_{yy}) in center crack without patch (units: m and Pa)

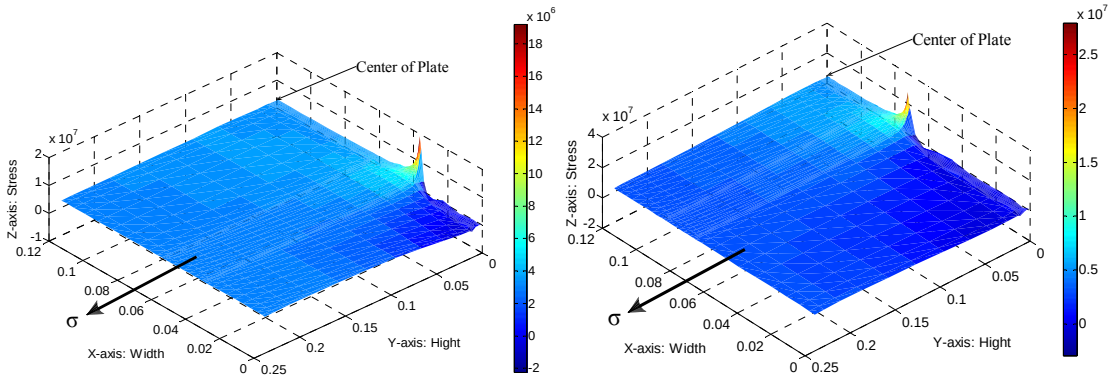

(a) $a/W_{al} = 0.3$ (b) $a/W_{al} = 0.6$

Fig. 5.93 Stresses (σ_{yy}) in double edge crack without patch (units: m and Pa)

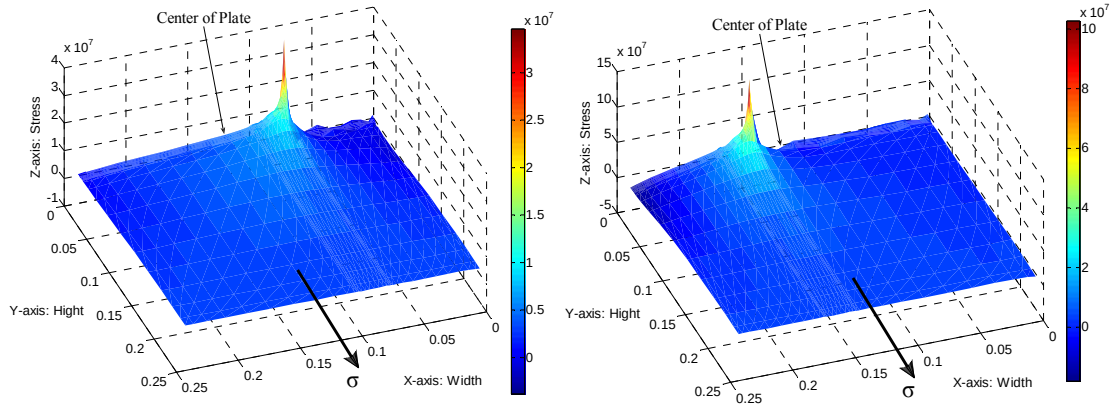

(a) $a/W_{al} = 0.3$ (b) $a/W_{al} = 0.6$

Fig. 5.94 Stresses (σ_{yy}) in single edge crack without patch (units: m and Pa)

Fig. 5.95 presents the variation of total potential energy, U_{total}, versus the crack length for un-patched and patched plates with center crack, double edge crack, and single edge crack, respectively. As expected, these figures confirm that the strain energy stored in patched plates is significantly smaller than those of un-patched plates. Moreover, it is seen that the type of patch material used also affect the value of potential energy stored in the parent plate. Especially, in the case of un-patched plate with single- edge crack, the potential energy is found to increase sharply when the ratio of crack length is over 0.5. In the presence of patch, however, it is found that the change is remarkably gentle. Fig. 5.96 shows variation of stress intensity factor for opening mode, K_I, as a function of crack length and the type of patch material. Just as in the case of rate of variation of total strain energy, it is seen that the response of center crack and double edge crack are similar. Also, it is observed that the presence of patch weakens the driving forces for fracture, namely, the stress intensity factors, and the extent of such weakness in the driving force is a function of the stiffness of the patch material. In addition, it can be seen that the discrepancy in response between the two different patch materials tend to increase with increase in crack size. The variation of normalized stress intensity factor, F, with crack size for the three cases is shown in Fig. 5.97. As in the preceding figures, the influence of crack size on the discrepancy in F-values is noticed here as well. Contrary to plots for K_I, the plots for F, for patched plates show the tendency to decrease with increase in crack size, implying that patch repair may cause retardation of crack growth.

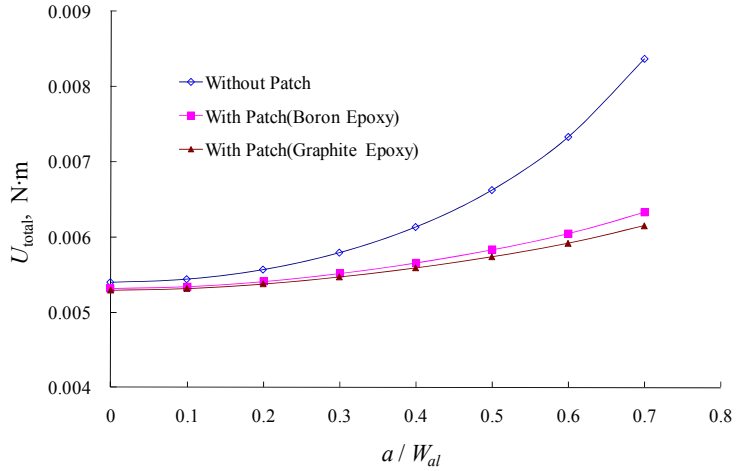

(a) Center crack

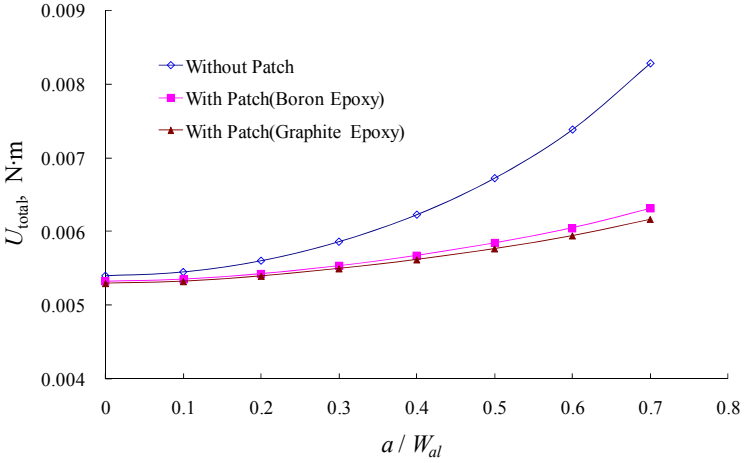

(b) Double-edge crack

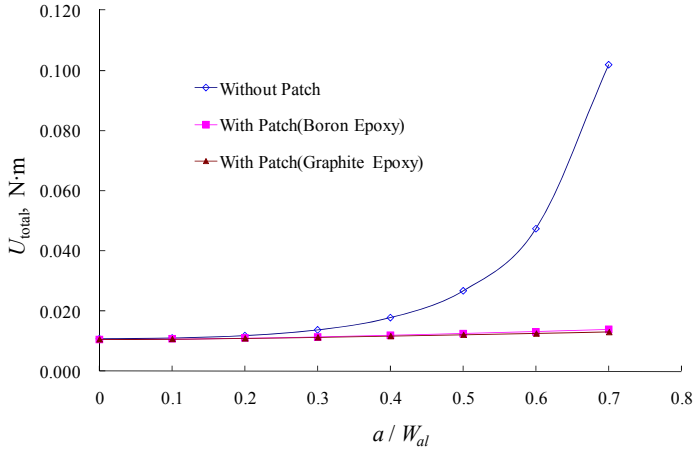

(C) Single-edge crack

Fig. 5.95 Variation of total potential energy with crack size

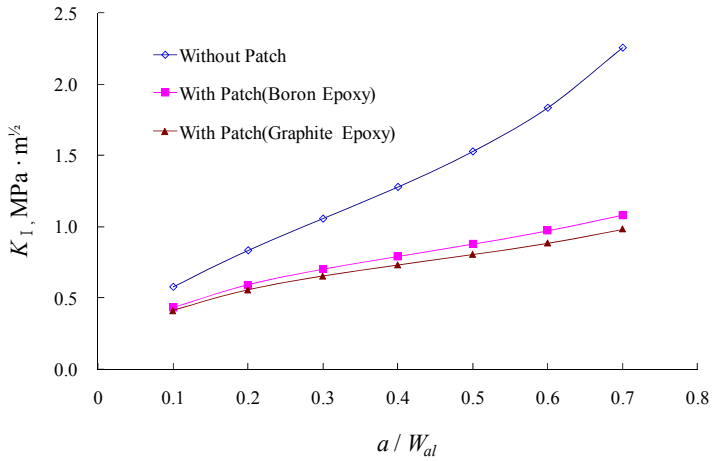

(a) Center crack

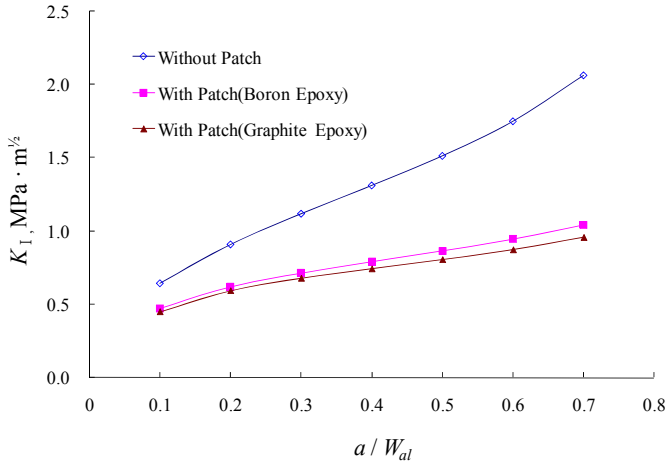

(b) Double-edge crack

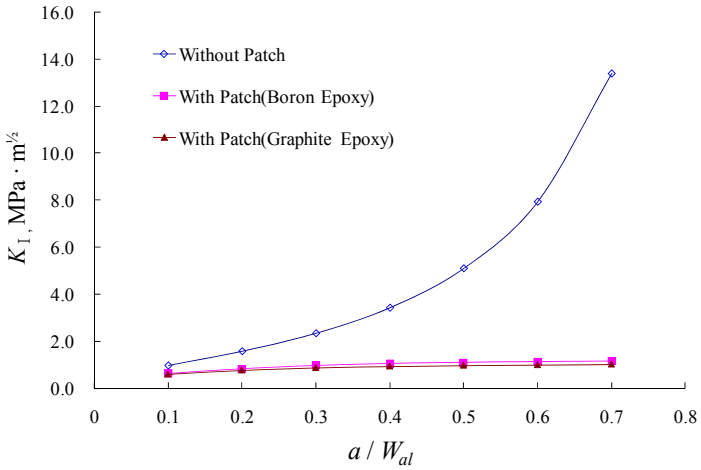

(c) Single-edge crack

Fig. 5.96 Variation of stress intensity factor with crack size

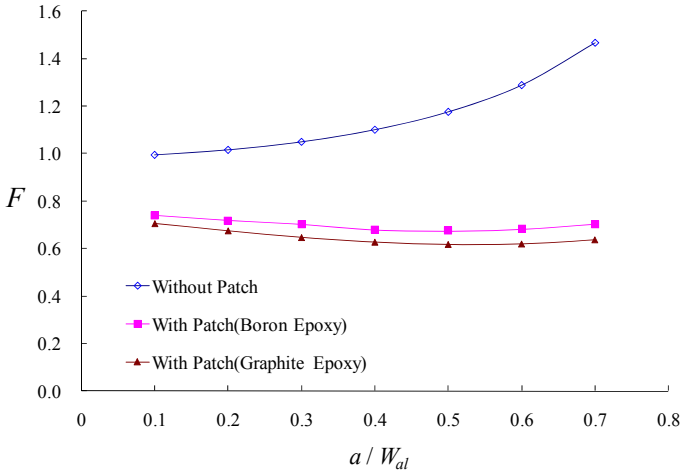

(a) Center crack

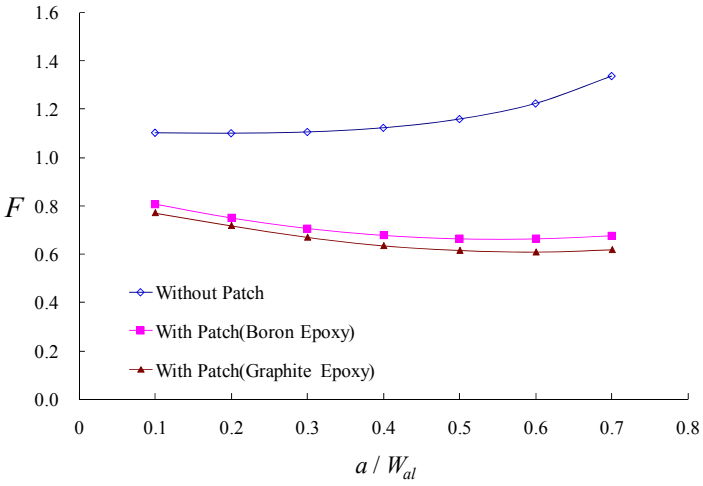

(b) Double-edge crack

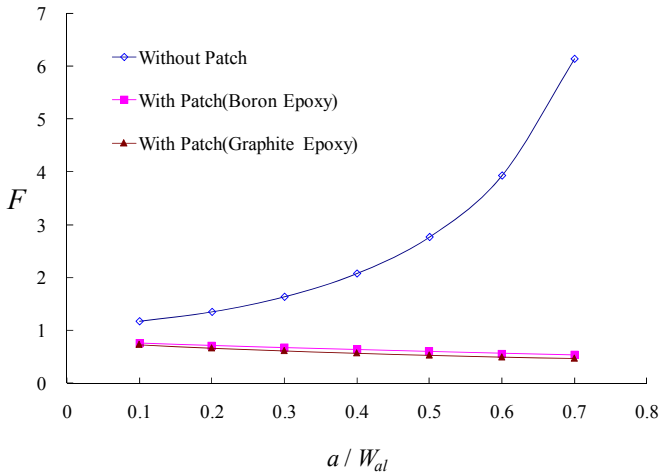

(c) Single-edge crack

Fig. 5.97 Variation of non-dimensional stress intensity factor with crack size

Fig. 5.98 shows the variation of σ_{yy} through the thickness at the crack tip of the center cracked plate without patch and with boron epoxy patch, respectively. Here, z represents the distance from upper surface of aluminum plate through the thickness, t, of the plate. As expected, Fig. 5.98 (a) shows that there is no variation in crack tip stress, confirming membrane behavior. On the other hand, in Fig. 5.98 (b), the value of σ_{yy}, as a function of the normalized distance from the top of patch, increases linearly, signifying bending in addition to membrane action. The maximum stress develops in the patch free surface of the plate. Moreover, it is seen that the slope of the rate of stress variation curve increases with crack size.

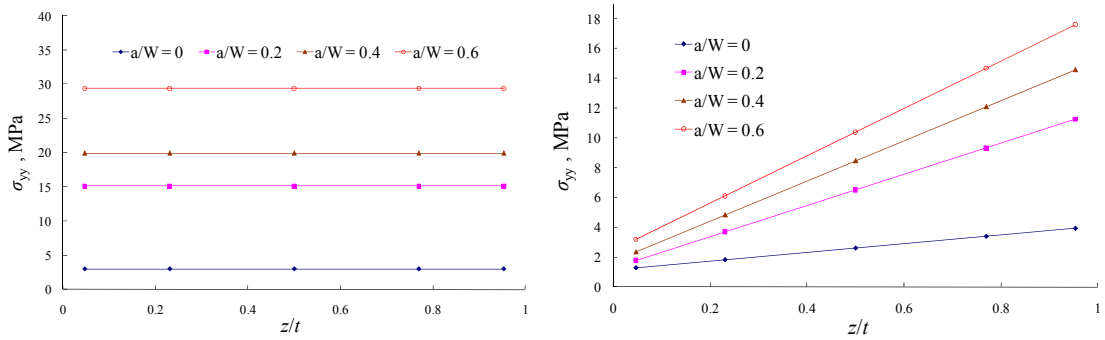

(a) Center crack without patch (b) Center crack with patch (boron epoxy)

Fig. 5.98 Thickness-wise variation of σ_{yy} at crack tip for different crack length

Fig. 5.99 shows the fringes of the normal stresses, σ_{yy}, in the boron epoxy patched surface, middle surface and patch-free surface of the plates when a/W_{al}=0.3. From Fig. 5.99 (a), it is seen that the stress singularity at crack tip get suppressed at the patched surface. The stresses over the patched region are found to be less than the average normal stress (σ_{yy} =3 MPa). However, at middle and free surfaces, high stresses are still induced

though of smaller intensity than those for the case with no patch. In addition, when the crack size ratio (a/W_{al}) is 0.6, the stress fringes for σ_{yy} in the aluminum plate with patch (boron epoxy) are shown in Fig. 5.100. As expected, in comparison to a/W_{al}=0.3, the stress concentration is more severe for a/W_{al}=0.6. In this respect, the behavior of center cracked plates is exhibited similarly in double-edge crack and single-edge crack cases as well.

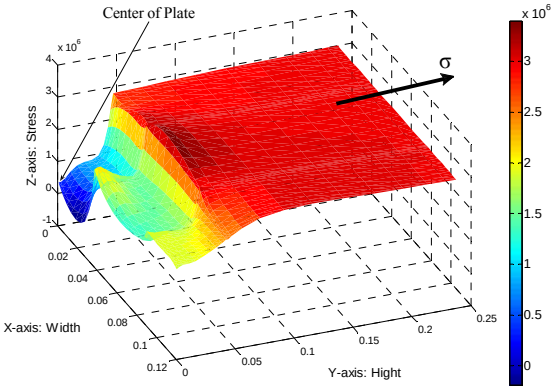

(a) Patched surface of plate

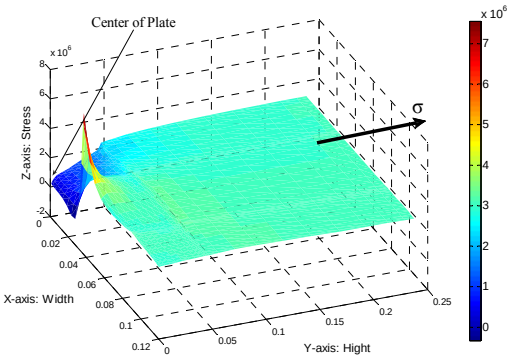

(b) Middle plane of plate

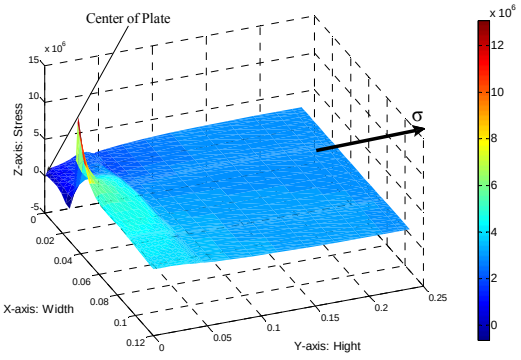

(c) Free surface of plate

Fig. 5.99 Fringes of stresses (σ_{yy}) with patch (a/W_{al}=0.3) (units: m and Pa)

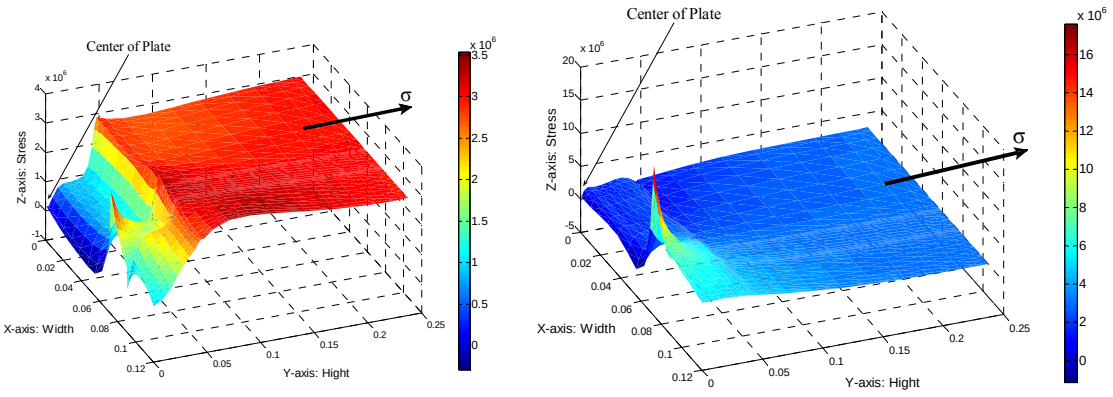

(a) Patched surface of plate (b) Free surface of plate

Fig. 5.100 Fringes of stresses (σ_{yy}) with patch (a/W_{al}=0.6) (units: m and Pa)

Fig. 5.101 (a) shows the variation of the ratio of strain energy stored in the center cracked plate, with total strain energy of the patched plate as crack size increases. Fig. 5.101 (b) displays the same results for patch-adhesive combination. As expected, a smaller share of the strain energy is stored in the patch material having higher stiffness; requiring the parent plate to store a larger shear of the strain energy of the system. In this respect, the adhesive plays a minor role.

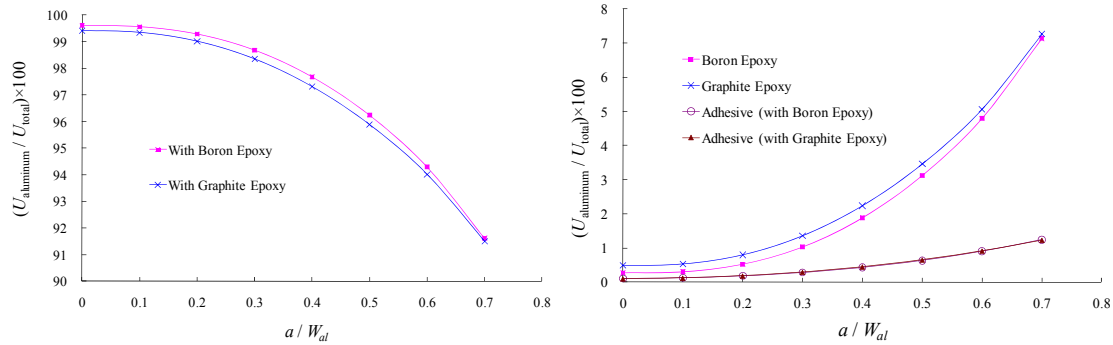

(a) Aluminum (b) Patch and adhesive

Fig. 5.101 Ratio of potential energy stored in each material in center crack

Similar behavior was noticed in the double-edge cracked case as well. In the case of patched single-edge crack case, Fig. 5.102 shows the variation of ratio of strain energy stored in each material with respect to total strain energy, as crack size increases. It is observed that when $a/W_{al} > 0.3$, the energy ratio of boron epoxy is more than that of graphite epoxy, unlike the case of single edge crack.

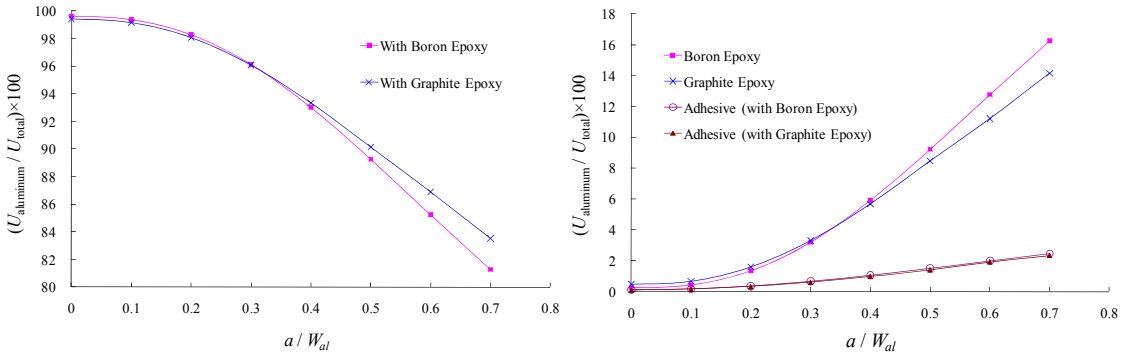

(a) Patch and adhesive (b) Aluminum

Fig. 5.102 Ratio of potential energy stored in each material in single-edge crack

Fig. 5.103 shows the variations of the ratio of each material's resistance force with respect to the total resistance force for center, double-edge and single-edge crack cases, respectively, when boron epoxy is used as the patch material. In the Fig. 5.103, R refers to resistance force against crack extension. Resistance forces can be calculated by taking the derivative of each material's strain energy, assuming that, due to the presence of patch, crack growth will be prevented at any crack length. In center and double-edge crack cases, it is noticed that boron epoxy has greater resistance against crack growth than aluminum when $a/W_{al} > 0.5$ and in the case of single-edge crack it occurs at $a/W_{al} > 0.2$. Also, it is found that the resistance force ratio of the adhesive material tend to increase slightly with the crack length.

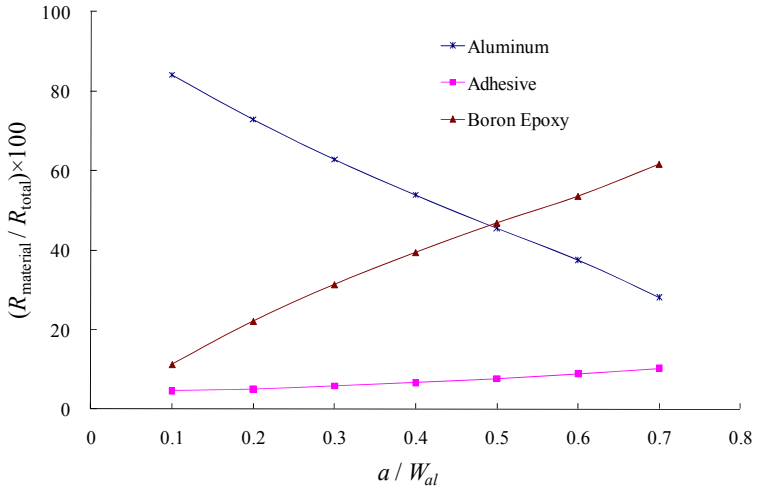

(a) Center crack

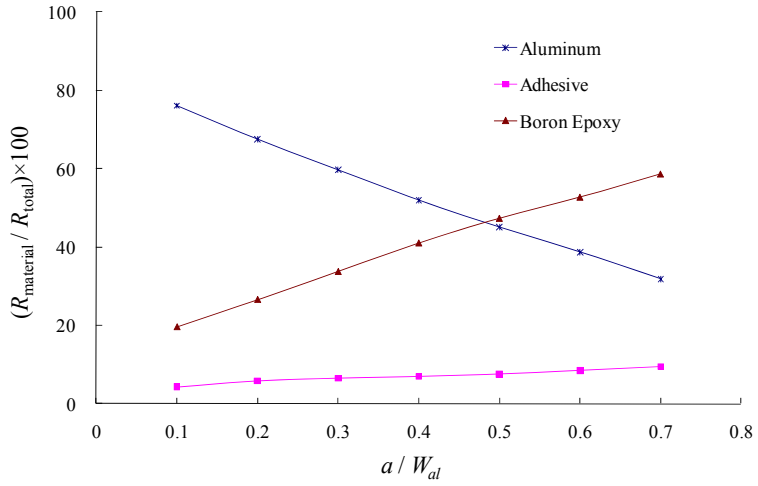

(b) Double-edge crack

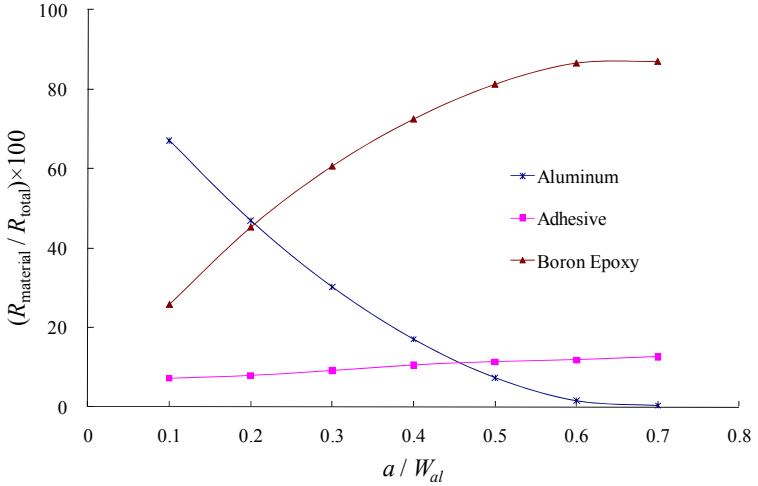

(c) Single-edge crack

Fig. 5.103 Ratio of resistance force against crack growth

5.5.3 Single-Edge Cracked Plate Repaired by Composite Patch

The objective of this example is to investigate efficient strategy for modeling externally repaired plates, to see characteristic of single-sided patch repair, and to undertake parametric studies. A single-edge-crack aluminum plate is shown in Fig. 5.104 as repaired by a bonded glass epoxy patch.

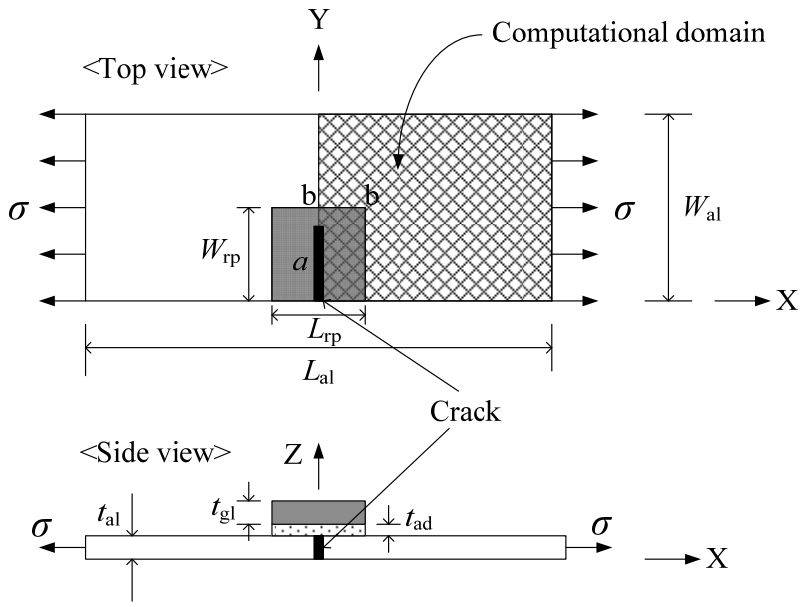

Fig. 5.104 Configuration of single-edge-crack plate with externally bonded repair

The aluminum plate and repair materials have the following dimensions: length of plate, L_{al} = 200 mm, width of plate W_{al} = 40 mm, thickness of aluminum, t_{al} = 1.5 mm, length and width of repair area, $L_{rp} = W_{rp}$ = 26 mm, thickness of glass epoxy patch, t_{gl} = 1.4 mm, and thickness of adhesive film, t_{ad} = 0.2 mm. The aluminum plate is subjected to a uniaxial tensile load of 3.5 kN giving a remote stress state of σ = 58.33 MPa. Since the geometry and loading are symmetric with respect to Y-axis, only one half of the whole domain is analyzed. The material properties of the aluminum plate, glass epoxy, and

adhesive film are given in Table 5.19.

Table 5.19 Material properties (unit: GPa)

	E_1	E_2, E_3	v_{12}, v_{13}	v_{23}	G_{12}, G_{13}	G_{23}
Aluminum	70	-	0.32	-	-	-
Glass Epoxy	38.6	8.27	0.168	0.035	4.14	3.14
Adhesive film	2.2	-	0.32	-	-	-

The main objectives of current analysis can be stated as follows.

(1) Verification of proposed elements in an un-patched case

(2) Identification of efficient models in the patched case

(3) Influence of single-side patch on plate behavior

(4) Influence of selected parameters on performance of patch repair

(5) Comparison of single- and double-side patch performance

(1) Verification of proposed elements in an un-patched case

The chosen mesh in the XY-plane, shown in Fig. 5.105, is used in 2D, 3D, and mixed modeling. Only ESLM-based elements are considered for 2D modeling, and FDLM-based elements are used for 3D modeling. Also, for mixed modeling, a combination of ESLM- and FDLM-based elements is considered, with FDLM appearing in critical local regions of the problem domain and ESLM in the remaining domain, and to avoid discontinuities in displacement values DLTM-based elements are used between ESLM and FDLM. The values of stress intensity factor based on these models are obtained both by the total strain-energy release rate method and VCCT. In Table 5.20, good agreement

is noted between current model values and reference values for non-patched plates. One of the two references (Umanaheswar and Singh, 1999) uses analytical solution; the other uses modified crack closure integral method with 3D solid elements.

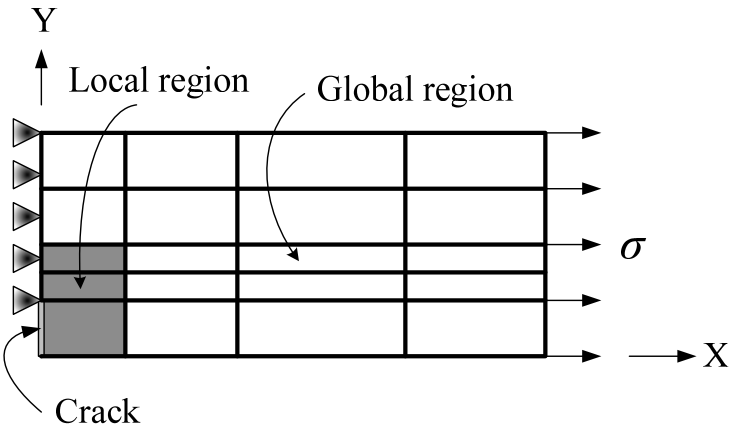

Fig. 5.105 Finite element 4×5 meshes on XY-plane for some models

Table 5.20 Comparison of stress intensity factors in non-patched plate ($\mathrm{MPa}\sqrt{\mathrm{mm}}$)

Types		Crack length		
		10 mm	14 mm	18 mm
Reference (Umanaheswar and Singh, 1999)	Analytical	491.42	719.10	1062.53
	3-D solid elements	484.14	712.77	1051.77
ESLM-based model	SERR	484.39	711.75	1050.32
	VCCT	489.02	717.49	1066.22
FDLM-based model	SERR	484.77	712.69	1053..20
	VCCT	490.17	718.67	1064.92
Mixed model	SERR	484.04	712.66	1053.15
	VCCT	489.85	716.64	1062.60

(2) Identification of efficient models in the patched case

Fig. 5.106 shows the mesh configurations solid elements for *h*-FEM and present *p*-FEM models, respectively. In order to reduce the number of elements and hence the required DOF in the *h*-FEM model, graded mesh densities are used with finer mesh biased near the crack region, as shown in Fig. 5.106 (a) (Umamaheswar and Singh, 1999). However, in *p*-FEM, such mesh refinement is unnecessary because the same effect can be realized by adding shape functions of sufficiently high order. Moreover, because of robustness of *p*-FEM when higher-order shape functions (*p*-level ≥ 5 or 6) are used, the aspect ratio of elements is not an issue, unlike the situation with *h*-FEM. These factors lend to a simple modeling scheme, as shown in Fig. 5.106 (b). In order to identify the most efficient modeling scheme based on the proposed *p*-FEM elements, three models are considered. In all three models (A, B, and C), a 4×5 mesh in the XY-plane is used, as shown in Fig. 5.106. Model A is composed of FDLM-based elements alone, and Model B and C are mixed models comprising of a combination of 2D and 3D elements placed in different configurations. In Model B, the region of the plate outside the patched area is modeled with ESLM-based elements while the patched region is modeled with FDLM-based elements. In the case of Model C, ESLM-based elements are used in both the unpatched region and the cross-checkered region of the patch, as shown in Fig. 5.106 (b). The small shaded region around the crack is modeled with FDLM-based elements. In all three models, the aluminum plate, adhesive, and composite material, are represented by only one layer in each. Taking advantage of one-way symmetry with respect to the crack line, only one-half of the plate is considered. The crack in the plate is assumed to extend to the adhesive layer as well and crack faces in both are treated as free surface.

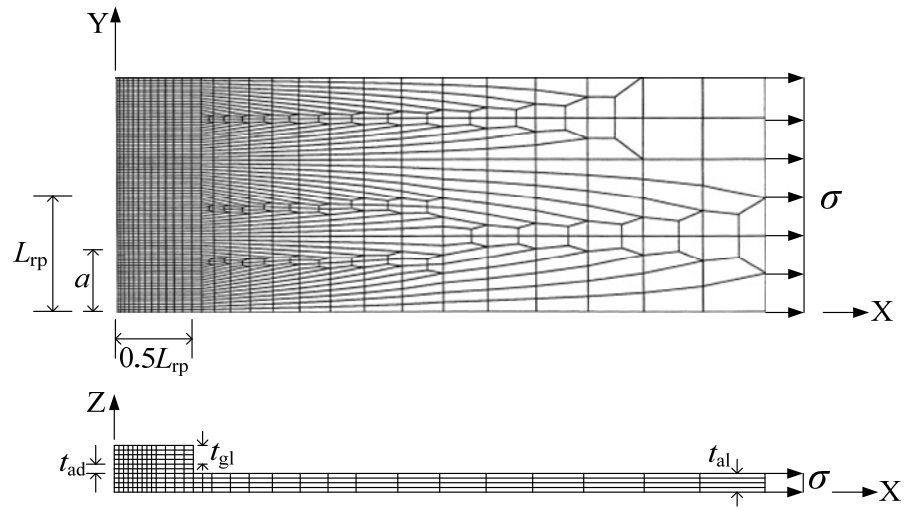

(a) Mesh strategy based on *h*-FEM

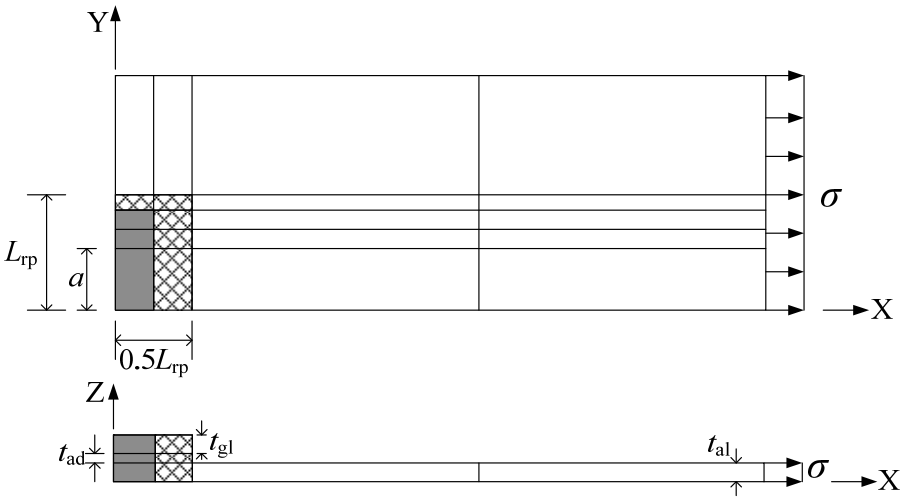

(b) Mesh strategy based on *p*-FEM

Fig. 5.106 Mesh configurations for *h*- and *p*-FEM based analyses

Unlike the behavior of unpatched plates, a combination of membrane and bending actions is expected to occur in a single-sided patch repaired plate. As a result, the stress intensity factor for such a plate is expected to vary along its thickness. Therefore, an average value of the stress intensity factor (K_{avg}) is considered as the representative value for the purpose of comparing the current results with the previously published results

(Umamaheswar and Singh 1999) using 3D solid elements when crack length is 15 mm. The results are shown in Table 5.21. The *p*-levels used in the current models are 7 for planer variations of displacement and 3 for thickness wise variation. For the most part, the discrepancies are found to be within 3%. In general, the results by current models and conventional solid element model show good agreement. However, the SIF values obtained by SERR method seem to be overestimated, though slightly, as compared to those by VCCT. Table 5.22 shows the number of elements and NDF used in each of the three current models, as well as the *h*-FEM model. Based on the numbers presented, Model C can be regarded as more efficient than the others.

Table 5.21 Average SIFs (K_{avg}) in patched plate with 15 mm crack ($\text{MPa}\sqrt{\text{mm}}$)

Types		Stress intensity factors
3-D solid elements (SERR method)		341.84
Model A	SERR method	346.94
	VCCT	337.29
Model B	SERR method	347.10
	VCCT	337.30
Model C	SERR method	344.35
	VCCT	334.34

Table 5.22 Comparison of the number of elements and degrees of freedom

	The number of elements	NDF
h-FEM using 3-D solid elements	10,920	40,176
Model A	36	9,992
Model B	36	8,037
Model C	17	4,868

(3) Influence of single-side patch on plate behavior

Fig. 5.107 shows the stress fringes of σ_{xx} at bottom, middle, and top surfaces, respectively when FDLM-based elements solely are used in the mesh, such as Model A considered in the preceding sub-section. Such results are also shown for the mixed models B and C. It is evident that the nature of stress distribution is dependent on the location of the reference plane across the thickness of the plate with single-sided patch; whereas, the stress distribution across the plate thickness happens to be constant in the un-patched case. Also, in the patched case the free surface (at bottom of plate) the stresses near the crack tip are found to be larger than those in the other two reference surfaces.

The expected variation of SIFs through the thickness cannot be represented by SERR method which is based on the change of total strain energy release rate of the whole domain and, instead, a method like VCCT needs to be used. Normally, 3D VCCT can determine only one value of SIF within a considered layer in the thickness direction. The value obtained can be regarded as the SIF at the middle of that layer. To determine the variation of SIF across a layer, it needs to be discretized into more layers. Fig. 5.108 shows the variation of K_{I} through the thickness when the aluminum plate is discretized into two, three, and four layers, respectively, and FDLM-based elements are considered. It is evident that the SIF tend to vary linearly across the plate thickness. Table 5.23 summarizes the results of SIFs and NDF for the three model of types A, B, and C discussed above. It is seen that though Model C is more efficient than Model B, yet these two models demand significantly less computational resources than Model A, comprising of only FDLM-based elements. However, there is little difference in the accuracy of

results obtained by the three model types. Fig. 5.109 shows the comparison of thickness-wise variations of SIFs between unpatched case and single-patched case. Fig. 5.110 shows that the slope of SIF line in the thickness direction are dependent on crack size.

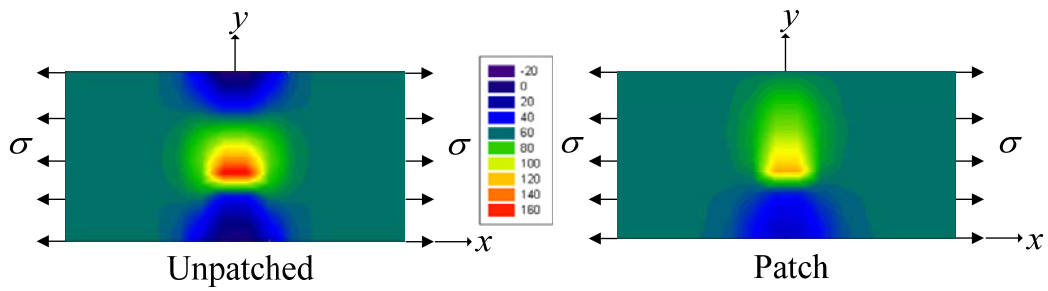

(a) Bottom surface

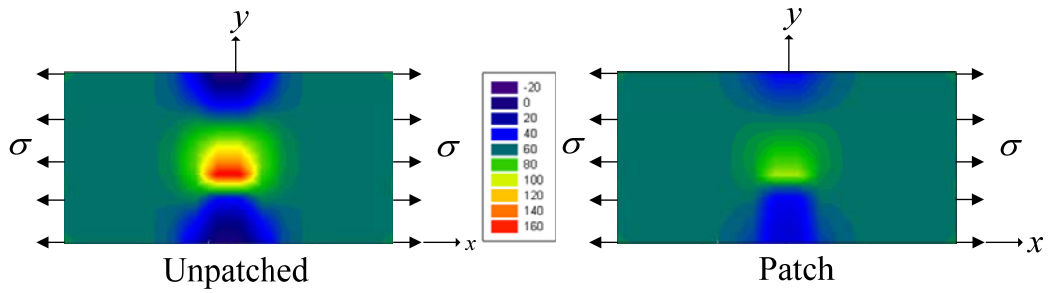

(b) Middle surface

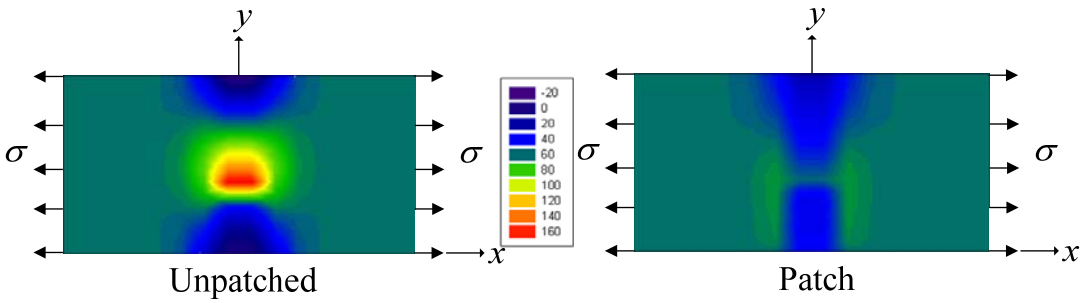

(C) Top surface

Fig. 5.107 Stress fringes of σ_{xx} in the plate

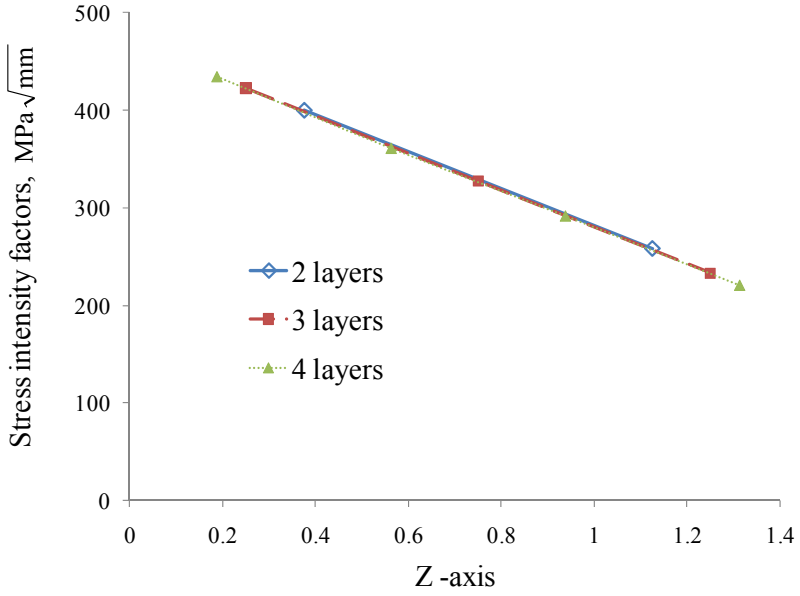

Fig. 5.108 Thickness-wise variation of K_I with the number of layers used

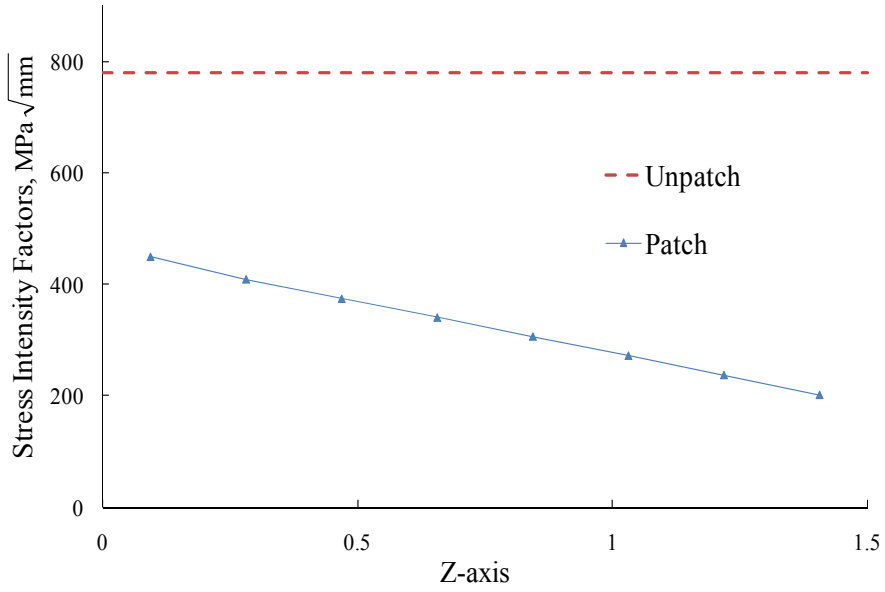

Fig. 5.109 Thickness-wise variation of K_I for unpatched, patched cases

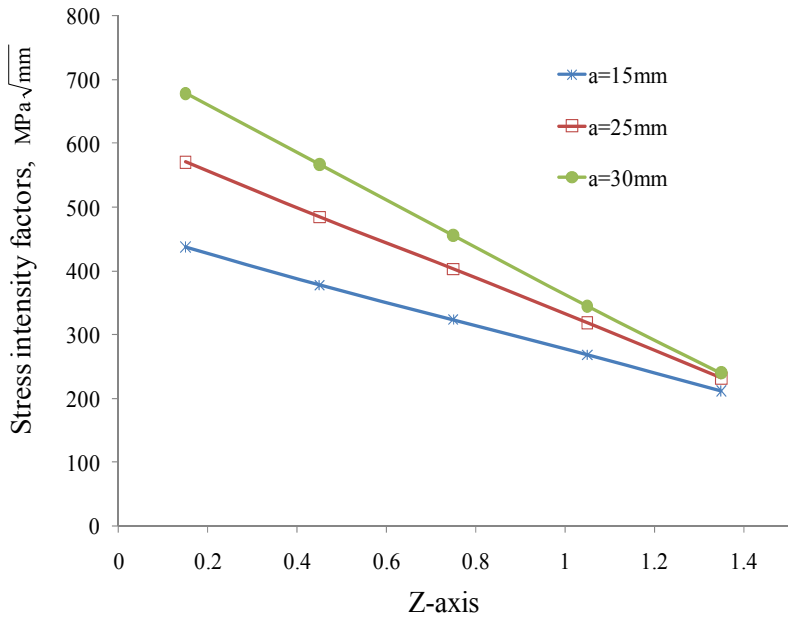

Fig. 5.110 Thickness-wise variation of K_I for three crack sizes

Table 5.23 Comparison of the number of elements and number of degrees of freedom

	Types	Stress intensity factors (K)		NDF
2 layers	Model A	Top layer Bottom layer	258.236 400.678	14,531
	Model B	Top layer Bottom layer	258.241 400.391	10,035
	Model C	Top layer Bottom layer	257,001 396.335	5,726
3 layers	Model A	Top layer Middle layer Bottom layer	232.955 327.142 422.852	19,070
	Model B	Top layer Middle layer Bottom layer	232.959 327.152 422.864	12,033
	Model C	Top layer Middle layer Bottom layer	232.162 324.688 418.364	6,584

(4) Influence of selected parameters on performance of patch repair

Having identified an efficient modeling scheme and an understanding of SIF determination in single-sided patch repaired plates, this section undertakes the parametric studies to determine the influence of some of the design variables on the performance of the patch repaired plate. SIF at the middle surface, K_I^{mid}, is considered as the representative value.

Fig. 5.111 shows the variation of SIFs as a function of patch length measured in the direction normal to the crack direction in the 2D plane for a crack size, a = 15 mm. It is found that if the patch length is taken as two times the crack size, a, the reduction in SIF can be approximately 54 %. Fig. 5.112 shows the influence of patch thickness on SIF. It is seen that when patch thickness is same as thickness of aluminum plate and the ratio, L_{rp}/a, is over about 1, the reduction of SIF is 57% as compared to unpatched plate. Also, SIF can be reduced by 69% for t_{gl}/t_{al} = 2.0. However, a thickness exceeding t_{gl}/t_{al} = 1.0 seems to be impractical.

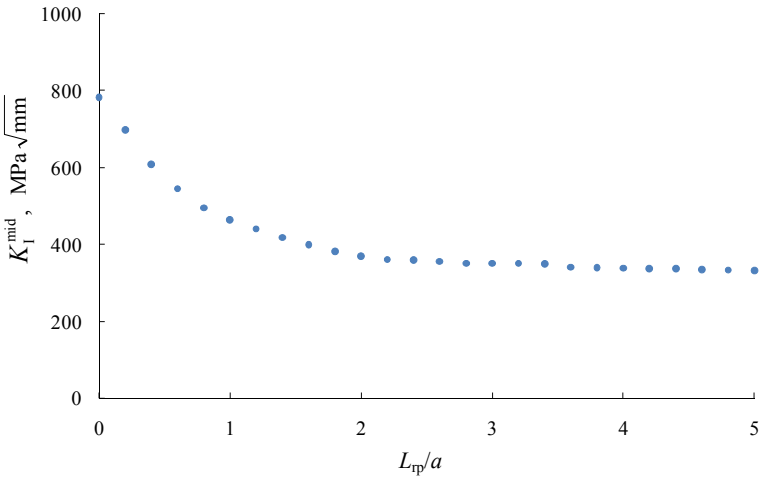

Fig. 5.111 Variation of K_I^{mid} with patch length

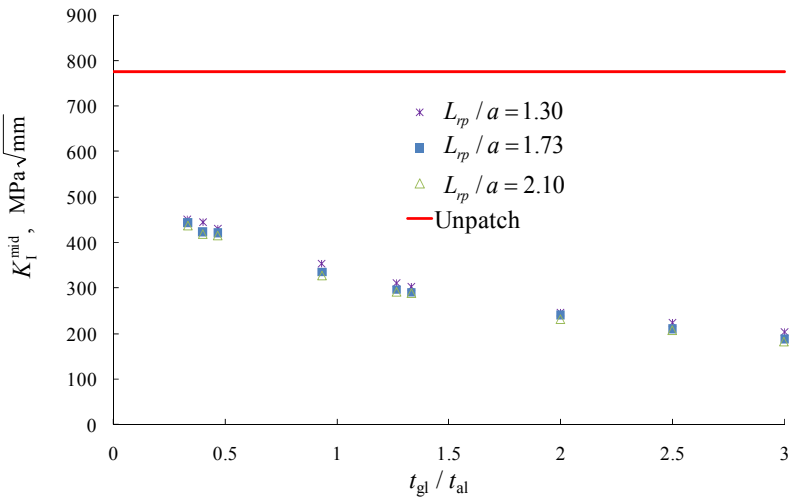

Fig. 5.112 Variation of K_I^{mid} with patch thickness

In patch repaired plates, the SIF value shows an asymptotic behavior with increase in crack length. The effects of adhesive thickness, patch material, patch size, and patch thickness on SIF are also investigated. The crack size is increased from $a/W_{al} = 0.1$ to 0.8. The crack tip For $a/W_{al} > 0.65$, the crack tip extends beyond the patch region. Fig. 5.113 shows the variation of SIFs with adhesive thickness. The results indicate that smaller adhesive thicknesses are desirable because thicker adhesive thickness tend to accentuate bending action. Fig. 5.114 shows the variation of SIFs with patch thickness. Unlike adhesive thickness, the use of thicker patch is may sometimes be advantageous. It is noticed that the positive effect of reinforcement can be greater larger than the negative effect resulting from the shift of neutral axis away from the middle surface of the plate as the patch thickness increases. However, too large a patch thickness would be impractical and unnecessary.

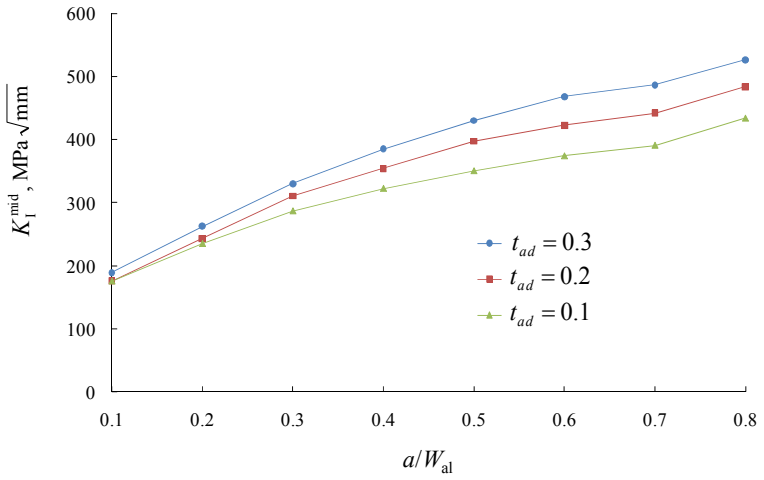

Fig. 5.113 Variation of K_I^{mid} with crack size for different adhesive thicknesses

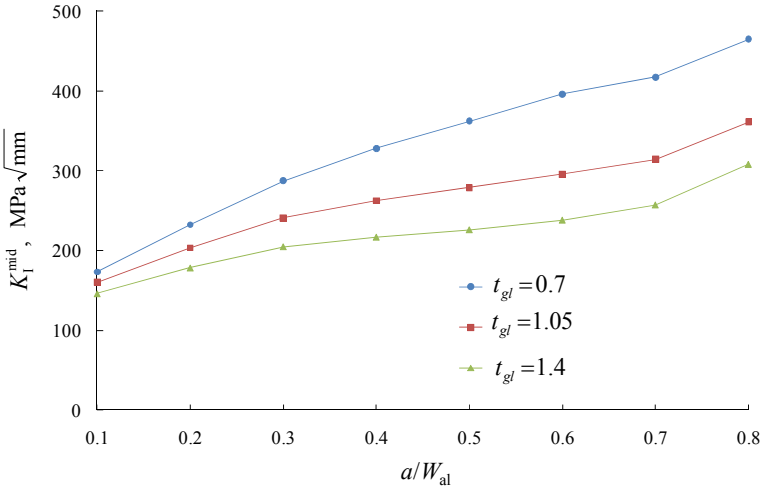

Fig. 5.114 Variation of K_I^{mid} with crack size for different patch thicknesses

Fig. 5.115 shows the variations of SIFs with respect to planar dimensions of the patch. Three cases with identical thickness, t_{gl} = 1.4 mm are considered. When crack sizes are small (namely, $a/W_{al} \leq 0.4$), it is seen that SIF is independent of the size of patch. However, as crack size is increased, the size of patch has noticeable effect on the values of SIF. Also, it is noted that the patch length in a direction normal to crack line has more

influence than the size in crack direction. The effect of material properties of patch is shown in Fig. 5.116. The considered patch materials are glass epoxy, boron epoxy, which is stiffer than glass epoxy, and. The material properties of boron epoxy are as follows: E_1 = 208.1 GPa, $E_2 = E_3$ = 25.44 GPa, $\nu_{12} = \nu_{13}$ = 0.168, ν_{23} = 0.035, $G_{12} = G_{13}$ = 7.24 GPa, and G_{23} = 4.94 GPa. From the results shown in Fig. 5.116, it is noticed that damaged plate can take favorable turn by stiffer patch material.

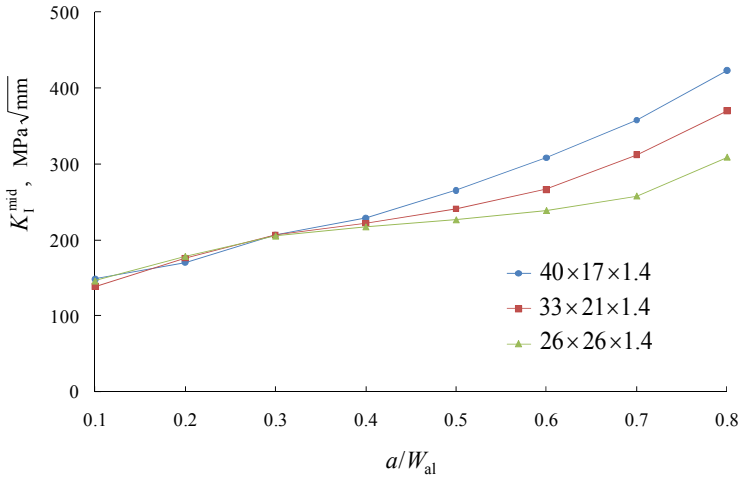

Fig. 5.115 Variation of K_I^{mid} with crack size for different patch size

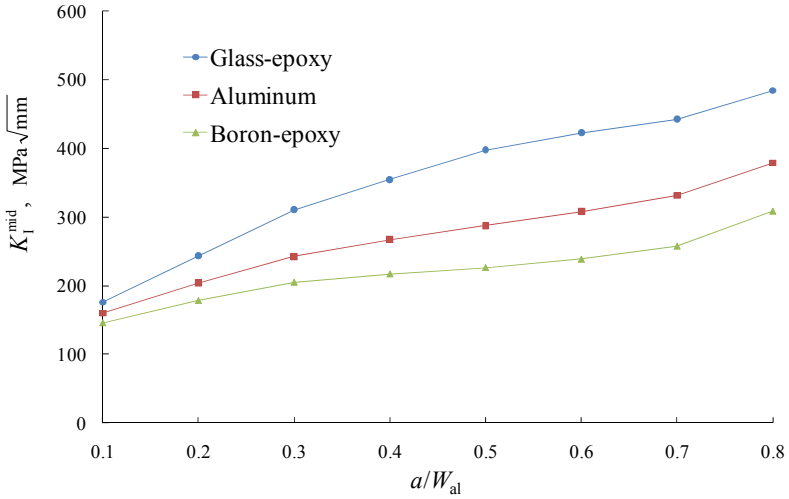

Fig. 5.116 Variation of K_I^{mid} with crack size for different patch materials

(5) Comparison of single- and double-sided patch performance

Fig. 5.117 presents the variation of SIFs according to the crack size for single- and symmetrically double-sided patches. Total thicknesses of the two patch types are same. It can first be noted that the deformation appears to be symmetric in both the cases as long as the crack tip appears well within the patch region ($a/W_{al} \leq 0.65$). Also, there is a reduction in the plateau part of the curve to about 40~50% with the double-sided patch. This observation signifies that such repair can improve the fatigue life of the repaired component.

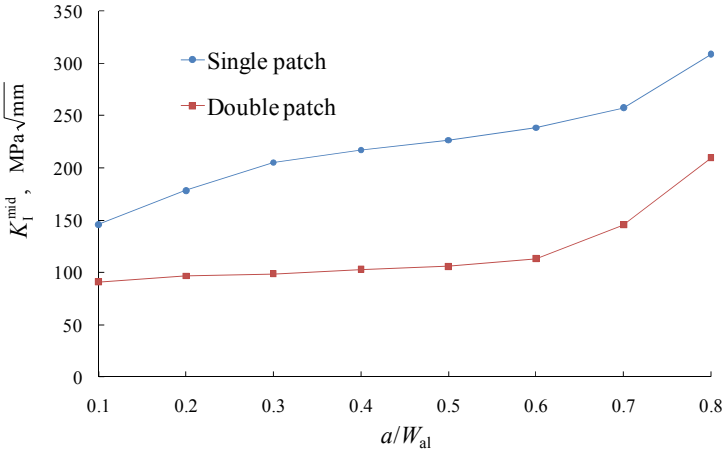

Fig. 5.117 Variation of K_I^{mid} in single- and double-sided patches

Fig. 5.118 shows the variation of transverse deflection at crack tip with increase in crack size. While the transverse deflection of double-sided patch are approximately close to be zero, the deflection of single-sided patch get increasingly larger with crack size. Fig. 5.119 presents the variation of normal stress resultants at crack tip of the aluminum plate with crack size. In the case of single patch, the line of normal stress resultant with respect to crack length has approximately a constant slope. In the case of double patch, on the

other hand, when crack tips are within the patched region, the slop of the line is close to be zero. If, however, the crack tip crosses over into the unpatched region, the line has a slope similar with that of the single patched case. Fig. 5.120 shows the variation of bending stress resultants with respect to crack size for single- and double-sided patches. It is noticed that bending moments hardly present in the case of double-sided patch; whereas, single patched plates develop considerable bending moment. Moreover, the line for single patch shows a discontinuity at the edge of the patch where $a/W_{al} = 0.65$.

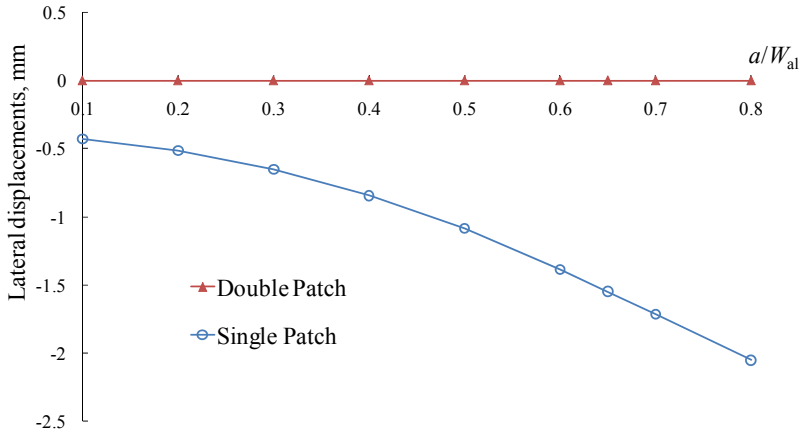

Fig. 5.118 Variation of deflection in single- and double-sided patches

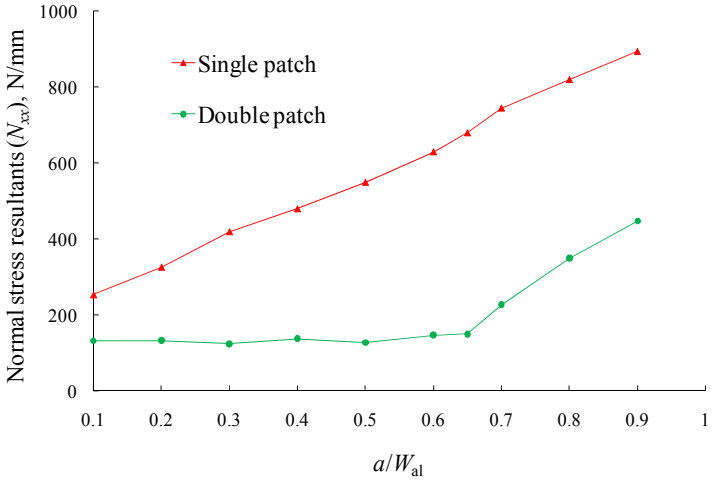

Fig. 5.119 Variation of normal stress resultants in single- and double-sided patches

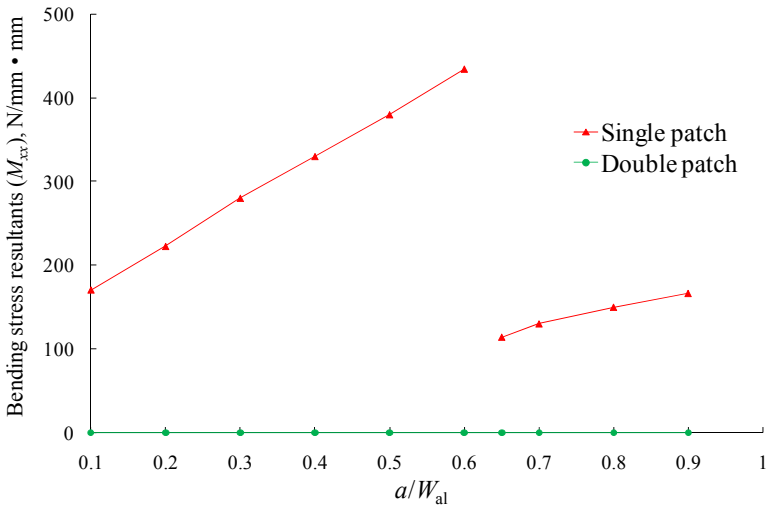

Fig. 5.120 Variation of bending stress resultants in single- and double-sided patches

In order to further investigate the underlying cause of such behavior at the edge of the single-patched region when a/W_{al} = 0.65, the distributions of normal and bending stress resultants along line b-b shown in Fig. 5.104 are plotted in Figs. 5.121 and 5.122, respectively. There exist two elements near crack tip on line b-b. One element is within patched region, and the other element is outside. The results of membrane behavior for the two elements are almost similar, although there is a slight difference, as shown in Fig. 5.121. On the other hand, the results of bending behavior obtained based on the same two elements have considerable difference, as shown in Fig. 5.122. Actually, bending moments in the patched region are found to be much larger than outside it. Such behavior is the underlying reason for the discontinuity in the line plotted in Fig. 5.120. Also, it is seen that high stresses at crack tip are the combined effect of membrane and bending responses.

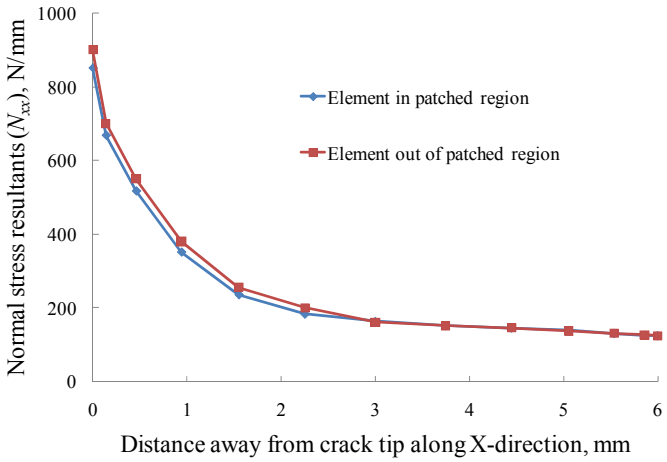

Fig. 5.121 Distribution of normal stress resultants at edge of patched region

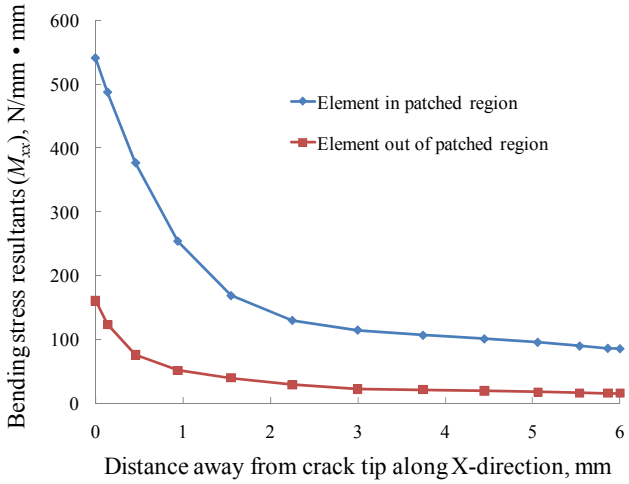

Fig. 5.122 Distribution of bending stress resultants at edge of patched region

5.6 Delamination Analysis Using VCCT

One of major failure modes of laminates composites is delamination. There are two basic approaches to characterize the delamination process. One involves the direct application of fracture mechanics. The other involves indirect application of fracture mechanics in the context of damage mechanics and/or softening plasticity, including the

application of cohesive models and interface elements. The main disadvantage of the first approach is that it cannot consider the initiation of the delamination process and also the case when more than one delamination processes are involved. The objective of the present analysis is, however, to examine the direct approach only by applying VCCT to finite element models based on the proposed elements. Two examples are considered – (a) the double cantilever beam (DCB) problem, and (b) the interior delamination problem.

5.6.1 Double Cantilever Beam Problem

The DCB problem represents a standard specimen for determining mode I energy release rate. The DCB problem considered here consists of unidirectional fiber-reinforced material with the length, L = 0.185 m, width, W = 0.025 m, and two layers of 2.5 mm thickness (t) each, as shown in Fig. 5.123.

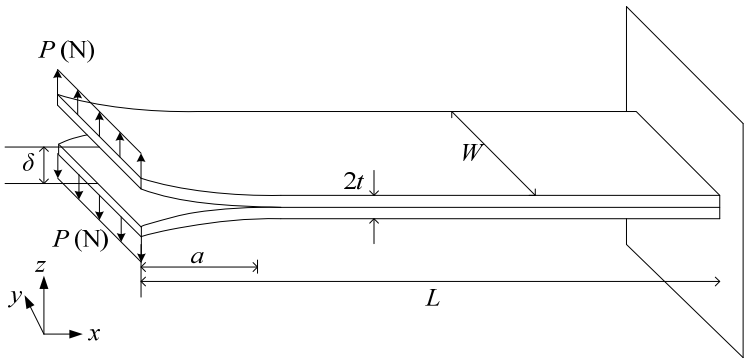

Fig. 5.123 Double cantilever beam

The initial length of the crack is 55 mm. The material properties are shown in Table 5.24. Taking advantage of two-way symmetry with respect to y- and z-directions, only one-quarter of the specimen is treated as the computational domain. Fig. 5.124 (a) shows the

conventional 3D model configuration used for *h*-FEM analysis (Kruger, 1994). The model used for present analysis is shown in Fig. 5.124 (b).

Table 5.24 Properties for DCB specimen (unit: GPa)

E_1	$E_2 = E_3$	$G_{12} = G_{13}$	G_{23}	$\nu_{12} = \nu_{13}$	ν_{23}	G_{Ic}
135 GPa	9 GPa	5.2 GPa	1.9 GPa	0.34	0.46	281 J/m^2

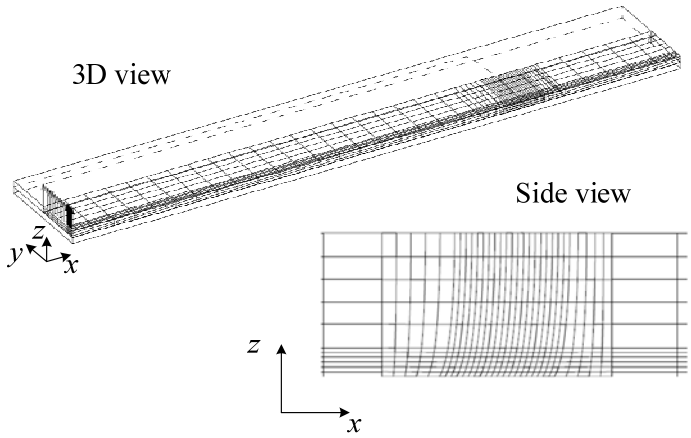

(a) *h*-FEM based 3D Model

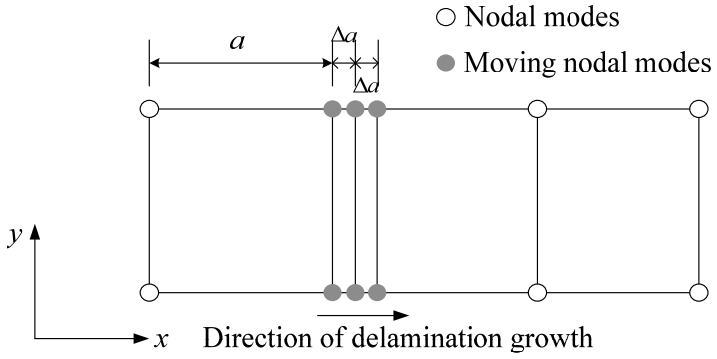

(b) Mesh configuration on *xy*-plane for present analysis

Fig. 5.124 Comparison of present mesh and *h*-FEM mesh

It can be seen that the mesh on *xy*-plane is composed of five FDLM-based elements placed in a single layer, unlike the *h*-FEM mesh shown in Fig. 5.124 (a), where a number of elements are used in the thickness direction. In the current model, *p*-levels of 8 and 3 are used to represent in-plane and out-of-plane behaviors, respectively. To simulate initiation and growth of delamination, energy rerelease rate computed by VCCT is utilized. In Fig. 5.124 (b), virtual crack closure length, Δa, is taken as 0.25 mm. Displacement-increment analysis is implemented as displacement δ increases by 0.01 mm ~ 0.25 mm. Before initiation of delamination, Eq. 5.14 is valid.

$$\frac{G_{\mathrm{I}}}{G_{\mathrm{I}c}} < 1 \tag{5.14}$$

The initiation of delamination occurs when the energy release rate (G_{I}) for a displacement increment is same as the critical energy release rate ($G_{\mathrm{I}c}$) corresponding to fracture toughness. Then, in the next procedural step, the crack length is increased by $2\Delta a$. Thereafter, for simulating delamination growth, it is checked if Eq. 5.15 is satisfied with the increase of displacement δ.

$$\frac{G_{\mathrm{I}}}{G_{\mathrm{I}c}} \approx 1 \tag{5.15}$$

By satisfying Eq. 5.15, displacement δ is obtained and delamination progresses forward again by $2\Delta a$. During the growth of delamination, the coordinates of movable nodes shown in Fig. 5.124 (b) are modified. The progress of delamination is achieved by repeated application of the above procedure.

Fig. 5.125 shows the variation of energy release rate with increase of displacement δ before the initiation of delamination. Also, in order to verify the validation of present delamination analysis, the results of force-displacement curves from reference (Meo and

Thieulot, 2005) including experimental as well as the *h*-FEM results and the current analysis results are plotted in Fig. 5.126.

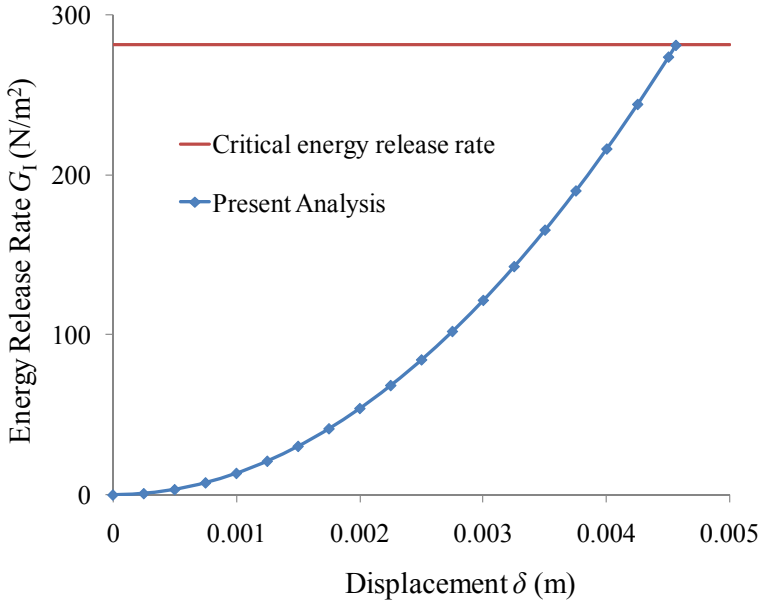

Fig. 5.125 Displacement-energy release rate curve before initiation of delamination

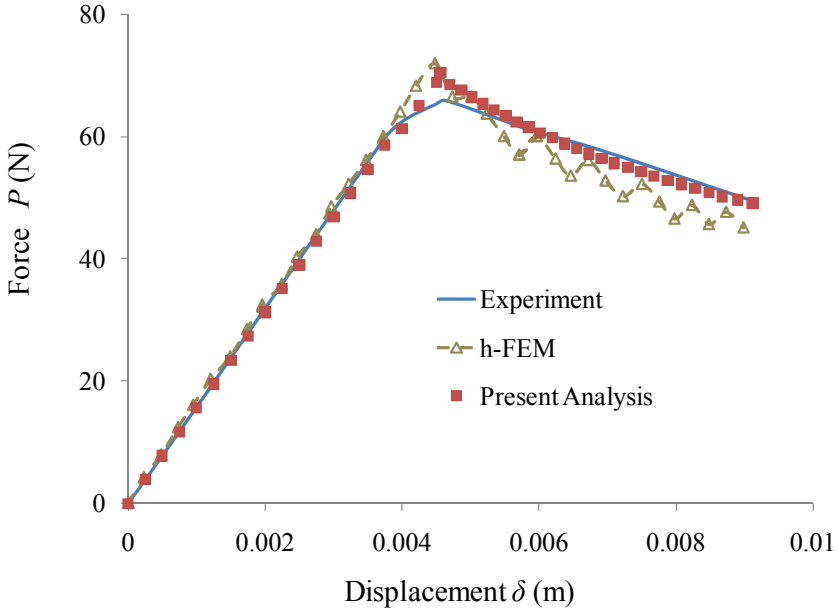

Fig. 5.126 Applied force vs. opening displacement of delamination curve

In reference (Meo and Thieulot, 2005), the numerical analysis is based on conventional solid elements and *Birth and Death* option based on VCCT used in the commercial code (ANSYS) was utilized. For simulating the growth of delamination, the option is to deactivate selected elements which are not actually removed from the model. In order to follow the delamination process closely, it calls for the use of a significant number of very small elements next to the expected path of delamination growth. Contrary to this strategy, in the current analysis, change of position of some nodes only is required. Unlike the existing *h*-FEM based models, in the current case, the resulting changes in the aspect ratio of elements do not affect the results, due to the inherent robustness of *p*-FEM based models. The maximum loads and corresponding opening displacements are shown in Table 5.25.

Table 5.25 Loads and opening displacements in delamination initiation

Experiment		*h*-FEM		Present analysis	
P	δ	P	δ	P	δ
65 N	4.6 mm	71 N	4.5 mm	70.4 N	4.56 mm

Fig. 5.126 shows that the current results are in good agreement with the reference values (Meo and Thieulot, 2005). Although, small discrepancy is noticed between the current result and the test data near the point of initiation of delamination, the good agreement with *h*-FEM results is notable. The delamination segment of the plot based on current results shows no oscillation as in the experimental data and unlike *h*-FEM results which show significant oscillations. Fig. 5.127 shows the variation of length of delamination with the increase in opening displacement.

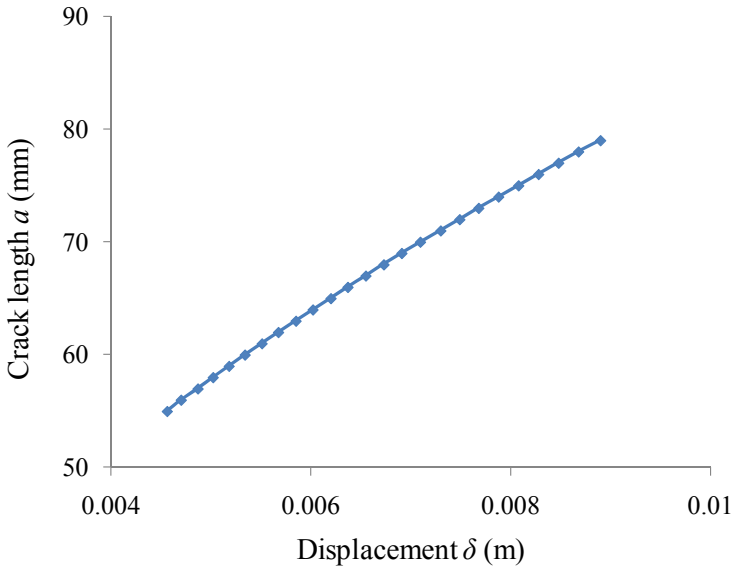

Fig. 5.127 Crack length-opening displacement curve

5.6.2 Interior Delamination Problem

In this example, a four-layer (90°/0°/0°/90°) laminate square plate with interior delamination shown in Fig. 5.128 is considered. Each layer comprises of a unidirectional fiber reinforced composite with the following material constants.

$$E_1 = 25\times10^6 \text{ psi};\quad E_2 = E_3 = 1\times10^6 \text{ psi};$$
$$G_{12} = G_{13} = 0.5\times10^6 \text{ psi};\ G_{23} = 0.2\times10^6 \text{ psi};\quad \nu_{12} = \nu_{13} = \nu_{23} = 0.25 \tag{5.16}$$

The side length of the square plate with interior crack a subjected to distributed uniform transverse load (q=10 psi) is $2L$=1 in and the thickness h=0.1 in. Location of delamination is at the interface of two inner layups, as shown in Fig. 5.128. Due to biaxial symmetry, only one-quarter of the plate is modeled. The 3×3 mesh used in the xy-plane for present analysis is shown in Fig. 5.129. Also, for modeling along the plate thickness, only four layers are considered which is identical with the number of layups in the plate.

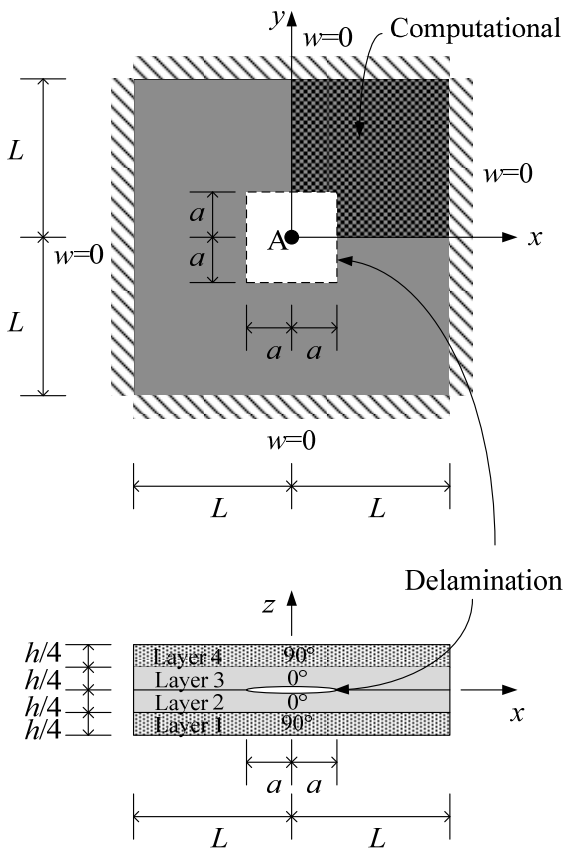

Fig. 5.128 Geometry and coordinate system used for the laminated square plate with interior delamination

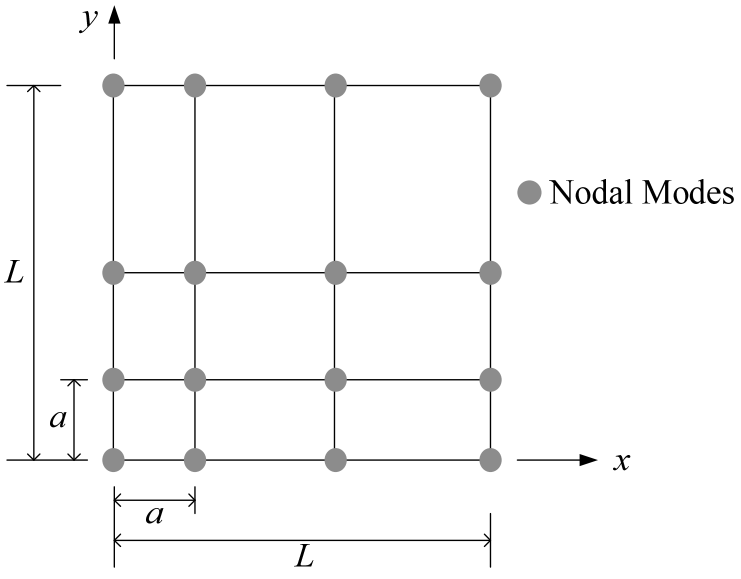

Fig. 5.129 Modeling scheme

Fig. 5.130 shows variation of deflection in the middle surface at Point A (in Fig. 5.128) with increase of size of delamination. It is seen that gap between the top and bottom surfaces of the delamination widens with the increase of size of delamination. However, the top surface at the center of delamination tends to depress due to local effect of the transverse loading on the top surface of the plate. If no delamination existed in the laminated plate (a=0), maximum tensile and compressive normal stresses (σ_{xx} and σ_{yy}) would have occurred at Point A. The variation of the maximum stresses at Point A with the size of delamination is shown in Fig. 5.131. It is seen that the tensile stresses increase smoothly with crack length, and the absolute values of compressive stresses decreasing with increasing of size of delamination, with the rate of change getting faster.

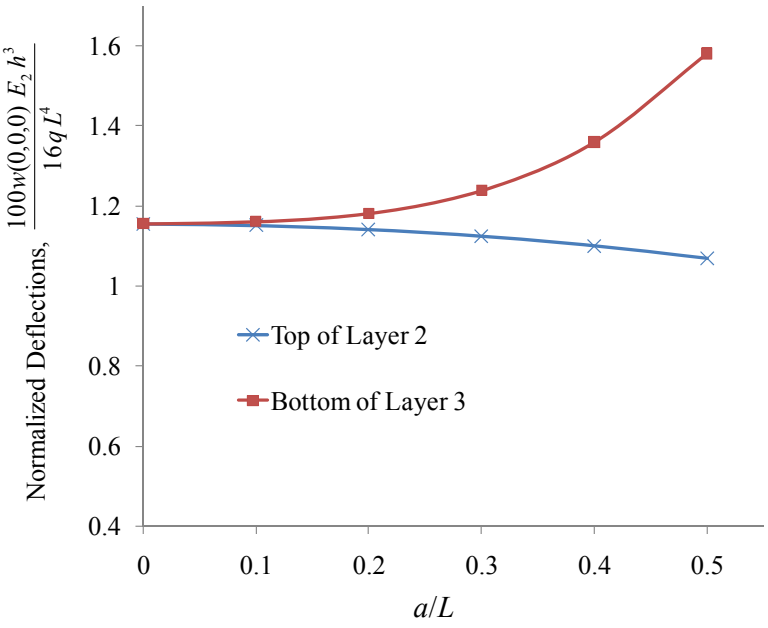

Fig. 5.130 Central deflections with variation of size of delamination

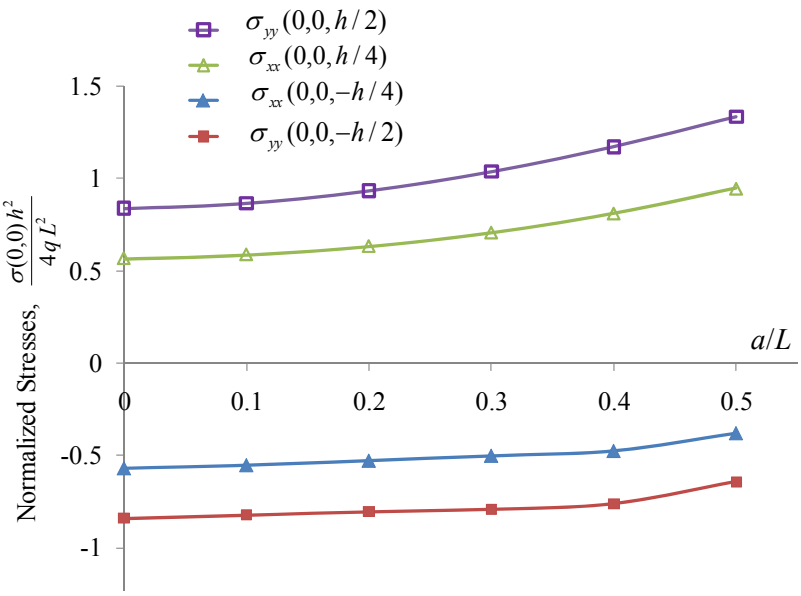

Fig. 5.131 In-plane stresses in central point with variation of size of delamination

In order to examine the behavior at delamination front where stress singularity is expected, energy release rates at the delamination front are obtained by VCCT. To apply VCCT, a new finite element mesh is needed, as shown in Fig. 5.132. Fig. 5.133 shows the variation of total ERR with the size of delamination with respect to edges A-A and B-B of the delamination. It is seen that the slope of the ERR curves become steeper with increase in size of delamination, the curve for edge B-B show large values because of the favorable disposition of the fibers in the interior layups. Fig. 5.134 shows the variation of ratio of ERR for opening mode (Mode I) and total ERR. It is seen that the contribution of opening mode decreases with increase in the size of delamination. It signifies that the share of contribution of shearing mode increases with increase with delamination size. It can further be noted that for edge A-A, the EPR ratio of shearing mode to total is more than 50% when $a/L > 0.2$.

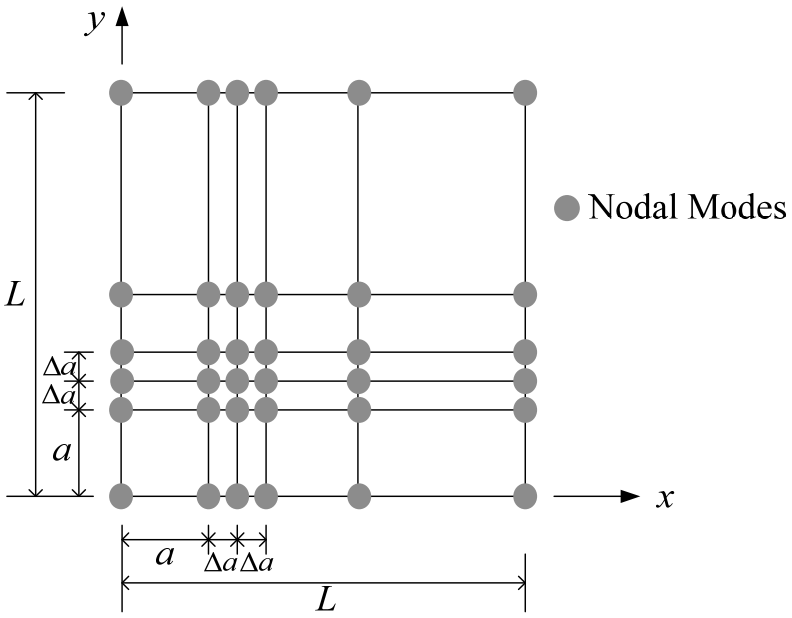

Fig. 5.132 Modeling scheme for VCCT

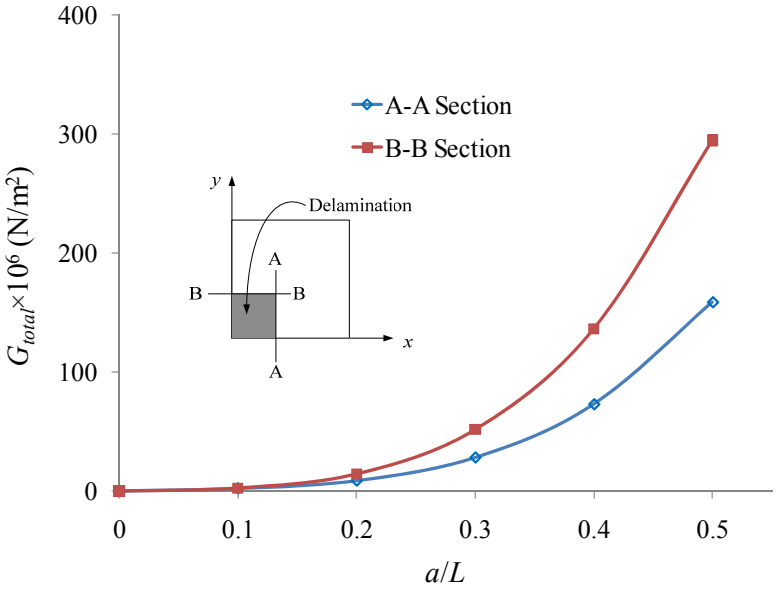

Fig. 5.6-133 Variation of total energy release rates with size of delamination

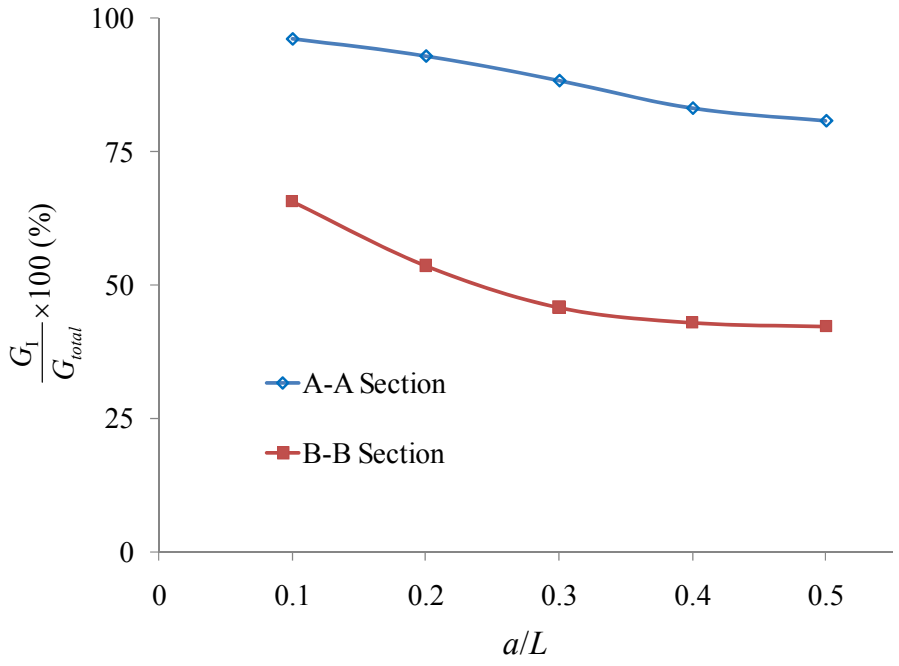

Fig. 5.6-134 Variation of ratios of opening ERR with respect to total ERR with size of delamination

CHAPTER VI

SUMMARY, CONCLUSIONS AND RECOMMENDATIONS

6.1 Summary of the Present Study

The summary of the outcome of the research effort to satisfy the stated objectives are as follows.

1. The state of the art for the modeling and simulation of single layer and laminated composite plates in the presence of various irregularities was reviewed. Also, the current status of patch repair of such structures was critically evaluated.
2. Improved finite element models were proposed for the analysis of unpatched and patched repaired plates. To represent the local 3D behavior of plate problems with localized irregularities, a set of improved and new elements, namely, ESLM, PDLM, and FDLM were proposed for the efficient analysis of such plates in the presence of various kinds of irregularities. On one extreme, FDLM simulated the 3D behavior closely in the context of 2D modeling. In the other extreme, ESLM simulated the 2D behavior in the context of a general plate element. These elements were based on hierarchical basis functions in the form of product of integrals of Legendre polynomials.
3. For computationally efficiency in non-smooth problems, that is those with any type of irregularity, transition elements designated as DLTM was developed for use in mixed models comprising two or three of the elements mentioned above. The efficiency of such modeling resulted from the fact that the computationally intensive elements

representing 3D behavior, say, FDLM need to be placed only in the region of irregularities where the behavior tends to be three dimensional.

4. Various special computational techniques associated with the proposed elements, like mapping of a non-parabolic curved boundary using blending functions, VCCT for efficient fracture mechanics computations, modified quadrature scheme specially adapted to the needs of the proposed elements, and the application of ordinary Kriging technique for post-processing of errors and mesh adaptation were covered for handling different modeling states related to non-routine problems.
5. To account for geometrically nonlinear behavior in the response of single-patch repaired plates, the necessary formulations based on total Lagrangian approach was developed.
6. All the formulations described above were implemented in the MATLAB as a series of script files.
7. The validity of efficient and reliable modeling scheme developed was demonstrated through a variety of plate problems with irregularities such as stepped plates, cutout problems, skew plates, cracked plates, laminated plates, and patch repaired plates as well as basic simple plate problems.
8. In order to study the characteristic behavior of patch repaired plates, some parametric studies were undertaken considering variables like damage type (cutout, center crack, double edge crack and single edge crack), patch type (symmetric and non-symmetric), patch materials, patch size, patch shape, adhesive thickness, nature of delamination, etc..

6.2 Conclusions

1. The analysis of a series of test problems with different types of irregularities using models based on the proposed elements led to results showing excellent agreement with those in the published literature. The main observations from these validation exercises are as follows.

   a) In the case of plates with the irregularity of stepped plates thickness, in addition to models with single element type, mixed models using the transition element DLTM was considered. Although both 3D single as well as mixed models gave excellent results, the mixed model was computationally most efficient.

   b) Developed models based on *p*-refinement were applied to rhombic plates with moment singularity of the type $r^{-0.8}$ at the obtuse corners. A very simple 5 element *hp*-mesh mesh with element size graded strongly towards the obtuse corner led to convergence to accurate displacements at *p*-level of 6 for planar variation and moments exhibiting the singular behavior accurately with *p*-level of 10, also for planar variation. The use of mixed model led to considerable reduction of computational effort without the loss of accuracy.

   c) In the case of rhombic laminated plates, excellent performance of the proposed modeling schemes was realized in comparison with reference values. In parametric studies involving skew angle and laminated plate thickness, the effect of shear deformation was found to decrease as the skew angle was increased, even in the case of thick laminated plates. However, for greater accuracy in computed transverse shear stresses in laminated plates with large skew angles, not only higher p_{xy}-levels but also higher p_z-levels were needed, so that oscillations in stress distribution could be

avoided.

d) In laminated plates with cross-ply and angle-ply laminates, stress singularities of transverse stresses near free edge could be clearly identified using the proposed finite element models. Also, the accuracy of the results was validated with reference values. In order to obtain reliable 3D stress field in the free-edge stress problems without excessive computational effort, the mixed modeling technique was helpful.

e) In the case of square plate with square cutout problem with stress singularities at the re-entrant corners, the simplest possible model using only one element led to results which agreed well with the published ones. In this case, the single element could accurately represent both the singular stress field at the re-entrant corner and the smooth field away from it. In the case of circular cutout problem with stress concentration at specific points around the free edge of the cutout, a five element mesh with special mapping technique based on blending functions was used in the case of the two elements abutting the circular cutout. The results were in excellent agreement with the published results based on conventional *h*-FEM as well as analytical solution.

f) The use of expanded Gauss-Lobatto numerical quadrature led to accurate evaluation of integrals and also enabled direct evaluation of stress at element boundary without the need for a special post-processing step.

g) In center cracked plates, it was shown that a posteriori error estimator using the modified SPR method, previously used for adaptive *h*-refinement, can be effectively used for adaptive *p*-refinement of a finite element model. Solutions of high accuracy were successfully obtained by using the ordinary Kriging interpolation technique in

which the weighted least-squares method was applied to finite element stress data at the Gauss points with the associated weight factors determined from a variogram model. The quality of these solutions was found to be superior to those obtained by the conventional polynomial interpolation of the stress data based on least squares approximation.

h) A delamination analysis scheme based on the proposed finite element models and VCCT was developed for application to the classical double cantilever beam problem and symmetrical cross-ply laminated plates with interior damage. For initiation and growth of delamination in the double cantilever beam, a very simple modeling scheme was suggested compared with those applied to conventional *h*-FEM based models. Excellent performance of present analysis was demonstrated by comparing with published values obtained from experiment and *h*-FEM. In delamination growth analysis, the results of proposed delamination analysis agreed with the experimental results very closely. Also, there no oscillations were noticed in the predicted response curve of delamination growth; whereas, the technique using conventional *h*-FEM and VCCT showed significant oscillations during delamination growth. In addition, the variation of ERR obtained by proposed VCCT based approach was investigated with increase of delamination size in a laminated plate with interior delamination. According to fiber directions of orthotropic material, rates of opening and shearing modes could be calculated successfully for different delamination sizes.

2. A series of patched repaired plates subjected to tensile loading were analyzed by using the developed software led to the following observations.

a) Bonded patch repaired plate with circular cutout

i. After successful validation of the FDLM based model along with exact mapping of the curved boundary boundaries in comparison with published values based on experiment and *h*-FEM modeling, the problem of patch repairing of the same hole was considered.

ii. In the case of single-sided patch repair, the effect of thickness of parent plate modeled with the proposed elements was investigated. In the presence of relatively thicker patch or thinner plate, the inclusion of geometric nonlinearity in the formulation gave results showing excellent agreement with published experimental values.

iii. In general, bonded patch repair led to reduction of the value of stress concentration factor. The reduction was more pronounced in the patched face of the plate.

iv. In the case of single-sided patch repair, undesirable bending effect tends to reduce the effectiveness of the patch in reducing the stress concentration factor.

v. The variation of stress concentration factor was found to be linear across the plate thickness, which is in contrast with the constant value in the unpatched case.

vi. Considerably high transverse shear stresses were founded near the edge of adhesive at interface of parent plate and adhesive. Such high stresses can initiate delamination of adhesive.

vii. The configuration, thickness and size of adhesive layer in single-sided patch can affect the behavior of the plate. It would be preferable to use adhesive from outside edge of patch to the perimeter of circular hole in the parent plate.

viii. Between rectangular and circular shaped patches, the circular patch is preferable

because of smaller patch area and lesser possibility of delamination.

ix. It was found that transverse stresses in the adhesive increased with the increase in patch thickness.

b) Analysis of single-sided patched plates with center crack, double-edge crack, and single-edge crack.

i. Advantages of simple modeling scheme and efficiency of calculation using PDLM were confirmed.

ii. Performance of patched plates in each case was shown in comparison with those of unpatched plates. It was found again that transverse stresses in the adhesive used in the patched plates tended to increase with increase in patch thickness.

iii. The stress fringe plots confirmed that the crack faces are stress free. This satisfaction of the natural boundary conditions at the crack faces supports the high accuracy of the results obtained.

iv. It was also noted from the stress fringe plots that, in general, the response of center crack and double-edge crack panels were somewhat similar.

v. The effect of patch repair was found to significantly reduce or eliminate the crack tip peak stress at the patched surface of the plate and increase it at the free surface, resulting from bending of the plate.

vi. The patch repair was found to reduce the SIF significantly; but as expected an increase in crack size causes it to rise at an increasing rate.

vii. In the presence of patch repair, the driving forces for fracture were found to weaken and the degree of such weakening is dependent on the stiffness of the patch material. Moreover, it was found that although the response curves with

boron-epoxy and graphite epoxy patch materials are quite similar, the gap between the two increases with growing crack size. The boron-epoxy curve normally appears above the graphite-epoxy based curve, except in the case of energy share ratio, where the two curves cross at a point.

viii. As single-sided patch repair causes bending of the cracked parent plate, causing the normal stress to vary across the plate thickness.

ix. The added resistance offered by composite patch material tends to inhibit crack growth in the parent cracked aluminum plate.

x. In order to uniformly reduce the crack driving force through the thickness of the aluminum plate, it is more advantageous to use patch repair on both the faces; but in real life situations that may not always be possible, especially if only one of the surfaces is inaccessible.

c) Parametric studies on cracked plates with single-sided patch repair.

i. To identify the best modeling strategy, different models using FDLM and mixed modeling were used to analyze patched plates with single-edge crack. The performance of the modeling schemes was demonstrated in terms of the accuracy of SIF calculated by VCCT and SERR in comparison with reference values obtained by conventional *h*-FEM. This led to the choice of a mixed model comprising FDKLM and ESLM elements with appropriate transition element.

ii. A series of parametric studies were undertaken to indentify the influence of patch size, patch thickness, adhesive thickness, and type of patch material on SIF. These were followed by suitable recommendations for effective patch repair. The SIF at the middle surface of the plate was reduced at least by 50%, when single-sided patch is

used. Actual reduction is a function of patch thickness. Among other factors, the magnitude of this reduction is also a function of the thickness of the glue relative to the plate thickness. A larger value means larger drop in SIF value. The SIF was also found to be a function of the ratio of patch length to crack size, any value of this ratio greater than or equal to 2 leads to the maximum reduction SIF value.

iii. The relative performance of single-sided and double-sided patch was studied. Apart from a detailed understanding of the behavior of two, the performance double-sided patch was significantly more favorable than the single-sided ones.

iv. The proposed modeling scheme, highlighting modeling simplicity aided by the accuracy of proposed *p*-FEM models, led to the possibility of a effective general tool for undertaking parametric evaluations related to the preliminary design of new composite structural components.

6.3 Recommendations

1. The developed element models based on *p*-FEM can be extended to laminated shells, thermal stress analysis, eigenvalue and transient analyses of laminated surface structures.
2. The scheme for error estimation and adaptive refinement needs to be extended to all the proposed element types in the presence of different types of irregularities and associated patch repairs, if present.
3. A very important area requiring significant effort is the extension of the proposed element models to handle various types of material nonlinearities which can often be the integral part of damage initiation and propagation near localized irregularities. This

may include the development of cohesive element models for the initiation and propagation of cracks and delamination in laminated composites.

4. For accurate characterization of damage initiation and propagation in a complex heterogeneous material environment, further refined versions of the modeling scheme need to be developed to represent behavior at mesoscopic and microscopic levels.
5. Research needs exist in accommodating into the proposed analysis scheme, the effects of meso or microscopic level behavior to accurately predict the behavior of damaged laminated plates, like those related to delamination initiation and propagation.
6. In patch repaired systems, the effect of variables like loading types and other environmental conditions, namely, temperature, humidity, chemical attacks, etc., need to be investigated.
7. The subject area of research is rife for extending it into the stochastic area to assess the variability of sensitive parameters like patch size, patch location, damage type, etc. and their influence on the reliability of the patch repair.

REFERENCES

Achour, T., Bouiadjra, B.B., Serier, B. (2003). Numerical analysis of the performances of the bonded composite patch for reducing stress concentration and repairing cracks at notch, *Computational Materials Science*, 28, pp. 41-48.

Ahmad, S., Irons, B.M., Zienkiewicz, O.C. (1970) Analysis of thick and thin shell structures by curved finite elements *International Journal for Numerical Methods in Engineering*, 2, pp. 419-451.

Ahmed, N.U. (1989). *Higher order analysis of laminated composite based on p-version of the finite element method*, Ph. D. Dissertation, Vanderbilt University.

Ahmed, N.U., Basu, P.K. (1994). Higher-order finite element modeling of laminated composite plates, *International Journal for Numerical Methods in Engineering*, 37, pp. 123-139.

Altus, E., Rotem, A., Shmueli, M. (1980). Free edge effect in angle ply laminates - a new three dimensional finite difference solution, *Journal of Composite Materials*, 14, pp. 21-30.

Akhtar, M.N. (1989). *Stability analysis of thin-walled members using p-version of finite element method*, Ph. D. Dissertation, Vanderbilt University.

Aminpour, M.A., McCleary, S.L, Ransom, J.B., Housner, J.M. (1992). Global/local analysis method for treating details in structural design, Adaptive, multilevel, and hierarchical computational strategies, *Applied Mechanics Division*, 157, 119-127.

Anderson, T.L. (2004). *Fracture mechanics: Fundamentals and applications*, CRC Press.

Ayatollahi, M.R., Hashemi, R. (2007). Computation of stress factors (K_I, K_{II}) and T-stress for cracks reinforced by composite patching, Composite Structures, 78, pp. 602-609.

Baker, A.A. (1984). Repair of cracked or defective metallic components with advanced fiber composites - an overview of Australian work, *Composite Structures*, 2(2), pp. 153-181.

Baker, A.A. (1987). Fiber composite repair of cracked metallic aircraft components-practical and basic aspects, Composites, 18(4), pp. 293-308.

Barut, A., Hanauska, J., Madenci, E., Ambur, D.R. (2002). Analysis method for bonded patch repair of a skin with a cutout, *Composite Structures*, 55, pp. 277-297.

Basu, P.K., Rossow, M.P., Szabo, B.A. (1977). *Theoretical documentation and user's manual: COMET-X*, Report No. R-340, Federal Railroad Administration.

Belhouari, M., Bouiadjra B.B., Megueni, A., Kaddouri, K. (2004). Comparison of double and single bonded repairs to symmetric composite structures: a numerical analysis, *Composite Structures*, 65, pp. 47-53.

Bert, C.W. (1973). Simplified analysis of static shear correction factors for beams of non-homogeneous cross section, *Journal of Composite Materials*, 7, pp. 525-529.

Bouiadjra, B.B., Belhouari, M., Serier, B. (2002). Computation of the stress intensity factors for repaired cracks with bonded composite patch in mode I and mixed mode, *Composite Structures*, 56, pp. 401-406.

Bowie O.L. (1972). Solution of plane crack problems by mapping technique methods of analysis of crack problems, *Noordhoff International Publishing Presents*, 1, pp.1-55.

Camanho, P.P., Davila, C.G., de Moura, M.F. (2003). Numerical simulation of mixed-mode progressive delamination in composite materials, *Journal of Composite Materials*, 37(16), pp. 1415-1438.

Carrera, E. (1996). C^0 Reissner-Mindlin multilayered plate element including zig-zag and interlaminar stress continuity, *International Journal for Numerical Methods in Engineering*, 39, pp. 1797-1820.

Carrera, E. (1998). Evaluation of layerwise mixed theories for laminated plates analysis, *AIAA Journal*, 36(5), pp. 830-839.

Carrera, E. (1999). Transverse normal stress effects in multilayered plates, *Journal of Applied Mechanics*, 66, pp. 1004-1012.

Chang, F.K., Perez, J.L., Chang, K.Y. (1990). Analysis of thick laminated composites, *Journal of Composite Materials*, 24, pp. 801-821.

Chen, Y., Jiao, X. (2001). Semivariogram fitting with linear programming, *Computers & Geosciences*, 27, pp. 71-76.

Cho, M., Kim, J.S. (2001). Higher-order zig-zag composite plate theory with multiple delamination, *Journal of Applied Mechanics*, 68, pp. 869-877.

Chow, T.S. (1971). On the propagation of flexural waves in an orthotropic laminated plate and its response to an impulsive load, *Journal of Composite Materials*, 5, pp. 306-319.

Crim, A.W. (1992). *Development of the boundary element method and combination with the finite method in p-version*, Ph. D. Dissertation, Vanderbilt University.

Crull, M.M. (1989) *Adaptive mixed method p-version finite element analysis of rotational shells*, Ph. D. Dissertation, Vanderbilt University.

Davila, C.G., Johnson, E.R. (1993). Analysis of delamination initiation in postbuckled

dropped-ply laminates, *AIAA Journal*, 31(4), pp. 721-727.

Davila, C.G. (1994). Solid-to-shell transition elements for the computation of interlaminar stresses, *Computing Systems in Engineering*, 5(2), pp. 193-202.

Davila, C.G., Camanho, P.P., Turon, A. (2007). *Cohesive elements for shells*, NASA/TP-2007-214869.

Denney J.J., Mall S. (1997). Characterization of disbond effects on fatigue crack growth behavior in aluminum plate with bonded composite patch, *Engineering Fracture Mechanics*, 57(5), pp. 507-525.

Dong, S.B., Pister, K.S., Taylor, R.L. (1962). On the theory of laminated anisotropic shells and plates, *Journal of Aeronautical Science*, 29(8), pp. 969-975.

Garusi, E., Tralli, A. (2002). A hybrid stress-assumed transition element for solid-to bema and plate-to-beam connections, *Computers and Structures*, 80, pp. 105-115.

Ghosh, D.K. (1996). *Parallelism in adaptive p-version finite element analysis*, Ph. D. Dissertation, Vanderbilt University.

Glaessgen, E.H., Riddell, W.T., Raju, I.S. (2002). Nodal constraint, shear deformation and continuity effects related to the modeling of debonding of laminates using plate elements, *Computer Modeling in Engineering and Sciences*, 3(1), pp. 103-116.

Gordon, W.J., Hall, C.A. (1973). Transfinite element methods: Blending-function interpolation over arbitrary curved element domains. *Numerische Mathematik*, 21, pp. 109-129.

Hall, R.L., Merrill, C.A. (1987). *Evaluation of the p-level finite element program 'FISTA'*, Army Engineer Waterways Experiments Station, ADA181511.

Hellen, T.K. (1975). On the method of the virtual crack extension, *International Journal for Numerical Methods in Engineering*, 9(1), pp. 187-207.

Hildebrand, F.B., Reissner, E., Thomas, G.B. (1938). *Notes on the foundations of the theory of small displacements of orthotropic shells*, NACA TN-1833, Washington D. C..

Hinton, E., Owen, D.R.J. (1984). *Finite element software for plates and shells*, Pineridge Press, Swansea, U.K.

Hrudey, T.M., Hrabok, M.M. (1986). Singularity finite elements for plate bending, *Journal of Engineering Mechanics*, 112(7), pp. 666-681.

Hwang, C.G., Wawrzynek, P.A., Tayebi, A.K., Ingraffea, A.R. (1998). On the virtual crack extension method for calculation of the rates of energy release rate, *Engineering Fracture Mechanics*, 59, pp. 521-542.

Irwin, G.R. (1956). Onset of fast crack propagation in high strength steel and aluminum alloys, *Sagamore Research Conference Proceedings*, 2, pp. 289-305.

Isida, M. (1971). Effect of width and length on stress intensity factors of internally cracked plates under various boundary conditions, *International Journal of Fracture*, 7(3), pp. 301-316.

Jin, Z.H., Sun, C.T. (2005). Cohesive zone modeling of interface fracture in elastic bi-materials, *Engineering Fracture Mechanics*, 72(12), pp. 1805-1817.

Jones, R. (1983). Neutral axis offset effects due to crack patching, *Composite Structures*, 1(2), pp. 163-174.

Jones, R., Callinan, R., Teh, K.K., Brown, K.C. (1984). Analysis of multi-layer laminates using three-dimensional super elements, *International Journal for Numerical Methods in Engineering*, 20(3), pp. 583-587.

Jones, R., Molent, L., Baker, A.A., Davis, M.J. (1988). Bonded repair of metallic components: Thick sections, *Theoretical and Applied Fracture Mechanics*, 9(1), pp. 61-70.

Jones, R., Chiu, W.K. (1999). Composite repairs to cracks in thick metallic components, *Composite Structures*, 44, pp. 17-29.

Kassapoglou, C. (1990). Determination of interlaminar stresses in composite laminates under combined loads, *Journal of Reinforced Plastics and Composites*, 9(1), pp. 33-58.

Kim, R.Y., Soni, S.R. (1984). Experimental and analytical studies on the onset of delamination in laminated composites, *Journal of Composite Materials*, 18(1), pp. 70-80.

Kruger, R. (1994). *Three dimensional finite element analysis of multidirectional composite DCB, SLB and ENF specimens*, ISD-Report No. 94/2.

Krueger, R. (2002). *The virtual crack closure technique: history, approach and applications*, NASA/CR-2002-211628.

Kulkarni, S.D., Kapuria, S. (2007). A new discrete Kirchhoff quadrilateral element based on the third-order theory for composite plates, *Computational Mechanics*, 39(3), pp. 237-246.

Kwon, Y.W, Akin, J.E. (1987). Analysis of layered composite plates using a higher-order deformation theory, *Computers and Structures*, 27, pp. 619-623.

Lee, K.H., Senthinlnathan, N.R., Lim, S.P., Chow, S.T. (1990). An improved zig-zag model for the bending of laminated composite plates, *Composite Structures*, 15, pp. 137-148

Lee, K.H., Lin, W.Z., Chow, S.T. (1994). Bi-directional bending of laminated composite plates using an improved zig-zag model, *Composite Structures*, 28, pp. 283-294.

Liao, C.L., Reddy, J.N., Engelstad, S.P. (1988). A solid-shell transition element for geometrically nonlinear analysis of composite structures, *International Journal for Numerical Methods in Engineering*, 26, pp. 1843-1854.

Lloyd, C.D., Atkinson, P.M. (2001). Assessing uncertainty in estimates with ordinary and indicator kriging, *Computers & Geosciences*, 27(8), pp. 929-937.

Lo, K.H., Christensen, R.M., Wu, E.M. (1977). A higher order theory of plate deformation, Part II: Laminated plates, *Journal of Applied Mechanics*, 44, pp. 669-676.

Lo, K.H., Christensen, R.M., Wu, E.M. (1978). Stress solution determination for high order plate theory, *International Journal of Solids and Structures*, 14(8), pp. 655-662.

Mao, K.M., Sun, C.T. (1991). A refined global-local finite element analysis method, *International Journal for Numerical Methods in Engineering*, 32, pp. 91-112.

Matthews, F.L., Camanho, P.P. (1999). Delamination onset prediction in mechanically fastened joints in composite laminates, *Journal of Composite Materials*, 33(10), pp. 906-927.

Megueni, A., Bouiadjra, B.B., Belhouari, M. (2004). Disbond effect on the stress intensity factor for repairing cracks with bonded composite patch, Computational Materials Science, 29 (2004) 407-413.

Mindlin, R.D. (1951). Influence of rotatory inertia and shear in flexural motions of isotropic elastic plates, *Journal of Applied Mechanics*, 18, pp. 1031-1036.

Meo, M., Thieulot, E. (2005). Delamination modeling in a double cantilever beam, *Composite Structures*, 71, pp. 429-434.

Morley, L.S.D. (1962). Bending of a simply supported rhombic plate under uniform normal loading, *The Quarterly Journal of Mechanics & Applied Mathematics*, 15(4), pp. 413-426.

Morley, L.S.D. (1970). A finite element application of the modified Rayleigh-Ritz method, *International Journal for Numerical Methods in Engineering*, 2, pp. 85-98.

Murakami, H. (1986). Laminated composite plate theory with improved in-plane responses, *Journal of Applied Mechanics*, 53, pp. 661-666.

Murakami, H., Toledano, A. (1987). A high-order laminated plate theory with improved in-plane response, *International Journal of Solids and Structures*, 23, pp. 111-131.

Naboulsi, S., Mall, S. (1996). Modeling of a cracked metallic structure with bonded

composite patch using the three layer technique, *Composite Structures*, 35(3), pp. 295-308.

Naboulsi, S., Mall, S. (1997). Characterization of fatigue crack growth in aluminum panels with a bonded composite patch, *Composite Structures*, 37, pp. 321-334.

Nguyen, V.T., Caron, J.F. (2006). A new finite element for free edge effect analysis in laminated composites, Computers & Structures, 84, pp. 1538-1546.

Noor, A.K. (1973a). Mixed finite-difference scheme for analysis of simply supported thick plates, *Computers and Structures*, 3, pp. 967-982.

Noor, A.K. (1973b). Free vibrations of multilayered composite plates, *AIAA Journal*, 11, pp. 1038-1039.

Ouinas, D., Bouiadjra, B.B., Serier, B. (2007a). The effects of disbonds on the stress intensity factor of aluminium panels repaired using composite materials, *Composite Structures*, 78, pp. 278-284

Ouinas, D., Bouiadjra, B.B., Serier, B., Saidbekkouche, M. (2007b). Comparison of the effectiveness of boron/epoxy and graphite/epoxy patches for repaired cracks emanating from a semicircular notch edge, *Composite Structures*, 80, pp. 514-522.

Owen, D.R.J, Fawkes, A.J. (1983). *Engineering fracture mechanics: Numerical methods and applications*, Pineridge Press Ltd., Swansea, U.K..

Owen, D.R.J., Li, Z.H. (1987a). A refined analysis of laminated plates by finite element displacement methods – I. Fundamentals and static analysis, *Computers and Structures*, 26(6), pp. 907-914.

Owen, D.R.J., Li, Z.H. (1987b). A refined analysis of laminated plates by finite element displacement methods – II. Vibration and stability, *Computers and Structures*, 26(6), pp. 915-923.

Pagano N.J. (1969). Exact solutions for composite laminates in cylindrical bending, *Journal of Composite Materials*, 3, pp. 398-411.

Pagano, N.J. (1970). Exact solutions for rectangular bidirectional composites and sandwich plates, *Journal of Composite Materials*, 4, pp. 20-34.

Pagano, N.J., Hatfield, S.J. (1972). Elastic behavior of multilayered bidirectional composites, *AIAA Journal*, 10, pp. 931-933.

Pagano N.J. (1978a) Stress fields in composite laminates, *International Journal of Solids and Structures*, 14(5), pp. 385-400.

Pagano, N.J. (1978b) Free edge stress fields in composite laminates, *International Journal of Solids and Structures*, 14(5), pp. 401-406.

Pagano, N.J., Soni, S.R. (1983). Global-local laminate variational model, *International Journal of Solids and Structures*, 19(3), pp. 207-228.

Papanikos, P., Tserpes, K.I., Pantelakis, S. (2007). Initiation and progression of composite patch debonding in adhesively repaired cracked metallic sheets, *Composite Structures*, 81, pp. 303-311.

Pardo-Iguzquiza, E., Dowd, P.A. (2001). VARIOG2D: a computer program for estimating the semi-variogram and its uncertainty, *Computers & Geosciences*, 27, pp. 549-561.

Park, J.W., Kim, Y.H. (2002). Re-analysis procedures for laminated plates using FSDT finite element model, *Computational Mechanics*, 29, pp. 226-242.

Pilkey, W.D., Pilkey, F.P. (2008). *Peterson's stress concentration factors*. Third edition, Wiley.

Pipes, R.B., Pagano, N.J. (1970). Interlaminar stresses in composite laminates under uniform axial extension, *Journal of Composite Materials*, 4(4), pp. 538-548.

Puppo, A.H., Evensen H.A. (1970). Interlaminar shear in laminated composites under generalized plane stress, *Journal of Composite Materials*, 4(2), pp. 204-220.

Quaresimin, M., Ricotta. M. (2006). Stress intensity factors and strain energy release rates in single lap bonded joints in composite materials, *Composite Science and Technology*, 66, pp. 647-656.

Raju, I.S. (1987). Calculation of strain-energy release rates with higher order and singular finite elements, *Engineering Fracture Mechanics*, 28(3), pp. 254-274.

Raju, I.S., Crews, J. (1988). Convergence of strain energy release rate components for edge-delaminated composite laminates, *Engineering Fracture Mechanics*, 30(3), pp. 383-396.

Ramesh, S.S., Wang, C.M., Reddy, J.N., Ang, K.K. (2009). A higher-order plate element for accurate prediction of interlaminar stresses in laminated composite plates, *Composite Structures*, 91, pp. 337-357.

Ratwani, M.M. (1979). Analysis of cracked, adhesively bonded laminated structures, *AIAA Journal*, 17(9), pp. 988-994.

Reddy, J.N. (1984). A simple higher-order theory for laminated composite plates, *Journal of Applied Mechanics*, 51, pp. 745-752.

Reddy, J.N. (1987). A generalization of two-dimensional theories of laminated composite plates, *Communications in Applied Numerical Methods*, 3, pp. 173-180.

Reddy, J.N. (2004a). *An introduction to nonlinear finite element analysis*, Oxford

University Press.

Reddy, J.N. (2004b). *Mechanics of laminated composites plates and shells; theory and analysis*, Second Edition, CRC Press.

Reddy, J.N. (2006). *An introduction to the finite element method*, Third Edition, McGrawHill.

Reissner, E. (1945). The effect of transverse shear deformation on the bending of elastic plates, *Journal of Applied Mechanics*, 12, pp. 69-76.

Reissner, E., Stavsky, Y. (1961). Bending and stretching of certain types of aeolotropic elastic plates, *Journal of Applied Mechanics*, 28, pp. 402-408.

Reissner, E. (1972). A consistent treatment of transverse shear deformation in laminated anisotropic plates, *AIAA Journal*, 10(5), pp. 716-718.

Reissner, E. (1975). Transverse bending of plates including the effect of transverse shear deformation, *International Journal of Solids and Structures*, 11, pp. 569-573.

Reissner, E. (1979). Note on the effect of transverse shear deformation in laminated anisotropic plates, *Computer Methods in Applied Mechanics Engineering*, 20, pp. 203-209.

Ren, J.G. (1987). Exact solutions for laminated cylindrical shells in cylindrical bending, *Composite Science and Technology*, 29, pp. 169-187.

Rice, J.R. (1968). A path independent integral and the approximate analysis of strain concentration by notches and cracks, *Journal of Applied Mechanics*, 35, pp. 379-386.

Robbins Jr., D.H., Reddy, J.N. (1996). Variable kinematic modeling of laminated composite plates, *International Journal for Numerical Methods in Engineering*, 39, pp. 2283-2317.

Rohwer, K. (1992). Application of higher order theories of the bending analysis of layered composite plates, *International Journal of Solids and Structures*, 29(1), pp. 105-119.

Rohwer, K., Friedrichs, S., Wehmeyer, C. (2005). Analyzing laminated structures from fibre-reinforced composite materials-an assessment, *Technische Mechanik*, 25(1), pp. 59-79.

Rybicki, E.F., Kanninen, M.F. (1977). A finite element calculation of stress intensity factors by a modified crack closure integral, *Engineering Fracture Mechanics*, 9(4), pp. 931-938.

Rybicki, E.F., Schmueser, D.W., Fox, J. (1977). An energy release rate approach for stable crack growth in the free-edge delamination problem, *Journal of Composite*

Materials, 11, pp. 470-487.

Savoia, M., Reddy, J.N. (1992). A variational approach to three-dimensional elasticity solutions of laminated composite plates, *Journal of Applied Mechanics*, 59, pp. S166-S175.

Senthilnathan, N.R., Lim, S.P., Lee, K.H., Chow, S.T. (1987). Buckling of shear-deformable plates, *AIAA Jouranl*, 25(9), pp. 1268-1271.

Sheikh, A.H., Chakrabarti, A. (2003). A new plate bending element based on higher-order shear deformation theory for the analysis of composite plates, Finite Element in Analysis and Design, 39, pp. 883-903.

Soutis, C., Hu, F.Z. (1997). Design and performance of bonded patch repairs of composite structures, *Proceedings of the Institution of Mechanical Engineers, Part G: Journal of Aerospace Engineering*, 211(4), pp. 263-271.

Spiker, R.L, Chou, S.C. (1980). Edge effects in symmetric composite laminates: importance of satisfying the traction-free-edge condition, *Journal of Composite Materials*, 14, pp. 2-20.

Srinivas, S., Rao, C.V.J., Rao, A.K. (1970). An exact analysis for vibration of simply-supported homogeneous and laminated thick rectangular plates, *Journal of Sound and Vibration*, 12, pp. 187-199.

Srinivas, S., Rao, A.K. (1970). Bending vibration and buckling of simply supported thick orthotropic rectangular plates and laminates, *International Journal of Solids and Structures*, 6, pp. 1463-1481.

Stavsky, Y. (1961). Bending and stretching of laminated aeolotropic plates, *Journal of Engineering Mechanics*, 87(6), pp. 31-56.

Sun, C.T., Whiteny J.M. (1973). Theories for the dynamic response of laminated plates, *AIAA Journal*, 11(2), pp. 178-183.

Sun, C.T., Liao, W.C. (1990). Analysis of thick section composite laminates using effective moduli, *Journal of Composite Materials*, 24, pp. 977-993.

Surana, K.S. (1980). Transition finite elements for three-dimensional stress analysis, International *Journal for Numerical Methods in Engineering*, 15, pp. 991-1020.

Tada, H., Paris, P., Irwin, G.R. (1985). *The stress analysis of cracks handbook*, Paris Production Inc..

Tahani, M., Nosier, A. (2003a). Free edge stress of general cross-ply composite laminates under extension and thermal loading, *Composite Structures*, 60, pp. 91-103.

Tahani, M., Nosier, A. (2003b). Three-dimensional interlaminar stress analysis at free

edges of general cross-ply composite laminates, *Materials and Design*, 24, pp. 121-130.

Thompson, D.M., Griffin, Jr., O.H. (1990). 2-D to 3-D global/local finite element analysis of cross-ply composite laminates, *Journal of Reinforced Plates and Composites*, 9, pp. 492-502.

Ting, T., Jones, R., Chiu, W.K., Marshall, I.H., Greer, J.M. (1999). Composite repairs to rib stiffened panels, *Composite Structures*, 47, pp. 737-743.

Turon, A., Camanho, P.P., Costa, J., Davila, C.G. (2006). A damage model for the simulation of delamination in advanced composites under variable-mode loading, *Mechanics of Materials*, 38, pp. 1072-1089.

Ugural, A.C. (1998). *Stresses in plates and shells*, Second Edition, McGraw-Hill Science/Engineering/Math.

Ugural, A.C., Fenster, S.K. (2003). Advanced strength and applied elasticity, Fourth edtion, Prentice Hall PTR.

Umanaheswar, T.V.R.S., Singh, R. (1999). Modelling of a patch repair to a thin cracked sheet, *Engineering Fracture Mechanics*, 62, pp. 267-289.

Varadan, T.K., Bhaskar, K. (1991). Bending of laminated orthotropic cylindrical shells – an elasticity approach, *Composite Structures*, 17, pp. 141-156.

Wang, A.S.D., Crossman, F.W. (1977). Some new results on edge effect in symmetric composite laminates. Jouranl of Composite Materials, 11, pp. 92-106.

Wang, A.S.D., Crossman, F.W. (1978). Calculation of edge stresses in multi-layer laminates by sub-structuring, *Journal of Composite Materials*, 12, pp. 76-83.

Wang, C.H., Rose, L.R.F., Callinan, R. (1998). Analysis of out-of-plane bending in one-sided bonded repair, *International Journal of Solids and Structures*, 35(14), pp. 1653-1675.

Wang, S.S., Choi, I. (1982a). Boundary-layer effects in composite laminates: Part 1 – Free-edge stress singularities, *Journal of Applied Mechanics*, 49, pp. 541-548.

Wang, S.S., Choi, I. (1982b). Boundary-layer effects in composite laminates: Part 2 – Free-edge stress solutions and basic characteristics, *Journal of Applied Mechanics*, 49, pp. 549-560.

Whitcomb, J.D., Raju, I.S., Goree, J.G. (1982) Reliability of the finite element method for calculating free edge stresses in composite laminates, *Computers and structures*, 15(1), pp. 23-37.

Whitcomb, J.D., Woo, K. (1993a). Application of iterative global/local finite analysis.

Part I: Linear analysis, *Communications in Numerical Methods in Engineering*, 9(9), pp. 745-756.

Whitcomb, J.D., Woo, K. (1993b). Application of iterative global/local finite analysis. Part II: Geometrically non-linear analysis, *Communications in Numerical Methods in Engineering*, 9(9), pp. 757-766.

Whitney, J.M., Leissa, A.W. (1969). Analysis of heterogeneous anisotropic plates, *Journal of Applied Mechanics*, 36(2), pp. 261-266.

Whitney, J.M., Pagano, N.J. (1970). Shear deformation in heterogeneous anisotropic plates, *Journal of Applied Mechanics*, 37(4), pp. 1031-1036.

Whitney, J.M. (1973). Shear correction factors for orthotropic laminates under static load, *Journal of Applied Mechanics*, 40(1), pp. 302-304.

Whitney, J.M., Sun, C.T. (1973). A higher order theory for extensional motion of laminated composites, *Journal of Sound and Vibration*, 30, pp. 85-97.

Whitney, J.M., Nuismer, R.J. (1974). Stress fracture criteria for laminated composites containing stress concentrations, *Journal of Composite Materials*, 8(3), pp. 253-265.

Whitney, J.M. Sun, C.T. (1974). A refined theory for laminated anisotropic, cylindrical shells, *Journal of Applied Mechanics*, 41, pp. 471-476.

Wittrick, W.H. (1987). Analytical three-dimensional elasticity solutions to some plate problems and some observations on Mindlin's plate theory, *International Journal of Solids and Structures*, 23, pp. 441-464.

Woo, K.S. (1988) *High precision analysis of plates and cylindrical shells in the presence of singularities by the p-version of the finite element method*, Ph. D. Dissertation, Vanderbilt University (1988).

Yang, P.C., Norris, C.H., Stavsky Y. (1966). Elastic wave propagation in heterogeneous plates, *International Journal of Solids and Structures*, 2, pp. 665-684.

Yugawa, G., Nishioka, T. (1979). Finite element analysis of stress intensity factors for plate extension and plate bending problems, *International Journal for Numerical Methods in Engineering*, 14, pp. 727-740.

Zaghloul, S.A., Kennedy, J.B. (1975). Nonlinear behavior of symmetrically laminated plates, *Journal of Applied Mechanics*, 42, pp. 234-236.

Zienkiewicz, O.C., Zhu, J.Z. (1992). The superconvergent patch recovery and a posteriori error estimates, part 1: the recovery technique, *International Journal for Numerical Methods in Engineering*, 33, pp. 1331-1364.